ON THE INTERACTIONS BETWEEN THE INNER AND OUTER REGION MOTIONS IN TURBULENT BOUNDARY LAYERS

By

Joseph Charles Klewicki

A DISSERTATION

Submitted to
Michigan State University
in partial fulfillment of the requirements
for the degree of

DOCTOR OF PHILOSOPHY

Department of Mechanical Engineering

1989

ABSTRACT

ON THE INTERACTIONS BETWEEN THE INNER AND
OUTER REGION MOTIONS IN TURBULENT BOUNDARY LAYERS

By

Joseph Charles Klewicki

Time resolved spanwise vorticity measurements were made in very thick zero pressure gradient boundary layers over the Reynolds number range $1,010 \le R_\theta \le 4,850$. The scale of the flow field relative to the size of the four-wire spanwise vorticity probe resulted in very good spatial resolution measurements. Detailed results relating to the accuracy of the present measurements are presented.

Physical arguments are employed to justify the hypothesis that the important instantaneous vortical motions in turbulent boundary layers organize into essentially two geometries. Near the solid surface it is proposed that the vorticity distributions have a two dimensional sheet-like character. Farther away from the wall it is proposed that the important vortical motions organize in the form of closed loops. From these deductions, it is hypothesized that the essential features of the so-called inner/outer interaction in turbulent boundary layers may be described in terms of the interaction of these loop-like and sheet-like vortical motions.

The single probe results suggest that in the near-wall region the

spanwise vorticity statistics are universal under inner variable scaling. However, inner variable normalizations of the Reynolds stress and velocity vorticity correlations related to the transport of the stress exhibit significant R_θ variations. The present higher order spanwise vorticity statistic profiles are shown to be consistent with the process of high intensity hairpin vortex-like and/or lifted shear layer-like motions arising from the sublayer. Interpretation of $\langle u\omega_z \rangle$ data reveals a plausible initiating mechanism for the formation of these lifting sublayer motions.

Two point spanwise vorticity correlations at a constant spanwise probe separation decreased in magnitude as the distance from the wall increased. Analysis of the correlations with probe separations normal to the wall revealed the frequent occurrence of organized counter-rotating spanwise vorticity interactions in the wall region. In general, the correlations did not provide evidence supporting the existence of large scale motions endowed with significant spanwise vorticity. Preliminary results from two-view flow visualization movies support the present hypotheses.

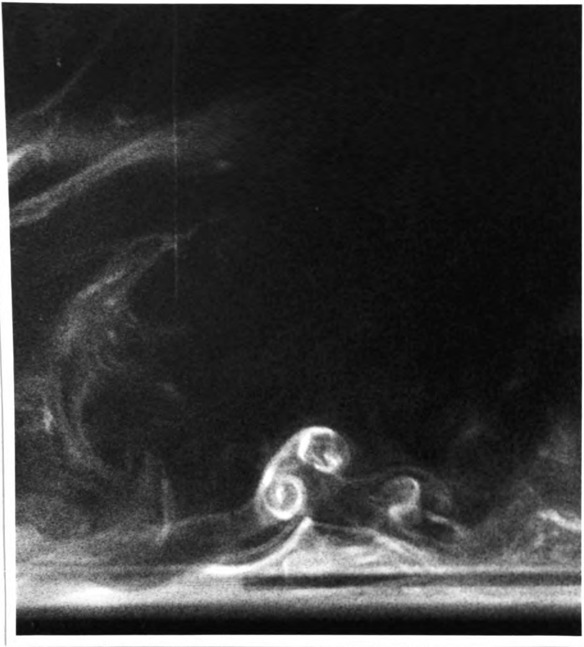

"... one should also consider the existence of small-scale convected vortices to explain the observed sublayer structure ..." W. W. Willmarth (1975)

ACKNOWLEDGMENTS

Although this dissertation has only one author, its completion depended on the help and support of a number of people.

First and foremost I would like to acknowledge the support of my family. Over the course of my graduate studies I have benefited from the patience, love and understanding of my wife Cindy, our two children Brian and Maureen, my parents, my brother and my sisters. Also I would like to specifically thank my sister Casey who inspired me to become a mechanical engineer.

I would like to express gratitude to my advisor, Robert Falco, for his guidance and assistance, and for allowing me the freedom in the laboratory to explore interesting issues.

Concerning the work presented here I would like to acknowledge the support of the Air Force Office of Scientific Research, and specifically to our grant monitor Dr. J. McMichael.

Concerning my work in the Turbulence Structure Laboratory, thanks are due to all of my co-workers, but especially to Daniel Chu, Frank Cummings and Chuck Gendrich.

Finally, I would like to thank my committee members, Steve Shaw, John Foss, Manooch Koochesfahani, and T. Y. Li for their useful guidance throughout my Ph.D. program. Special thanks go to Steve for his friendship, and to John for his detailed reading and remarks concerning this manuscript.

TABLE OF CONTENTS

LIST OF TABLES

LIST OF FIGURES

LIST OF SYMBOLS

Roman

A Additive constant in King's law calibration equation

B Multiplicative constant in King's law calibration equation

C Additive "law of the wall" constant; Calibration correction

C_f Skin friction coefficient = $\tau_w/(1/2\rho U_\infty{}^2)$

C_p Pressure coefficient = $dp/\rho U_\infty{}^2$

d Channel flow width

E Hot-wire voltage

f Frequency

f_c Cut-off frequency

f_k Kolmogoroff frequency = $U_1/2\pi\eta$

f_s Sampling frequency

h Wire spacing appropriate to velocity gradient measurements

H Boundary layer shape factor

ℓ Hot-wire length

K Kurtosis, fourth central statistical moment

n Exponent in King's law calibration equation

p Pressure

rms Root mean square

R Number of A-to-D registers representing S_{max}

R_λ Microscale Reynolds number = $u'\lambda/\nu$

R_θ Boundary layer flow Reynolds number = $U_\infty\theta/\nu$

$R_{d/2}$ Channel flow Reynolds number = $U_c d/2\nu$

s X-array wire spacing

S Skewness, third central statistical moment

S_{max} Maximum hot-wire signal level

t Time

T Averaging time

u Streamwise velocity

u_τ Friction velocity = $(\tau_w/\rho)^{1/2}$

U_1 Local mean velocity

U_c Mean channel centerline velocity; Convection velocity

U_∞ Boundary layer free stream velocity

v Normal velocity

V Calibration velocity vector

w Spanwise velocity

x Streamwise Cartesian coordinate

y Normal Cartesian coordinate

z Spanwise Cartesian coordinate

Greek

α Angular frequency

β Hot-wire angle correction

δ Boundary layer thickness also δ_{99}

Δd Digitizing increment = S_{max}/R

Δt Time increment = $1/f$

ΔU^+ Deviation of mean wake profile from the logarithmic law

Δx Small displacement in the streamwise direction

Δy Small displacement in the normal direction

Δz Small displacement in the spanwise direction

ϵ Dissipation rate; Signal noise level

ϵ_{ijk} Alternating tensor

${\epsilon_u}^2$ Streamwise velocity signal noise level

γ Angle of probe axis with the free stream

η Kolmogoroff microscale = $(\nu^3/\epsilon)^{1/4}$

κ von Karman's constant = 0.41

λ Taylor microscale = $u'/(\partial u/\partial x)'$

ν Kinematic viscosity

Π Coles wake parameter

Φ Frequency spectrum

Ψ Spectral function = $\alpha \cdot \Phi$

ρ Fluid density

θ Momentum deficit thickness

τ Shear stress

τ_w Wall shear stress

ω Vorticity, may be fluctuating or total depending on context

ω_x Streamwise vorticity component

ω_y Normal vorticity component

ω_z Spanwise vorticity component

Ω_z Mean spanwise vorticity component

Superscripts

i Refers to an inner variable normalization

o Refers to an outer variable normalization

+ Normalized by ν and u_τ

Subscripts

f Refers to "forward" x-array wire orientation, flow => \

i Refers to inner parallel-array elements

o Refers to outer parallel-array elements

r Refers to "rearward" x-array wire orientation, flow => /

x Refers to streamwise direction

y Refers to normal direction

z Refers to spanwise direction

Other

' Indicates an rms quantity

< > Indicates a time averaged quantity, same as an overbar

CHAPTER 1

LITERATURE REVIEW AND THE OBJECTIVES OF THIS STUDY

1.1 INTRODUCTION

Studies of the production of turbulence in wall bounded shear flows have revealed a process generically termed bursting. This process takes place intermittently within (predominantly) the inner region[1], and is comprised of two major events, see for example, Kline, Reynolds, Schraub and Runstadler (1967) or Corino and Brodkey (1967). One of these events involves the local deceleration of streamwise velocity, and the ejection away from the wall of low momentum sublayer fluid. The other of these events is termed a sweep, and is characterized by a larger scale high speed front entering the near-wall region at a shallow angle. Both of these events have been identified with significant Reynolds stress production, see for example, Kim, Kline and Reynolds (1971) and Lu and Willmarth (1973).

The bursting events are complex and involve a broad spectrum of length and time scales. Much of the research has therefore attempted to dissect this process and discern those scales of motion which initiate bursts from those scales of motion which are a result of the process. In his review Bushnell (1985) poses the question of understanding turbulence

---

[1]The inner or wall region may be roughly identified as $0 \leq y/\delta \leq 0.2$, and then the outer region is thus identified as $y/\delta > 0.2$. The near-wall region will be used in this study to mean $y^+ \leq 50$, and the viscous sublayer is identified as the region $y^+ \leq 5$.

production in boundary layers as understanding "the origin of ubiquitous wall streaks, and details of the inter-relationship(s) between the three (or more) scales involved". The three scales of motion to which he refers may be generally labeled as those which are characteristic of the inner region (i.e. are approximately invariant with Reynolds number when normalized by ν and u_τ), those which characterize the outer region (i.e. are approximately invariant with Reynolds number when normalized by δ and u_τ or U_∞), and those which are intermediate in scale to the inner and outer region motions.

The large scale outer flow eddies are of order one to three boundary layer thicknesses, and have been observed to maintain their identity for more than ten δ as they convect in the streamwise direction, see for example, Kovasznay, Kibens and Blackwelder (1970), Falco (1977) and Brown and Thomas (1977). Furthermore, while the overall scale of the outer region eddies is relatively insensitive to R_θ (in relation to the total thickness of the flow), Murlis, Tsai and Bradshaw (1982) and Antonia, Rajagopalan, Subramanian and Chambers (1982) show that the shape of the turbulent/nonturbulent interface at the outer edge of the boundary layer is Reynolds number dependent for R_θ less than roughly 5,000. The intermediate scale motions have predominantly been identified by Falco (1974), (1977), (1983) as vortex ring-like motions of the order of 100 inner variable units in scale. These motions, which can be found both in the inner and outer regions, have also been shown to exhibit a significant Reynolds number dependence, see Falco references above. Within the wall region numerous vortical motions have been observed and studied. These motions, which will be discussed in the context of an inner/outer region interaction below and in terms of their viscous unit scale in the introduction to Chapter 2, are the inner region "flow modules" that participate in the bursting phenomena.

For the purposes of boundary layer control, one would like to determine whether the flow conditions initiating the bursting phenomena arise mainly from inner region dynamics or are dominantly a function of the scales that characterize the outer region. A popular method by which this determination has been attempted is to utilize the intermittent nature of the bursting events and estimate the scaling properties of the so-called bursting frequency (i.e. the time between bursts). Numerous studies, using a variety of techniques, have been conducted with this intent, and have often yielded conflicting results. For example, one can compare the results in the earlier studies of Rao and Narasimha (1971) and Blackwelder and Haritonidis (1983) or compare the more recent studies of Luchik and Tiederman (1987) with Shah and Antonia (1988). These conflicting results pertaining to the scaling of the bursting frequency persist even though many of the reasons for the conflicting results, such as the spatial resolution of the sensor, have been explained.

There does however, seem to be general agreement regarding the scaling of the duration of sweeps and ejections. The duration of the bursting events have been shown to exhibit wall layer scaling; see for example, Lu and Willmarth (1973) and Sabot and Comte-Bellot (1976). This result appears reasonable. That is, even if the bursting events were initiated by outer region motions, the duration of these events would probably remain a function of the response of the inner region motions to this external perturbation. A similar argument however, cannot be applied to the scaling of the times between the bursting events. One can easily envision either inner region and/or outer region physics controlling the bursting frequency.

Outer variable scaling of the bursting frequency is supported by the classical spectral energy distribution that associates the production of the Reynolds stresses to the large scale motions; see for example Hinze (1975). Inner variable scaling is supported by the apparent universality of the constants in the scaling law for the logarithmic mean velocity profile. Evidently however, the dynamics that take part in sustaining and initiating the bursting events are either too complex, have no preferred scaling, or this scaling cannot be determined by current experimental techniques. Most assuredly, the present understanding of the bursting process is based upon incomplete evidence and is probably biased by preconceptions about what the process should entail[2]. Therefore, it is felt that the most useful models used to explain the essence of the process should allow for enough variability so as to embrace those areas of doubt where either evidence is scarce or conflicting.

The problem of determining a definite scaling behavior for the bursting frequency leads one to consider a significant interaction between the inner and outer region motions. Kline (1978), using the logical method of negative inference, gives convincing reasons why either an inner region dominated or an outer region dominated physical model of the production process should be rejected and replaced by a model that incorporates a significant interaction between the motions of the inner and outer regions. The data to be discussed in the following section

[2]While it is a certainty that the bursting phenomenon appears to repeat itself (presumably randomly in space and time), based upon the existing disagreement pertaining to the frequency of its quasi-periodicity, perhaps all that should be assumed about the process is that it might be regenerative.

indicate that a significant level of control of the transport across the boundary layer may be achieved through modifying this interaction. Modifications of this kind appear preferable in that they would alter the underlying mechanisms sustaining the bursting events, rather than only suppressing the symptoms of the process.

1.2 DETAILS PERTAINING TO INNER/OUTER INTERACTIONS

This section presents a partial review of previous studies that have addressed issues pertinent to understanding and quantifying the existence of the interaction between the motions of the inner and outer regions.

1.2.1 Average Structure

In the boundary layer, the turbulence is maintained via the continual degradation of streamwise momentum (initially extracted from the free stream) through the irreversible action of the Reynolds stresses. As early as the studies of Laufer (1950) and Klebanoff (1954) it was known that the streamwise intensity, u', and both the production term, $P = -\langle uv\rangle \partial U/\partial y$, and the dissipation term, $\epsilon = 2\nu\langle s_{ij}s_{ij}\rangle$, in the equation for the turbulent kinetic energy exhibit distinct peak values very close to the wall ($y^+ \cong 15$). The spatial location of these peak values indicate that, on average, the boundary layer does not convert the streamwise momentum extracted from the free stream into three dimensional turbulent fluctuations until very near the wall. Thus, in an average sense, the there is a continual transport of (predominantly) streamwise momentum through the outer region to the inner region; where this momentum is converted into three dimensional turbulent fluctuations and eventually lost through dissipation. Sreenivasan (1989), suggests that "a potentially useful point of view to take in explaining the boundary layer dynamics is to consider the wall as sink of momentum, and that the inward flux of momentum governs the boundary layer dynamics to a first approximation".

Evidence for the existence of an interaction between the inner and outer region motions may in found by examining the effects of changing the inner and outer boundary conditions. Concerning the boundary condition at the outer edge of the flow, there is a substantial body of evidence suggesting that in general the profiles of many statistical measures of wall bounded turbulent flows are (approximately) universal under an inner variable scaling for some region near the wall regardless of outer flow boundary condition. (The extent of this scaling region depends on the particular statistic.) This indicates that to some degree the dynamics near the wall are independent from the source of energy for the flow (i.e. the irrotational free stream for flat plate boundary layers or the mean pressure gradient for channels and pipes).

Concerning the boundary condition at the wall, it is useful to consider the effect of a step change in surface roughness as studied by Antonia and Luxton (1971) and discussed by Kline (1978). Immediately downstream of the roughness and near the surface the axial intensity exhibits a distinct rise, but the outer region profile is almost identical to the smooth wall case. As one moves downstream of the step change in roughness, deviations from the smooth wall case become increasingly apparent until the entire intensity profile is significantly different from the smooth wall case. This example clearly illustrates that the outer region structure is not independent of the boundary condition at the wall.

1.2.2 Inner Region Motions

That fact that many statistics in the inner region exhibit approximate inner variable scaling has provided useful criteria in constructing physical models of this region of the flow. One of the most popular inner region models was first proposed by Townsend (1956). Townsend's model (which originated through the interpretation of two point velocity correlation data, and which continues to gain experimental support, see for example Guezennec (1985)) features counter-rotating vortex pairs oriented predominantly in the streamwise direction that scale with distance from the wall, and thus in this sense are "attached" to the wall. In agreement with inner region data, these motions are independent of the outer flow boundary condition and scale with distance from the wall. Furthermore, there is substantial experimental evidence supporting the existence of streamwise vorticity containing motions in the near-wall region, see for example, Bakewell and Lumley (1967) and Blackwelder and Eckelmann (1979). These motions have been associated with producing the flow fields responsible for the low speed streaks, as well as ejections -- since they are proposed to "pump" low speed sublayer fluid away from the wall.

However, given the intermittent nature of the bursting phenomenon in addition to the highly unstable environment of the buffer region, it is doubtful that a sustained double-roller eddy interpretation accurately represents the instantaneous physical reality. It seems more likely that the average character of the near-wall region comes from the continual interaction, creation and destruction of motions rather than the long term properties of any sustained resident motion. Thus in order to retain the above mechanism for the ejection of sublayer fluid one must account for the continual regeneration of counter-rotating streamwise vortices near the wall.

The presence of organized motions in the near-wall region that contain streamwise vorticity have been explained by many models. Typical examples are given by Willmarth and Tu (1967), and Offen and Kline (1975) (also see for example, Head and Bandyopadhyay (1981), Wallace (1982) and Smith and Lu (1988)). These models feature hairpin vortex-like motions which are formed predominantly by the organized reorientation and lifting of sublayer vorticity filaments originally oriented such that their vorticity vector points in the spanwise direction. The legs of the hairpin vortices are then seen to account for the observed counter-rotating vortex pairs -- thus preserving the above mentioned mechanism for the ejection of sublayer fluid. In general, these models propose that the regeneration and subsequent breakdown of the hairpin vortex-like motions are intimately related to the observed bursting phenomena.

The Offen and Kline model suggests that the cyclic occurrence of bursts is due to convected vortical motions organized during an upstream burst promoting the instability of the motions associated with the sublayer streaks further downstream. The proposed instability mechanism comes in the form of locally adverse pressure gradients, observed by Kim et al. (1971), which serve to lift up the streaks in a process they view as a local separation of the sublayer. The initiating pressure disturbances are proposed to be a result of wallward moving motions originating in the inner region. Offen and Kline suggest that the large scale outer flow eddies are maintained through a pairing process involving newly organized vortical motions resultant from bursts. Thus, models such as theirs propose that the interaction between the motions of the inner and outer regions is triggered predominantly by inner region dynamics.

Willmarth (1975), along with Kibens, Winkel and Christians, performed conditional sampling on wall pressure and Reynolds stress signals. These results are in agreement with Offen and Kline's in that they give evidence for the presence of locally adverse pressure gradients associated with the occurrence of bursts. However, additional to the results of Offen and Kline, Willmarth attributed the initiation of the bursting phenomena to a "massaging" action on sublayer by the pressure field due to the large scale outer flow eddies. This pressure field is seen as responsible for the occurrence of the locally adverse pressure gradients, and the formation of unstable high-shear layers associated with the creation of hairpin vortices. Thus in models such as that this, the interaction between the motions of the inner and outer regions is initiated through the outer region pressure field.

In contrast to Willmarth's results however, Thomas and Bull (1983) have performed experiments to test the role of the outer region pressure field on initiating the bursting events. From their conditional sampling study using wall pressure transducers and hot-wire anemometry, they concluded that although there is an identifiable pressure pattern closely associated with the passage of large scale outer region motions, this characteristic pressure pattern is not of sufficient magnitude (as compared with local inertial forces in an order of magnitude analysis) to initiate the bursting events. Their results also indicate that at the beginning of the burst sequence the near-wall flow field experiences a favorable pressure gradient. Furthermore, they concluded that while adverse pressure gradients may be associated with stages of the bursting process, this pressure pattern is not responsible for its initiation.

A more recent model that features lifted sublayer motions other than hairpin vortices has also been proposed by Jimenez, Moin, Moser and Keefe (1988). In their interrogation of the computational results of Kim, Moin and Moser (1987) they found large scale (relative to experimentally observed hairpin-type motions) vortex sheet or shear layer-type motions extending from the wall at shallow angles. Furthermore, they tentatively associated the creation of these nearly two dimensional sheet-like motions to near-wall instability mechanisms observed during transition. Thus this physical model (plausibly) associates the occurrence of ejections with the instability of motions almost exclusively resident within the near-wall region. At high Reynolds numbers the validity of this type of generation process in supporting the outer region turbulence becomes questionable. This is because as the Reynolds number increases the ratio of the near-wall region to the boundary layer thickness becomes extremely small.

A different model for the initiation of the bursting phenomena near the wall that apparently embraces the existence of a significant interaction between the inner and outer region motions (as well as the conflicting results pertaining to establishing the scaling behavior of the bursting frequency) has been proposed by Falco (1977), (1983), (1987). In these studies, Falco has identified the above mentioned intermediate scale vortex-ring like motions as important contributors to the Reynolds stress in both the inner and outer regions. Furthermore, the convection of these motions toward the wall and their subsequent interaction with the vorticity distributions of the sublayer has been identified as an initiating mechanism for significant turbulent stress production. In a related study, Chu (1988) has simulated the interaction of these vortex ring-like motions with the sublayer in experiments with laminar vortex rings impinging on the flow field produced by a suddenly accelerated plate. In these physical simulations it was shown that many motions associated with the near-wall region (such as hairpin vortices, pockets, streaks and lifted shear layers) may be produced.

The model of Falco includes a significant interaction between the intermediate scale vortex ring-like motions and the large scale outer region motions (which are plausibly seen to influence the frequency in which the vortex ring-like motions interact with the sublayer). Thus a Reynolds number dependence in the interaction between the vortex ring-like and outer region motions would appear to account for the ongoing lack of agreement concerning the scaling of the time between bursts. This model is also apparently supported by the wall pressure data of Emmerling (1973) indicating that the most energetic motions perturbing the sublayer are of small to intermediate scale. In connection with this, Willmarth (1975) has suggested "that one should also consider the existence of small-scale convected vortices to explain the observed sublayer structure". Given the existence of an interaction between the inner and outer region motions, Willmarth's suggestion appears to be the emerging picture; with the large scale outer region motions playing a possibly major role in the convection of highly vortical small scale motions above and toward the wall.

1.2.3 Outer Region Motions

Probably due to their spatial extent, the large scale motions in turbulent boundary layers are not as easily characterized as the motions near the wall. Furthermore, the existence of organized large scale motions remains in doubt. For example, Coles (1987) states that "the large coherent structure in a boundary layer, if it exists, is concealed in a tremendous clutter of noise". However, while the body of evidence supporting the existence of a dominant and well defined outer region motion is small, some information is known concerning specific features of the outer region flow.

Brown and Thomas (1977) and Falco (1977) present an approximately equivalent picture of the generic outer region motion. This large scale motion, termed a bulge, is tilted in the streamwise direction at an average acute angle with the wall reported to be between 18 and 48 degrees. These bulges, which convect at about $0.8U_\infty$, have also been observed to exhibit a low frequency overturning motion in their interior consistent with the sign of the mean vorticity. Furthermore, the above investigators have also revealed the existence of deep valleys of essentially non-turbulent fluid between the large scale bulges (sometimes extending well within the wall region). This feature has also been confirmed in the temperature contamination study of Chen and Blackwelder (1978). In connection with this, Wallace (1982) states that the results of Chen and Blackwelder "provides direct evidence that a relation between the large scale outer structure and the events occurring near the wall exists", and he further interprets this as evidence for hairpin vortex-like motions extending well into the outer region, see also Head and Bandyopadhyay (1981).

The upstream portion, or back, of a large scale bulge is exposed to the irrotational stream, and in this region a stagnation point-type flow (in a convected reference frame) has been observed to exist. Brown and Thomas (1977) and Falco (1977) show that this stagnation-point type flow redirects irrotational fluid around the bulge such that a wallward motion occurs in the irrotational valleys between the bulges. The existence of strong wallward velocities in these nonturbulent valleys was also clearly exhibited in the earlier study of Kovasznay, Kibens and Blackwelder (1970). Falco has further identified the backs of the large scale bulges as a region in which one is likely to observe the intermediate scale vortex ring-like motions.

Relevant to an interaction between the motions of the inner and outer regions, both the studies of Brown and Thomas and Falco as well as the study of Praturi and Brodkey (1978) associate the region near the wall, in the proximity of the non-turbulent valleys, with highly turbulent activity. In the Brown and Thomas study this region was associated with wallward sweep-type motions. Consistent with this observation, Falco (1983) has noted the frequent observation of the vortex ring-like motions convecting wallward in this region. Thus it appears that the introduction of essentially non-turbulent fluid near the wall as a result of the shape of the large scale bulges plays a role in initiating the bursting events.

Other large scale features of the boundary layer have more recently been educed in the studies of Guezennec (1985) and Wark (1988). Both of these studies used multi-point multi-sensor detection and mapping techniques in an effort to uncover the details of the outer region motions, and their influence on the observed wall region events. From his study Guezennec concluded that large scale counter-rotating streamwise vortex-like motions encompass much of the outer region. (Note he did not actually measure streamwise vorticity.) Furthermore, he linked these motions with the occurrence of sweeps or ejections near the wall depending on their sense of rotation and the presence of inflow or outflow between them. Thus these motions may either directly effect wall region dynamics, or play a role in the convection of smaller scale highly vortical motions consistent with the suggestion of Willmarth (1975), see previous section. In general, the study of Wark further reinforced the results of Guezennec, but tended to support a strong inner/outer interaction through a "hierarchy" of scales of motion. Furthermore, her study gives evidence for alternating sweeps and ejections to exist in the spanwise direction.

1.3 OBJECTIVES AND METHODOLOGY

1.3.1 Objectives

The intent of the present study is to uncover essential details pertaining to the interaction between the inner and outer region motions in turbulent boundary layers. Mechanisms relating to the transport of the turbulent stresses are identified and investigated. Furthermore, when possible, links are made between average structure and observed instantaneous motions. In particular, plausible initiating mechanisms responsible for the lifting of vortical sublayer motions are identified and discussed. This entails examining data relevant to the spatial structure of the vorticity field in the inner region. Pertinent issues relating to possible Reynolds number dependencies in boundary layer structure are also addressed.

1.3.2 A Bias Toward Vorticity Measurements

Blackwelder (1983) and Hussain (1986) give the following definitions of coherent motions[3].

> Blackwelder: "A coherent eddy structure consists of a parcel of vortical fluid occupying a confined spatial region such that a distinct phase relationship is maintained between the flow variables associated with the structure's constituent components as the structure evolves in space and time."

> Hussain: "A coherent structure is a connected turbulent fluid mass with instantaneously phase-correlated vorticity over its spatial extent."

Note that both of these definitions attribute the intrinsic vorticity of a coherent motion to be an essential property. Based upon this feature of coherent motions, it is a hypothesis of this study that the optimal description/understanding of turbulence may be gained through the study of the vorticity field. In practice, this hypothesis translates into the hope that statistical descriptions in terms of one or more of the vorticity components will give a more unique indication of the important instantaneous turbulent motions than that provided through the interpretation of velocity statistics.

---

[3]Within this dissertation the suggestion of Kovasznay (1979) is followed in that instantaneous properties will be referred to as "motions" and the permanence implied by the word "structure" will be reserved for time averaged properties.

1.3.3 The Inner/Outer Interaction in Terms of Vorticity

The solenoidal condition on the vorticity field,

$$\nabla \cdot \omega \equiv 0,$$

holds at every instant throughout a turbulent wall flow. As a consequence, the vorticity filaments comprising the flow must either end at isolated points on the solid surface, close upon themselves or extend to infinity.

Very near the wall the dominance of viscous diffusion and the geometric constraints imposed on the flow through the no-slip condition results in the vorticity distributions of this region to be predominantly oriented in the spanwise direction, and to (presumably) have a two dimensional vortex sheet-like character. Further away from the wall, the three dimensional effects of stretching and reorientation dominate, and the important vorticity distributions (i.e. coherent motions) develop a more limited spatial extent in the x and z directions. Attaching this physical observation to the constraints imposed by the solenoidal condition on the vorticity field leads to the hypothesis that <u>at some distance away from the wall the local instantaneous vorticity distributions are predominantly no longer connected to the sheet-like distributions characteristic of the sublayer, but instead take the form of closed loops</u>[4]; the simplest of which comes in the form of a vortex ring. This hypothesis finds support in the outer region by the fact that the velocity intermittency profiles of free shear flows and boundary layers are virtually identical, see for example Hinze (1975). Note also that the above notions concerning the limited spatial extent of coherent

[4]In this dissertation these vortical motions will be referred to as "reconnected".

motions lessens the possible significance of vorticity distributions that extend to infinity -- especially outside the sublayer. In connection with this hypothesis, it is further hypothesized that the essential features of the interaction between the inner and outer region motions can be described in terms of the interaction between the reconnected and locally[5] three dimensional vorticity distributions characteristic of the outer region, and the locally two dimensional (disturbed sheet-like) distributions that arise out of the sublayer.

A general goal of this study is to assess the usefulness and validity of the above hypotheses. Furthermore, in making the last hypothesis it is fully realized that complications affecting its validity probably exist; such as the effect of possible large scale vortical motions in the outer region, and the influence of the irrotational valleys associated with the large scale bulges as discussed in Section 1.2.1.

1.4 PREVIOUS MEASUREMENTS OF TIME RESOLVED VORTICITY AND VELOCITY GRADIENTS, SMALL SCALE STRUCTURE, AND REYNOLDS NUMBER DEPENDENCE IN WALL TURBULENCE STATISTICS

1.4.1 Previous Measurements of Time Resolved Vorticity and Velocity Gradients

In order to better understand the significance of the present spanwise vorticity measurements, it is important to have a knowledge of previous studies that have made time resolved velocity gradient and/or vorticity measurements. As implied by the above coherent motion

[5] In this hypothesis the term "locally" is implied to mean relative to the scale of the interacting sheet-like sublayer vorticity distributions and the reconnected vorticity distributions hypothesized to occur away from the wall.

definitions of Blackwelder and Hussain, it is generally believed that coherent motions embody organized vorticity, or that they result from the action of organized vorticity. This belief has lead to an increased emphasis on the measurement of velocity gradient quantities and their associated statistical properties.

As a rule of thumb it is generally acknowledged that to measure the smallest scales in a turbulent flow the probe must be capable of resolving motions of approximately the Kolmogoroff scale, η ($\equiv (\nu^3/\epsilon)^{1/4}$). In the near-wall region of a fully turbulent boundary layer this corresponds to less than $3\nu/u_\tau$. Few flow facilities or computations allow for studies that have the capability to achieve this. Since multi-wire probes are needed to directly obtain spatial gradients, both the length of the wires and the spacing between wires should, in principle, satisfy this criterion. The following partial survey gives an indication of resolutions and integration times that have been used in studies of wall-bounded turbulent shear flows that have made time resolved velocity gradient and/or vorticity measurements.

Early boundary layer studies used probes which were relatively large compared to the Kolmogoroff scale. Corrsin and Kistler (1954) studied the intermittent region of a rough wall turbulent boundary layer at $R_\theta \cong 7{,}900$ using a streamwise vorticity probe designed by Kovasznay (1950). This probe's wire length, $\ell^+ \equiv \ell u_\tau/\nu$, was approximately 100 wall units, and the average wire spacing was $\cong 70$ wall units. Using an estimate of η (Tennekes and Lumley 1972, p. 159), at $y/\delta = 0.9$ yields $\eta^+ \cong 5.6$. Kovasznay, Komoda and Vasudeva (1962) used a parallel array with spacing $y^+ \cong 8$ and wires of length $\ell^+ \cong 24$ to study the later stages of the transition process. The wire spacing in this study was about one tenth of the total boundary layer thickness. Kovasznay, Kibens and Blackwelder (1970) used a pair of single wire probes configured to measure $\partial u/\partial y$ to detect the vorticity fronts and backs of the large scale motions in a fully turbulent boundary layer at $R_\theta \cong 3,100$. Their wires had a length of 25 wall units and a spacing that varied from 40 to 60 wall units (or about 10 to 16 Kolmogoroff scales). Using the result of Wyngaard (1969), Blackwelder and Kovasznay (1970) estimate that this spacing results in resolving only 70% of the true rms gradient.

Later works involved more complicated multi-wire probes that enabled one or more vorticity components to be measured. Eckelmann, Nychas, Brodkey and Wallace (1977) studied ω_z and ω_y as close as $y^+ = 15$ in a channel flow at $R_{d/2} = 4,000$. Their five film probe had films with an average spacing and length of 1.75 wall units. An interesting additional point is that they found that averaging times, $2TU_c/d$, of greater than $\cong 5,000$ were needed to obtain stable ensemble averages. Falco (1980) using the same type of probe as in the present study, measured ω_z in a fully turbulent boundary layer at $y^+ = 16$ for $R_\theta = 1,068$. The spatial scale of this probe was approximately $3.6\Delta y^+$ and $11.5\Delta z^+$, and the wire length, ℓ^+, was 3.6. In this combined visualization/hot-wire study, approximately 210 boundary layer thicknesses were observed. Kastrinakis (1977) studied a turbulent channel flow using Kovasznay (1950) type ω_x probes ($\ell^+ \cong h^+ \cong 5$ at $R_{d/2} \cong 6,250$). He measured both ω_x and two point ω_x correlations as close as $y^+ \cong 9$. Further study of this probe by Kastrinakis, Eckelmann, and Willmarth (1979), indicated that since the four wires were not independently operated the probe output was significantly sensitive to all three velocity components. Later Kastrinakis and Eckelmann (1983) measured streamwise vorticity with a 4 wire (independently operated) probe in a fully developed channel flow as close as $y^+ \cong 19$ for $R_{d/2} = 12{,}000$. The scales of this probe were $h^+ = 11.5$, $\ell^+ = 9.1$, and their signal record lengths were $2TU_c/d = 2{,}670$. Subramanian, Kandola and Bradshaw (1985) studied the low wave number aspects of the outer part of a fully developed turbulent boundary layer at $R_\theta = 14{,}500$. Their probe had a wire spacing $h^+ \cong 375$, a wire length of $\ell^+ \cong 75$, and they averaged for $TU_\infty/\delta \cong 7{,}700$. Balint, Vukoslavcevic, and Wallace (1987a) in a study of a fully turbulent boundary layer at $R_\theta = 2{,}100$ measured for the first time all three components of vorticity from $y^+ = 14.5$ to $y/\delta = 0.95$. Their nine wire probe had an average wire spacing appropriate for computing gradients of 8.9 wall units (Wallace, private communication), with wire lengths $\ell^+ = 2.3$. Their averaging time was $TU_\infty/\delta \cong 3{,}100$. More recently (Balint et al. (1987b)) they have used a probe with an improved signal to noise ratio that had an average wire spacing of 10.4 wall units, with $\ell^+ = 2.3$ at $R_\theta = 2{,}850$. Klewicki and Falco (1986, 1987) using the same apparatus described herein (Chapters 2 and 4), have measured spanwise vorticity distributions and two point ω_z correlations across turbulent boundary layers in the range $1{,}010 \le R_\theta \le 4{,}850$.

Using an array of two probes in a 'v' configuration that is flush-mounted in the wall, it is possible to obtain vorticity measurements in the immediate vicinity of the wall. Hogenes and Hanratty (1982) in a conditional averaging study of turbulent pipe flow at $R_{d/2} = 18{,}040$ used electrochemical probes with an $\ell^+ \cong 8.5$ and a $\Delta z^+ \cong 3.8$, and $2TU_c/d = 540$. Blackwelder and Eckelmann (1979) studied the wall region vorticity associated with the bursting phenomena in a turbulent channel flow at $R_{d/2} = 3{,}850$. The elements of this v-array were positioned at 45 degrees to the mean flow direction. The length of these films was $\ell^+ = 1.3$, and they were spaced $\Delta z^+ = 5.3$ apart. The averaging time used was $2TU_c/d = 3{,}440$. Kreplin and Eckelmann (1979), also using the Gottingen oil channel, used v-array probes to obtain long time averaged statistics. Using the same probe at the same Reynolds number as Blackwelder and Eckelmann, they determined that an averaging time $2TU_c/d = 2{,}870$ was required to obtain "adequate" convergence for velocity statistics up to the fourth moment.

Recently Alfredsson, Johansson, Haritonidis, and Eckelmann (1988) have attempted to clarify sources of measurement error using wall shear stress sensors, and hot-wire/film probes in the sublayer. With respect to probe resolution effects, they found that for streamwise velocity measurements in the sublayer, probes of length $\ell^+ = 2$ and 10 resulted in no differences within experimental error. (Measurements made with a probe of $\ell^+ = 8$ in air resulted in discrepancies that were attributed to wall heat transfer effects.) These experiments covered a range of Reynolds numbers up to approximately $R_\theta = 2{,}800$.

Resolution problems are also inherent in computational studies of turbulent wall flows. The accuracy of a solution of the discretized Navier-Stokes equations is affected by spatial resolution constraints in a way different from that of laboratory measurements. In a laboratory experiment the job of the measurement device is to resolve the physical flow field. In contrast, the job of the computation is to create the physical flow field. Therefore to computationally create a flow field to a given accuracy, grid spacings smaller than the probe scale necessary to measure an equivalent physical flow field to the same accuracy are probably required.

To date the two highest resolution computations of fully turbulent wall flows have been performed by Kim Moin and Moser (1987) in a channel flow, and Spalart (1988) in boundary layers. Kim et al. used a grid spacing of $\Delta x^+ \cong 12$, $\Delta z^+ \cong 7$, and $0.05 < \Delta y^+ < 4.4$ at the wall and channel center line respectively (a 192 x 129 x 160 grid), for $R_{d/2} \cong 3{,}300$. Spalart in a study of turbulent boundary layers at $R_\theta = 300$, 670 and 1,410 varied the number of grid points to maintain a grid spacing of $\Delta x^+ \cong 20$, $\Delta z^+ \cong 6.7$, and a non-uniform Δy^+ such that there were 10 grid points in the first 9 wall units (a maximum grid of 432 x 80 x 320). Spalart's computational duration was only about $TU_\infty/\delta = 40$. However, as stated in Kim et al., the computations allow averaging over planes parallel to the wall. For example, using the computations of Spalart, if averages were computed from data in a given plane separated by 7 displacement thicknesses (to maintain statistical independence), then the total averaging time is $TU_\infty/\delta \cong 140$.

Investigators using computational techniques thus have used grid spacings which are comparable to the probe scales used by experimentalists. However, since it is currently unknown what scales are important with respect to the formation of turbulent motions, it is not clear that this is sufficient resolution to create the correct instantaneous representation of the flow.

1.4.2 Evidence of Small Scale Structure

What measurement resolution is necessary to resolve the origin of coherent events in the wall region? Emmerling (1973) using an array of wall pressure transducers (of scale $\cong$ 54 viscous units) in a turbulent boundary layer at $R_\theta = 2{,}000$ found examples of strong pressure disturbances that were at least as small as 1/10 the transducer size. Schewe (1979) working in the same tunnel at $R_\theta \cong 1{,}400$ showed that the wall pressure intensity, skewness, kurtosis and the frequency of the occurrence of pressure peaks continue to change with decreasing transducer size. Even for his smallest diameter transducer, $d^+ = 19$, there was no indication that these trends had leveled off. Willmarth and Bogar (1977) working in a boundary layer at $R_\theta = 11{,}700$ with hot-wires that were $\ell^+ = 2.5$ and $s^+ = 2.5$ (s = the spacing between a pair of x-wires) estimated that velocity gradients "in the small scale structure near the wall will only become small over a distance that is less than approximately 1/20 of the Kolmogoroff length". Later Willmarth and Sharma (1984) using probes of length less than one viscous length (at $R_\theta = 6{,}840$ and 9,840) give direct evidence for the existence of near-wall "shear layer fluctuations whose scale is of the order of the viscous length". On the other hand, Johnson and Eckelmann (1983) working in the Gottingen oil channel at the $R_{d/2} = 3{,}800$ and using x-films with $\ell^+ \cong s^+ \cong 1.7$ did not find evidence of these ultra-small scale motions. However, as they noted, the Reynolds number of this study was approximately thirty times lower than that of Willmarth and Bogar.

Experiments at widely varying Reynolds numbers using probes of equivalent ℓ^+ may not be comparable. This is based upon the hypothesis that important changes in the small scale physics of the flow may occur with Reynolds number. This is suggested by the disagreement between the results of Johnson and Eckelmann and Willmarth-Bogar, Willmarth-Sharma discussed above. Table 1.1 presents a summary of the spatial resolutions of the velocity gradient and vorticity studies discussed above.

is c

con

flo

mea

Com

R_d

Bra

low

pr

de

in

Bu

bo

nu

mea

num

and

regi

to 4

monot

coeffi

decreas

found th

showed a

and Jovan

1.4.3 Evidence of Reynolds Number Dependence

The Reynolds number dependence of near wall turbulence statistics is currently unclear. This is due to excessive data scatter and existing contradictory results. Laufer (1950) in fully developed turbulent channel flows ($12{,}300 \le R_{d/2} \le 61{,}600$, $12.3 \le \ell^+ \le 61.7$) found that the maximum measured value of u'/u_τ decreased as the Reynolds number increased. Comte-Bellot (1963) also investigating turbulent channel flows ($57{,}000 \le R_{d/2} \le 230{,}000$, $26.0 \le \ell^+ \le 90.6$) found a similar trend. Huffman and Bradshaw (1972) in a analysis of wall bounded flow data, showed that at low Reynolds number (say $R_\theta < 5{,}000$) the logarithmic mean velocity profile showed a dependence in the intercept but not the slope. This dependence was shown to be proportional to the gradient in shear stress in the direction normal to the wall, $\partial\tau^+/\partial y^+$. Purtell, Klebanoff and Buckley (1981) support this conclusion in their study of turbulent boundary layers in which they found that the logarithmic law was Reynolds number independent for R_θ as low 465. However, their highest resolution measurements ($\ell^+ \cong 8$) of turbulence intensity, u'/u_τ, show a Reynolds number dependence opposite that of Laufer and Comte-Bellot. Murlis, Tsai and Bradshaw (1982) using an x-array ($\ell^+ \cong 30$, $s^+ \cong 25$) studied the outer region of turbulent boundary layers ($y/\delta > 0.2$) over the range $R_\theta = 791$ to 4,750. They found that the anisotropy parameter, "$\langle u^2\rangle/\langle v^2\rangle$ increases monotonically with Reynolds number while the shear correlation coefficient, $\langle uv\rangle/u'v'$, reaches a weak maximum at $R_\theta = 2{,}000$ and then decreases to an asymptotic value at high Reynolds number". They also found that the triple products normalized by the local shear stress showed a weak increase with Reynolds number. Andreopoulos, Durst, Zaric' and Jovanovic (1984) using probes with $20 \le \ell^+ \le 100$ measured the statistics up to the fourth moment of the streamwise fluctuating velocity. Their intensity profiles showed the same trend with Reynolds number as Laufer and Comte-Bellot. Furthermore, their skewness and kurtosis profiles exhibited experimentally significant differences over a Reynolds number range $3{,}624 \le R_\theta \le 15{,}406$. Erm, Smits and Joubert (1985) also show a Reynolds number independence of the von Karman constant, but found an increase in u'/u_τ, v'/u_τ and $<uv>/u_\tau^2$ with Reynolds number across the inner region for $y^+ > 15$. The length of their wires were in the range $24 \le \ell^+ \le 51$ for $617 \le R_\theta \le 5{,}010$. Wei (1987) using laser doppler anemometry in a channel flow, found a stronger but qualitatively the same Reynolds number dependence in u'/u_τ and $<uv>/u_\tau^2$ for $y^+ \ge 15$, and in v'/u_τ for $y^+ \ge 4$. Furthermore, Wei's higher order statistics and spectra of the above quantities also show a significant Reynolds number dependence. His probe dimension in viscous lengths ranged from 0.66 to 6.43 over a Reynolds number range $2{,}970 \le R_{d/2} \le 39{,}580$. To date, little information is available on the effect of Reynolds number on the vorticity field in turbulent wall flows.

Reynolds number dependence however, has been observed to affect the results of coherent motion studies of turbulent wall flows. Blackwelder and Haritonidis (1983) found that the results obtained using the VITA turbulence detection technique were strongly influenced by the probe length. Over a range of $R_\theta \cong 10{,}000$, they observed that the bursting frequency scaled on inner layer variables when they used wires of length smaller than 20 viscous lengths. From this they concluded that earlier results were erroneous due to spatial resolution problems. Falco (1974,1977) using combined visualization/anemometry techniques observed that important vortex ring-like motions found throughout the boundary layer undergo a rapid decrease in scale (relative to δ) as R_θ increases for $R_\theta \leq 10{,}000$. This implies that quantifying these motions in the most objective way would require decreasingly smaller probes as R_θ increases. In the outer part of the boundary layer both Antonia et al. (1982a) and Murlis et al. (1982) have found significant changes in the structure of the turbulent/non-turbulent interface as R_θ increases; especially at low R_θ. Antonia et al., using temperature as a marker, found that for R_θ less than about 3,000 the average time between coherent temperature fronts was strongly R_θ dependent. Also using temperature as a marker, Murlis et al. found similar results, and hypothesized that as R_θ increases (for $R_\theta \leq$ 5,000) the motions determining the shape of the turbulent/non-turbulent interface shift from small to large scale. In a study nearer the wall, Wei (1987) has attributed the non-universality of wall layer scaling of u, v, and uv statistics and spectra to a relative increase in the production of streamwise vorticity. He has conjectured that this increase is due to the legs of the resident hairpin vortex-like motions becoming more intense and smaller in wall unit scale as the Reynolds number increases. Note that this is consistent with the conflicting results of Johnson and Eckelmann and Willmarth and Bogar discussed above. Issues pertinent to Reynolds number dependence are further addressed in Chapter 3 of this study.

CHAPTER 2

ON ACCURATELY MEASURING STATISTICS ASSOCIATED WITH SMALL SCALE STRUCTURE IN TURBULENT BOUNDARY LAYERS

2.1 ON RESOLVING NEAR-WALL MOTIONS

It is becoming increasingly apparent that experiments intending to educe boundary layer physics (especially near the wall) must take in to account the spatial scale of the measurement device. Within the near wall region, various small to intermediate scale motions have been observed or deduced. These motions include: a) low speed sublayer streaks with lengths varying from 50 to greater than 1,000 wall units, with widths between 5 and 30 wall units, and an average spanwise spacing of approximately 100 wall units (Kline, et al. (1967), (also see Smith and Metzler 1983)), b) longitudinal counter-rotating streamwise vortices, (see for example, Blackwelder and Eckelmann (1979), Lee, Eckelman and Hanratty (1974), Bakewell and Lumley (1968)) which have an average transverse spacing of 20-150 wall units, c) intermediate scale and Reynolds number dependent vortex ring-like motions, with scales between 50 and 150 wall units, observed by Falco (1977, 1983) to be present in the regions both near and away from the wall, d) intense wall pressure pulses, of diameter 30 to 70 wall units, characterized in both the visual studies of Falco (1982), and the interferometric pressure transducer study of Emmerling (1973), and, e) hairpin or horseshoe shaped vortices with scales ranging from 5 to 70 wall units which have their legs connected to the vorticity distribution at the wall, reviewed in detail by Willmarth (1975) and Wallace (1982). Probes that are large compared to the above motions do not accurately resolve their kinematic signatures.

Long time averaged statistics depend upon the instantaneous nature of the flow. Therefore, in order to obtain accurate long time statistics one must resolve the above mentioned instantaneous motions. Reliable experimental guidelines related to obtaining an accurate statistical representation of wall turbulence are incomplete. Examination of the scales of motion reviewed above indicates that measuring their vortical signatures with sufficient resolution requires compact probes and/or relatively large scale flow fields. Furthermore, little is known about the convergence of statistics derived from time resolved velocity gradient measurements. The problem of the convergence of statistics, in general, further limits the accuracy of both experimental and computational studies.

Numerous problems have hindered progress in understanding the physical processes and motions occurring near a wall, but perhaps the most important is related to the spatial resolution of probes used for measurements. Uberoi and Kovasznay (1953) were the first to show analytically that for isotropic turbulence the output of a hot-wire is attenuated as the length of the wire is increased. In their channel flow study of imperfect spatial resolution of single wire probes Johansson and Alfredsson (1983) found significant attenuation in the measured value of u' due to spatial averaging caused by a finite wire length. They also concluded that the dependencies of u velocity statistics on the flow Reynolds number are small compared to finite probe scale effects. Similar results have more recently been found in boundary layers by Ligrani and Bradshaw (1987). They concluded that for studies outside of the sublayer adequate resolution for single wire probes may be obtained if $\ell^+ \leq 20$, and the wire length to diameter ratio is $\ell/d > 200$. However, they also showed that at $y^+ = 17$ significant changes in the high frequency end of the u spectrum occur for variations in ℓ^+ from 14.0 to 3.3. Mestayer (1982), using Wyngaard's (1968) correction, showed significant attenuation occurs in the high wave number spectra of u and especially v for s/η and ℓ/η both equal to 4.5. Therefore, since vorticity is concentrated in the higher wave numbers, it is expected that the accurate measurement of derivative quantities requires even better resolution. Furthermore, the accuracy of derivative measurements as obtained by two wires is degraded by problems additional to finite wire length. Antonia Browne and Chambers (1985) discuss the most important of these to be due to unequal time constants of the wires, mismatch in the wire calibrations, and the effects of finite wire separation.

Most analytical studies of the effect of finite wire spacing in multi-wire arrays, such as Wyngaard (1968), Wyngaard (1969), and Roberts (1973), use isotropic assumptions. A recent compilation by Browne, Antonia and Shah (1987) shows that most turbulent shear flows exhibit significant levels of anisotropy. Thus, the results of the above analytical studies may be best thought of as instructive but not definitive under anisotropic conditions.

As indicated above, both wire length and wire spacing effects hinder the accurate measurement of turbulent statistics. As efforts are made to make probes smaller, presumably a more accurate representation of a given probability distribution can be obtained. This increased information comes as the result of resolving the fine scale motions. Nearer wall however, the scales of the important motions decrease with respect to the size of any given probe. Thus, it is unclear how the enhanced resolution of wall region motions affects the convergence of statistics.

The purpose of this chapter is to document the experimental equipment and procedures of the present study, and to examine some of the factors concerning the accurate measurement of various turbulence statistics. Results were obtained using a four wire spanwise vorticity probe in a very thick turbulent boundary layer flow that resulted in very good resolution measurements. The experiments were carried out in fully developed zero pressure gradient turbulent boundary layers at the three Reynolds numbers R_θ = 1,010, 2,870, and 4,850. A description of the flow facility and the experimental conditions is given in Section 2.2. Section 2.3 describes the probe, its physical characteristics, and its calibration. The experimental procedure and the accuracy of data are considered in Section 2.4. Results in Section 2.5.1 include information concerning the measurement of gradients in an anisotropic flow, as well as, an evaluation of the effect of the probe's asymmetry on its measurement accuracy. Section 2.5.2 presents information pertaining to statistical convergence as a function of Reynolds number and position in the boundary layer. Finally, Section 2.6 includes a discussion and conclusions concerning the results of this chapter.

2.2 EXPERIMENTAL FACILITIES AND CONDITIONS

The experiments were performed in the 17 meter low speed wind tunnel in the Turbulence Structure Laboratory at Michigan State University. A schematic of this tunnel is shown in Figure 2.1. The test section of this suction tunnel is 17.1 m long, 1.21 m wide and nominally 0.61 m high. The top and one side wall of the tunnel are made of plexiglass to allow for flow visualization, and the other two sides are made of plywood. The tunnel is positioned in the center of a 18.3 m x 30.5 m x 6.1 m pressure and temperature controlled laboratory which acts as the return circuit when the tunnel is used in the closed return mode. Suction for the tunnel is provided by a low-noise axial fan, and is kept at constant speed by an eddy current speed controller. The fan assembly is mounted on vibration absorbers and is isolated from the test section via flexible joints. A carefully adjusted set of screens and honeycombs developed via an iterative procedure, and based upon the work of Loerke and Nagib (1977) and deBray (1967), make up the tunnel inlet. This inlet configuration was constructed to avoid the formation of Taylor-Gortler vortices associated with tunnel inlet contractions. The resulting free stream turbulence intensities at the speeds of the present experiments are less than 0.2%. The tunnel exit consists of a 2:1 axial diffuser followed by a 2:1 radial diffuser. For the present experiments the adjustable top wall of the tunnel was set at a divergence of 0.25 degrees over its entire length; resulting in a differential pressure coefficient, dC_p/dx (where $C_p = dp/\rho U_\infty^2$), of less than ±0.002. This value is well within the tolerance of 0.02 deemed negligible by Murlis, Tsai and Bradshaw (1982). The spanwise uniformity of the flow at the present measurement location is ± 2.3% peak-to-peak across the center 0.46 m as determined by the Preston tube surveys of Rashidnia (1985). For more details concerning the flow facility and its qualification the reader is referred to Rashidnia (1985).

The data acquisition, signal conditioning, and probe positioning apparatus consisted of the vorticity probe (described in Section 2.3.1), 4 DISA 55M01 constant temperature anemometers, a custom built analog signal amplifier, a MKS baratron model 398 differential pressure transducer, 2 Krohn Hite model 3323 analog filters, a Data Translation DT3368/DT3369 simultaneous sample and hold A/D subsystem contained within a PDP 11/23 computer, a cathetometer capable of measuring vertical distances to within 0.01 mm (± 0.001mm) used to locate the probe center from the wall, and a vertical traverse mechanism capable of positioning to within 0.0254 mm (± 0.00254 mm). Detailed discussion of the use of this equipment is given in Sections 2.3 and 2.4.

The zero pressure gradient boundary layers studied develop along the lower wall of the flow facility. A 6.35 mm threaded rod is used to trip the flow approximately 0.5 m downstream of the tunnel inlet. Tripping the flow was not necessary to obtain a fully developed state at the measurement station but did serve to localize transition and ensure spanwise uniformity. The measurement station was approximately 15.25 m downstream of the tunnel inlet. This extreme flow development length resulted in enhanced spatial resolution of the vorticity probe even for highest Reynolds number considered. A summary of the principal characteristics of the boundary layers at the three Reynolds numbers considered is given in Table 2.1. Logarithmic mean velocity profiles as measured by the spanwise vorticity probe's x-array are presented in Figure 2.2. Determination of the friction velocity was made using the Clauser plot technique, in conjunction with Coles (1968) law of the wall. As can be seen in the R_θ = 1,010 data of Figure 2.2 this method of obtaining u_τ is in very good agreement with the slope of the sublayer profile.

2.3 THE SPANWISE VORTICITY PROBE; ITS CHARACTERISTICS AND CALIBRATION

2.3.1 Physical Characteristics

The spanwise vorticity probe used is similar to that described by Foss, Klewicki, and Disimile (1986a). However, the calibration and computational scheme used to obtain the vorticity time series was less comprehensive than theirs. The probe, shown in Figure 2.3, consists of a parallel-array, and an x-array located at the same streamwise position but displaced in the spanwise direction. The spacing of the wires in the parallel-array is nominally 1.0 mm, as is the spacing of the rearward and forward slant wires comprising the x-array. The spacing between the centers of the parallel and x-arrays is ≅ 3.4 mm. The slant wires of the x-array are nominally at an angle of 45° with respect to probe axis; a refined determination of their "effective" angles are made during calibration.

The individual hot-wires of the probe are 5 μm diameter tungsten wire which are copper plated at the ends. The copper plating allows the wires to be soft soldered to the ends of the support prongs, and also aerodynamically isolates the active region from the support prongs. The overall wire length is 3 mm with a center active region of 1 mm. This gives a length/diameter ratio of ≅ 200. For the measurements discussed in this chapter all of the hot-wires were operated at an overheat ratio of 1.7. According to the study of Champagne, Sleicher, and Wehrman (1967), under these conditions end heat conduction loss from the wires should be less than 8% of the convective heat loss. The wires of the parallel and x-arrays are mounted on ≅ 20mm long jeweler's broaches. The ratio of the broach length to the tapered probe head diameter is about 8. This is believed to greatly reduce possible probe body effects on the gradient measurements, as discussed by Bottcher and Eckelmann (1985). For further details concerning the probe's physical characteristics one is referred to Foss, Klewicki, and Disimile (1986a).

2.3.2 Calibration

Calibration of the parallel-array wires was performed by fitting the data to a King's Law type equation; $E^2=A+BV^n$, where the best least squares fit was chosen from set having $n = 0.40$ to 0.60. To minimize errors in $\partial u/\partial y$ resultant from mismatched calibration of the parallel-array wires, one wire was calibrated with velocities inferred from the pressure transducer and the second wire was then calibrated against the first; a procedure suggested by Foss (private communication). The procedure used for the x-array was initially devised by Foss and Falco in the late 1970's, has been used extensively (see Falco 1980, Signor 1982, Lovett 1982), and is a variation of the "effective angle" technique assessed in the recent study of Browne, Antonia and Chua (1989). In this procedure, equations of the type first used by King (1914) are derived for the x-array wires oriented to measure u and v, and with the probe body axis at $\gamma = 0°$ to the flow.

$$E_r^2 = A_r + B_r V_r^{n_r} \qquad (2.1a)$$

$$E_f^2 = A_f + B_f V_f^{n_f} \qquad (2.1b)$$

Under the assumptions that the slant wire angles (subscripts refer to rearward and forward orientations) with the probe axis are close to ±45° (i.e., $= \pm 45° + \delta\beta$) and that the A's, B's, and n's in equations 2.1 are insensitive to small angle changes one can arrive at the following relations for the u and v velocity components.

$$v = (V_f - V_r)/(C_f + C_r) \tag{2.2a}$$

$$u = C_f V_r/(C_f + C_r) + C_r V_f/(C_f + C_r) \tag{2.2b}$$

The angle correction parameters, C_r and C_f, in equations 2.2 are related to their respective slant wire angle deviations from ±45° by

$$\delta\beta_r = (C_r - 1)/(1 + C_r) \text{ rad} \tag{2.3a}$$

$$\delta\beta_f = (1 - C_f)/(1 + C_f) \text{ rad} \tag{2.3b}$$

By gathering data with the probe at small yaw angles, $\gamma \leq \pm 10°$, to the known flow direction, and computing the relative u and v velocities via the relations

$$u = V\cos\gamma$$

$$v = V\sin\gamma,$$

one can then use equations 2.3 to determine C_r and C_f. For the experiments of this chapter, the average slant wire angles (averaged over different flow speeds) were,

$$\beta_r = 43.1° \pm 0.7°$$

$$\beta_f = -48.6° \pm 1.0°.$$

These small angle variations presumably arise from changes in the aerodynamic forces at different flow speeds, as well as, other uncontrolled effects as discussed by Vukoslavcevic and Wallace (1981). Repeatable probe alignment with the free stream is accomplished by positioning the probe in line with the cross-hairs of a telescope positioned about 12 m upstream, and a stationary marker about 2.5 m downstream. The yaw angles of ±5 and ±10 degrees used for calibration were accomplished by a device similar to that described by Bradshaw (1971). All calibrations were performed using mean flow data (i.e., are static), and based upon results of Foss et al. (1986b) no corrections are used to compensate for transverse velocity contamination of the x-array data. At least one determination of the King's law constants was made both prior to and following each acquisition session.

2.4 EXPERIMENTAL PROCEDURE AND FACTORS AFFECTING DATA QUALITY

In subsections 2.4.1-2.4.5 information is presented pertaining to what are considered to be "standard" factors indicative of data quality. Furthermore, in subsection 2.4.6 possible data inadequacies associated with maintaining the constant, but relatively low speed free stream velocities of the present study are examined.

2.4.1 Sampling Rate and Cut-Off Frequency

The frequency response of the wires and anemometers were checked using the standard square wave test. For the $R_\theta \cong 1{,}010$ free stream velocity, this test indicated a response greater than 5 kHz. The fluctuating signals from the four hot-wires were filtered[1] via 4th order Butterworth filters (24 db/octave) at the cutoff frequencies indicated in Table 2.1. The signals were then digitized at the Nyquist criterion based upon the free stream velocity and the minimum Kolmogoroff length scale

[1] Using a known input, the channel-to-channel phase shift caused by the filters was measured. This was found to be about ± $2\mu s$.

found across the layer (using equation 2.6 and the preliminary measurements of Klewicki and Falco 1986). This conservative criterion resulted in digitizing anywhere from approximately 3 to 6 times the given local Kolmogoroff frequency, $f_K = U_1/2\pi\eta$, (U_1 is the local mean velocity) found in the layer. This relatively high sampling rate ($f_s = 1/\Delta t$) was used to ensure that the Δx between consecutive data points under Taylor's hypothesis ($\Delta x = U_c \Delta t$) was less than 1.0 mm. In the study by Antonia et al. (1982b) in a circular jet flow it was found that the optimal low-pass cut-off frequency is approximately $1.75 f_K$ for the purposes of measuring higher order statistics of both velocities and velocity derivatives. The low-pass cut-off frequency in the present study was set at $0.5 f_s$. This resulted in f_c being anywhere from 1.5 to 3.0 times the given local f_K.

2.4.2 Digitizer Resolution

Digitizer resolution is an important consideration concerning the accurate computation of the even-order moments, as well as, the closure of the tails of a probability distribution. Tennekes and Wyngaard (1972), describe the digitizer resolution problem as a trade-off between having enough digital registers to faithfully reproduce large fluctuations, and not so many that the signal noise causes registers to shift. In their study they developed an approximate criteria for laboratory scale flows based upon the maximum signal level, S_{max}, the number of registers being flipped by the largest excursion, R, the digitizing increment, Δd ($= S_{max}/R$), and the rms noise level of the digitized signal, ϵ (not to be confused with the dissipation rate). The criteria:

$$2\epsilon \leq \Delta d \leq 0.1,$$

states that the A/D register width should be at least twice the signal noise level, and less than one tenth the largest excursion. The hot-wire voltages in the current study were amplified prior to filtering in order to increase the 12 bit (plus sign bit) A/D resolution ($\cong$ 2.5 mv per register). As estimated in Figure 2.11 (see Section 2.5) the total electronic noise on the digitized signals was always less than a millivolt -- thus satisfying the first inequality in the above criteria. Considering the problem of resolving large excursions, it was desired to obtain a worst case estimate of the digitizer resolution. To do this, an estimate of the maximum v fluctuation was found at $y^+ \cong 4.5$ in the $R_\theta \cong$ 1,010 boundary layer. This estimate for a typical large excursion was obtained using the kurtosis of v and the rms of v at that location. It was found for this case that $\Delta d \cong 0.050$; thus satisfying the second inequality above.

2.4.3 Total Integration Times

The near-wall data files for the three Reynolds number single-ω_z probe considered contained $4\text{x}10^6$ points ($1\text{x}10^6$ points in each channel), whereas away from the wall the data file size was $2.4\text{x}10^6$ points ($6\text{x}10^5$ points in each channel). Acquisition times ranged between 8.3 and 33.3 minutes depending on the sampling rate and the sample size. This corresponded to sampling between about 3,600 and 8,600 integral scales as defined by TU_∞/δ. Following acquisition, each file was transferred to a PDP 11/73 computer, and then written to tape. A detailed discussion on the convergence of various statistics is given in Section 2.5.2.

2.4.4 On Taylor's Hypothesis

Numerous studies have been devoted to assessing the validity of the Taylor's hypothesis method of measuring streamwise derivatives (i.e.,

$[\partial()/\partial t \equiv -U_c\partial()/\partial x)]$. Included are the four component LDA study of Lang (1985) in a two dimensional turbulent mixing layer, and the spatial temperature derivative study of Browne, Antonia and Rajagopalan (1983) in a plane turbulent jet. Lang concluded that the use of Taylor's hypothesis produces, at best, "fair" results. Browne et al. (1983) found the hypothesis to produce satisfactory results regardless of the choice of U_c (either the average or instantaneous velocity), and deemed corrections to be unwarranted. Given the current undecided state within the turbulence community, and for lack of a better method[2,3], Taylor's hypothesis was used in the present study with the equivalent $\Delta x \leq 2.5\eta$ and U_c defined to be a short time average local velocity averaged over time intervals ranging from $\Delta t u_\tau^2/\nu = 10.6$ to 42.3.

2.4.5 Data Reduction

The data reduction was performed on a PDP 11/73 computer. This consisted of demultiplexing the hot-wire voltages, converting from voltages to velocities, and then computing derivatives, spanwise vorticity, etc., and their statistics. The components of ω_z ($\equiv \partial v/\partial x - \partial u/\partial y$) were resolved by computing $\partial u/\partial y$ via a 2 point finite difference approximation using the fluctuating velocities from the parallel-array, and $\partial v/\partial x$ ($\equiv -(1/U_c)\partial v/\partial t$) by evaluating the derivative of a local second order least squares fit (using 5 points centered about the point of interest) of the v-component velocities derived from the x-array data. This method of computing $\partial v/\partial x$ is preferred to multipoint finite

[2] Actually, Foss et al. (1986a) have devised a method which takes into account the direction of U_c.
[3] Perhaps the best method, in principle, is to measure all of the other gradients as do the workers at the University of Maryland (i.e., Balint et al. 1987a,b), and then check accuracy of the hypothesis through the continuity equation.

difference approximations in that it has been observed to be both less sensitive to the choice of step size and to signal noise. A simple illustration of this is presented in Appendix 2.1.

With such large data samples the possibility existed for stray, non-turbulence related noise spikes, to corrupt the data. A small number of these points, if sufficiently far from the mean, could significantly effect higher order statistics; especially quantities dependent on time derivatives. To avoid this possibility, a point to point check (see Appendix 2.2 for details) of all the velocities was made during the voltage to velocity conversion process. This check consists of defining a criterion based upon the standard deviation of the velocities for a 100 point moving averaged sample, and correcting those points which fail to be within this criterion. The criterion was optimized such that it best eliminated isolated discontinuous points. The criterion used was three standard deviations. This resulted in affecting less than 0.0060% of any given data file (i.e., ≤ 60 points per million). In all but very few cases data was altered only during quiescent times when the criterion became very small.

2.4.6 Free Stream Uncertainty

Due to the relatively low flow speeds and the long integration times involved in this study it became necessary to quantify the variations in the free stream velocity. In particular, answers to the following two questions were desired: 1) Within a given data record acquisition time, what is the maximum uncertainty associated with a possible low frequency variation in U_∞? 2) Was there a quantifiable change in the wire calibration constants or the free stream conditions over the duration of an entire measurement session? Answering the first question is particularly important in assessing the level of certainty to which the convergence results in Section 2.5.2 are meaningful. The answer to the second question provides a more general statement about the overall experiment quality.

2.4.6.1 Short Term Low Frequency Variation in U_∞

In order to quantify the effects of low frequency variation in U_∞ it is felt to be unsatisfactory to simply measure the variation in the mean velocity over the duration of a data record (say by computing the variance of an ensemble of short time averages). This is believed because changes in the mean velocity do not necessarily provide an accurate measure of this effect on fluctuating quantities. Instead an optimal measure would be to examine this effect on the fluctuations directly. One would expect higher order odd moments to be most sensitive to mean variations. In general however, a skewness converges very slowly, and thus using the variance of a short time skewness would also include additional convergence error. Given these considerations it was decided to quantify the possible effects of low frequency variations by observing the maximum percent variation in $\langle uv \rangle$ from its final converged value at $y/\delta \cong 0.37$, as seen in Figure 2.17. This variable was chosen since it is both an odd (i.e. the first) moment of a turbulence quantity and it converged quite rapidly. The criterion was employed at $y/\delta \cong 0.37$ since, in general, statistics in this region of the flow converged most rapidly. Thus a criterion was established that best isolates the convergence errors from those that result from a low frequency variation in U_∞. The uncertainties as indicated by this criteria for the $R_\theta = 1,010$, 2,870, and 4,850 boundary layers are 1.9%, 1.5%, and 1.2% respectively. These values are interpreted as the "noise" level in the convergence data of Section 2.5.2.

2.4.6.2 Long Term Variations in Experimental Conditions

To ensure quality control over calibration drift errors at least one determination of the King's Law constants (but often several determinations) was performed before and after each experiment. Visual inspections were made of the calibration data taken both immediately before and after each experiment. If an identifiable trend could be discerned between the "before" and "after" calibrations, then the entire experiment was repeated. If the variation was deemed acceptable, the individual "before" and "after" calibration equations were averaged; with the exponent set at a constant (see equation 2.1). It is worth noting that the probability of having to repeat an experiment was greatly reduced by allowing the wind tunnel, as well as the electronics, to "warm up" until stable conditions were obtained. This was done by placing the probe in a constant free stream and monitoring (say, every half hour) the A/D (integer) output until subsequent runs produced the same numbers. Typically it took between 1 1/2 to 4 hours for the equipment to stabilize.

Since there was good climate control within the laboratory (± 0.25°C and no detectable variation in barometric pressure), the variation in U_∞ over the duration of an experiment could be attributed to the performance of the fan speed controller. To measure this performance, and also to get an indicator of experiment reproducibility, an auxiliary experiment was run. Furthermore, comparisons were made with data derived from the two-point ω_z correlation experiments described in Chapter 4. In these experiments, a single ω_z probe was positioned at a given y^+ value for the duration of the experiment. The auxiliary experiment consisted of positioning the ω_z probe at $y^+ \cong 6.2$ in the $R_\theta = 1{,}010$ boundary layer and collecting 5 data files at equal time intervals over the course of approximately 8 hours. The size of each data file was 1/5 the size of the data file represented at that location in Figure 2.14. The results of this experiment, in terms of $\omega_z'^+$, as well as the data from the correlation experiments (with probes fixed at $y^+ \cong 13.4$ and 100.5) are given as a function of experiment time in Figure 2.4. The horizontal lines represent data taken from the distribution of Figure 2.14. A least squares fit of each of the three data sets in Figure 2.4 was made using the model $\omega_z' = B_0 + B_1 t$ (where t is the experiment time). Given the assumptions of additive, zero mean, constant variance, uncorrelated, and normally distributed errors associated with the measurement of ω_z' as a function of experiment time, and that the parameters B_0 and B_1 are non-random, an F-test of these results indicated that to a level of significance of 0.99 one cannot reject the hypothesis that $B_1 = 0$. Thus, it was concluded that over extended periods of time U_∞ did remain constant. Note also that the auxiliary experiment results tend to show a greater variation about the data from Figure 2.14 than the correlation experiment data, which had much longer averaging times. Due to the relatively small sample size of the auxiliary experiment, a good part of this point-to-point variation is probably attributable to convergence error. This conclusion is further supported by the convergence results in Section 2.5.2.

To obtain an error bar on ω_z', standard deviations were developed from the data of Figure 2.4. The error bars in Figure 2.14 are represented by ±1 standard deviation. The maximum standard deviation (at

$y^+ = 6.2$) is 4.6% of the measured value. Two significant points pertaining to these error bars are:

a) the agreement between the mean values of the data of Figure 2.4 and the corresponding points in the distribution of Figure 2.14 are within ±2%; indicating, in general, an ability to accurately reproduce the free stream condition and,

b) the largest error bar represents a maximum error estimate for all of the distributions since it may be conservatively estimated that 1/3 of this error bar's length is attributable to a lack of convergence and, as shown above, the $R_\theta = 1{,}010$ boundary layer had the largest percentage of experimental uncertainty associated with low frequency drift in U_∞.

As a final comment on data quality, it should be noted that no wire breakages occurred during the course of acquiring the three R_θ distributions described in Chapters 2 and 3. Thus this eliminates the consideration of probe related uncertainties in comparing the different Reynolds number results.

2.5 SPATIAL RESOLUTION AND STATISTICAL CONVERGENCE RESULTS

In this section spatial resolution and convergence results from the four wire ω_z probe measurements are presented, and compared with other wall flow studies. Section 2.5.1 presents results which are used to infer conclusions about the spatial resolution needed to accurately resolve near-wall physics. Also included in this section is information specifically pertaining to the validity and accuracy of the present measurements. Section 2.5.2 presents results concerning the averaging times necessary to obtain statistical convergence.

2.5.1 Spatial Resolution

Assessing the overall effect of finite spatial resolution on multi-component probe measurements is difficult due to the numerous contributing factors involved. In general however, it appears to be fairly well documented that increasing the spatial scale of a probe will result in an attenuation of the statistical moments of the probe's signal. Given a wire construction with a sufficiently large length to diameter ratio this attenuation can occur by two major effects. Finite wire length effects (see for example, Johansson and Alfredsson (1983) or Ligrani and Bradshaw (1987)) tend to average high amplitude small scale fluctuations with spatially adjacent low amplitude motions over the length of the sensing element. Finite wire spacing effects (as discussed by Subramanian et al. (1985)) tend to spatially filter derivative signals at wave-lengths about equal to the wire spacing. Both of these effects, primarily by causing a failure to resolve high amplitude fine scale information represented in the tails of a given probability distribution, will generally cause an attenuation in the measured values of both the even and odd moments of that distribution.

2.5.1.1 Wire Length Effects

An apparent indicator of wire length effects on wall flow velocity measurements is the maximum measured value of u'/u_τ. Figure 2.5 presents a comparison of the maximum u'/u_τ value versus the non-dimensional wire length as found using the u-wire closest to the wall in the ω_z probe, as well as, from other wall flow investigations. Also included is a curve fit of the data of Johansson and Alfredsson (1983) and Ligrani and Bradshaw (1987). This curve fit shows that, at a given Reynolds number, if one increases the length of a sensor the peak value of u'/u_τ will decrease.

However, the variation in the peak value of u'/u_τ cannot be explained in terms of non-dimensional wire length alone. For example, the present data, that of Wei (1987), and Ueda and Hinze (1975) (all having $\ell^+ < 8$) show a consistent decreasing trend as probes of smaller ℓ^+ are used. Furthermore, the data of Purtell, Klebanoff and Buckley (1981) as well as that of Andreopoulos et al. (1984) apparently contradict the trend shown by the curve fit. In the case of Purtell et al. a difference of 15% in the peak value is obtained for probes of nearly identical $\ell^+ \cong 8$, and then for larger ℓ^+ the attenuation is less severe than either the Johansson and Alfredsson or Ligrani and Bradshaw data. In the case of Andreopoulos et al., the data is roughly 15% higher than that predicted by the curve fit.

To gain an understanding of this apparent scatter, the possibility of a Reynolds number dependence in the "true" value of $u'/u_\tau|_{max}$ was examined. To do this, the curve fit of Figure 2.5 was used to correct the data by removing the attenuation caused by finite probe scale effects. Note that the use of this curve fit implies that this attenuation is only a function of the non-dimensional probe scale, ℓ^+. Figure 2.6 presents the corrected data of Figure 2.5 as a function of Reynolds number. This figure clearly suggests that the "true" peak u'/u_τ value is Reynolds number dependent. Note that only the data of Purtell et al. (for wire lengths $\ell^+ \cong 10.9, 20.4, 29.9$), and that of Andreopoulos et al. ($\ell^+ \cong 20.9, 33.4$) actually required the correction for spatial attenuation in order to exhibit this trend. This apparent Reynolds number dependence explains why the low Reynolds number data of Purtell et al. is 15% lower, and why the data of Andreopoulos et al. is 15% higher than that suggested by the curve fit in Figure 2.5.

Thus it appears that there are, in practice, competing effects between an increase in $u'/u_\tau|_{max}$ as a result of a Reynolds number dependence in its "true" value, and an attenuation in its measured valued resultant from finite probe scale effects. Given that many lower resolution studies in wall flows predict that the maximum in u'/u_τ decreases as the Reynolds number is increased, detecting the opposite may provide a simple measure of the minimum probe spatial resolution required to study Reynolds number effects. Using the above conclusion, the data of Purtell et al. shows the correct Reynolds number dependence for small ℓ^+, but then as the Reynolds number increased (and thus increasing the non-dimensional probe scale) an opposite trend is observed. This trend is presumed to be a consequence of spatial averaging effects. It therefore appears that the attenuation effect is stronger than the Reynolds number effect.

These results show that a Reynolds number dependence occurs in the fine scale structure. Furthermore they support the hypothesis mentioned in the discussion of Table 1.1 that an even greater Reynolds number effect may exist. However, this effect may possibly only be demonstrated by using probe/flow configurations whose R_θ/ℓ^+ are increased even further.

To gain an understanding of the effect of wire length on time derivative statistics the values of the skewness of $\partial u/\partial t$ in the near wall region were examined. The present results are derived from the u-wire closest to the wall contained in the ω_z probe. Figure 2.7 presents an adaptation of a plot by Johansson and Alfredsson (1983) with additions from other channel and boundary layer investigations (also see Table 2.4). The generally good agreement between the present data and that of Wallace et al. (1977) and Ueda and Hinze (1975) for $y^+ \geq 15$ probably reflects the fact that the spatial resolution (either wire length and/or wire spacing) of the probes in all of these investigations is about equal. It should be noted that Reynolds number effects apparently do not manifest themselves in this region of the flow over the range $300 \leq R_\theta \leq 5{,}000$ for this statistic. Apparently the data of Johansson and Alfredsson shows attenuation due to their relatively large wire lengths. Closer to the wall this figure also shows that considerable data scatter exists (up to 30%) for wire lengths in the range $5 < \ell^+ < 15$. In light of the discussion above concerning u'/u_τ this could be due to spatial resolution and/or Reynolds number effects. Estimates of the $S(\partial u/\partial t)$ have also been obtained from the x-array of the ω_z probe. As the Reynolds number increased these profiles showed an identifiable decrease in the magnitude for $y^+ < 50$. This trend is consistent with an attenuation due to the additional spatial averaging effects resultant from the wire spacing of the x-array. Thus, it appears that spatial averaging has a greater effect on skewness of $\partial u/\partial t$ than on those of u'/u_τ. This result is consistent with the notion that greater spatial resolution is required to obtain derivative information with the same accuracy as the variable itself.

It should be noted that comparisons between v statistics (rather than u statistics) would provide a much more stringent measure of spatial resolution. This is because v statistics are associated with smaller scale motions. This objective however, proves to be difficult since there is significant scatter in the v statistic data. This scatter is probably due to numerous factors such as Reynolds number effects as indicated by

Wei (1987) and the results in Chapter 3, and inherent spatial resolution effects due to the need for multiple wires.

Figure 2.8 presents measurements of the skewness of v along with a representative sample of existing profiles from turbulent boundary layers and channel flows. Comparing Figure 2.8a with 2.8b, the data in the buffer region shows two distinctly different trends. Figure 2.8a (which includes all of the present measurements) shows S(v) data which are positive in the range $5 \le y^+ \le 30$. Figure 2.8b shows data which are negative in this range. Note that in Figure 2.8b one of the data sets is from the discrete Navier-Stokes simulations of Kim et al. (1987). Of particular interest, is the apparent fact that there is no obvious dependence on either probe spatial resolution or Reynolds number in either Figures 2.8a or 2.8b.

To gain insight into the potential causes behind the observed data scatter, Table 2.2 was prepared. In this table the sign and magnitude of S(v) at $y^+ \cong 20$ was chosen to enable more data to be represented, even though in both cases the maximum deviation from zero occurs at about $y^+ \cong 13$. Table 2.2 gives information pertaining to experiments of different flow types, Reynolds number, probe scales, facility types, and the presence/absence of a tunnel inlet contraction. There does not appear to be a clear-cut indicator among these parameters that explains the observed data scatter.

Looking more carefully however, a correlation possibly exists between the influence of a tunnel contraction and the sign of S(v) in the buffer layer. In the three boundary layer studies in which S(v) is positive in the buffer layer, the flow facilities either have no contraction, or the layers developed along a plate suspended in the center of the tunnels. Furthermore, for these studies S(v) was measured using an x-array of wires or films. In the two boundary layer studies in which S(v) is negative in the buffer layer the flow facilities have inlet contractions and the layers develop along the tunnel wall. The possibility of creating streamwise vorticity in a contraction has long been acknowledged. This vorticity, which is approximately fixed in spanwise location, could account for the near wall differences in S(v).

For the channel flow data, the results of Wei appear to indicate a clear Reynolds number dependence -- with S(v) changing sign from negative to positive as the Reynolds number increased. However, this observation is in direct contrast with the results of Kreplin and Eckelmann (1979) who found S(v) to be positive at about the same low Reynolds number. It is also interesting to note that only the low speed LDA measurements of Wei (1987) and Barlow and Johnston (1985) (and the nine wire probe of Balint et al. (1987a)) have reported negative values of S(v) for $5 < y^+$ 30. As noted above the Kim, Moin and Moser computation also gives negative values.

2.5.1.2 Wire Spacing Effects

According to the study by Wyngaard (1969), to resolve fluctuating velocity gradients in an isotropic turbulent flow the wire separation, h, should satisfy the inequality

$$1.0 < h/\eta \leq 3.33 \qquad (2.4)$$

where, $\eta = (\nu^3/\epsilon)^{1/4}$. In the present study ϵ was estimated using four of the twelve terms.

$$\epsilon/\nu = \langle(\partial u/\partial x)^2 + (\partial v/\partial x)^2 + 3.5(\partial u/\partial z)^2 + 2.5(\partial u/\partial y)^2\rangle \quad (2.5)$$

This relation is derived by making the following assumptions:

$$\langle(\partial w/\partial y)^2\rangle = \langle(\partial u/\partial y)^2\rangle,\ \langle(\partial v/\partial z)^2\rangle = \langle(\partial u/\partial z)^2\rangle,$$

$$\langle(\partial v/\partial y)^2\rangle = 1/2\langle(\partial u/\partial y)^2\rangle,\ \langle(\partial w/\partial z)^2\rangle = 1/2\langle(\partial u/\partial y)^2\rangle,$$

$$\text{and } \langle(\partial w/\partial x)^2\rangle = \langle(\partial u/\partial z)^2\rangle,$$

as well as assuming that the sum of the three cross derivative terms is negligible. These assumptions are similar to those given by Klebanoff (1954).

While describing probe dimensions in viscous units allows objective comparisons to be made between different studies, often times one would also like to know the probe scale in terms of η. Many wall flow studies do not have the capability to accurately estimate ϵ, and thus it would be advantageous to have a simple compact formula for ϵ. An inner variable non-dimensionalization of the turbulence energy equation under the assumptions of production equals dissipation, $\langle uv\rangle/u_\tau^2 = 1$, and that the law of the wall is valid allows ϵ^+ ($\equiv \epsilon\nu/u_\tau^4$) to be expressed as:

$$\epsilon^+ = 1/\kappa y^+ \quad (2.6a)$$

or

$$\epsilon = u_\tau^3/\kappa y. \quad (2.6b)$$

Figure 2.9 presents estimates of ϵ^+ obtained using equation 2.5, as well as the estimate derived by assuming isotropy. For $R_\theta \geq 3{,}000$ equation 2.6b provides a good agreement with the given dissipation rate estimate for $y^+ > 10$. As the Reynolds number decreases the agreement becomes progressively worse in the inner region. Note also that by using the isotropic estimate ($\epsilon \equiv 15\nu\langle(\partial u/\partial x)^2\rangle$) one obtains differences with the estimate of equation 2.5 (or 2.6) of over 300% in ϵ (or 40% in η), and thus the estimate given by equation 2.6 is preferred.

Table 2.3 presents a summary of the minimum and maximum non-dimensional wire separations encountered in the three boundary layers of the present study. In this table Δy represents the wire spacing in the parallel-array and Δz represents the separation between the centers of the parallel and x-arrays. It should be noted that the resolution of ω_z does not depend on $\partial()/\partial z$ gradients. However, the given probe arrangement does assume that $\partial v/\partial x$ at $z = \partial v/\partial x$ at $z+\Delta z$. Thus, it was necessary to evaluate the validity of this assumption, as well as, the validity of equation 2.4 under anisotropic conditions. Furthermore, since many multi-wire probes use spatial averages of temporal and streamwise derivatives to approximate measurements at the given probe center, the effect of wire separation on this process is also examined.

Evaluation of wire spacing effects on the measured value of the associated spatial gradient was done by performing an auxiliary experiment. The geometry of this experiment consisted of fixing a parallel-array about a given point in the $R_\theta = 1,010$ boundary layer, and then positioning at equal Δy spacings above and below this array a pair of y-traversable single wire probes. The arrangement is shown as an insert in Figure 2.10. In this figure Δy_i is the wire spacing between the parallel-array elements, and Δy_o is the spacing between the two single wire probes. Simultaneous data from all four wires was taken for various Δy_o; keeping the center position of Δy_i and Δy_o the same. The matching calibration procedure described in Section 2.3.2 was performed using the lower wire of the parallel-array as the reference wire. The experiment was performed at $y^+ \cong 53$ and at $y^+ \cong 38$.

Results pertaining to the attenuation in the measured rms of

$(\partial u/\partial y)_o$ ($\equiv (\partial u/\partial y)'_o$) as Δy_o was increased are given in Figure 2.10. The data in this figure are presented as the ratio of $(\partial u/\partial y)'_o$ over $(\partial u/\partial y)'_i$. Since data from all four wires was taken simultaneously for each Δy_o, data presentation in this way greatly eliminates from the results the effect of the observed ±3% variation in $(\partial u/\partial y)'$ from run to run. It is important to note that for the given boundary layer $\Delta y_i^+ \cong 1.84$, and $\Delta y_i/\eta \cong 1.04$ and 0.94 at $y^+ \cong 38$ and 53 respectively. Thus the data in Figure 2.10 are (in principle) equal to 1.0 at these values and not at the origin. One thing to notice about both the $y^+ \cong 38$ and $y^+ \cong 53$ data is that for $\Delta y/\eta \leq 3$ very little attenuation ($\cong$ 3%) occurs, and that changing the level of mean shear has little effect. This suggests that Wyngaard's estimate (equation 2.4) is valid to a good approximation, even under anisotropic conditions. Another thing to note is the rapid attenuation (~ 15%) for wire spacings between $\Delta y/\eta = 3$ to 6; which agrees well with the results to be shown in Figure 2.15. These results are seemingly in contrast with those of Bottcher and Eckelmann (1985) which predict that the inner array would give smaller rms values than the outer array for small Δy_o. Significant differences, however, such as flow type (laminar vs. turbulent), probe type (hot-wire vs. hot film), probe construction, and calibration method exist between the two studies. Further reference is made to these factors in the discussion of Figure 2.14. Also, data pertinent to assessing the accuracy of the parallel-array measurements of the mean gradient, $\partial U/\partial y$, are presented in Appendix 2.3.

In order to quantify possible spatial filtering effects of finite wire separation, spectra of the individual $(\partial u/\partial y)_i$ and $(\partial u/\partial y)_o$ time series were computed. Examples of the frequency spectra for $\Delta y/\eta = 0.94$, 4.83, and 9.01 at $y^+ \cong 53$ are presented in Figure 2.11. By using the wire spacing to construct an approximate frequency, $f_{\Delta y} = U_1/(2\pi\Delta y)$, it can be clearly seen that the effect of wire spacing is to attenuate the gradient intensity at higher frequencies. Furthermore, creating separate spectral plots from each pair of simultaneously acquired $(\partial u/\partial y)_i$ and $(\partial u/\partial y)_o$ time records allowed for the determination of effective low-pass cut-off frequencies (i.e. the frequencies at which the $(\partial u/\partial y)_o$ spectra diverged from the $(\partial u/\partial y)_i$ spectra). These results, as derived from the $y+ \cong 53$ data, are presented in Figure 2.12 as a function of outer array separation. In this figure the ordinate is the ratio of the approximate cut-off frequency over $f_K \equiv U_1/(2\pi\eta)$. The error bar to the left of the spectral curves in Figure 2.11 represents the data scatter at 1hz, and was used in determining the cut-off frequencies in Figure 2.12.

Interesting results concerning how noise in the velocity signals enters into the $\partial u/\partial y$ signals are also described in Figure 2.11. Heuristically, one would expect that at the highest measured frequencies the energy in the u spectra is due entirely to electronic noise. This noise level, labeled $\epsilon_u{}^2$ in Figure 2.11, is associated with the white noise portion of the spectrum at high frequencies. For the u spectra in this figure $\epsilon_u{}^2$ is about $e^{-15.75}$ (ft^2/s), or equivalently, less than 0.3 mv of electronic noise. Assuming that the $\epsilon_u{}^2$ for each wire is uncorrelated, then in the noise dominated part of the spectrum one may approximate $\Phi(\partial u/\partial y)$ by $\epsilon_u{}^2/\Delta y^2$. Using this equation and the above cited value for $\epsilon_u{}^2$ allowed for estimates of the associated noise levels in $\Phi(\partial u/\partial y)$ for the various Δy. The predicted noise levels are given as the horizontal lines through the $\partial u/\partial y$ spectral curves. As one can see, the predicted values agree very well with the actual noise levels in the

$\partial u/\partial y$ spectra. These results suggest that the noise level in a single velocity signal can be used to determine the minimum acceptable Δy spacing used to measure $\partial u/\partial y$.

Another problem associated with multi-wire array measurements is that often it is necessary to average the same quantity obtained at two spatial locations in order to approximate point-wise measurements at the probe center (Balint and Wallace private communication). The data of the above described experiment provided a means by which to measure the effect of this averaging procedure. For each wire a $\partial u/\partial t$ time series was computed. Then at each instant a spatial average of $\partial u/\partial t$ was computed using the inner two wires and the outer two wires respectively. From these $(\partial u/\partial t)_i$ and $(\partial u/\partial t)_o$ time series' rms values were computed. As with the $\partial u/\partial y$ data, the ratio of rms $(\partial u/\partial t)_o$ ($\equiv (\partial u/\partial t)'_o$) over $(\partial u/\partial t)'_i$ is presented in Figure 2.10. The attenuation shown by the data is very rapid for wire spacings $\Delta y/\eta \leq 15$, and then continues to attenuate, only more slowly, for greater Δy values. Clearly, for a given non-dimensional wire spacing the effect of increasing the mean shear (moving closer to the wall) is to cause further attenuation due to this averaging procedure. Note that this effect is not readily apparent in the $\partial u/\partial y$ data. It is also interesting to note that the attenuation of $(\partial u/\partial t)'$ (due to spatial averaging) for small Δy is greater than that of $(\partial u/\partial y)'$. These results suggest that significant changes in the temporal gradients exist across Kolmogoroff scale eddies. This spatial sensitivity in the temporal gradients is also suggested by the comparison that was made between $S(\partial u/\partial t)$ as derived from the x-array and the single wire of the parallel array in the discussion of Figure 2.7.

It should be noted that the utility of the results in Figures 2.10, 2.11, and 2.12 are dependent on the absolute accuracy of the inner array results. Of course the absolute values of $(\partial u/\partial y)'$ will never be easily verified. However, for the $\partial u/\partial t$ data no statistically significant difference was found between $(\partial u/\partial t)'$ from the inner array ($\Delta y/\eta \cong 1$) and the $(\partial u/\partial t)'$ values derived from the individual wires of the inner array.

An assessment of the validity of the assumption:

$$\partial v/\partial x \text{ at } (z) = \partial v/\partial x \text{ at } (z + \Delta z),$$

(as required to compute ω_z from the present probe) was made by spatially separating two x-arrays in the spanwise direction and computing the $\partial v/\partial x$ correlation coefficient for various Δz separations. The results of this experiment are shown in Figure 2.13 as a function of the non-dimensional spanwise spacing at $y^+ \cong 140$ in the $R_\theta = 1{,}010$ boundary layer. Two runs were made per Δz spacing to increase confidence in the results. At this point in the boundary layer $(\partial v/\partial x)'/(\partial u/\partial y)'$ is about equal to 0.38; indicating significant anisotropy. Also included in this figure (for reference) are the u and v correlation coefficients.

The results in Figure 2.13 show, for example, that at the given y^+ location an average error of approximately 20% can be expected in the instantaneous $\partial v/\partial x$ values for Δz separations of approximately 7 Kolmogoroff scales (which is $\cong$ 14 viscous scales at the given position in the boundary layer). Examination of Table 2.3 shows that in the $R_\theta \cong$ 1,010 boundary layer the separation between the parallel and the x-array center is always less than $\eta = 7$. Most of the $R_\theta = 2{,}870$ data, and about half of the $R_\theta = 4{,}850$ data satisfy this condition. However, these results should be viewed with some reservation since in general integral scales decrease as the wall is approached. Furthermore, a significant Reynolds number dependence may exist for this correlation coefficient. In any case, these results suggest that $\partial v/\partial x$ (and probably all v gradients) are largely comprised of small scale contributions, and attempts to resolve v gradients over wire spacings much greater than a few Kolmogoroff scales will result in serious errors. Foss, Ali, and Haw (1986b) support these results in that in a similar experiment done in a free shear flow they show that the angle of the velocity vector changes significantly for small spanwise separations. On the plus side however, the contribution of this error to the spanwise vorticity is diminished in the near-wall region since in this region $\partial u/\partial y$ dominates $\partial v/\partial x$ (see Figure 2.14).

2.5.1.3 The Resolution of ω_z

To investigate probe scale effects on ω_z' the distributions of two different non-dimensional functions containing ω_z' were examined. Figure 2.14 shows an inner variable normalization versus y^+. As can been seen, the wall variable normalization results in a very good scaling of the data. This is further shown by the fact that ω_z' for the present data varies by a factor of ten over the given Reynolds number range. The results of this figure suggest that spatial resolution effects not only attenuate the present data, but also the data of Balint et al. (1987a). In the wall region, a small but identifiable attenuation with increasing R_θ can be observed. This attenuation is consistent with a decrease in spatial resolution resultant from an increase non-dimensional probe scale caused by an increase in the Reynolds number. Note that if one has confidence in the apparent scaling of ω_z' by ν/u_τ^2 (at least in this region of the flow) then the under-estimation of ω_z' for small wire spacings (via the under-estimation of $\partial u/\partial y$) as predicted by Bottcher and Eckelmann (1985) is not apparent in the present results. An explanation of the error bars presented in this figure was given in Section 2.4.6. Additionally, it should be noted that the computations of Kim, Moin and Moser agree well with this scaling except as one nears the sublayer.

To further examine the spatial resolution effects suggested in Figure 2.14 an alternate non-dimensional function containing ω_z' was examined. Figure 2.15 shows distributions of $y\omega_z'/u_\tau$ versus y/θ. (The data set of Kim et al. was left off this figure because of the large differences in the wake structure of boundary layers and channel flows.) This function was chosen since it shows a distinct Reynolds number trend when plotted versus y/θ. One can see in the present data a clear Reynolds number trend in the opposite direction as that predicted by spatial resolution effects. Given this Reynolds number dependence (and assuming that at each R_θ this function is represented by a single curve), the distribution of Balint et al., (R_θ = 2,100, $h^+ \cong 8.9$), should lie between the two lower Reynolds number distributions of the present study. The fact that it does not is probably due to the relatively larger wire separation (in viscous units) of their probe. This figure indicates that their ω_z' measurements show an attenuation between 10% and 15%. This result is in remarkable agreement with the findings in Figure 2.10.

2.5.2 Convergence of Turbulence Statistics

Numerous results concerning the convergence of statistics in turbulent flows may be found throughout the literature. In fact, most studies presenting higher order statistics (especially those investigating the dissipation scales) report, to varying extent, information pertaining to statistical convergence. Typically however, since these studies are investigating small scale structure, little attention is paid to more global effects such as the level of mean shear and the flow Reynolds number, R_θ. Wall-bounded shear flows present perhaps the most demanding conditions for obtaining statistical convergence. In boundary layers one has both the turbulent/non-turbulent interface at the outer edge, and the highly intermittent production process near the wall. Furthermore, wall flows (versus free shear flows) generally have relatively more energy concentrated at higher wave numbers due to the presence of the wall. This section presents a fairly comprehensive look at the statistical convergence of a variety of variables in four regions of the boundary layer in which the physics is different, and for the R_θ range given in Table 2.1.

A short review of popular analytical/empirical relations concerning the estimation of convergence times necessary to ensure a given accuracy is given by Antonia et al. (1982b), and therefore will not be repeated here. Rather, the goal of this section is to both document some of the factors influencing statistical convergence, and to provide a purely empirical basis by which to design experiments.

2.5.2.1 Methodology

Cumulative estimates of the statistics up to the fourth moment were computed for u, v, uv, $\partial u/\partial t$, $\partial v/\partial x$, $\partial u/\partial y$, ω_z and $v\omega_z$. (In the following presentation only the results of u, uv, $\partial u/\partial t$, ω_z and $v\omega_z$ are shown.) These estimates were output at regular intervals of 200,000 points (the corresponding integration times depend on the sampling rate). The relatively long times between the intermediate averages were chosen to facilitate statistically meaningful convergence results. The convergence data for the above variables were compiled for the three Reynolds numbers given in Table 2.1, and for four regions of the boundary layer. These regions are denoted by:

I	near-wall	$y^+ = 12 - 18$
II	strong-shear	$y^+ = 40 - 50$
III	weak-shear	$y/\delta = 0.36 - 0.40$
IV	intermittent	$y/\delta = 0.75 - 0.80$

Convergence data was compiled for each variable and arranged in the form of Figure 2.16. In these figures, which are comprised of 12 component plots, each row shows data from a different region, whereas each column shows different Reynolds number data. The ordinates of the individual component plots are in units of absolute percent convergence as given by:

$$\frac{(X_i - X_f)}{X_f} \times 100\%$$

where X_i is the intermediate value of the moment, and X_f is the final value found using the entire data record. Thus, presenting data in this way assumes that X_f has converged. This assumption proved to be valid in the vast majority of cases. The abscissae of the component plots are in non-dimensional time units of TU_∞/δ, where T is the averaging time. These units were chosen to represent approximate non-dimensional integral time scales. Data presentation as described above allows for the identification of Reynolds number and/or boundary layer regional trends. To facilitate the identification of trends, the convergence data were curve fit by second order polynomials (note that in Figures 2.16, 2.17, 2.20, 2.21 and 2.23 points above the ordinate range in the component plots are not shown).

Before the convergence data were examined they were divided into three groups. These groups are velocity and Reynolds stress, velocity gradients, and velocity-velocity gradient products. Within each one of these categories convergence rate comparisons are first made between the variables within a group. Then, general trends in convergence among the four boundary layer regions are examined. Finally, Reynolds number trends in convergence are explored.

2.5.2.2 Velocities and Reynolds Stress

Comparisons between the convergence data for u, v and uv were made. The convergence data for u are in Figure 2.16 and that for uv are in Figure 2.17 (note that the ordinate scales of the component plots may be different for different figures). Somewhat surprisingly, the present results indicate that in general the uv statistics converged at least as fast as the u statistics. Furthermore, the skewness of uv shows a distinctly more rapid convergence than that of u. For all four regions, Reynolds numbers, and statistical moments, the v statistics showed the slowest convergence rates. Except for perhaps the intermittent region of the $R_\theta = 1{,}010$ flow (see Figure 2.16), the skewness of both u and v showed the slowest convergence rate. This is not surprising since odd order moments tend to converge more slowly than even order moments. Antonia et al. (1982b) showed this to be true for both u and $\partial u/\partial t$ statistics at the centerline of turbulent jets. Oddly enough however, the kurtosis of the Reynolds stress converged just as slowly, and in some cases distinctly more slowly, than the skewness of the Reynolds stress. Figures 2.18 and 2.19 show the present distributions of S(uv) and K(uv). Note, that the K(uv) distributions show much greater change across the layer than the S(uv) distributions. A possible cause for the slower convergence of K(uv) may be related to the greater variation in K(uv) itself. Similar results are suggested by the data of Wei (1987) which has been reproduced in Figures 2.18 and 2.19. It should be noted that the S(uv) and K(uv) profiles shown are central moments.

An examination is now made of the effects of mean shear, and the near-wall and outer region intermittency on the convergence of u, v, and uv statistics. As one can see in the left hand columns of Figures 2.16 and 2.17, for the lowest Reynolds number layer there is little variation from region to region across the layer. Comparisons among the four regions at the two higher Reynolds numbers indicate distinct trends; showing the need for increased signal length nearer the wall. These trends are about the same for the u, v, and uv statistics. In almost all cases (and, generally, for all of the variables observed) the weak-shear region showed the most rapid convergence. Both the intermittent region and the weak-shear region show about the same convergence rate for the two higher Reynolds number flows.

The intermittent region at the lowest R_θ showed slightly slower convergence rates than the same region at the higher R_θ. For the other regions, however, the velocities and Reynolds stress show poorer statistical convergence as the Reynolds number is increased. Given that all other factors are equal, this finding is consistent with the hypothesis that as R_λ ($R_\lambda = u'\lambda/\nu$, where λ is the Taylor microscale) increases, so does the time to convergence. This however, should not be viewed as a general rule -- as suggested above by the possible reverse trend in the intermittent region. This is also shown more clearly in the following subsection.

2.5.2.3 Velocity Gradients

The convergence results for $\partial u/\partial t$, $\partial v/\partial x$, $\partial u/\partial y$ and ω_z were quite different from those of the velocities and Reynolds stress. While the overall convergence times necessary to achieve a given accuracy were about equal to or slightly less than those found for the velocities, significant changes across the boundary layer and with Reynolds number were observed. Of all of the gradient quantities examined, the $\partial u/\partial t$ statistics exhibited by far the most rapid convergence, whereas the $\partial v/\partial x$ statistics were clearly the slowest to converge[4]. The $\partial u/\partial y$ and ω_z statistics converged at almost exactly the same rates; presumably due to the dominance of $\partial u/\partial y$ over $\partial v/\partial x$ over most of the boundary layer. The $\partial u/\partial t$ and ω_z convergence data are shown in Figures 2.20 and 2.21 respectively. Almost without exception, and for all R_θ and positions in the boundary layer, the skewness of the gradient quantities examined demonstrated the slowest convergence rates. It is worth noting that in the weak-shear region the skewness data of Figure 2.20 are in good agreement with the results of Mestayer (1982). He showed that it takes between 250 and 1,400 TU_∞/δ to achieve ±5% accuracy in the 3rd order moments of fluctuating temperature and fluctuating temperature differences at $y/\delta \cong 0.33$.

The gradient quantities generally showed less region to region variation than did the velocities and Reynolds stress. Perhaps the most striking feature was the relatively long convergence times for the gradient quantities in the intermittent region (shown in both Figures 2.20 and 2.21). This makes apparent physical sense in that gradient quantities should be highly sensitive to rapid changes in the flow

[4]Since Taylor's hypothesis is used, it is unclear whether the relatively slow convergence of $\partial v/\partial x$ is a consequence of this.

associated with the turbulent/non-turbulent interface. The time to convergence of the gradient quantities, in general, did not show the same increase in the presence of high mean shear as did the velocities and Reynolds stress. In the near-wall region for the two lower Reynolds numbers the skewness of ω_z and $\partial v/\partial x$ took relatively long times to converge. Figure 2.22 shows the present skewness profiles of ω_z. $S(\omega_z)$ is negative over the entire layer, with a distinct peak at $y^+ \cong 40$. Reasonable scaling on wall variables is suggested for $y^+ < 40$. (Further discussion and implications of these features are given in Chapter 3.) The smoothness of these curves suggests that the values obtained using the entire record have little uncertainty associated with a lack of convergence. Also, this data shows good agreement with that of Balint et al. (1987a). Their integration time was $TU_\infty/\delta \cong 3{,}100$, which according to Figure 2.21 should give approximately ±5% uncertainty.

Reynolds number trends for the gradient quantities were in general also less significant than for the velocities and Reynolds stress. In more than one instance however, there appeared to be faster convergence within a given region as the Reynolds number increased. This is shown in the weak-shear region in both Figures 2.20 and 2.21. For reference the microscale Reynolds number, R_λ, is given in these component plots. The results here are in direct contrast to the aforementioned hypothesis that as R_λ increases so does the integration time. This suggests that basing comparisons of fine scale structure experiments on matching R_λ may not be sufficient, and that other features such as the level of mean shear should also be considered.

2.5.2.4 $v\omega_z$

As the need to understand the finer details of turbulence structure increases, the experimental measures required will also increase in complexity. This subsection presents convergence data as it relates to the fluctuating quantity $v\omega_z$. This quantity is known to be related to the Reynolds stress gradient (e.g. Tennekes and Lumley (1972) p. 78, also see the present Chapter 3). As might be expected, the convergence rates of the $v\omega_z$ statistics were much slower than the other variables examined. The convergence data for $v\omega_z$ are presented in Figure 2.23. Note that for the highest Reynolds number and in the near-wall region the skewness of $v\omega_z$ never converged. This is due to the fact that for different record lengths $S(v\omega_z)$ kept reversing sign, thus making it difficult to compute a meaningful percent convergence. As can be seen, in the other regions of the layer the skewness shows the slowest convergence rate. The trends across the boundary layer are very similar to those exhibited by the velocities in that as the level of mean shear is increased so does the time to convergence. A fairly consistent Reynolds number trend can also be seen for all of the regions. Apparently, convergence times for $v\omega_z$ statistics are adversely effected by increasing R_θ.

2.5.2.5 Convergence Summary

Table 2.5 presents a compilation of general convergence criteria based upon the above described data. Note that these criteria are based upon the assumption that one wishes to obtain profiles across the entire boundary layer, and thus are conservative for, say, someone wishing to take data only in the weak-shear region. It is hoped that these criteria will facilitate better experiment design in wall-bounded shear flows.

2.6 DISCUSSION AND CONCLUSIONS - RELATIVE TO CHAPTER 2

Aside from documenting the present experimental arrangement and procedures, this chapter has examined some features of turbulent boundary layer hot-wire measurements that are sensitive to small scale structure. These features may be grouped into two (not necessarily independent) categories relating to the probe and its spatial and temporal resolution, and the type of information one wishes to extract -- mainly pertaining to the practical constraints imposed by the integration times necessary to achieve statistical convergence. In this section a discussion, conclusions, and some general recommendations based upon the results herein will be given. Furthermore, a critical evaluation of the overall quality of the present four-wire ω_z probe experiments is presented.

Based upon the data of Figure 2.6 it appears that the maximum value in u'/u_τ increases with increasing R_θ. Imperfect spatial resolution can hide this dependence because the attenuation (due to increasing wire length in viscous units as a consequence of increasing R_θ) is apparently greater than the increase due to Reynolds number. It is therefore submitted that detecting this Reynolds number trend provides an indicator of good probe resolution, and constitutes a practical necessary condition for studies investigating Reynolds number dependencies. It is probably true that as a wire of given length becomes greater than about $8u_\tau/\nu$ (as R_θ is increased) spatial averaging effects will begin to wipe-out this trend. The data of Purtell et al. (1981) in Figure 2.5 clearly demonstrate this. The competing effects between spatial resolution and Reynolds number have apparently hidden the true flow physics, and have led many to the belief that the maximum value of u'/u_τ is indeed a constant. In fact, if one were to ignore both of these effects then the data of Figure 2.5 would appear to support this result in that most of the data are located in a narrow band about $u'/u_\tau \cong 2.8$. Furthermore, in regards to previous studies investigating wire length effects, the present results suggest that Reynolds number effects are smaller but not small compared to spatial averaging effects (as concluded by Johansson and Alfredsson (1983)), and that the general criterion set down by Ligrani and Bradshaw (1987) is somewhat generous since identifiable attenuation can clearly be seen in Figure 2.5 for $5 < y^+ < 20$. Concerning the spatial averaging effects due to finite wire length on velocity derivative fluctuations, the data of Figure 2.7 support the notion that a greater resolution is required than for the velocity fluctuations.

In principle, examining the influence of spatial averaging effects due to finite sensor size on v velocity fluctuations (as compared to u fluctuations) would provide more stringent criteria. In practice however, this is currently not possible because existing excessive data scatter results in a lack of reliable reference values necessary for meaningful comparisons. The primary cause of this scatter can no doubt be attributed to the increased difficulties associated with measuring the v fluctuations (relative to u). Evidence was presented suggesting that other factors such as the tunnel and measuring device characteristics may also be significant. Furthermore, it is not yet clear that the skewness of v (or other v statistics) are the same in boundary layers and channels, and thus this issue also need to be clarified.

Perhaps the main result concerning wire spacing effects on the computed value of spatial velocity gradients is that Wyngaard's (1969) criterion, equation 2.4, is to a very good approximation valid, even under anisotropic conditions. Furthermore, changing the level of mean shear seems to have little effect on the criterion's validity.

Conversely however, the $\partial u/\partial t$ results indicate that instantaneously spatially averaging velocity gradients (in order to, for instance, approximate pointwise measurements at a probe center) both causes dramatic attenuation in the resulting rms, and is highly sensitive to the level of mean shear. This result suggests that for probes with even small off-center measuring sites (say greater than 3η) one is probably better off accepting non-centered measurements rather than instantaneously spatial averaging. For example, for the given probe arrangement one would probably not improve the accuracy of the estimated value of $\partial v/\partial x$ by adding another x-array at $-\Delta z$ from the parallel-array center and then spatially averaging over the $2\Delta z$ separation between the two x-arrays. These results also suggest that there are differences between the temporal and spatial structure of the fine scale motions in the wall region. Further experiments into these differences (especially as a function of Reynolds number) may lead to new insights concerning the conflicting results (at very different Reynolds numbers) of Willmarth and Bogar (1977) and Johnson and Eckelmann (1983) as discussed in the Section 1.4.

The results in Figure 2.11 give a good indication of how electronic noise in the velocity signals enters into the $\partial u/\partial y$ signals. It was demonstrated that to a very good approximation $\Phi(\partial u/\partial y) \cong \epsilon_u{}^2/\Delta y^2$ in the noise dominated part of the spectrum. This relation allows one to optimize the choice of Δy for a given system noise level by simply performing a single wire measurement. The strategy here would be to make Δy as small as possible in order to resolve the motions within the flow, but not so small such that the noise level becomes intolerable. Also, it was demonstrated that the main effect of finite wire separation is to remove energy from frequencies higher than an approximate cut-off value of $f_c = U_1/(2\pi\Delta y)$.

The assumption that the instantaneous values of $\partial v/\partial x(z) = \partial v/\partial x(z + \Delta z)$ specific to the current ω_z probe proved to be on average only about 80% valid for $\Delta z/\eta \cong 7$ in the logarithmic region of the $R_\theta = 1{,}010$ boundary layer. Thus for the present study its validity is in question for a good part of the highest R_θ distribution. Given the very good spatial resolution of the parallel array for all of the Reynolds numbers considered, the recent elimination of this error by the new compact probe design of Mitchell (1987) is certainly warranted.

In regards to the present experimental procedure it should be stated that the existing guidelines as put forth mainly by Tennekes and Wyngaard (1972) and Antonia et al. (1982b) were adequate; excepting the convergence criteria in the case of Antonia et al. (see below). Furthermore, it was documented that the low speed nature of the present experiments caused little overall uncertainty in the results. Also the matching calibration procedure used for the parallel array elements proved to greatly eliminate any detectable correlated errors in $(\partial u/\partial y)'$. This is shown indirectly in that virtually all of the noise in $\Phi(\partial u/\partial y)$ in Figure 2.11 may be attributed to electronic noise. Perhaps however, the lowest quality experimental technique was the calibration procedure used for the x-array elements. Evaluation of the relative errors in using a variation of the present technique, as compared to more sophisticated methods (such as that used by Foss et al. (1986a) or Lueptow, Breuer, and Haritonidis (1988)) has, however, been performed by Browne et al. (1989).

They found that, in general, a technique similar to the one of this study performed quite satisfactorily. Also dynamic calibration techniques (cf. Perry and Abell (1975)) would provide greater accuracy, but they put multi-sensor probes at a greater risk to wire breakage. On the data reduction end, results are given in Appendix 2.1 that suggest the present least squares method of computing streamwise derivatives can be far superior to a conventional finite difference technique.

There were many interesting results pertaining to statistical convergence. Generally it can be concluded that, due to the factors involved such as the level of mean shear, the intermittency level, and Reynolds number effects, existing convergence formulas should be used with caution in wall flows. Also, one should not apply criteria developed in other flow fields to wall flow studies. For example, at the centerline of a turbulent jet flow with a centerline velocity U_c and an approximate transverse scale of L_o, Antonia et al. (1982b) show that it takes a time of approximately $12L_o/U_c$ to obtain ±5% accuracy in the skewness of $(\partial u/\partial t)$. This criteria, applied to boundary layer flows (using δ and U_∞) is orders of magnitude smaller than that cited in the present study or in that of Mestayer (1982).

Distinct boundary layer regional and Reynolds number trends in convergence were observed for the statistical moments of the u, v and uv fluctuations. These trends showed that increasing either R_θ or decreasing the distance from the wall generally increased the time to convergence. Both of these trends may possibly be lumped into one which simply states that for these variables increasing the absolute level of mean shear increases the time to convergence. Also comparisons between the velocities and Reynolds stress showed that the uv statistics converged at least as fast as either of the measured velocity components.

The convergence of the velocity gradient statistics showed much smaller regional or R_θ variations than the u, v, or uv statistics. Their convergence did however, appear to be adversely affected in the intermittent regions both very near and very far from the wall. In terms of absolute time to convergence, the gradient quantities appeared to converge slightly faster than the velocities or Reynolds stress. However, since δ/U_∞ is probably an integral time scale most appropriate for the velocities, the equivalent number of integral time scales appropriate to the gradient quantities necessary for convergence is probably greater than that found in terms of δ and U_∞. The results also suggest that spatial gradients converge much more slowly than temporal gradients. Again this may be connected to the differences between the fine scale spatial and temporal structure. As was expected, the $v\omega_z$ statistics took a very long time to converge.

Finally, the overall convergence criteria developed indicated the necessity for considerably longer averaging times than expected. It is felt that there are three plausible explanations for this. The first being that this subject has never been (to this author's knowledge) thoroughly investigated, and thus the expectations were based upon limited evidence. The second is that because of the very good resolution of the probe, more of the high intensity fine scale information in the tails of the respective probability distributions was represented than in earlier studies. And third is that statistical convergence may be profoundly adversely effected by even small levels of "noise" (as described in Section 2.4.6) due the inconstancy of the free stream velocity.

CHAPTER 3

REYNOLDS STRESS TRANSPORT AND ITS REYNOLDS NUMBER DEPENDENCE

3.1 INSTANTANEOUS MOTIONS, AVERAGE STRUCTURE AND TOWNSEND'S DECOMPOSITION

All statistical characteristics of a turbulent flow field are a consequence of the instantaneous dynamics associated with its complicated spatial-temporal evolution. This complicated spatial-temporal behavior makes it difficult to educe the true dynamics that produce the kinematical information acquired from a small number of stationary probes. Furthermore, interpretations based upon statistical information derived from a small number of stationary probes tend to endow the proposed turbulent motions with an unjustified permanence of form associated with their spatial extent. Therefore, in physically interpreting the long-time statistical information presented in this chapter, the bias toward this tendency was recognized and avoided.

Based on the information reviewed in Chapter 1, it is clear that the complicated interactions of the bursting events occur over a significant spatial extent and involve motions covering a range of scales. Given the discussion at the end of Section 1.2.2, the spatial phase relationships between the different scales of motion would seem to be an essential feature associated with transport across the boundary layer. This chapter examines data relevant to the transport of the Reynolds stresses normal to the wall.

As it pertains to boundary layers, the reality of the opening sentence to this chapter leads one to assess the implications of the active/inactive motions decomposition first put forth by Townsend (1961) from the point of view of the instantaneous physics. In this highly plausible as well as physically appealing decomposition Townsend hypothesized that at any given point the motion consists of "an active component responsible for turbulent transfer and determined by the stress distribution and an inactive component which does not transfer momentum or interact with the universal component". Given the present knowledge of the existence and importance of the various coherent motions that have been shown to reside in the wall region of turbulent boundary layers, concerning turbulent transport Townsend's decomposition appears highly justified. That is, there is a large body of evidence suggesting that these coherent motions are associated with the bulk of turbulent transport in the wall region. However, a model that demands that the local shear stress, τ, and the distance from the wall, y, solely determine the statistical properties of a universal active component may not incorporate enough of the essential physical mechanisms by which turbulent stresses are created and transported.

Townsend's original justification for the active/inactive motions decomposition was based upon the fact that the velocity intensities in the wall region can vary dramatically between different flows having the same stress -- even though the logarithmic mean velocity distribution for these flows is universal. Since Townsend's article, the universality of the constants κ and C in the log law profile,

$$U/u_\tau = (1/\kappa)\ln y^+ + C, \qquad (3.1)$$

has been investigated in numerous studies; Simpson (1970), Huffman and

Bradshaw (1972), White (1981), Purtell, Klebanoff and Buckley (1981), Murlis, Tsai and Bradshaw (1982), Andreopoulos, Durst, Zaric' and Jovanovic (1984), and Erm, Smits and Joubert (1985). The general findings of these investigations (excluding Simpson's) is that (except possibly at Reynolds numbers approaching reverse transition and over the range of Reynolds numbers examined) κ is constant, and that at low Reynolds number C shows a slight variation. Thus, under Townsend's original description the universal active motions are determined by τ and y and are also responsible for the universality of the mean velocity profile. Bradshaw (1967) further supports this hypothesis, and points out that "indeed, the only other course would be to believe that the scales of the mean motion were universal but that the scales of the shear-stress-producing turbulence were not -- a sentiment open to doubt". The data of this chapter suggest that the spanwise vorticity field in the near-wall region is universal, but not the average ability of the spanwise vorticity containing motions to create and/or transport the stress.

Regardless of the validity of Townsend's hypothesis however, it remains plausible that there exist other time averaged properties of the flow field that remain invariant under an inner variable normalization over approximately the same y^+ range as does the mean profile. These properties, along with the logarithmic mean velocity profile, could then be interpreted as the "defining" features of the turbulence in the inner region in that self-similarity is maintained with respect to what Barenblatt (1979) refers to as the local and global Reynolds numbers, yu_τ/ν and, say, $\theta u_\tau/\nu$. Given that perhaps the most definitive feature of a turbulent flow is the presence of a three dimensional fluctuating vorticity field and that the logarithmic law is essentially derived from a statement about the mean vorticity (i.e. $\partial U/\partial y$), one might expect that if the above proposed invariant non-dimensional functions exist they would be related to the vorticity field.

Following Hinze (1975, p.680), one may introduce an approximate decomposition that separates the mean Reynolds stress gradient of a two dimensional boundary layer flow into rotational and irrotational parts,

$$\partial\langle uv\rangle/\partial y = \langle w\omega_y\rangle - \langle v\omega_z\rangle + \partial\langle v^2 + w^2\rangle/\partial x - \partial\langle u^2\rangle/\partial x. \qquad (3.2)$$

Under this decomposition, Hinze identified the first two terms on the right as an active rotational part, and the last two terms as an inactive and virtually irrotational part. One of the major goals of this chapter is to examine the motions contributing to $\partial\langle uv\rangle/\partial y$, and the gradients of other components of the Reynolds stress tensor. Furthermore, contained within the present results there are certain functions which, when normalized by inner variables, apparently remain invariant over all or a portion of the boundary layer (over the given R_θ range). The physical relevance of the plausible invariance of these functions is discussed.

The experimental conditions and procedures for the data presented in this chapter were documented in Chapter 2. The following section gives a general documentation of the Reynolds number dependence/invariance of pertinent velocity, Reynolds stress, and spanwise vorticity statistics. In presenting the data, many comparisons and contrasts are made between the current results and previous investigations. A detailed look at the contributions to the Reynolds stress transport is given in Section 3.3. Finally, in Section 3.4 a discussion and general summary of the present results in the context of an interaction between the motions of the inner and outer regions is presented.

3.2 REYNOLDS NUMBER DEPENDENCE OF BOUNDARY LAYER STATISTICS

In this section the observed Reynolds number dependence of velocity, Reynolds stress, and spanwise vorticity statistics are examined and discussed. Since the main emphasis of this section will concentrate on inner region phenomena, almost exclusive attention will be paid to inner variable normalizations. (One is referred to Appendix 3.2 for outer variable normalizations.) In this section the u statistics presented are derived from the lower wire of the parallel array contained in the ω_z probe (to use the information closest to the wall). The v and uv data are derived from the ω_z probe's x-array. In the comparisons with previously reported results care was taken to select studies using probes of comparable spatial resolution, and in those cases where this is not possible the effects of finite spatial resolution are discussed.

3.2.1 Mean Flow Characteristics

Perhaps the most recognizable structural change that occurs in boundary layer flows at low Reynolds number is observed in the wake region of the mean profile. Coles (1956), (1962), (1968) was the first to thoroughly document and describe these changes. In a more recent study and following the hypothesis of Huffman and Bradshaw (1972), Murlis et al. (1982) give evidence suggesting that the disappearance of the strength of the wake component, $\Delta U/u_\tau$, is associated with the direct effects of viscosity outside the sublayer, and is due to a relative increase in the dynamical significance of the viscous superlayer for R_θ less than about 5,000. Antonia, Rajagopalan, Subramanian and Chambers (1982) give further details relating to this hypothesis, and also its relevance in terms of observed outer region coherent motions. Concerning the instantaneous features of the wake region, both of these studies tend to support the conclusion that the motions determining the shape of the turbulent/non-turbulent interface change from small to large scale as R_θ increases. In these studies it has also been shown that for $R_\theta > 3{,}000$ the average structure of the wake region changes very little. We will return to this point throughout this section and especially in the discussion of the spanwise vorticity intensity profile. Pertinent to Coles wake parameter, Π, the present values of ΔU^+ (1.7, 3.0, 3.2 at R_θ = 1,010, 2,870, 4,850 respectively) agree reasonably well with the values given by Coles and Hirst (1968), 1.9, 2.8 and 3.0 at $R_\theta \cong$ 1,000, 3,000 and 5,000 respectively.

3.2.2 Fluctuating Velocities and Reynolds Stress

3.2.2.1 Mean and RMS Quantities

The existence of a universal mean velocity profile has prompted some to hypothesize that a similar "law of the wall" type of analysis is also appropriate for scaling the velocity intensities. However, analytical approaches, such as that of Phillips 1987, while providing useful approximate formulas for the normalized intensities, have limited relevance to the questions concerning Reynolds number dependence since they are based upon an infinite Reynolds number assumption. As of yet the validity of this type of analysis is unclear since the high Reynolds number data necessary to verify the asymptotic profiles are unavailable.

Furthermore, attempts at experimental verification of a "law of the wall" type of hypothesis for the intensities are clouded by other factors. For example, Perry and Abell (1975) give evidence suggesting that axial velocity intensity profiles in turbulent pipe flow are universal for $y/R \le 0.1$ under an inner variable scaling. However, the higher resolution LDV data of Wei (1987) in a channel, and the boundary layer data of Ueda and Hinze (1975), Purtell et al. (1981), and Erm et al. (1985) all show a clear R_θ trend in u'/u_τ for $y^+ \ge 10$. This trend is also shown in the present profiles of Figure 3.1. Included in Figure 3.1 are the profiles of Purtell et al. (1981), Ligrani and Bradshaw (1987) and Alfredsson et al. (1988). As one can see, the present data agree very well with the results of the other studies.

Concerning the detection of the trend shown in Figure 3.1 for $y^+ \ge 10$, evidence was presented in Chapter 2 suggesting that spatial averaging effects due to finite probe scale can begin to obscure this R_θ dependence for probe scales $\ell^+ \ge 8$ (depending on the Reynolds number). Thus the data of Perry and Abell, which if anything show a slightly opposite R_θ trend, may be affected more by spatial averaging effects than they suspected[1] (see Table 3.1).

The data of all of the above cited references, do however, tend to suggest that for $y^+ \le 10$ the u'/u_τ profile is universal for all R_θ. Furthermore, data of the recent three-facility study of Alfredsson, Johansson, Haritonidis, and Eckelmann (1988) support this result as well as the hypothesis that in the region $y^+ \le 10$ boundary layer and channel flow data fall on the same curve. Wei (1987) makes the conjecture that the R_θ trend for $y^+ \ge 10$ in a channel flow is primarily due to changes in the structure of the inner region, and not due to the indirect effect of non-universal and large scale outer region motions influencing the wall

[1]This conclusion is tentative however, since it is based upon comparisons between channel, pipe, and boundary layer data. In general however, there is a fairly large body of experimental evidence suggesting that the inner regions of these flows are highly similar.

region structure.

The v velocity intensities, when normalized by wall variables, show an even more dramatic R_θ trend. This suggests that the mechanisms responsible for transport across the boundary layer are strongly Reynolds number dependent. The trend in the present data of Figure 3.2a is in very good agreement with the trend in the data of Wei (1987) shown in Figure 3.2b, and in it is in good agreement with the findings of Erm et al. (1985) (not shown). The data of Erm et al. however, exhibit a significantly smaller Reynolds number trend. Since their non-dimensional probe scale (see Table 3.1) was significantly greater than in either the present study or that of Wei, spatial resolution effects may be responsible for this smaller variation. Also, the different Reynolds number data of Erm et al. apparently fall on a single curve when normalized by u_τ and plotted versus y/δ (not shown). The present profiles do not exhibit this feature.

It is of interest to note that the observed rise in v′ in the region $4 \leq y^+ \leq 10$ shown in $R_\theta = 1{,}010$ distribution of the present data can also be seen in Figure 3.2a in the data of Andreopoulos et al. (1984) at $R_\theta = 3{,}624$. Furthermore, at $y^+ \cong 4.8$ Andreopoulos et al. give evidence that the probability density function of the v velocity fluctuations is bimodal. This feature however, has not been observed in any of the v fluctuation probability density functions of the present data. Note that this increase in v′ very near the wall has not been observed (to this author's knowledge) in any studies of channel flow. Note also that while the overall shape of the profile of Andreopoulos et al. is in very good agreement with the present profiles, its relation to the $R_\theta = 2{,}870$ and 4,850 profiles is inconsistent from a Reynolds number dependence point of view. This may be due to the significantly poorer spatial resolution of their sensor (see Table 3.1) than in either the R_θ = 2,870 or 4,850 distributions of the present study.

Note that in both Figures 3.2a and 3.2b the y^+ position at which the peak value is attained increases with increasing R_θ. This trend has been previously observed by Sreenivassan (1989). However, by comparing the data in parts a and b of this figure, one can also see that the channel flow v'/u_τ profiles tend to reach their peak at significantly smaller y^+ values, and in general have a distinctly different shape than the boundary layer profiles -- even in the inner region. In the outer region this can easily be attributed to the differences in the wake structure of channels and boundary layers, but in the inner region one cannot resolve this discrepancy by the same argument without assuming a strong interaction between the motions of the inner/outer regions. These differences could also be due to the presence of the opposing wall in the channel, as referred to as the "geometry effect" by Wei. Even in this case however, one would still have to assume a strong inner/outer coupling. Also, both the present data and the data of Wei suggest that the normal velocity intensity profiles (as non-dimensionalized in Figure 3.2) do not merge for $y^+ < 20$. Wei hypothesizes that this feature is due to a relative increase in the creation of streamwise vorticity as the Reynolds number increases.

A feature seen in both Figures 3.1 and 3.2a is that the R_θ variation is much greater between the R_θ = 1,010 and 2,870 distributions than between the R_θ = 2,870 and 4,850 distributions. This is reminiscent of what occurs in the wake region of the mean velocity profile, and leaves open the possibility that these two phenomena are both a symptom of the R_θ dependence of the same internal mechanisms. This correspondence is apparently incomplete however, since as pointed out by Purtell et al. (1981) the low Reynolds number effect "penetrates much deeper in terms of the turbulence intensity than it does for the mean velocity". If there is such a connection however, given Purtell's observation this would also suggest the existence of a strong interrelation between the physics in the inner and outer regions. Also, in general, the smaller magnitudes found in the lower Reynolds number profiles of Figures 3.1 and 3.2 are consistent with the notion that at low R_θ viscous effects serve to damp the turbulent motions.

The tendencies exhibited by the present Reynolds stress distributions in Figure 3.3 are similar to those of the streamwise intensities. For $y^+ \geq 15$ a clear R_θ dependence is observed, and once again this dependence appears to be much stronger between the two lower R_θ distributions. Very similar tends have been reported by Wei and to a lesser degree by Erm et al. The data of Figure 3.3 also suggest that for $y^+ \leq 15$ the two lower Reynolds number profiles merge. A universal profile in this region is also consistent with the findings of Wei.

Examination of the present $R_\theta = 2,870$ data in Figure 3.3 and that of Andreopoulos et al. (1984) ($R_\theta = 3,624$) indicates that for y^+ values greater than about 20 the two profiles exhibit very good agreement. Nearer the wall however, the present data tend to fall below theirs. Comparison of the $R_\theta = 1,010$ profile with the $R_\theta = 1,140$ profile of Barlow and Johnston (1985) (not shown) also shows this same feature. The reasons for these observed differences are currently unknown. As with the normal intensity profiles, the channel flow Reynolds stress profiles of Wei also tend to reach their peak values at lower y^+ values.

Even better measures of the internal structure of the turbulent field are the Reynolds stress correlation coefficient, $\langle uv \rangle/u'v'$, and the velocity variance ratio, $\langle u^2 \rangle/\langle v^2 \rangle$. As can be seen in Figure 3.4, the present $\langle uv \rangle/u'v'$ distributions for $y^+ \geq 15$ show a clear R_θ trend. These profiles decrease from a peak value of near 0.49 in the $R_\theta = 1,010$ profile to a peak value of about 0.41 in the $R_\theta = 4,850$ profile. If one assumes that for $R_\theta < 1,010$ the peak $\langle uv \rangle/u'v'$ value decreases with decreasing R_θ, then the present data are in qualitative agreement with both the studies of Murlis et al. (1982) and Wei (1987). These studies show that the peak value (as a function of Reynolds number) occurs at an R_θ value intermediate to the low Reynolds number limit necessary for fully turbulent flow, and a proposed asymptotic value as the Reynolds number approaches infinity. The data of Murlis et al. show that this peak occurs at about $R_\theta = 1,900$. However, their $\langle uv \rangle/u'v'$ profiles also show a much smaller variation with R_θ than the present. This may be a result of the significantly poorer spatial resolution of their x-array measurements (see Table 3.1).

As with the streamwise velocity intensity profiles, the present correlation coefficient distributions indicate that they probably merge for $y^+ \leq 15$. A universal $\langle uv \rangle/u'v'$ profile for y^+ less than about 15 suggests that the presence of the wall restricts the organization of the turbulent shear stress producing motions directly above the wall in such a way that the mean turbulent shear stress production is directly proportional to the total (uncorrelated) rms of the these motions (i.e. $u'v'$) at all R_θ. The lack of universality for $y^+ \geq 15$ however, indicates that the organization/interaction of the stress producing motions may be quite different at different R_θ. Conceptually then, one might envision at different R_θ different types of turbulent motions and interactions above the wall. As one nears y = 0 however, the presence of the wall limits the manner in which these motions can interact with either themselves or the instantaneous vorticity distributions in the sublayer.

Murlis et al. (1982) identify the velocity variance ratio, $\langle u^2\rangle/\langle v^2\rangle$, as an approximate measure of the efficiency of turbulent mixing, as well as a measure of the coherence of turbulent eddies. The present $\langle u^2\rangle/\langle v^2\rangle$ distributions, as derived from the ω_z probe's x-array, are given in Figure 3.5. Included in this figure are some of the data of Wei (1987) for $y^+ \leq 100$. Following the reasoning of Murlis et al. (1982), one can roughly associate a decrease in $\langle u^2\rangle/\langle v^2\rangle$ with an increase in the efficiency of turbulent mixing. Thus the present data and the data of Wei in Figure 3.5 imply that predominantly in the near-wall region (and in a very dramatic way) as the Reynolds number increases the turbulent mixing process becomes more efficient. These results are obviously a consequence of the trends in Figures 3.1 and 3.2 which show that (especially in the inner region) v′ exhibits a much greater R_θ dependence than does u′.

It is also interesting to note that the data of Wei suggest that the position of the peak in the $\langle u^2\rangle/\langle v^2\rangle$ profile shifts to larger y^+ values as the Reynolds number increases, while the present data suggest that the position is fixed at y^+ about equal to 12. This is a consequence of the observed significant differences between the channel and boundary layer v'/u_τ profiles shown above. It may be indicative of a subtle but true difference between the inner flow structure of channels and boundary layers.

3.2.2.2 Higher Order Statistics

Since higher order statistics are representative of the information in the tails of a probability distribution, in general they are a more sensitive measure of the turbulent structure. The present higher order velocity and Reynolds stress statistics tend to agree well with previously reported results, although there are some differences. These points of agreement and disagreement will now be discussed.

The u skewness profiles of Figure 3.6a exhibit reasonable to excellent agreement with the boundary layer studies of Gupta and Kaplan (1972), Ueda and Hinze (1975), Andreopoulos et al. (1984), Barlow and Johnston (1985), Ligrani and Bradshaw (1987) and Alfredsson et al. (1988), as well as the channel flow studies of Kreplin and Eckelmann (1979), Johansson and Alfredsson (1983), Kim, Moin and Moser (1987), Wei (1987) and Alfredsson et al. (1988). The present data show a small but consistent and discernable difference between the $R_\theta = 1{,}010$ and the $R_\theta = 2{,}870$ and $4{,}850$ flows. In addition to the present data, shown in Figure 3.6b are the channel flow results of Wei, Kim et al. (a computation), Kreplin and Eckelmann and Alfredsson et al., and the boundary layer data of Andreopoulos et al., Barlow and Johnston, Ligrani and Bradshaw and Alfredsson et al. As one can see, for $y^+ \geq 10$ the $R_\theta = 2{,}870$ and $4{,}850$ distributions of the present study and the data of Andreopoulos et al., Ligrani and Bradshaw, and Wei exhibit remarkable agreement. (Note that the boundary layer data of Alfredsson et al. are also in good agreement but are not well represented in this region of the flow.) It is important to note that all of the data (except that of Wei, $R_\theta \cong 1{,}500$) has $R_\theta \geq 2{,}600$.

On the other hand however, over the same region of the flow the data of Kreplin and Eckelmann, Kim et al. and the channel flow data of Alfredsson et al. of Figure 3.6b also show good agreement; however, they define a significantly different curve. Given that this second set of flows are all at about the same very low R_θ (see Table 3.1), and that the present $R_\theta = 1{,}010$ profile and the data of Barlow and Johnston ($R_\theta = 1{,}140$) are intermediate to the two different (but well defined) curves in Figure 3.6b, it is probably true that there is a Reynolds number dependence in the skewness of u for $y^+ > 10$ and $R_\theta \leq 3{,}000$.

Note that this trend in S(u) has been previously hypothesized by Andreopoulos et al. (1984) to be a Reynolds number dependence. However, since the study of Johansson and Alfredsson (1983) showed that this type of trend may also be produced by spatial averaging effects due to finite probe scale, the relatively low resolution higher R_θ results of Andreopoulos et al. remained inconclusive. Given that the resolution of the u component in the present study is very good (see Table 2.3) and that the $R_\theta = 2{,}870$ and 4,850 flows define a single curve, it is presently felt that the trend in the higher R_θ results of Andreopoulos et al. predominantly represents spatial resolution effects. Once again, note that the R_θ range over which the proposed trend is shown to be significant is about the same as that over which Reynolds number effects are significant in the wake region of the mean velocity profile.

Data comparisons become more difficult very near the wall. This is because wall heat transfer and/or blockage effects, as for example studied by Alfredsson et al. (1988), may cause significant errors. Thus before discussing the data of Figure 3.6b for $y^+ < 10$ some qualifications need to be made. First of all it is important to note that heat transfer and/or blockage effects should be negligible in the present results since the lower wire of the parallel array of the ω_z probe (i.e. the most susceptible wire) never got closer to the wall than 2.3 mm. Also, based upon a comparison between the "affected" and "unaffected" u'/U results in Alfredsson et al., the boundary layer results of that study are probably only valid down to $y^+ \cong 4$. Furthermore, given that the trend in the data of Andreopoulos et al. for $y^+ \leq 4$ has been shown by Alfredsson et al. to be symptomatic of wall effects, we shall also consider their data valid down to only $y^+ \cong 4$. Also, since it is well known that the mean data acquisition rate of an LDA system is dependent on the mean velocity (for a given particle density), the reliability of the measurements of Wei is in question for $y^+ < 6$ (Wei, private communication). Barlow and Johnston state that the accuracy of their u and v velocity data is in question for y^+ less than 4 and 7 respectively. Thus for $y^+ \leq 4$ the only data sets remaining for consideration on Figure 3.6b are at very low R_θ (one of which is from the computation which may have spanwise and/or streamwise grid resolution problems in the near-wall region, see S(uv) data below). This therefore eliminates any discussion of an R_θ dependence in this region of the flow. It does however, point out the need for more measurements in this region of the flow at higher R_θ. In the range $4 \leq y^+ \leq 10$, the present measurements, those of Andreopoulos et al. and a comparison of the high and low R_θ data of Alfredsson et al. suggest that the R_θ dependence detected for $y^+ > 10$ may continue down to at least the edge of the sublayer, $y^+ \cong 5$.

The present u kurtosis profiles of Figure 3.7a show very good agreement for all three Reynolds numbers. Also for $y^+ > 10$ the present results show good agreement with those of Andreopoulos et al. (1984), Barlow and Johnston (1985), Ligrani and Bradshaw (1987) and Wei (1987) (see Figure 3.7b). The general trends of the data presented in Figure 3.7b suggest that there may also be a very slight Reynolds number dependence in the K(u) profiles for $y^+ \geq 10$. In the lower Reynolds number profiles of Figure 3.7b the shallow minimum near $y^+ \cong 12$ tends to be a smaller value, while the shallow maximum near $y^+ \cong 40$ reaches a greater value. The observed trends in Figure 3.7b are in agreement with the Reynolds number variations found by Andreopoulos et al. Although, once again, it is presently felt that their probe scale may have significantly affected their higher Reynolds number results. Nearer the wall the K(u) data in Figure 3.7b are quite scattered, and thus at this time questions concerning a Reynolds number dependence in this region remain unresolved -- although the deviation of the boundary layer data of Alfredsson et al. and Andreopoulos et al. for $y^+ < 4$ can probably be explained in terms of "wall effects". Once again these results tend to support the notion that by $R_\theta \geq 3{,}000$ the effects of Reynolds number become small.

The scatter in the higher order v statistic profiles reported in the literature is much greater than that of the higher order u statistics. Much of this variation is undoubtedly associated with the increased difficulty in resolving the v component. Factors such as the calibration technique employed and the dynamic loading of heated wires as examined by Perry and Abell (1975), spatial resolution effects and probe orientation errors as examined by Vukoslavcevic and Wallace (1981) all increase the difficulty of resolving the v fluctuations. Furthermore, in Chapter 2 it was shown that, in general, the v statistics take significantly longer to converge than the u statistics[2].

The present v skewness profiles shown in Figure 3.8 (also in Figure 2.8a) exhibit a discernable positive peak near $y^+ = 10$, and then decrease toward zero as the sublayer is approached. These results are in reasonable agreement with the findings of Gupta and Kaplan (1972) and show very good agreement with the results of Andreopoulos et al. (1984). Other boundary layer studies however, such as Barlow and Johnston (1985), give negative values for S(v) near $y^+ \cong 10$ and a zero crossing to positive values in the sublayer and at $y^+ \cong 30$ (see Chapter 2). Similar discrepancies in the reported values of S(v) in the near-wall region can also be found in the channel flow literature.

These discrepancies leave open the possibility that slight variations in different flow facility and/or measuring instrument characteristics may cause large differences in the measured value of S(v) (again see Chapter 2). The channel flow data of Wei also suggest that the sign of S(v) in the range $5 \leq y^+ \leq 30$ is strongly Reynolds number dependent; ranging from a value of about -0.65 at $y^+ \cong 12$ at his lowest Reynolds number, to a value of about +0.65 at $y^+ \cong 20$ at his highest Reynolds number. Thus Reynolds number may also play a role in the variation of the reported value of S(v). The present data show only a slight (if any) R_θ dependence in S(v). At $y^+ \cong 12$ a comparison of the $R_\theta = 1{,}010$ and 2,870 profiles suggests that as R_θ increases the v component probability distribution becomes less positively skewed. However, examination of the $R_\theta = 4{,}850$ profile suggests that the peak value at $y^+ \cong 12$ probably increases for $R_\theta > 2{,}870$. Thus at this time it is unclear whether these relatively small differences are indicative of structural

[2]This may be in part due to the problems associated with resolving v. However, as long as these problems cannot be eliminated the longer convergence times will remain an experimental reality.

changes with Reynolds number, or reflect the difficulty in accurately measuring S(v).

The v kurtosis profiles of the present study are shown in Figure 3.9. These profiles exhibit the same clear-cut R_θ trend of most of the data presented thus far (i.e. the two higher R_θ flows show good agreement, and are noticeably different from the $R_\theta = 1,010$ distribution). The trend in the data is toward an increased peak in K(v) near $y^+ = 12$ at the higher Reynolds numbers. This suggests an increasing intermittency in the motions producing large v fluctuations with increasing Reynolds number. Increasingly intermittent behavior in these motions is in apparent agreement with the aforementioned hypothesis of Wei (1987) that proposes the legs of the hairpin vortex-like motions found near the wall become smaller and disproportionately more intense, in relation to inner variable scaling, as the Reynolds number increases. Given this Reynolds number dependence, one would expect it to be reflected much more dramatically in the v kurtosis than the u kurtosis since streamwise vorticity has a v-gradient contribution ($\omega_x \equiv \partial w/\partial y - \partial v/\partial z$). Comparison of Figures 3.7 and 3.9 shows that K(v) undergoes a much greater R_θ variation than K(u). It is interesting to note however, that the K(v) data of Wei at $y^+ \cong 12$ (not shown) exhibit just the opposite Reynolds number trend of the present data.

The second, third, and fourth central moments of the Reynolds stress signals are presented in Figures 3.10, 3.11, and 3.12 respectively.

The $(uv)'/u_\tau^2$ distributions show a Reynolds number trend that resembles the v'/u_τ distributions above. Like the v'/u_τ distributions the

$(uv)'/u_\tau^2$ distributions do not suggest that the three data sets merge anywhere in the inner region. It is interesting to note however, when $(uv)'$ is used to normalize $\langle uv \rangle$ the resulting profiles are almost identical to the $\langle uv \rangle/u'v'$ profiles shown in Figure 3.4. This indicates that the correlated, $(uv)'$, and the uncorrelated, $u'v'$, "intensities" associated with the Reynolds stress are nearly identical in magnitude over the entire boundary layer, and that they are (apparently) self-similar with $\langle uv \rangle$ for $y^+ \leq 15$. Finally, it is worth noting that the present $(uv)'/u_\tau^2$ distributions are in very good agreement (in both trend and magnitude) with those of Wei (not shown).

The uv skewness distributions exhibit good agreement for all three Reynolds numbers, and in particular across the inner region the two higher R_θ distributions very convincingly define a single curve. That these distributions show very little R_θ variation (even though the $\langle uv \rangle/u_\tau^2$ and $(uv)'/u_\tau^2$ do) suggests that the motions/interactions responsible for the instantaneous uv signal undergo distinct Reynolds number changes, but that average proportion of $\pm uv$ content remains nearly invariant.

The present S(uv) distributions are in excellent agreement with those of Wei. Both data sets show a zero crossing between $5 < y^+ < 10$. Both data sets show remarkable agreement across the inner region at higher Reynolds numbers (in both cases the data for $y^+ \geq 20$ define a single curve at a nearly constant value of about -1.6). Furthermore, in both data sets the lowest Reynolds number distributions exhibit a slightly more negative plateau at about -2.0 across the inner region. The agreement between the present data and those of Gupta and Kaplan (1972) is also very good.

However, none of the experimental data show good agreement with the computational profile of Kim et al. (1987) for $y^+ < 20$. Note also that this disagreement apparently cannot be attributed to Reynolds number since the lowest Reynolds number profile of Wei is at a lower $R_{d/2}$ than that of the computation. It is presently believed that this discrepancy may be related to the inability of this computation (due to the relatively large spanwise and streamwise grid spacings) to correctly create the true physics near the wall[3]. Under the assumption that the characteristics of the uv producing motions that interact with the sublayer are important element of near-wall physics, the results in Figure 3.12 suggest that this computation probably has limited application in uncovering the true details of the physical motions and mechanisms in the near-wall region.

The K(uv) profiles show more variation than do the S(uv) profiles. Generally however, the three distributions exhibit reasonable agreement in the range $20 \leq y^+ \leq 100$. For $y^+ < 20$ the $R_\theta = 1{,}010$ data show a decrease until about $y^+ = 7$, and then begin to increase rapidly as the sublayer is approached. This apparent deviation from the two higher R_θ distributions means that even though S(uv) is nearly invariant (over R_θ) for $y^+ \leq 20$, the shape of the uv probability distribution for the R_θ = 1,010 is different. The present data suggest that the motions associated with large uv fluctuations are less intermittent for $7 < y^+ < 20$ at low R_θ. Given the u and v data presented above, it is probably true that the observed variations in K(uv) for $y^+ \leq 20$ are predominantly due to the non-universality exhibited by the v component. As with the skewness, the

[3]This notion is further substantiated by the poor agreement between the u-v quadrant breakdown results of the computation and experiments for $y^+ < 20$, see Kim et al. (1987).

present K(uv) distributions (excepting the R_θ = 1,010 flow for $y^+ \le 20$) are in very good agreement with both the data of Wei (1987), and Gupta and Kaplan (1972).

3.2.3 Spanwise Vorticity Statistics

Numerous profiles of non-dimensional functions containing the spanwise vorticity intensity have been examined. Figures 3.13a, b, c, and d present outer, inner, and mixed variable non-dimensional functions containing ω_z'. In Figure 3.13b the computational channel flow results of Kim et al. (1987) and the experimentally derived boundary layer data of Balint et al. (1987a) are also plotted for comparison (same as in Figure 2.14). Under the outer variable normalization of Figure 3.13a the present data exhibit a small but discernable Reynolds number trend in the outer part of the boundary layer. This trend becomes increasingly distinct as the wall is approached. The observed trend is also opposite to that which would be indicative of probe resolution effects, and thus measurements with a probe of poorer resolution might give apparent evidence for universality under this scaling. Also it is worth noting that scaling with u_τ and θ (rather than U_∞ and θ) makes the trend more pronounced since u_τ/U_∞ decreases with increasing Reynolds number.

The data of Figure 3.13b (a normalization using ν and u_τ) suggest a universal scaling of the three data sets for $y^+ \le 80$. In this region, except for the leveling-off of the R_θ = 1,010 profile near y^+ = 12, the small differences between the present three profiles and that of Balint et al. (1987a) were shown in Chapter 2 to probably be a consequence of the small differences in the respective non-dimensional wire spacing relevant to the measurement of $\partial u/\partial y$. Concerning the deviation in the R_θ

= 1,010 profile near $y^+ = 12$, it is worth pointing out that this feature has also been observed in the previous measurements of Klewicki and Falco (1986). Also it is interesting to note that as the wall is approached the present profile shows a distinctively different shape than the computational results of Kim et al. (1987), even though the two data sets apparently have about the same limiting value as y^+ approaches zero. This difference may be indicative of numerous factors such as unaccounted for measurement errors, a true difference between channel and boundary layer flows, a Reynolds number dependence, or, as suggested by the S(uv) profiles above, the inability of this computation (due to its relatively large spanwise and streamwise grid spacings) to correctly create the true small scale vortical motions near the wall. The present data appear to level-off at a value of $\cong 0.37$ near the edge of the sublayer. This value is in good agreement with the recent findings of Alfredsson et al. (1988) of 0.38 ± 0.02 for the value at the wall. For y^+ values greater than about 80 the $R_\theta = 2,870$ and 4,850 data and the data of Balint et al. ($R_\theta \cong 2,100$) show very good agreement, while the $R_\theta = 1,010$ distribution shows considerably higher values. The occurrence of this deviation is consistent with the observed structural changes in the wake region of the mean velocity profile at low R_θ. This deviation also agrees with the hypothesis of Huffman and Bradshaw (1972) relating to the increased dynamical significance of the viscous superlayer at low R_θ as a result of the direct influence of viscous effects in the outer region. Note that the channel flow profile of Kim et al. do not and should not have this trend (under the Huffman and Bradshaw hypothesis) because of the confined nature of their flow. Note also that the $R_\theta = 1,010$ mean velocity profile (see Figure 2.2) begins to deviate from the logarithmic law at about $y^+ = 120$, which is in reasonable agreement with the value at which the data of

Figure 3.13b begin to deviate from the higher R_θ distributions.

In regard to the hypothesis of Townsend concerning the statistical universality of the active motions, the present ω_z' distributions have also been normalized by the variable quantity, y/u_τ. These distributions are shown in Figure 3.13c. As one can see, the trends between the different Reynolds number profiles are very similar to those in Figure 3.13b. Both non-dimensional representations suggest universality for $y^+ \leq 80$. In the outer region the two higher R_θ distributions show little difference, while the lower R_θ distribution gives significantly larger values. Note also that if $y/\langle uv\rangle^{1/2}$ is used rather than y/u_τ (in correspondence with Townsend's hypothesis), then examination of the stress distributions of Figure 3.3 indicates that the differences between the three profiles of Figure 3.13c would increase. However, given that there are only small differences between the higher Reynolds number distributions of both Figures 3.3 and 3.13c, leaves open the possibility that the appropriate scaling for both the mean and fluctuating spanwise vorticity fields in the constant stress region uses y and τ (or τ_w) as $R_\theta \rightarrow \infty$.

The present result indicating that the data of Figure 3.13b apparently merge for y^+ less than about 80 over the given Reynolds number range is in disagreement with the findings of Spalart (1988). In his computational study ($300 \leq R_\theta \leq 1{,}410$) Spalart found that in the near-wall region the vorticity intensity profiles (when scaled by ν and u_τ) exhibit a significant increase with increasing R_θ. This is demonstrated by his $\nu\omega_z'/u_\tau^2|_w$ values which are indicated by the arrows in Figure 3.13b. Furthermore, Spalart states that the mixed normalization, $(u_\tau^3/\delta\nu)^{1/2}$, for the vorticity intensities when plotted versus y/δ, provides for a good scaling of different R_θ data. Figure 3.13d shows the present data under this normalization. Note that over virtually all of the boundary layer the three distributions exhibit very good agreement. However, the insert to this figure shows that for $y/\delta < 0.02$ this scaling apparently fails. Examination of the $R_\theta = 1{,}010$ distribution in Figure 3.13b indicates that the points nearest the wall in Figure 3.13d reach their peak (a value of about 7) at $y/\delta \cong 0.013$. On the other hand, at the same y/δ position the $R_\theta = 2{,}870$ and 4,850 distributions are both already greater than 7. Furthermore, examination of the $R_\theta = 2{,}870$ and 4,850 data of Figure 3.13b strongly suggests that points nearer to the wall in these distributions are going to continue to increase. This observation is directly substantiated by the results of Alfredsson et al. (1988) that indicate that the limiting value of $\omega_z{}'$ is 0.38 ± 0.02 over the approximate Reynolds number range $300 < R_\theta < 2{,}800$. This indicates that the normalization of Figure 3.13d does not produce a universal profile of different Reynolds number data for $y/\delta < 0.013$. To explicitly illustrate this point, if one assumes that the $R_\theta = 4{,}850$ $\omega_z{}'^{+}$ profile has a value of 0.37 at $y^+ = 4.5$, then under the scaling of Figure 3.13d this distribution would have a value of approximately 16 -- which is more than twice the peak value of about 7 in the $R_\theta = 1{,}010$ flow. Thus, while the apparently universal scaling of Figure 3.13b remains to be explicitly verified at higher R_θ for $y^+ \leq 10$, the above results strongly suggest that the mixed normalization of Figure 3.13d does not produce a universal scaling of the data near the wall.

The present ω_z-skewness and kurtosis profiles are shown in Figures 3.14 and 3.15 respectively. Included in these figures for comparison are the nine wire probe data of Balint et al. (1987a). As one can see the agreement between the two studies is very good.

The dominant feature of the three $S(\omega_z)$ distributions is the large negative peak reached near $y^+ = 40$. This feature is consistent with a process of high intensity negative spanwise vorticity containing motions (of the same sign as that of the mean vorticity) lifting from the sublayer. These motions may plausibly be associated with either the head portion of hairpin vortices as recently studied in detail by Lu and Smith (1988), and/or the lifted vortex sheet-like shear layers observed in the physical simulations of Chu (1988) and in the computational data base interrogation of Jimenez, Moin, Moser and Keefe (1988). Given these types of processes, the present skewness data suggest that the proposed lifted sublayer motions on average reach a maximum relative intensity near $y^+ = 40$, and then decrease in relative strength at greater distances from the wall[4]. This type of physical picture is given further support by both the template-matching results of Lu and Smith (1988) which indicate that the most probable region of observing a hairpin head is in the range $28 < y^+ < 32$, and the computational results of Jimenez et al. (1988) which show that the tip of the lifted vortex sheets tend to level-off at about $y^+ \cong 35$. This observed feature in the skewness profile could also be in part resultant from spanwise vorticity interactions involving the intermediate scale vortex ring-like motions studied by Falco, see Chapter 1. Under this type of interaction (and given the scale of these motions), as the positive vorticity in lower lobe of the ring-like motion interacts with the sublayer, the center of the upper lobe (which has the same sense of rotation as the mean vorticity) would be located at about $y^+ = 40$.

[4]Of course the number of proposed motions lifting from the sublayer that actually reach a given y^+ value and the presence of other ω_z-containing motions, would also influence the value of $S(\omega_z)$.

The $S(\omega_z)$ data of Figure 3.14 exhibit good agreement for $y^+ < 50$, but farther away from the wall the three distributions are different and do not exhibit a clear-cut Reynolds number trend. The tendency for the two higher R_θ distributions to agree, and be different from the R_θ = 1,010 profile, is however, still observable. That these profiles exhibit apparent near-wall universality is consistent with the notion that near the wall the single dominant resident features are the lifted sublayer motions discussed above. Given that the statistical properties of uv, discussed in Section 3.2.2.2, tended to exhibit universality under wall variable scaling for $y^+ < 15$, it is probably true that the active motions for $y^+ < 15$ are predominantly represented by these lifted sublayer vorticity distributions and their associated initiating mechanisms. However, since in the range $15 < y^+ < 50$ the Reynolds stress statistics are clearly not universal under an inner variable normalization while the spanwise vorticity statistics apparently are (up to $K(\omega_z)$), one cannot associate the universality of the spanwise vorticity field in this region with a universal Reynolds stress-producing active motion. Physically however, one can reconcile this discrepancy under a process in which the lifted sublayer motions are initiated by mechanisms which are on average universal in their ω_z content, but are not universal in their ability to produce Reynolds stress[5] (due to, say, relative changes in scale or in the manner in which these motions interact within the flow).

Features similar to $S(\omega_z)$ are also observed in the $K(\omega_z)$

---

[5]Also note that implicit in this argument is that the initiation of the lifted sublayer motions is predominantly resultant from external excitation, rather than from instability mechanisms that are local to the sublayer. This sentiment can be given support by a significant body of experimental evidence; see, for example, Bradshaw (1967), Willmarth (1975), Falco (1983) and Wark (1988).

distributions of Figure 3.15. However, the higher Reynolds number data of this plot for $y^+ > 50$ show reasonable agreement. That the $K(\omega_z)$ profiles increase with increasing y^+ in the near-wall region is consistent with the lifting sublayer motion model discussed above. For example, as an average vortical motion (say of scale about equal to the sublayer thickness and of strength characteristic of u_τ^2/ν) moves outward from the sublayer, its relative scale will decrease and its relative circulation will increase with respect to the average surrounding motions. Thus if one interprets an increasing kurtosis as an indication of increasingly intermittent behavior, this process predicts that the $K(\omega_z)$ profile should initially increase for increasing y values outside of the sublayer. At some distance far enough from the wall, the probability of observing only hairpin-type or lifted shear layer-type motions decreases. At this point $K(\omega_z)$ may cease to increase, and $S(\omega_z)$ will probably cease to decrease.

Under the above type of physical model the $S(\omega_z)$ data suggest that the relative intensity of the lifted motions decreases from their maximum for $y^+ \geq 40$. Combining this with the observation that the $K(\omega_z)$ profiles continue to increase for y^+ values significantly greater than 40 (at least at the higher Reynolds numbers) suggests that intermittent high intensity positive ω_z containing motions (of sign opposite that of the mean) are also present in the near-wall region. Finally, the apparent near-wall self-similarity of the $S(\omega_z)$ and $K(\omega_z)$ profiles (when plotted versus y^+) adds further support to the notion suggested by the "law of the wall" and the present $\omega_z'\nu/u_\tau^2$ profiles that the structure of ω_z for $y^+ \leq 50$ is universal under inner variable scaling.

3.2.4 Summary of u, v, uv and ω_z Results

Before proceeding on to the data presentation concerning the transport of the Reynolds stresses, it is useful to summarize the results of this section.

Concerning the velocity intensities for $y^+ \geq 10$, an apparent Reynolds number variation is observed which is consistent with other high resolution studies. In general, the observed trends are consistent with an increased damping of the turbulent fluctuations as suggested by a relative increase in the importance of viscous forces resultant from a decrease in Reynolds number. Nearer the wall the u intensities appear to merge, while the R_θ variation of the v intensity is much more pronounced and is maintained over the entire layer. These observed Reynolds number trends have been hypothesized by Wei (1987) to a result of a near-wall increase in $D\omega_x/Dt$, and are consistent with the results of Willmarth and Bogar (1977) and Willmarth and Sharma (1984) which indicate that significant changes in the small scale structure occur with increasing R_θ. Physically, the greater R_θ variation in the v intensities suggests that changing the Reynolds number (within the given range) significantly changes those features of the flow associated with momentum transport across the layer. Most of the Reynolds number dependencies observed occur predominantly for R_θ less than about 3,000. This is the same approximate Reynolds number range (given by Antonia et al. (1982a)) over which significant changes in the wake region of the mean velocity profile are most readily observable.

The higher order velocity statistics are shown to be in good agreement with previously reported results. The $R_\theta = 1{,}010$ S(u) and K(u) profiles differ subtly from the present two higher Reynolds number distributions; which in both cases exhibit excellent agreement over the entire inner region. The present S(v) distributions exhibit only a small near-wall variation with Reynolds number, while the K(v) profiles demonstrate a clear rise with increasing R_θ near the wall. This trend is apparently consistent with the previously mentioned hypothesis of Wei (1987).

The present $\langle uv \rangle / u_\tau^2$ profiles exhibit an R_θ variation very similar to that of the streamwise intensities (i.e for $y^+ \geq 15$ they diverge, and for $y^+ \leq 15$ they apparently merge). As with the velocity intensities, the observed variations in the $\langle uv \rangle / u'v'$ profiles were more dramatic at lower R_θ. These profiles also appear to merge for $y^+ \leq 15$. The velocity variance ratio distributions exhibit a definite decrease with increasing Reynolds number for $y^+ < 100$; implying an increased efficiency in turbulent mixing in this region as R_θ increases.

The $(uv)'/u_\tau^2$ profiles show a high degree of similarity with the v intensity profiles in that they apparently do not merge over any portion of the boundary layer. The S(uv) distributions show only a very slight Reynolds number dependence, and are in excellent agreement with the data of Wei (1987). This lack of significant Reynolds number dependence is interpreted to indicate that the average relative $\pm uv$ content of the Reynolds stress producing motions is also nearly R_θ invariant, and that the changes in $\langle uv \rangle / u_\tau^2$ and $(uv)'/u_\tau^2$ are resultant from a Reynolds number dependence in the manner in which the stress producing motions interact within the flow. In general, changes in these interactions may be tied to the above suggested increased significance of viscous forces at lower R_θ, or as inferred in the Section 3.3 changes in scale and/or convection velocity of the motions responsible for the stress transport. The K(uv) profiles exhibit good agreement for $y^+ \geq 20$, but for $y^+ < 20$ the $R_\theta = 1,010$ distribution shows a distinct decrease until about $y^+ = 7$, and then for smaller y^+ increases rapidly.

The spanwise vorticity intensities apparently define a universal profile in the inner region when normalized with ν and u_τ and plotted versus y^+. However, in the outer portion of the boundary layer the lowest Reynolds number distribution (under inner variable scaling) exhibits distinctly higher values, while the higher Reynolds number distributions continue to show excellent agreement and are in very good agreement with the results of Balint et al. (1987a). The low Reynolds number deviation is apparently consistent with the structural changes seen to occur in the wake region of the mean profile. The mixed normalization proposed by Spalart (1988) produced a very good scaling of the present ω_z' data for $y/\delta > 0.013$. However, nearer the wall available data strongly suggest that this normalization fails to produce a single profile from different Reynolds number data.

Both the $S(\omega_z)$ and the $K(\omega_z)$ profiles are shown to be consistent with the physical process of high intensity negative spanwise vorticity containing motions (i.e having the same sign as the mean vorticity) lifting from the sublayer. The given shapes of these distributions not only suggest that, on average, the lifted sublayer motions reach a maximum relative intensity at about $y^+ = 40$, but also provide indirect evidence supporting the existence of high intensity positive spanwise vorticity containing motions (having sign opposite that of the mean vorticity) in the wall region.

3.2.5 Conclusions Pertaining to u, v, uv and ω_z Results

Having reiterated some of the main features of the preceding data presentation, a brief listing of what are believed to be the main conclusions relevant to the discussion in the following sections.

- In many ways the present measurements support the notion that the changes observed in the wake region of the mean velocity profile for R_θ less than about 3,000 are symptomatic of structural changes that also affect many of the u, v and uv statistics throughout most of the boundary layer for $R_\theta < 3{,}000$.

- The present v'/u_τ measurements indicate that those features of the flow associated with transport across the layer are highly sensitive to Reynolds number (over the given R_θ range).

- The Reynolds number trends in the present u'/u_τ, v'/u_τ, $\langle uv\rangle/u_\tau^2$ and $(uv)'/u_\tau^2$ distributions are consistent with the notion that viscous forces are more prevalent at lower R_θ.

- The present measurements give strong support to the hypothesis that for $y^+ < 50$ and under inner variable scaling the statistical characteristics of the spanwise vorticity field are universal. However, as it pertains to an active Reynolds stress producing component of the flow, it was shown that this universality does not imply the same for $\langle uv\rangle/u_\tau^2$ for $y^+ > 15$.

- The present spanwise vorticity statistics support a physical model in which negative ω_z containing motions are lifted from the sublayer up to the most probable y^+ location of about 40. Also, examination of these statistics further from the wall gives indirect evidence for the existence of intermittent positive ω_z containing motions in the wall region.

• Finally (as an aside) comparisons (mainly with the data of Wei) support the conclusion that there exist subtle but possibly significant differences between the inner region physics in channel and boundary layer flows.

3.3 THE ACTIVE AND INACTIVE MOTIONS

For the purposes of boundary layer control one would like to determine ways in to reduce or alter the Reynolds stress distribution. One way of accomplishing this would be to alter the mechanisms responsible for the transport of the stress. In this section, in an effort to uncover the nature of the motions directly involved in the transport $\langle uv \rangle$, most of the terms of equation 3.2 are examined. Furthermore, velocity vorticity correlations related to the y gradients of $\langle u^2 \rangle$, $\langle v^2 \rangle$, and $\langle w^2 \rangle$ are also examined. These results are then related to the findings of the preceding section.

While the equation for the mean transport of $\langle uv \rangle$ as given by equation 3.2 is exact, the association of $\langle w\omega_y \rangle - \langle v\omega_z \rangle$ with an active rotational part and $\partial\langle v^2 + w^2 \rangle/\partial x - \partial\langle u^2 \rangle/\partial x$ with an inactive purely irrotational part is, as pointed out by Hinze (1975), an approximation. It is clearly true by its composition that $\langle w\omega_y \rangle - \langle v\omega_z \rangle$ is always associated with rotation. However, since $\partial\langle v^2 + w^2 \rangle/\partial x - \partial\langle u^2 \rangle/\partial x$ is not identically zero in a boundary layer (as it is in a channel) it could make significant contributions to $\partial\langle uv \rangle/\partial y$. In what follows an assessment is made regarding the validity of this approximate decomposition. In doing so, the contributions of the motions participating in the mean transport of the Reynolds stresses will be examined.

3.3.1 The Inactive Motions

Using the ω_z probe x-array data, $\partial\langle u^2\rangle/\partial x$ and $\partial\langle v^2\rangle/\partial x$ profiles were computed. An inner variable normalization of these profiles is given in Figures 3.16 and 3.17. As one can see, these profiles are essentially zero across most of the boundary layer. Furthermore, comparison of these profiles with the data in Figure 3.20 and Figure A3.1.3 indicates that the $\partial\langle u^2\rangle/\partial x$ and $\partial\langle v^2\rangle/\partial x$ (and presumably $\partial\langle w^2\rangle/\partial x$) contributions to $\partial\langle uv\rangle/\partial y$ are between one and three orders of magnitude smaller than the $\langle v\omega_z\rangle$ and $\langle w\omega_y\rangle$ contributions. Thus the active/inactive motions decomposition proposed by Hinze (1975) in the form of equation 3.2 appears to be consistent in this respect with Townsend's original model. It is also worth noting that these results are in good agreement with the results of Bradshaw (1967) in that they show that the mean effect of the "irrotational component" (i.e the inactive motions) is small. Furthermore, these results show that to a very good approximation the present boundary layers may be considered homogeneous in the streamwise direction, and that virtually all of the mean transport of the Reynolds stress is due to the "rotational" terms of equation 3.2.

The rms profiles of $\partial(u^2)/\partial x$ and $\partial(v^2)/\partial x$ have also been obtained. These are shown under an inner variable normalization in Figures 3.18 and 3.19. A comparison of the data of these figures with the data of Figure 3.22 shows that unlike the mean values, the variance of these quantities is at least of the same order of magnitude as that of the rotational contributions to $\partial\langle uv\rangle/\partial y$. This is consistent with the comment of

Bradshaw (1967) that, "it is only in the mean that we can call the large-scale motion 'inactive' in the simplest sense of Townsend's hypothesis".

The $\partial\langle u^2\rangle/\partial x$ and $\partial\langle v^2\rangle/\partial x$ profiles of Figures 3.16 and 3.17 tend to suggest reasonable agreement under an inner variable scaling. However, given the very small magnitude of these profiles as well as the data scatter (especially at $R_\theta = 1{,}010$), this issue remains unresolved. The rms profiles shown in Figures 3.18 and 3.19 exhibit the same feature of most of the data presented thus far. The two higher Reynolds number distributions show only small differences, but are significantly different from the $R_\theta = 1{,}010$ profiles. The rms $\partial(v^2)/\partial x$ profiles clearly do not follow inner variable scaling. However, it is interesting to note that the y^+ position of the peak in each distribution is apparently Reynolds number invariant.

Under Bradshaw's (1967) interpretation the inactive component is made up of truly irrotational contributions associated with outer region pressure fluctuations, as well as large scale vortical motions presumed to be present in the outer region. To this point in the discussion and data presentation it has been shown that the streamwise gradient terms of equation 3.2 have a negligible mean contribution to $\partial\langle uv\rangle/\partial y$, and thus in this respect fit the definition of the inactive component. However, it has been implicitly assumed that these terms are predominantly associated with the large scale motions in the boundary layer, and that the large scale motions are essentially irrotational. In Chapter 4 evidence is given supporting the hypothesis that, on average, large scale spanwise vorticity containing motions are not present in the inner region.

3.3.2 The Active Motions

The relationship between the y gradient of $\langle uv \rangle$ and the velocity vorticity correlations given in equation 3.2 may be extracted either from a more general tensor identity, or may be derived directly from the equations of motions as shown in Appendix 3.1. The results of the previous section indicate that to a very good approximation (for the present flow field) equation 3.2 may be written as

$$\partial\langle uv\rangle/\partial y = \langle w\omega_y\rangle - \langle v\omega_z\rangle.$$

This section will examine the terms on the right hand side of the above expression. Interpretations of the data in this section will pertain to issues concerning the scaling of the active motions proposed by Townsend (1961), and in a context relevant to an interaction between the motions of the inner and outer regions.

3.3.2.1 $\langle v\omega_z\rangle$ Data

Figure 3.20 shows the present $\langle v\omega_z\rangle$ profiles normalized by ν and u_τ. As can be seen the R_θ =1,010 profile reaches a distinct positive peak near the edge of the sublayer. Closer to the wall the distribution drops off sharply, as it must, since $\langle v\omega_z\rangle|_w = -1/2\partial\langle uv\rangle/\partial y|_w = 0$. Further from the wall the R_θ =1,010 distribution melds smoothly with the R_θ = 2,870 distribution, and both cross zero at $y^+ \cong 13$. Between y^+ = 15 and 20 the data of Figure 3.20 suggest the three profiles merge under the inner variable scaling; although the R_θ = 4,850 flow is not well represented in this region. For y^+ values greater than 20 however, an apparent Reynolds number dependence is observed. This dependence indicates that at low Reynolds numbers the spanwise vorticity fluctuations and the normal velocity fluctuations are much more negatively correlated in the logarithmic region than at higher R_θ. Note that the apparent universality in $\langle v\omega_z\rangle^+$ for y^+ less than about 20 is consistent with the same feature in the $\langle uv\rangle^+$ profiles shown in Figure 3.3. This correspondence further supports the notion that in terms of their ability to create and transport $\langle uv\rangle$ the active turbulent motions are self-similar under inner variable scaling for y^+ less than about 20. In connection with the lifted sublayer motions known to be prevalent in this region, this result probably indicates that certain average features of these motions (such as, say, the average amount of sublayer fluid lifted per unit area and time) scales with the wall shear.

As discussed in Section 3.1, Townsend's notion of the active component in the flow included that its statistical properties in the inner region are universal functions of distance from the wall, y, and the local shear stress, τ. Given that the velocity vorticity correlations shown in equation 3.2 have the units of $[L/T^2]$, one can satisfy Townsend's proposed scaling by normalizing these variables by ν and τ (or possibly u_τ) and plotting versus y^+, or by creating a new non-dimensional function by using y and τ (or possibly u_τ) and plotting versus y^+. As can be seen in Figure 3.20, the familiar inner normalization fails except for $y^+ < 20$. Furthermore, examination of Figure 3.3 indicates that an inner-type non-dimensional function formed by using a velocity scale derived from the local turbulent shear stress, $\langle uv\rangle^{1/2}$, causes the differences in the distributions of Figure 3.20 (for $y^+ > 20$) to become greater. Thus, while both the $\langle uv\rangle^+$ and $\langle v\omega_z\rangle^+$ distributions show a Reynolds number dependence, these dependencies are not self-similar.

Profiles of the non-dimensional function, $y\omega_z'/u_\tau$, are shown in Figure 3.21. As with the profiles of Figure 3.20, these profiles also fail to merge except for y^+ less than about 20. Also the use of y and $\langle uv\rangle^{1/2}$, once again, only makes matters worse. With respect to the $\langle w\omega_y\rangle$, examination of the data deduced in Appendix 3.1 indicates that the profiles of $\langle w\omega_y\rangle$ will exhibit essentially the same behavior as in Figures 3.20 and 3.21. These results indicate that over the given R_θ range the individual contributions to $\langle uv\rangle$ transport normal to the wall are not universal functions of y and τ across the inner region.

3.3.2.2 $(v\omega_z)'$ Data

Further insight into the validity of Townsend's proposed scaling for the active motions (assuming they are represented by $v\omega_z$) can be gained by examining the rms $v\omega_z$ profiles. Figure 3.22 shows an inner variable normalization of $(v\omega_z)'$. As can be seen, near the wall all of the profiles appear to be distinctly different. However, at the two higher Reynolds numbers and for $y^+ \geq 30$ very good agreement is observed. Note that the region over which this agreement is observed corresponds very well with the logarithmic region of the respective mean velocity profiles. Furthermore, normalizing the function $(v\omega_z)'$ with the function $\nu/\langle uv\rangle^{3/2}$, see Figure 3.23, convincingly removes the near-wall deviations between the higher Reynolds number profiles, and brings the $R_\theta = 1{,}010$ data into much better agreement. Equally interesting is the normalization employing the function y/u_τ shown in Figure 3.24. Under this scaling good agreement between of all three profiles is observed, and exceptionally good agreement is seen at the higher Reynolds numbers. Note that the extent of the agreement between the different R_θ profiles corresponds very well with the extent of the logarithmic mean velocity profile at each R_θ.

The above results concerning the rms of $v\omega_z$ correspond very well with Townsend's proposed scaling for the active motions. However, the $\langle v\omega_z \rangle$ results show that the net mean contribution of the $v\omega_z$ motions to the transport of $\langle uv \rangle$ is not universal under any inner-type scaling. This is interpreted to indicate that the organizational features of the flow, as they pertain to the transport of $\langle uv \rangle$, are Reynolds number dependent over the given R_θ range. Information is presented below that indicates the flow field changes affecting $\langle v\omega_z \rangle$ may be associated with an R_θ dependence in the average scale and/or convection velocity of the $v\omega_z$ containing motions.

3.2.2.3 $v\omega_z$ Spectra

In an effort to further understand the observed R_θ dependence in $\langle v\omega_z \rangle$, frequency spectra were examined. Following Perry and Abell (1975), inner and outer variable non-dimensionalizations of the power spectrum[6], Φ, are defined as follows.

Inner normalization:

$$\int_0^\infty \Phi^i[v\omega_z(t)]d\alpha^i \equiv \left[\frac{\nu(v\omega_z)'}{u_\tau^3}\right]^2 \tag{3.3}$$

where $\alpha^i = 2\nu\pi f/u_\tau^2$ is the non-dimensional angular frequency.

Outer normalization:

$$\int_0^\infty \Phi^o[v\omega_z(t)]d\alpha^o \equiv \left[\frac{\theta(v\omega_z)'}{U_\infty^2}\right]^2 \tag{3.4}$$

[6]The power spectrum, Φ, of a function x(t) is defined as,

$$\Phi(\alpha) = \{\mathrm{Re}[X(\alpha)]\}^2 + \{\mathrm{Im}[X(\alpha)]\}^2,$$

where α is the angular frequency ($\equiv 2\pi f$), and $X(\alpha)$ is the Fourier transform of x(t).

where $\alpha^o = 2\theta\pi f/U_\infty^2$. The data to be shown are in the form of a spectral function, Ψ, defined for the given non-dimensionalizations as

$$\Psi^i = \alpha^i \cdot \Phi^i, \qquad (3.5)$$

and

$$\Psi^o = \alpha^o \cdot \Phi^o. \qquad (3.6)$$

The spectral functions shown in Figures 3.25 and 3.26 were derived by averaging ensembles of 250 1,024 point digital Fast Fourier Transforms of $v\omega_z$ for each y^+ location and R_θ. In the computation of the individual Fourier transforms a 1/10 cosine taper function was used to suppress "side lobe leakage".

Examination of Figures 3.25a and 3.25b indicates that near $y^+ = 20$ neither inner or outer normalizations scales the data; although the high frequency end of the $R_\theta = 2,870$ and 4,850 spectral functions apparently merge under the inner scaling in Figure 3.25a. The outer normalization of Figure 3.25b shows no hint of scaling the data over any frequency range. This conclusion is also reached for the outer normalization at $y^+ \cong 120$ in Figure 3.26b. Concerning the inner normalization of Figure 2.26a it is interesting to note that at low frequencies the spectral functions appear to merge for all R_θ, while at higher frequencies there is an apparent trend. This is just the opposite of what is observed nearer the wall.

An interesting result concerning the scale of the $v\omega_z$ motions can be deduced from Figures 3.25 and 3.26. As indicated by the arrows, the peak in the inner variable scaled spectral functions of Figure 3.25a (and to a lesser degree in Figure 3.26a) show a significant shift toward lower frequencies with increasing Reynolds number. Conversely, the outer normalizations of Figures 3.25b and 3.26b show very clearly that the peak in the spectral function moves to higher non-dimensional frequencies with increasing Reynolds number.

In general, the cause of a shift in a spectral function may be due to either a change in the scale of the associated motions and/or a change in the convection velocity of the motions. Given that the $\Delta\alpha$ shift in log frequency ranges from about 0.15 to 0.3 under the inner normalization, and from about 0.25 to 0.4 under the outer normalization, it is unlikely that convection velocity (which is relatively insensitive to R_θ) is the sole cause for the observed variations. Therefore, if one associates large scale motions with low frequencies and small scale motions with high frequencies, the results in Figures 3.25 and 3.26 indicate that under an inner normalization the $v\omega_z$ containing motions increase in scale with increasing Reynolds number, while under an outer normalization these motions decrease in scale with increasing Reynolds number. These changes in scale are probably associated with the Reynolds number dependence in $\langle v\omega_z \rangle$ discussed above.

In connection with instantaneously observed motions, it is interesting to note that the above deduced changes in scale correspond well with the scale dependence of the vortex ring-like motions observed by Falco (unpublished). Figure 3.27 shows the observed R_θ dependence for these motions. As can be seen, the scale of these motions increases under an inner normalization and decreases under an outer normalization with increasing R_θ.

3.2.2.4 The Dependence of $\langle v\omega_z \rangle$ on Probe Scale

Having identified an apparently significant Reynolds number dependence in the motions contributing to $\langle v\omega_z \rangle$, it is now important to assess the significance of the observed trends in the data relative to measurement inaccuracies.

The largest error source associated with the measurement of $v\omega_z$ is readily identified as the Δz spacing between the centers of the parallel and x-array elements contained within the ω_z probe. In assessing the errors resultant from the x-array and parallel-array separation it is useful to expand $\langle v\omega_z \rangle$.

$$\langle v\omega_z \rangle = \langle v\partial v/\partial x \rangle + \langle v\partial u/\partial y \rangle$$

Notice that the first term in the expansion is equal to $1/2\partial\langle v^2 \rangle/\partial x$, which is derived solely from the x-array and was shown in Figure 3.17 to be negligible for all R_θ. Therefore, the major effect of the Δz separation is associated with the resolution of $\langle v\partial u/\partial y \rangle$.

To get an estimate of the error in this correlation, the data of Figure 2.13 will be used. A general result that might be concluded from Figure 2.13 is that velocity gradient correlations decrease more rapidly than velocity correlations. From this, a logical extension is to assume that velocity-velocity gradient correlations decrease at a rate somewhere between velocity and velocity gradient correlations. Based on this hypothesis, one would expect $\langle v\partial u/\partial y \rangle / v'(\partial u/\partial y)'$ data to fall somewhere between the u and $\partial v/\partial x$ data of Figure 2.13 for a given Δz separation. To be very conservative, let us assume that the $\langle v\partial u/\partial y \rangle$ correlation decreases like the $\partial v/\partial x$ data, and that the error due to the Δz separation corresponds to the case for which $\Delta z/\eta = 15.6$ (the largest value given in Table 2.3). Based on these values the predicted attenuation in the $\langle v\partial u/\partial y \rangle$ correlation coefficient is about 50%.

Figure 3.28 shows the $v\omega_z$ correlation coefficient distributions.

Assume that the $R_\theta = 1{,}010$ data in this figure are correct. If the differences between the $R_\theta = 1{,}010$ profile and the $R_\theta = 4{,}850$ profile were only due to attenuation caused by the finite Δz separation, then at $y^+ = 140$ (the position at which the data of Figure 2.13 were derived) the above error estimate indicates that the $R_\theta = 4{,}850$ profile should attain a value of approximately 0.24. The actual value of the $R_\theta = 4{,}850$ distribution at the given location is about 0.07, or less than 1/3 the predicted value.

The above analysis strongly suggests that the observed differences between the $\langle v\omega_z \rangle$ profiles at different R_θ cannot be solely attributed to measurement errors. Examination of the data also suggests this to be the case. For example, using probe separation error as an explanation, it is difficult to reconcile the apparent non-zero agreement between the $R_\theta = 1{,}010$ and 2,870 data for $y^+ < 20$ in Figures 3.20 and 3.28. All available studies suggest that probe resolution errors should become more pronounced in this region of the flow. Similarly, it is difficult to account for the interesting and physically appealing scaling properties observed in the $(v\omega_z)'$ profiles if the $v\omega_z$ signals were substantially affected by finite probe scale effects.

3.2.2.5 The Vortex Force: A Plausible Mechanism For Lifting Vortical Sublayer Motions

Tennekes and Lumley (1972 p.78) discuss velocity vorticity cross products in terms of the body force per unit mass that they generate,

$$F_i = \epsilon_{ijk} u_j \omega_k .$$

This phenomenon was first documented in experiments by Magnus (1853). An example of this force is given in Batchelor (1967 p. 427), in which it is shown that a rotating cylinder exposed to a velocity normal to its axis experiences a lift force in the direction of the high flow speed side of the cylinder[7]. In the present context the vortex force will be used in physically interpreting velocity vorticity correlations relevant to experimental observations concerning vortical motions lifting from the sublayer.

For reference Figure 3.29 illustrates the lift forces experienced by vorticity filaments in directions pertinent to the correlations presented in the previous section and in Appendix 3.1. Concerning $u\omega_z$ notice that the associated vortex force is in the y direction[8]. The generation of this lift force may provide for a simple and quite general mechanism by which vortical sublayer fluid is transported away from the wall.

Evidence is presented in Chapter 4 indicating that in an absolute sense the spanwise vorticity in the viscous sublayer is to an extremely good approximation always of the same sign as the mean vorticity. In the coordinate system of the present experiments this sign is negative. To be consistent, this means that the instantaneous streamwise velocity near the wall is always positive. Given these signs for the velocity and vorticity components, Figure 3.29 indicates that instantaneously the direction of the vortex force acting on spanwise vorticity containing motions in the sublayer is always in the positive y direction. This however, does not mean that the sublayer is undergoing continuous

[7]Although it is clearly realized that vorticity filaments in a flow do not act like solid bodies, it is true that the velocity and vorticity vectors, in general, are independent of each other. Thus when vorticity filaments have a velocity relative to the surrounding motions they will experience this body force.

[8]Notice that the $w\omega_x$ force is also in the y direction. This force is, on average, significantly smaller than the $u\omega_z$ force, see Appendix 3.1. The negative sign of this correlation in the sublayer is however, consistent with the flow field associated with Falco's (1980) pocket vortex which has been observed to induce itself towards the wall.

ejections in the sense of the bursting terminology, since instantaneously this force may be quite weak compared to, say, viscous forces.

Coupled with the experimental observation of sweeps, the interpretation of the lift force due to $u\omega_z$ provides a plausible causal link between sweeps and the initial movement of vortical sublayer fluid away from the wall. Consider first an essentially irrotational high speed motion of limited spatial extent coming toward the wall at a shallow angle. If the instantaneous velocity associated with this high speed front is far enough from the mean, then the ω_z containing motions in the sublayer subjected to this front will experience a significant lift force.

Consider further this process in the context of convecting vortical motions interacting with the sublayer as discussed in Chapter 1. Given that the magnitude of the local lift force acting on the sublayer spanwise vorticity depends on the local streamwise velocity, it is easy to verify that vortical motions of rotation opposite that of the mean vorticity convecting above the sublayer will impose a local positive velocity perturbation on the sublayer. This will result in a perturbation vortex force in the positive y direction. Note that if the positive vorticity of the convecting vortical motion is of sufficient magnitude, this result is independent of its convection velocity. The region under this type vortical motion will always be a region of locally accelerated flow.

The above analysis suggests that a positive streamwise velocity perturbation imposed at, say, the outer edge of the sublayer will cause the effected region of the sublayer to experience a lift force. This represents a plausible causal relationship between sweeps and ejections. Note that this mechanism is consistent with the conclusions of Bull and Thomas (1983) indicating that "fluid involved in the bursting process is subjected to a favourable streamwise pressure gradient ... at the time that the lift-up of low-speed streaks in the wall region begins". In terms of an interaction between the inner and outer region motions it is easily seen that the above analysis suggests that a motion with vorticity of sign opposite that of the mean embedded in a high speed front is the optimal configuration for providing lift to sublayer fluid through the $u\omega_z$ vortex force. This result is consistent with the observations of Falco (1977, 1983) in that the lower lobes of the vortex ring-like motions (which interact with, and apparently lift sublayer fluid) have a rotational sense opposite of that of the mean vorticity.

Figure 3.30 shows the present $\langle u\omega_z \rangle$ distributions normalized by ν and u_τ. Under this normalization the data of Figure 3.30 exhibit good agreement for all R_θ. This indicates that, on average, the vortex force experienced by ω_z containing motions is Reynolds number independent. Note further that

$$\langle u\omega_z \rangle = \langle u\partial v/\partial x \rangle - 1/2\langle \partial u^2/\partial y \rangle.$$

Given the experience with Figures 3.16 and 3.17, it is probably true that the first term on the right hand side is negligible. Furthermore, the recent evidence of Alfredsson et al. (1988) suggests that for $y^+ < 10$ u'/u_τ is Reynolds number invariant over the range $300 \leq R_\theta \leq 2,800$. This evidence indicates that the $\langle u\omega_z \rangle^+$ profiles should be universal for $y^+ < 10$. Invariance of profiles of $\langle u\omega_z \rangle^+$ in this region are also consistent with the notion that the average contributions to the transport of $\langle u^2 \rangle$ from the active motions (in the form of lifting sublayer motions) are universal for y^+ less than about 15.

Clearly, the most distinctive feature of Figure 3.30 is the large negative correlation attained near the edge of the sublayer. The sign of this correlation is consistent with either an average lifting force due to a positive streamwise velocity perturbation acting on a negative ω_z perturbation, or the converse. Since however, S(u) is positive and $S(\omega_z)$ is negative in this region, the largest contributions to this correlation are probably from the (+)u - (-)ω_z perturbation combination. When considered in an absolute sense, this combination represents the largest lift force. Under the inner variable normalization shown the correlation reaches a value of about -0.63 at $y^+ \cong 5.2$. This indicates that, on average, the correlation between the u and ω_z perturbations represents a force that is about 63% of the associated mean viscous forces in this region. Note that this average force is substantially greater than the peak average force represented by any of the other correlations shown in Appendix 3.1.

Further away from the wall $\langle u\omega_z \rangle$ decreases rapidly, and is essentially zero for $y^+ > 25$. Note however, that the $R_\theta = 1{,}010$ data show a small positive trend up to a value of about 0.04 after crossing zero near $y^+ = 20$. Although in a relative sense this slight positive trend would seem to be negligible, examination of the $\langle v\omega_z \rangle$ correlations indicates that values of this magnitude may have significance in this region of the flow. In connection with vortical motions lifting from the sublayer, the rapid decrease in this correlation indicates that, on average, the force due to the fluctuating u and ω_z exists only out to about $y^+ = 25$. Plausibly, after this y^+ location these motions would start to undergo complex three dimensional interactions, and thus would begin to lose their lifted vortex sheet-like and/or hairpin vortex-like character. This interpretation is apparently consistent with the interpretation of the $S(\omega_z)$ and $K(\omega_z)$ profiles in Section 3.2.

As shown in Appendix 3.1 $<u\omega_z>$ appears in the equation for the transport of the diagonal terms of the Reynolds stress tensor. Thus in this respect the motions characterized by their $u\omega_z$ content may be considered the active motions pertinent to the transport of the normal stresses. Figure 3.30 indicates that Townsend's proposed scaling for the active motions apparently holds for $<u\omega_z>$. Furthermore, examination of Figures 3.32 and 3.33 indicates that the $(u\omega_z)'$ profiles also tend to follow this scaling. The scaling region for these profiles extends to approximately the edge of the logarithmic region of the mean velocity profiles. In contrast, it is interesting to note that the normalization of $<u\omega_z>$ by the function y/u_τ, shown in Figure 3.31, produces a universal profile only for y^+ less than about 20. In general however, it seems safe to say that the mean and rms of the motions responsible for $u\omega_z$ follow inner-type scaling.

3.4 DISCUSSION AND CONCLUSIONS - RELATIVE TO CHAPTER 3

Numerous results were discussed in this chapter. Some of these will now be summarized and discussed in the context of an interaction between the motions of the inner and outer regions. One is referred to Sections 3.2.4 and 3.2.5 for further summary information.

It is well established (see Chapter 1) that not only is the wake region of the mean velocity profile strongly Reynolds number dependent for R_θ less than about 3,000, but so are the instantaneous motions of the outer region. A general result of the data presented in this chapter is that many of the turbulence statistics (and especially those related to momentum transport normal to the wall) exhibit a Reynolds number dependence across much of the layer that is most evident for R_θ less than about 3,000. It is tempting to associate these two results through an interaction between the motions of the inner and outer regions.

Important results indicating the universality of the spanwise vorticity statistics under an inner variable normalization for $y^+ < 50$ were given. Furthermore, this apparent universality in ω_z did not imply the same for $\langle uv \rangle$ or $\langle v\omega_z \rangle$ for $y^+ > 15$. This leads to the conclusion that away from the wall one cannot associate the spanwise vortical content of the turbulent motions with their ability to create and transport $\langle uv \rangle$.

With respect to $\langle v\omega_z \rangle$, evidence was given indicating that with increasing Reynolds number these motions exhibit a decrease in size with respect to total thickness of the flow (i.e. outer variables) and an increase in size with respect to the thickness of the viscous sublayer (i.e. inner variables). Given that the ratio, u_τ/U_∞, and the total thickness of the flow change relatively little with Reynolds number, these results indicate a decrease in the absolute scale of the motions characterized by $v\omega_z$ with increasing R_θ. These changes in scale lend themselves to the interpretation that at low Reynolds numbers, due to their larger scale relative to the width of the flow, the motions responsible for the transport of $\langle uv \rangle$ interact with each other more significantly. This increased level of interaction may decrease the average coherence of these motions, and thus interfere with the creation of $\langle uv \rangle$. Under this interpretation, due to a relative decrease in scale at higher Reynolds numbers these motions interact less. This interpretation (coupled with the universality of ω_z under inner variable scaling) tends to be supported by the apparent y/u_τ scaling found for the rms $v\omega_z$ profiles. An alternate possibility is that at low Reynolds number (again due to their larger relative scale) the motions responsible for the transport of $\langle uv \rangle$ interact differently with the larger scale outer region motions than they do at higher R_θ. This possibility would be indicative of a change in the interaction between the inner and outer region motions.

Nearer the wall the $\langle uv \rangle$ and $\langle v\omega_z \rangle$ data provide evidence that under an inner normalization the different Reynolds number profiles merge. This leads to the conclusion that near the wall the average ω_z content of the turbulent motions can be associated with their ability to create and transport $\langle uv \rangle$. Combining this with the observed universality of the ω_z statistics out to $y^+ \cong 50$, suggests a physical picture in which the initial lifting of a hairpin-type motion is dependent on the spanwise vorticity content of the initiating mechanism, but not the ability of the initiating mechanism to create $\langle uv \rangle$. The apparent universality of the $\langle uv \rangle^+$ and $\langle v\omega_z \rangle^+$ profiles for $y^+ < 15$ also lends support to the hypothesis that there are a limited number of turbulent stress producing mechanisms in this region of the flow. These mechanisms are probably associated with the lifted vortex sheet-like and/or hairpin vortex-like motions, as well as the motions responsible for their formation.

In an average sense it was found that the streamwise gradient terms of equation 3.2 were negligible relative to velocity vorticity correlation terms. However, the rms values of these terms were found to be at least as large as $(v\omega_z)'$. This indicates that instantaneously these motions could be quite important. In the context of an inner/outer coupling through the convection of small scale vortical motions embedded in a larger scale and relatively irrotational motion, it is tempting to associate these streamwise gradient terms with the latter.

The data of Section 3.2.2.5 support the suggestion that the vortex force due to the introduction of a high speed velocity perturbation at the outer edge of the sublayer is a viable mechanism for initiating the observed lifted shear layer and/or hairpin vortex-like motions. In a very general sense this plausible initiating mechanism associates a cause and effect relationship between sweeps and ejections. In terms of the influence of convecting vortical motions above the sublayer, it was deduced that small scale motions that have spanwise vorticity of sign opposite that of the mean would be most effective in imposing a distortion force normal to the wall on the sublayer vorticity distribution via the $u\omega_z$ vortex force. In terms of essentially irrotational outer region sweeps interacting with the sublayer, the vortex force mechanism, in general, predicts that the size of the lifted sublayer motion is determined by the surface area of the sublayer affected by the sweep. Thus this mechanism may provide a link between the observation of relatively large scale lifted shear layers and the direct influence of the outer region flow.

CHAPTER 4

ON THE SPATIAL STRUCTURE OF SPANWISE VORTICITY IN TURBULENT BOUNDARY LAYERS

4.1 ISSUES PERTINENT TO AN INNER/OUTER INTERACTION

Very little data exist that are relevant to understanding the spatial structure of the vorticity field in turbulent wall flows. Kastrinakis (1977) performed two point streamwise vorticity correlation experiments in a turbulent channel flow using a four wire Kovasznay-type probe[1]. These measurements, which were for spanwise probe separations, revealed peak negative correlation values between -0.075 and -0.15 for Δz^+ separations equal to about 40 and y^+ values less than about 30. These significant negative values are readily interpreted as strong evidence for the existence of counter-rotating streamwise vorticity containing motions near the wall. However, for greater distances from the wall the zero crossing to negative correlations disappears. This may indicate that the hairpin vortex-type motions believed to be responsible for the counter-rotating ω_x begin to lose their coherence by $y^+ \cong 30$. For y^+ less than roughly 100 the two point ω_x correlations become essentially zero at separation values of $\Delta z^+ \cong 60$. Further away from the wall these correlations maintain non-zero values for separations out to $\Delta z^+ \cong 120$.

[1]Even though it was later shown that significant errors in the instantaneous measured values of ω_x are associated with this probe, relevant to long-time statistics Foss and Wallace (1989) conclude that "comparison with other measurements ... indicate that these errors, which can instantaneously be very large, may statistically be small". It is therefore believed that these correlation curves are reasonably accurate.

Contrary to the popular belief in the dominance of streamwise vorticity containing motions near the wall, the vorticity field for $y^+ \leq 10$ is predominantly oriented in the spanwise direction. In this region, the ratio $\omega_z'/|\Omega_z|$ is about equal to 0.4 (see Figure 4.9), and the ratio ω_x'/ω_z' is in the range 0.3 to 0.5, see for example, Lee et al. (1974) or Kim et al. (1987). (Due to the no-slip condition ω_y' is significantly less than either ω_x' or ω_z' in this region of the flow.) Therefore, for $y^+ \leq 10$ $(|\Omega_z| \pm \omega_z')/\omega_x'$ ranges from at least about 3 to at most about 12. Farther from the wall, the importance of the mean vorticity diminishes (see Figure 4.9), and by $y^+ \cong 40$ all three rms vorticity components are about equal, see Balint et al. (1987a). In the outer region the mean contribution is negligible, and all three rms components are about equal, again see Balint et al. (1987a).

The predominance of the spanwise vorticity very near the wall argues for the validity (at least in an average sense) of the sublayer vortex sheet approximation discussed in Chapters 1 and 3. This type of sublayer vorticity distribution predicts that spanwise vorticity correlations in this region remain non-zero for greater Δz separations than they do further from the wall. The diminished importance of the mean vorticity and the nearly equal rms values of the fluctuating components indicates that away from the wall the average vortical motions are highly three dimensional.

Pertinent to the results in Chapter 3, the results of this chapter shed light on the issue of whether large scale spanwise vorticity containing motions (on average) exist. In terms of an interaction between the motions of the inner and outer regions, this issue is important because it gives a rough but direct indication of the scales of vortical motions involved. The success or failure of plausible mechanisms for boundary layer control would undoubtedly be dependent on their ability to effectively interact and/or alter these scales of motion. In terms of Townsend's active/inactive motions decomposition, the issue of organized large scale vortical motions is relevant to the validity of identifying the outer region as being characterized by inactive motions which are, on average, essentially irrotational.

In Chapter 3 evidence was presented suggesting the existence of intermittent motions in the near-wall region that have positive spanwise vorticity (i.e. of sign opposite that of the mean vorticity). Furthermore, in examining the vortex force mechanism for the initial lifting of vortical sublayer motions it was deduced that small scale positive vorticity containing motions convecting above the sublayer would be most effective in generating a local lift force on the sublayer vorticity distribution. Evidence pertaining to the issue of positive ω_z in the near-wall region is also presented in this chapter.

4.2 EXPERIMENTAL PROCEDURES AND CONDITIONS

Most of the details pertaining to the experimental procedures, equipment and factors affecting data quality as they relate to the experiments of this chapter were documented in Chapter 2. Therefore, Section 4.2.1 will document and describe only those aspects of the two point spanwise vorticity correlation experiments that are additional to the single point experiments described in Chapter 2. In Section 4.2.2 the conditions of the two point experiments are given, as well as information pertinent to relating these experiments to the single point experiments.

4.2.1 Additional Equipment and Procedures

The data acquisition, signal conditioning, and probe positioning equipment used in the correlation experiments included all of the equipment described in Chapter 2. However, since the correlation experiments employed a second spanwise vorticity probe additional hardware was required.

The additional spanwise vorticity probe was operated by four TSI model 1755 anemometers at an overheat ratio of 1.7. The electronic noise level associated with these anemometers was found to be comparable to the electronic noise associated with the DISA 55M01 anemometers used to operate the other probe. Stable operation of the TSI anemometers at the two lower Reynolds numbers of the single-point experiments (i.e. R_θ = 1,010 and 2,870) required the manual adjustment of their "trimming" capacitance. While the effect of increasing this capacitance increased the low velocity end of the operating range, it also reduced the frequency response of the anemometers.

Following this adjustment to the anemometers, a standard square-wave test was performed in the free stream of the R_θ = 1,010 boundary layer. The results of the test indicated frequency responses ranging between 3.3 and 3.5 kHz. This response is somewhat less than the better than 5 kHz found for the DISA anemometers under the same conditions. The effect of this decreased frequency response was felt to be negligible however, since the maximum Kolmogoroff frequencies in the R_θ = 1,010 and 2,870 flows have been estimated to be about 130 Hz and 300 Hz respectively.

An additional set of (previously custom built) DISA low-pass filters were used to remove the high frequency electronic noise from the TSI anemometers. Unlike the nearly continuously adjustable Krohn-Hite filters, these low-pass filters allow for only a few discrete cut-off frequency settings ranging from 1,000 Hz to 5,000 Hz. Thus in using the 1,000 Hz setting an adherence to the Nyquist criterion could not be maintained. However, inspection and comparison of the output signals from the two sets of anemometers/filters indicated that there were no discernable differences in noise levels. This is probably because the electronic noise on the signals prior to filtering was solely at high frequencies. As was previously found for the Krohn-Hite filters, the channel-to-channel phase shifts between the signals entering the DISA filters were very small (less than $\pm$ 5μs). The phase shifting between the signals from the two sets of anemometers/filters was also found to be about the same small value.

The traverse gear for the Δy separation experiments was the same as that used in the single probe experiments. The stationary probe in the Δy separation experiments was mounted directly to the floor of the tunnel, and was positioned at the proper y location via thin metal shims. By using the cathetometer (described in Chapter 2), the stationary probe was observed under experiment conditions. No detectable vibration of this probe (due to being directly attached to the floor) was observed. The initial y distances of the probes from the floor, and the initial Δy distances between the two probes were also measured using the cathetometer.

An additional 3-D traverse gear was built and installed for the Δz probe separation experiments. This mechanism, shown in Figure 4.1 consists of a drilled-out aluminum base that is mounted on two 3/4 inch aluminum rods, and is traversed in the spanwise direction by a 32 turns per inch worm gear. Mounted on this base is a vertical traverse mechanism that allows for probe positioning in the y direction by a 24 turns per inch worm gear. Finally, mounted on this y-traverse is 3/8 inch stainless steel rod that extends approximately 16 inches in the upstream direction. A ±0.5 inch fine adjustment of this extension rod in the x direction is accomplished via an axially mounted spring-loaded micrometer. The probe is mounted at the end of this extension rod. This results in the measurement location being approximately 24 inches upstream of the z-traversable base.

Due to this extension rod, the possibility existed for unwanted vibration. To test for this, the probe was (once again) examined through the cathetometer at the experiment flow speeds. As with the stationary probe in the Δy separation experiments, no discernable vibration was detected. The good agreement with the statistics from the other probe (see Section 4.2.2) further supports this conclusion.

A 0.254 mm (0.01 inch) division scale and a pointer were mounted such that the relative position of the z-traversable base could be measured. The x and y-traverses were used, with the aid of the cathetometer, to initially position the z-traversing probe at the same x and y locations as the stationary probe. The stationary probe in the Δz separation experiments was mounted on the y-traverse used in the single probe experiments. The initial Δz distance between the two probes was determined by placing a 0.254 mm (0.01 inch) division scale flat on the floor beneath the probes. By lowering the two probes near the wall and looking from overhead the distance between the probe centers was measured. The x-array and parallel-array configurations for the Δz

separation experiments were such that the for one ω_z probe the x-array was offset in the +z direction while for the other probe the x-array was offset in the -z direction. The two spanwise vorticity probes were then oriented such that the two parallel-array elements were interior to the two x-array elements. The probe center was then defined to be the parallel-array support prong closest to its "partner" x-array contained within a given ω_z probe.

The method of determining the initial Δz separation was significantly less accurate than in the Δy separation experiments. A conservative estimate of the uncertainty associated with this method is felt to be approximately ±2 scale divisions or ±0.5 mm; which translates to about $\pm 1.0\Delta z^+$ and $\pm 2.4\Delta z^+$ at $R_\theta = 1{,}010$ and 2,870 respectively. The given x-array and parallel-array configuration was used because on average $\partial u/\partial y$ dominates $\partial v/\partial x$ in the near-wall region.

Based upon the preliminary results of Klewicki and Falco (1986), the smallest achievable probe separations (in wall units) at $R_\theta = 4{,}850$ were too large to yield significantly non-zero correlation coefficient values. Therefore it was decided to run the correlation experiments only at the two lowest Reynolds numbers. In order to increase the integration time of the $R_\theta = 1{,}010$ experiments for a given sample size, the sampling rate of the analog-to-digital converter was reduced by a factor of 2 from the value given in Table 2.1. Over the range of y^+ positions of the correlation experiments, the sampling rate ranged between about 2 and 5 times the local Kolmogoroff frequency. The sample size of all of the data records was $4.8\text{x}10^6$ points ($6\text{x}10^5$ points in each channel). The corresponding sampling times resulted in averaging over $TU_\infty/\delta \cong 6{,}700$ and 5,000 at $R_\theta = 1{,}010$ and 2,870 respectively. All other data reduction procedures for the correlation experiments were the same as given in Chapter 2.

4.2.2 Experimental Conditions

4.2.2.1 Correlation Experiment Overview

In order to compare with the results of the single probe experiments, as well as for convenience in data processing, the two point spanwise vorticity correlation experiments were run (nominally) at R_θ = 1,010 and R_θ = 2,870. The positions of the stationary probe and Reynolds numbers for these experiments are given in Table 4.1. All of the correlations to be reported are for stationary probe positions in the inner region of the boundary layer. As one can see, for $y^+ < 10$ only the lower Reynolds number data were experimentally available. Note also that for the Δy separation experiments the moving probe was always at a greater distance from the wall than the stationary probe.

4.2.2.2 Matching the Reynolds Numbers of the Single Point Experiments

In order to use the friction velocities from Table 2.1 in normalizing distances in the correlation coefficient profiles presented in Section 4.3, the Reynolds numbers had to be matched. This section presents data relevant to the accuracy at which this Reynolds number matching was accomplished.

Figure 4.2 presents mean velocity profile data acquired from the moving probe of the Δy separation experiments. In this figure, the data from these correlation experiments (solid symbols) were normalized using the friction velocities from Table 2.1, and are overlaid on the single point velocity profile data of Figure 2.2 (open symbols). As one can see (except for a few points) in terms of mean velocity the Δy correlation experiments matched Reynolds number with the single point experiments quite well.

Assessment of the degree to which the correlation experiments matched the Reynolds number of the single point experiments was also performed by comparing the rms spanwise vorticity profiles. Figure 4.3 shows the moving probe data from the Δy separation experiments overlaid on the R_θ = 1,010 and 2,870 ω_z' profiles of Figure 2.14. (Figure 2.4 shows some of the Δy correlation experiment stationary point $\nu\omega_z'/u_\tau^2$ data.) Figures 4.4 through 4.8 present comparisons between the ω_z' data of the Δz separation experiments and the relevant data of Figure 2.14. In all of these figures the correlation experiment data are normalized by the friction velocities given in Table 2.1. The comparison in Figure 4.3 with the single point profile data provides further evidence that these correlation experiments had about the same Reynolds numbers as the profiles of Figure 2.14. For the most part, the same can also be said for the Δz separation data shown Figures 4.4 through 4.8. Note however, that the data in Figure 4.6 indicate that two attempts of the stationary probe at $y^+ \cong 30$ experiment were made at $R_\theta \cong 1,010$, and both failed to identically match the Reynolds number.

Other useful information can also be extracted from Figures 4.4 through 4.8. By comparing Figures 4.4, 4.5 and 4.6 with Figures 4.7 and 4.8 one can see that, in general, the point-to-point scatter and the differences with the single point profiles are less in the higher Reynolds number experiments. This indicates that it is relatively easier to match Reynolds numbers as R_θ increases. Note further that in general the stationary probe in all of these figures tended to give slightly higher values than the moving probe. These differences are presently felt to be indicative of the probe-specific biases associated with the measurement of ω_z'.

In general, the above results indicate that the Reynolds numbers of the correlation experiments were nominally the same as in the single probe experiments. Therefore, in the data presentation of Section 4.3 the friction velocities of Table 2.1 are used in normalizing the distances from the wall and the probe separations.

4.2.3 On Interpreting Spanwise Vorticity Correlations

The data presentations in the following section feature spanwise vorticity correlation coefficients that are derived from the fluctuating ω_z signals of the two probes. Unlike the streamwise and normal components, in a boundary layer the spanwise vorticity component has a significant non-zero mean value, $\Omega_z \cong -\partial U/\partial y$. Therefore in order to interpret two point ω_z correlations in the context of instantaneous motions one must take into account the mean vorticity at any given location.

Figure 4.9 shows the ratio of the rms spanwise vorticity as measured in the $R_\theta = 1{,}010$ boundary layer to the mean vorticity as given by the formula of Van Driest (1956) and shown in Figure A2.3.1. As can be seen, for y^+ less than about 20 the mean spanwise vorticity is greater than the rms. Thus, near the wall the presence of positive vorticity in an absolute sense indicates the presence of positive fluctuations greater in absolute value than the mean vorticity at that location. For y^+ values greater than 20 the rms is greater than the mean. For large enough distances from the wall (in the outer region) the fluctuations dominate the mean.

The Reynolds decomposition leaves both the mean and fluctuating vorticity divergenceless. From an instantaneous physics point of view however, it is easier to understand and interpret vorticity in terms of a total (mean + fluctuating) quantity. This is because the geometry of "real" (as opposed to Reynolds decomposed) vortical motions in a flow depends on the absolute value of the vorticity. From a statistical point of view, the description in terms of the vorticity fluctuations alone seems most desirable. This is because from this viewpoint one gains an indication of the average spatial extent of the time dependent vortical motions (note that the mean vorticity is indefinitely correlated). Undoubtedly, the most complete understanding is gained by examining the data from all points of view, while the correct interpretation makes physical sense regardless of the point of view.

4.3 TWO POINT SPANWISE VORTICITY CORRELATIONS

This section presents the two point fluctuating spanwise vorticity correlations listed in Table 4.1. As stated in the previous section these correlations were run at the nominal Reynolds numbers of R_θ =1,010 and 2,870. Since all of these correlations are for probe positions within the inner region, only an inner variable normalization of probe separations is given. Also in examining these data it is very important to remember that, as with all self-correlated variables, the normalized value of the correlation is 1.0 for zero separation.

4.3.1 Probe Separations Normal to the Wall

Figure 4.10 presents the results of the Δy separation experiments for the stationary probe positioned at $y^+ \cong 100$. As can be seen, all of the lower Reynolds number data in this figure exhibit significant positive values[2]. For a probe separation of $\Delta y^+ \cong 14.5$ the $R_\theta = 1{,}010$ correlation coefficient is about 0.41. For greater probe separations however, the correlation decreases quite rapidly. At $\Delta y^+ \cong 60$ the correlation coefficient has decreased to about 0.12.

All of the higher Reynolds number data in Figure 4.10 are essentially zero; a result that is in striking contrast to $R_\theta = 1{,}010$ data of this figure. Using the correlation as a rough measure of the average scale of organized ω_z containing motions, one might conclude that these motions become smaller relative to an inner normalization with increasing Reynolds number. Caution should be taken in making such conclusions however, since other factors, such as the range of spatial orientations a given vortical motion is likely to acquire at a given Reynolds number, could also contribute to the observed zero correlation values. On the other hand, it is probably safe to say that none of the data of Figure 4.10 support the (on average) existence of large scale spanwise vorticity containing motions in the region $100 \leq y^+ \leq 200$.

Figure 4.11 presents the results of the Δy separation correlations for the stationary probe near $y^+ = 30$. The $R_\theta = 1{,}010$ data in this figure show positive values for probe separations less than about 25 wall layer units and significant negative values for greater separations. A peak negative correlation coefficient of -0.142 for a probe separation of $\Delta y^+ \cong 42$ is observed. This rather modest negative value increases in significance if one considers that at the given probe positions ($y^+ \cong 30$ and 72) the ratio of the product of the mean vorticity values to the rms

[2]Actually two other data files were taken at larger Δy^+, but later these files could not be read from the tape.

vorticity values is about 0.26. Thus if normalized by the local mean vorticity values this correlation would reach a value of about -0.56; giving a fairly strong indication that the most significant contributions to this correlation probably involve positive total spanwise vorticity at one of the probes. After the negative peak, the correlation coefficient decreases to a value of about -0.04 at a probe separation of $\Delta y^+ \cong 100$. For reference with the data of Figure 4.10 the correlation is equal to 0.1 at a probe separation of $\Delta y^+ \cong 55$.

As in Figure 4.10, the $R_\theta = 2,870$ data of Figure 4.11 show significantly smaller magnitudes than the $R_\theta = 1,010$ data for a given Δy^+. Furthermore, the negative peak in the higher Reynolds number data has apparently shifted to a smaller Δy^+ value. As stated above, caution should be taken in associating these observations strictly with a change in scale. Qualitatively, the high and low Reynolds number data in Figure 4.11 show the same trend of a zero crossing to negative values before eventually becoming zero. In connection with Figure 4.11 it is also worth noting that in previous measurements at $R_\theta \cong 4,850$ Klewicki and Falco (1986) found essentially zero correlation in experiments with a stationary probe at $y^+ \cong 30$ and probe separations as close as $\Delta y^+ \cong 50$.

Figure 4.12 presents the results of the Δy separation experiments for the stationary probe near $y^+ = 15$. The $R_\theta = 1,010$ correlation coefficient data in this figure, which are negative for all measured values, show an increasingly negative trend for decreasing probe separations. The trend in these data suggest that at the smallest probe separation the correlation has yet to reach its negative peak. The value of the correlation coefficient at the probe separation of $\Delta y^+ \cong 18$ is -0.325. At a separation of $\Delta y^+ \cong 65$ the correlation coefficient has decreased in magnitude to -0.10. As with the low Reynolds number data of Figure 4.11, the zero crossing to significantly negative values indicates the presence of organized opposing sign fluctuating spanwise vorticity interactions.

In general, the R_θ = 2,870 correlation coefficients in Figure 4.12 show much better agreement with the R_θ = 1,010 data than in either Figures 4.10 or 4.11. However, at the smallest Δy^+ separations the high Reynolds number data are still about 50% lower. As with Figure 4.11, the high and low Reynolds number correlation coefficient profiles are qualitatively the same, although it is undetermined whether the negative peaks in the two curves occur at the same Δy^+ value. The value of the R_θ =2,870 correlation at the closest probe separation of $\Delta y^+ \cong 38$ is -0.11.

Figure 4.13 presents the Δy separation correlation coefficient profile for the stationary probe positioned at $y^+ = 7.5$ in the R_θ = 1,010 boundary layer. As can be seen, this correlation is negative over the entire range of measured values. At the point of smallest probe separation the correlation coefficient is about equal to -0.42. Furthermore, as with the data in Figure 4.12 the trend in this profile gives no indication that -0.42 is the peak negative value. As the probe separations increase the correlation coefficients decrease quite rapidly. At a Δy^+ separation of about 55 the correlation coefficient has reduced in absolute magnitude to 0.1. The correlation coefficient profile in Figure 4.13 is very similar to that in Figure 4.12 in both shape and magnitude.

Note that the negative trends in both Figures 4.12 and 4.13 are unlike the negative trend in the R_θ = 1,010 data of Figure 4.11 in that the negative peak value occurs at much smaller Δy^+ separations. Given that the correlation is 1.0 at zero probe separation, this result indicates that the region of positive correlation (for probe separations smaller than those which are experimentally attainable) also becomes smaller. Given a process such as that proposed by Falco (1983, 1987) in which vortical fluid is initially lifted from the sublayer through an interaction with positive spanwise vorticity containing motions external to the sublayer, it is tempting to interpret the correlations of Figures 4.12 and 4.13 as being representative of the interaction between the motions arising from the sublayer and the $(+)\omega_z$ motion, and to then interpret the correlation of Figure 4.11 as being representative of the average structure of the initiating positive spanwise vorticity containing motion.

The strong negative correlation for small probe separations in Figures 4.12 and 4.13 indicates the average existence of closely spaced positive and negative spanwise vorticity fluctuations in the near-wall region. In order to further understand the contributions to this strong negative correlation, a two dimensional probability distribution was constructed from the individual fluctuating ω_z records that generate the data point of closest separation in Figure 4.13. Figure 4.14 shows this probability distribution in relation to the coordinates of the fluctuating signals from the upper and lower probes, as well as in coordinates relevant to the absolute sign and magnitude of these signals.

Relative to the fluctuating spanwise vorticity coordinates, Figure 4.14 clearly shows that the major contributions to the negative correlation coefficient come from fourth quadrant-type motions. These motions feature positive sign fluctuating ω_z being measured at the upper probe, in conjunction with negative sign fluctuating ω_z being measured at the lower probe. In a relative sense, this was the type of motion identified in Chapter 3 as being most effective in producing the vortex lift force on vortical sublayer fluid.

Note that in the fluctuating coordinates all quadrants contain probability contours. This fact might lead one to physically questionable interpretations regarding the nature of the vortical motions involved. For example, contours in quadrant 2 readily lead to the interpretation of counter-rotating ω_z containing motions with the positive sign vorticity occurring nearer the wall. When observed relative to the absolute coordinates of Figure 4.14 however, this interpretation is clearly shown to be incorrect since in an absolute sense positive vorticity is essentially never seen at $y^+ = 7.5$. This finding of a unidirectional ω_z vorticity component (in an absolute sense) near the wall further supports the proposed sublayer vortex sheet model introduced in Chapter 1.

Figure 4.14 also gives important information pertinent to the presence of positive sign spanwise vorticity containing motions in the near-wall region. As can be seen, in absolute coordinates the ω_z-ω_z probability distribution is contained entirely in quadrants 3 and 4. As discussed above, in an absolute sense the lower probe measured only negative spanwise vorticity (i.e. of the same sign as the mean). The upper probe data however, show a significant number of probability contours that are positive in an absolute sense, and that approach very near to the peak of the distribution. This figure shows that the probability represented by ω_z-ω_z combinations in which positive ω_z containing motions are at the upper probe is approximately 1/4 the total probability. Furthermore, the shape of the probability distribution indicates that the presence of positive vorticity at the upper probe is most likely to be coupled with negative vorticity at the lower probe that is of magnitude greater than the local mean. This observation is readily explained by a physical process in which a positive ω_z containing motion (possibly embedded in a larger scale high speed front) convects above the sublayer. Under this process, the lower probe measures a positive velocity fluctuation commensurate with the presence of the positive ω_z containing motion above the sublayer. Through the no-slip condition at the wall, this results in a negative ω_z fluctuation. The upper probe, due to its intersection with the convecting vortical motion measures a positive ω_z fluctuation greater in magnitude than the local mean. Recall from Figure 4.9 that at $y^+ = 20$, $\omega_z{}' \cong \Omega_z$. The interaction between the sublayer vorticity and the convecting vortical motion would probably also serve to intensify the respective ω_z in these interacting motions. It is worth recalling that this type of interaction is precisely the mechanism identified as being most effective in producing a local vortex force in the positive y direction on the sublayer ω_z containing motions.

4.3.2 Spanwise Probe Separations

Figure 4.15 presents the results of the Δz probe separation experiments at $y^+ \cong 30$. The results of the two low Reynolds number runs are in excellent agreement[3]. As can be seen, all of the non-zero correlations in this figure are positive. Furthermore, unlike the Δy probe separation results, the high and low Reynolds number data in this figure agree quite well. The peak value of the low Reynolds number correlation coefficient is about 0.31 at a probe separation of $\Delta z^+ \cong$

[3]Recall that in both of these experiments the Reynolds numbers are about the same, but are slightly less than $R_\theta = 1{,}010$.

17.3. At a probe separation of $\Delta z^+ \cong 30$ this correlation decreases to 0.1. The $R_\theta = 2,870$ correlation coefficient of Figure 4.15 reaches a peak value of about 0.075 at a probe separation of $\Delta z^+ \cong 43$.

Figure 4.16 presents the Δz probe separation experimental results for $y^+ = 15.3$ at $R_\theta = 1,010$ and $y^+ = 20.4$ at $R_\theta = 2,870$. The results in this figure are very similar to those above in that the correlations are either positive or essentially zero. Furthermore, as in Figure 4.15, the agreement between the high and low Reynolds number correlation coefficients is good. The $R_\theta = 1,010$ correlation coefficient attains a value of 0.39 at a probe separation of $\Delta z^+ \cong 17.5$. At the same Reynolds number the normalized correlation has reduced to 0.1 at probe separation of $\Delta z^+ \cong 40$. The $R_\theta = 2,870$ correlation coefficient attains a value of 0.1 at $\Delta z^+ \cong 43$.

Like the correlations in Figures 4.15 and 4.16, the $R_\theta = 1,010$ Δz probe separation results at $y^+ = 6.7$ in Figure 4.17 are either positive or essentially zero. Furthermore, consistent with the trend between the correlations at $y^+ \cong 15$ and 30, the results in Figure 4.17 give still higher correlation coefficient values for the same Δz^+ separation. This trend indicates that on average the spanwise extent of correlated instantaneous ω_z containing motions increases as the wall is approached. The correlation coefficient of this figure is about 0.62 at a probe separation of $\Delta z^+ \cong 17$. The value of this correlation is 0.1 at a probe separation of $\Delta z^+ \cong 47$.

4.4 DISCUSSION AND CONCLUSIONS - RELATIVE TO CHAPTER 4

In general, the correlations with probe separation normal to the wall indicate the increased significance of opposing sign spanwise vorticity interactions with decreasing distance from the wall. Furthermore, by comparing the correlations in which the stationary probe was at $y^+ \cong 7.5$ and 15 with those at $y^+ \cong 30$, it is evident that the position of the negative peak in the correlations nearer to the wall occurs at a probe separation about three times as small as in the correlation profile in which the stationary probe was at $y^+ \cong 30$. Thus nearer the wall the average positive and negative fluctuating spanwise vorticity interactions become more closely spaced. This is probably indicative of the motions responsible for the interactions nearer the wall (say $y^+ \leq 20$) being of a different nature than those occurring away from the wall (say $y^+ > 20$).

All of the Δz separation correlations were positive over the range of y^+ values explored. Thus it is safe to say that the average spanwise spatial structure of ω_z does not feature counter-rotating motions; from either a fluctuating or total ω_z point of view. Furthermore, for a given probe separation, generally higher magnitude correlation values were measured in the Δz separation experiments than in the Δy separation experiments. On average this indicates a greater spatial coherence in the spanwise direction. As discussed below, this may be associated with a smaller number of probable spatial orientations that organized ω_z containing motions achieve in the spanwise direction as opposed to in the direction normal to the wall.

One may use the correlations as a rough measure of the average scale of the instantaneous spanwise vorticity containing motions at a given Reynolds number. In connection with this, the Δy separation correlations suggest that while the average nature of the motions contributing to the correlation changes quite dramatically with distance from the wall, the spatial extent of these motions normal to the wall is insensitive to the distance from the wall. This can be seen by examining the position in each $R_\theta = 1{,}010$ correlation coefficient curve at which the magnitude has (presumably) permanently decreased to less than about 0.1. For the stationary probe positions of $y^+ \cong 7.5$, 15, 30, and 100, the Δy^+ separations corresponding to this point are 55, 65, 55 and about 60. In connection with the spanwise extent of ω_z containing motions, the Δz separation results suggest that while the average nature of the motions contributing to the correlation changes little with distance from wall, the average spanwise extent of these motions decreases with increasing distance from the wall. Once again, using the probe separation at which the magnitude of the $R_\theta = 1{,}010$ correlation coefficient has (presumably) permanently decreased to about 0.1, the corresponding Δz^+ values at $y^+ \cong$ 6.7, 15 and 30 are 47, 40 and 30 respectively. Thus between $y^+ = 6.7$ and 30 the average spatial extent of the spanwise correlation decreases in scale by about 36%. This trend may plausibly be due to either changes in the average scale or orientation of contributing motions. In general however, this trend supports the notion that the sublayer vorticity distribution has a sheet-like character relative to the ω_z containing motions away from the wall. Note that none of the correlation data presented suggest the average existence, in the wall region, of large scale motions that contain spanwise vorticity.

The observed Reynolds number dependence in the Δy separation correlations is dramatic. The obvious trend in these results is for the higher Reynolds number correlations to become zero at much smaller Δy^+ values. Furthermore, this trend is more apparent for the results in which the stationary probe is further away from the wall. In presenting these results it was noted that caution should be taken in associating the more rapid decrease in the correlation strictly with a Reynolds number dependence in the scale of the contributing motions.

In Chapter 3 evidence was presented suggesting that the motions most responsible for the $\langle v\omega_z \rangle$ correlation increase in scale under an inner variable normalization with increasing Reynolds number. The present Δy correlations seem to contradict this result. However, in Chapter 3 evidence was also presented suggesting that the motions most responsible for the $\langle v\omega_z \rangle$ correlation decrease in scale under an outer variable normalization with increasing Reynolds number. Assuming this to be the case for the vortical motions represented in the Δy correlations, one may conclude that these motions are smaller relative to the total width of the flow with increasing Reynolds number. If one associates these correlations with the presence of small to intermediate scale motions convecting throughout the inner and outer regions, the above apparent discrepancy may be resolved. That is, since these motions are smaller with respect to the total width of the flow at higher Reynolds number, then at higher Reynolds number they are probably more apt to take on a greater number of orientations in space. Thus the observed Reynolds number dependence in the Δy separation correlations may be due to an increasing number of probable spatial orientations in the x-y plane that the motions contributing to these correlations may acquire with increasing Reynolds number. It is easily envisioned how a correlation measured by a pair of stationary probes could be attenuated through such a Reynolds number dependence.

The trends in the present correlations tend to support this suggestion. In the case of the Δy probe separation experiments, with increasing Reynolds number zero correlations occurred at smaller Δy^+ as the distance between the stationary probe and the wall increased. If one thinks in terms of the possible orientations that local spanwise vorticity interactions (eddies) can assume per total flow volume, then the degradation of these correlations as a function of Reynolds number appears consistent with the indicated trends, as well as the deduced changes in scale (relative to δ) for the $\langle v\omega_z \rangle$ producing motions. Furthermore, it was shown in Figure 4.14 that as a probe is positioned nearer the sublayer the probability of it measuring positive vorticity (in an absolute sense) is greatly diminished. Given that one of the two probes is in this region, this fact probably represents a constraint on the types of interactions that can lead to a negative correlation coefficient at any Reynolds number. Thus one would expect correlations at different Reynolds number to come into better agreement as the stationary probe is brought closer to the wall. This notion is also consistent with the results in Chapter 3 suggesting the universality of the average ω_z content of the initiating mechanisms leading to the ejection of vortical sublayer fluid.

The Δz separation results provide evidence that it is only the average orientation of the ω_z containing motions in the x-y plane that may be Reynolds number dependent. In these correlations, generally good agreement was found between the high and low Reynolds number data and, if anything, slightly higher correlation values for a given Δz^+ probe separation were found at $R_\theta = 2,870$. Thus it appears that the average spanwise spatial structure of the ω_z containing motions in the near-wall region is essentially Reynolds number invariant when normalized by inner variables.

The following major conclusions are drawn from the two point fluctuating spanwise vorticity correlation experiment results.

• In an average sense, no evidence was found that supports the existence in the inner region of organized large scale motions that contain spanwise vorticity.

• For the stationary probe positioned at a y^+ value less than about 30, negative correlation coefficients are observed in the Δy probe separation results. The peak in this negative correlation coefficient increases in magnitude and shifts to smaller probe separations as the stationary probe is brought closer to the wall.

• For probes positioned at $y^+ = 7.5$ and 22 in the $R_\theta = 1,010$ boundary layer, examination of the two dimensional ω_z-ω_z probability distribution indicated the statistically significant occurrence of positive vorticity (of sign opposite the mean) at $y^+ = 22$ coupled with negative vorticity at $y^+ = 7.5$ of magnitude greater than the local mean.

• From the same two dimensional ω_z-ω_z probability distribution, it was shown that at $y^+ = 7.5$ the probability of measuring positive vorticity is essentially zero.

• The Δz probe separation experiments resulted in positive correlations throughout the near-wall region.

• The Δz probe separation experiment correlation coefficients decreased in magnitude for a given Δz^+ as the distance from the wall increased. The Δy probe separation experiment correlation coefficients did not.

• The Δy probe separation experiment correlation coefficients showed a significant decrease in magnitude for a given Δy^+ as the Reynolds number increased. The Δz probe separation experiment correlation coefficients did not.

CHAPTER 5

CONCLUSIONS AND PROSPECTUS

5.1 CONCLUSIONS

Very good resolution four wire spanwise vorticity probe measurements have been made in equilibrium zero pressure gradient turbulent boundary layers over a Reynolds number range $1{,}010 \leq R_\theta \leq 4{,}850$. In Chapter 2 issues relating to the accuracy of these measurements were examined and discussed in detail. In Chapter 3 single point measurements were presented and interpreted in a context pertinent to both the active/inactive motions decomposition of Townsend (1961), and an interaction between the motions of the inner and outer regions. In Chapter 4 two point spanwise vorticity correlation results were presented and discussed in the context of an inner/outer interaction. In this chapter the results of the previous chapters are discussed in relation to the hypotheses presented in Chapter 1.

In Chapter 1 of this dissertation three hypotheses were introduced. These hypotheses are listed below.

Hypothesis #1: The optimal description/understanding of turbulence may be gained through the study of the vorticity field.

Hypothesis #2: At some distance away from the wall the local instantaneous vorticity distributions are predominantly no longer connected to the sheet-like distributions characteristic of the sublayer, but instead take the form of closed loops.

Hypothesis #3: The essential features of the interaction between the inner and outer region motions can be described in terms of the interaction between the reconnected and locally three dimensional vorticity distributions characteristic of the outer region, and the locally two dimensional (disturbed sheet-like) distributions that arise out of the sublayer.

Before proceeding on to a discussion of these hypotheses relevant to the results of this study, some preliminary statements need to be made. It is recognized that relatively few hypotheses about the nature of turbulent flows can be undeniably proven. Therefore, in the discussion below the results will often be posed in the context of being consistent or inconsistent (explicable or inexplicable) in relation to the given hypothesis. That is, do these hypotheses represent a useful and accurate model of physical reality.

5.1.1 Hypothesis #1

Clearly, a given study is not going to prove or disprove the first hypothesis above. In general however, numerous results from the present investigation support the notion that through the examination of vorticity data insights may be gained that are unattainable through velocity data alone. A specific example will serve as evidence.

Results in Chapter 3 provide important clarifications pertaining to the validity of Townsend's (1961) hypothesis. Recall that in this hypothesis Townsend decomposed the motions at any point into an active component responsible for the production and transport of the shear stress, and an inactive component that does not interact with the active component or produce/transport appreciable shear stress. Given the inner region universality of the logarithmic mean velocity profile, Townsend then hypothesized that the statistical properties of this active component (again in the inner region) are universal functions of τ and y. Following Hinze (1975), the association of equation 3.2 with this decomposition allowed for questions concerning the validity of this hypothesis to be addressed.

The present $\langle uv \rangle/u_\tau^2$ data (as well as that of Wei (1987) in a channel) exhibit a clear Reynolds number dependence for $y^+ > 15$. Townsend's hypothesis predicts that the statistical properties of the active component should exhibit a Reynolds number dependence consistent with this. The present $\nu\langle v\omega_z \rangle/u_\tau^3$ and $y\langle v\omega_z \rangle/u_\tau^2$ results very clearly indicate that this is not the case. Furthermore, examination of the $v\omega_z$ spectra indicated that the most energetic motions associated with $v\omega_z$ shift to lower frequencies under an inner variable normalization, and shift to higher frequencies under an outer variable normalization with increasing Reynolds number. These results indicate that the motions responsible for the transport of $\langle uv \rangle$ undergo either changes in scale and/or convection velocity with Reynolds number. If one assumes that vortical eddies are responsible for stress transport and production, then the present results indicating the near-wall universality of the statistical properties of the spanwise vorticity field (up to kurtosis) suggest that even though the average vortical content of these motions is invariant, their stress transport signatures are not. The observed Reynolds number dependence in the ω_z-ω_z correlations for probe separations normal to the wall suggest that this may be due to either changes in the average scale or orientation of these eddies in the x-y plane.

In support of Townsend's hypothesis and as might be expected, for the present flows the streamwise gradient terms associated with the inactive motions in equation 3.2 were found to be negligible. However, examination of the intensities of these gradients indicated that instantaneously these terms may be quite important. Furthermore, the ω_z-ω_z correlation results did not support the average existence of large scale motions in the inner region that contain spanwise vorticity. Also, the profiles of both of the inner-type non-dimensional functions, $\nu(v\omega_z)'/\langle uv\rangle^{3/2}$ and $y(v\omega_z)'/u_\tau^2$, showed good agreement across the inner region at the different Reynolds numbers. This result, coupled with the lack of agreement between the $\langle v\omega_z\rangle^+$ profiles, was interpreted to indicate that the organizational features of the motions responsible for stress transport are Reynolds number dependent. In relation to the normal stresses, both the $\nu\langle u\omega_z\rangle/u_\tau^3$ and $\nu(u\omega_z)'/u_\tau^3$ profiles provided evidence for inner region universality. Also, in general, the velocity vorticity correlation data suggest that Townsend's proposed scaling may become increasingly valid at higher Reynolds numbers.

The above results give an example of how the examination of vorticity data addressed questions posed through the examination of velocity data. In this instance, issues relating to the Reynolds number dependence of the Reynolds stress profile were approached though the examination of velocity vorticity correlation data relevant to the transport of the stress. As a corollary, it is also interesting to note that Wei (1987) hypothesized that the non-universality of the inner region velocity intensities and Reynolds stress profiles is due to a Reynolds number dependence in the creation of streamwise vorticity. The obvious means by which to address this hypothesis would also be through the examination of vorticity data. Given the limited spatial extent of coherent motions, descriptions in terms of vorticity appear to be optimal since the dynamics associated with vorticity transport are local in space.

5.1.2 Hypothesis #2

Several results provided direct evidence supporting the on average existence of approximately two dimensional sheet-like vorticity distributions very near the wall. As might be expected however, only indirect evidence (subject to interpretation) was provided supporting the existence of highly three dimensional reconnected vortical motions away from the wall. These results will now be summarized.

The two dimensional probability contour map of Figure 4.14 provided strong evidence indicating that instantaneously the vorticity vector at $y^+ = 7.5$ always has a spanwise vorticity component of the same sign as the mean vorticity vector. Furthermore, the simple analysis in Section 4.1 indicated that for $y^+ \leq 10$ the average instantaneous vorticity field is highly oriented in the spanwise direction. These two results are seen to provide direct evidence in favor of two dimensional sheet-like vorticity distributions existing near the wall. Furthermore, the trend in the ω_z-ω_z correlations for spanwise probe separations indicated a decrease in the scale of the correlation of about 36% as the distance from the wall increased from $y^+ = 6.7$ to about 34. This provides evidence supporting the hypothesis that, on average, regardless of the actual scale of the proposed two dimensional sheet-like vorticity distributions, in a relative sense they will always appear as such in comparison with the spanwise vorticity containing motions away from the wall.

The $S(\omega_z)$ profiles exhibited a distinct negative peak near $y^+ = 40$, and then decreased in magnitude for greater distances from the wall. The $R_\theta = 1,010$ $K(\omega_z)$ profile increased in magnitude with increasing distance from the wall out to near $y^+ = 40$, and then decreased for greater distances from the wall. However, the higher Reynolds number $K(\omega_z)$ profiles continued to increase out to $y^+ \cong 100$, and for greater distances from the wall showed only a slight decrease. These results, for $y^+ < 40$, were shown to be consistent with an average physical process in which negative spanwise vorticity containing motions arise from the sublayer. Given the evidence of previous studies, these are probably in the form of hairpin vortex-like and/or lifted vortex sheet-like motions.

The fact that the higher Reynolds number kurtosis profiles do not decrease for $y^+ > 40$ coupled with the rapidly decreasing significance of the mean vorticity for increasing y^+, provides evidence for the intermittent existence of positive spanwise vorticity containing motions in the near-wall region. Furthermore, direct evidence supporting the statistically significant presence of positive sign ω_z containing motions at $y^+ \cong 22$ was given in the two dimensional probability map of Figure 4.14.

The vorticity intensity results of Balint et al. (1987a) give strong evidence supporting the existence of highly three dimensional vortical motions away from the wall. The presence of positive spanwise vorticity containing motions in the inner region provides indirect evidence for the existence of reconnected vortical motions. This result is deduced from the fact that regardless of virtually any orientation that a vortex ring possesses in space, it will have both positive and negative spanwise vorticity containing sections. In contrast, very specific orientations of hairpin-like and/or vortex sheet-like motions are required (namely an inversion) in order for these motions to possess positive ω_z. Furthermore, the evidence of Falco (1974), (1977), (1983), (1987) also lends strong support for the existence of vortex ring-like motions in the inner region.

The evidence discussed above suggests that the lifting sublayer motions reach a maximum relative intensity at about $y^+ = 40$. Furthermore, the $<u\omega_z>$ data presented in Chapter 3 indicate that this average vortex force is essentially zero for $y^+ > 25$. Therefore, it is presently believed that by $y^+ \cong 50$ the lifted sublayer-type of motions begin to lose their coherence and/or evolve into a more (locally) three dimensional motions.

5.1.3 Hypothesis #3

The major conclusions concerning the third hypothesis come from the two point ω_z-ω_z correlation experiments. These are now summarized.

None of the correlations provided evidence for large scale ω_z containing motions in the wall region. Given that the inner/outer interaction involves spanwise vorticity containing motions, these motions must therefore be (on average) of small to intermediate scale. As discussed above, the correlations with spanwise probe separation decreased in scale with increasing distance from the wall. This result provides evidence that the vortical motions in the sublayer are relatively two dimensional in relation to the vortical motions above the wall. The magnitude of the correlations with probe separation normal to the wall (at $R_\theta = 1{,}010$) were relatively insensitive to the position of the stationary probe from the wall. This result is consistent with the notion of organized vortical motions of relatively the same scale convecting throughout the wall region. Analysis of the Δy correlation with the stationary probe at $y^+ = 7.5$ indicated the frequent occurrence of positive sign vorticity fluctuations of magnitude greater than the local mean vorticity at the upper probe ($y^+ \cong 22$) in combination with negative vorticity fluctuations at the lower probe. Given the above association of positive sign vorticity with the likelihood of ring-like motions, this result provides relatively strong but indirect evidence for the given hypothesis. Furthermore, this result is remarkably consistent with the numerous studies of Falco concerning the interaction of convecting vortex ring-like motions with the sublayer. The totality of these results support Willmarth's suggestion relating the observed sublayer structure with the presence and interaction with convecting small scale vortical motions.

In connection with the direct influence of sweeps (presumably originating in the outer region) on the motions near the wall, the $u\omega_z$ vortex force results predict that the size of any given lifted sublayer motion will be essentially the size of the high speed region above the sublayer. The importance of this plausible mechanism however, has yet to be fully determined.

5.2 PROSPECTUS

Extensive further study is necessary to fully verify the present hypotheses. Fortunately however, the utility of the existing data base has not been fully realized. Examination of the ω_z probability distributions as a function of distance from the wall should be able to locate the position in the boundary layer at which positive sign vorticity first appears. Furthermore, comparison of these p.d.f.s at different Reynolds number should shed further light on possible Reynolds number dependencies. Spanwise vorticity spectra are presently being examined. From the two point measurements, further analysis of the two dimensional p.d.f.s should go far in clarifying the statistical importance of particular ω_z-ω_z combinations. Specifically, it is of interest to determine whether the positive Δz correlation at $y^+ \cong 30$ has significant positive-positive ω_z contributions. Certain space-time correlations may also be of interest. Similar processing of the velocity and Reynolds stress data from the two point experiments should also yield important results. In order to gain a better understanding of the average instantaneous motions associated with, say, high Reynolds stress production, conditional sampling of both the single point and two point data has yet to be done.

The optimal verification of the given hypotheses however, would come from directly observing and quantifying the instantaneous vortical motions. To approximate this goal, numerous experiments combining two view flow visualization movies and two point spanwise vorticity measurements have been performed. In these experiments, which are similar to those of Falco (1974), Head and Bandyopadhyay (1981), Signor (1982) and Lovett (1982), the boundary layer is seeded at multiple locations with vaporized mineral oil. This oil vapor is then illuminated by a laser beam which has been split and spread into sheets perpendicular and parallel to the wall such that side and plan view slices of the boundary layer are visible. Also, in order to add increased depth of field to the plan view, overhead flood lighting was employed. Through the use of mirrors, high speed two view 35mm movies are then taken. Simultaneous with the movie and with the probes in its field of view, two point spanwise vorticity data are acquired[1]. Also in the field of view of the camera is a digital clock which is triggered by the data acquisition equipment, and thus allows the visual and hot-wire data to be correlated.

While the combined data from these experiments are just now being examined, some preliminary results purely based upon the visual data have been acquired. These results, which are pertinent to the nature of the motions lifting from the sublayer, are derived from a 15 second[2] realization (movie) at $R_\theta \cong 1{,}010$. In this movie, the laser sheet parallel to the wall is centered at $y^+ \cong 12$, and thus the plan view motions are most visible at this location.

The goal of this particular visual analysis was to gain information relating to the nature of the motions arising from the sublayer. To do this, specific features of the visualized motions were recorded. The following are a subset of these features.

- The maximum observed streamwise length of the lifted motion as measured from its intersection point with the sublayer

[1]The optimal overheat ratio for the operation of hot-wires in the oil fog environment has been previously determined, see Burkhardt (1982).
[2]This time corresponds to $797 u_\tau^2/\nu$.

- The acute angle the lifted motion makes with the wall when it has reached a position of $y^+ = 15$
- The position at which the head of the lifted motion is observed to start to roll-up

The total sample size of the preliminary visual data to be discussed is 27 events. Thus, on average, a lifting sublayer motion was observed about every 29.5 t^+.

Based upon their streamwise length and the angle they made with the wall, it became evident that two distinctly different motions arise from the sublayer. The most prevalent of these had an average maximum streamwise length of about $96x^+$ (maximum = $122x^+$, minimum = $50x^+$), and made an average acute angle with the wall of about 37 degrees (maximum = 48.9°, minimum = 28.5°). Of the 27 observations, 19 were of this type of motion. Thus on average this type of motion was observed every $42t^+$. It is worth noting that in 12 out of the 19 observations, apparent ring-like motions (in an orientation indicating that positive spanwise vorticity was brought near the wall) were seen to be above the lifted sublayer motions during some part of their development. The remaining 8 observed lifted motions had an average maximum streamwise extent of about $217x^+$ (maximum = $254x^+$, minimum = $188x^+$). These motions, which had an average frequency of occurrence of about once every $100t^+$, made an average acute angle with the wall of about 14.5 degrees (maximum = 19.7°, minimum = 11.5°). During the evolution of this type of motion, a pocket-like motion in the plan view or evidence of an initiation by or interaction with a ring-like motion was never observed. A distinct difference in the position at which the two types of motions began to roll-up was not observed. The overall average position at which both types of motions were seen to begin to roll-up was $y^+ \cong 32.7$ (maximum: $y^+ = 49.0$, minimum:

$y^+ = 16.9$). The sample size for this statistic was reduced to 22 since 5 of the higher angle events lost their coherence prior to roll-up.

Near the center of the side view portion of Figure 5.1a one can see an example of one the high angle lifted motions. This motion, which resembles a hairpin vortex, makes an acute angle of about 40 degrees with the wall. At this point in its evolution its head portion has rolled up and is centered between $y^+ = 35$ and 40. Above and slightly upstream of this motion one gets the hint of a vortex ring-like eddy. Further in the evolution of this hairpin-like motion (see Figure 5.1b), the ring-like motion can be more clearly seen. In the plan view and underneath the ring-like motion, one can also clearly see that marker has been moved away to form a pocket-type motion as described by Falco (1980).

Figure 5.2 shows an example of one of the less prevalent and larger scale low angle motions. The furthest downstream of these motions, of which there are apparently two, has just begun to roll-up at a y^+ position of about 30. By comparing this figure with Figure 5.1, the large difference in angles that the two types of lifted motions make with the wall is easily seen. Also note that, as with all of these types of motions observed, there is neither the presence of a ring-like motion in the side view or evidence of a pocket-type motion in the plan view. These motions have a striking resemblance to the lifted shear layer-like motions presented by Jimenez et al. (1988). For reference, the probes in Figures 5.1 and 5.2 are located a $y^+ = 7.6$ and 22.4.

These preliminary results are encouraging with respect to the validity of the hypotheses given in Chapter 1. The interaction represented by the visualization in Figure 5.1 lends credence to the notion of small scale convected vortices strongly interacting with the sublayer. Furthermore, the indicated average position at which the lifted motions begin to roll-up is consistent with the present interpretations of the higher order spanwise vorticity statistics. The presence of the large scale low angle lifting motions in Figure 5.2 probably indicates a different scale initiating mechanism than in Figure 5.1. In the context of the $u\omega_z$ vortex force, this may be due the direct influence of high speed fronts originating in the outer region. Also, in comparison with the computational interrogation of Jimenez et al. (1988) it is interesting to note that they found the larger scale low angle motions to be most prevalent. The evidence here does not support that finding. Clearly, further processing of these combined visual and hot-wire data should clarify many issues relating to the instantaneous motions in the boundary layer.

<u>TABLES</u>

Table 1.1 Summary information pertaining to the spatial resolution of wall-flow investigations cited in Section 1.4.

Studies(s)	Reynolds number	Probe type	Probe scale in viscous units: wire length	Probe scale in viscous units: wire spacing	R_θ/ℓ^+
Corrsin and Kistler (1954)	$R_\theta = 7{,}900$	ω_x	70	100	113
Kovasznay et al. (1962)	transitional	$\partial u/\partial y$	24	8	---
Kovasznay et al. (1970)	$R_\theta = 3{,}100$	$\partial u/\partial y$	25	40-60	124
Eckelmann et al. (1977)	$R_\theta \cong 400$	ω_y, ω_z	1.75	1.75	229
Kastrinakis (1977)	$R_\theta \cong 650$	ω_x	5	5	130
Willmarth and Bogar (1977)	$R_\theta = 11{,}700$	x-array	2.5	2.5	4,680
Falco (1980)	$R_\theta = 1{,}068$	ω_z	3.6	3.6	297
Kastrinakis and Eckelmann (1983)	$R_\theta \cong 1{,}200$	ω_x	9.1	11.5	132
Johnson and Eckelmann (1983)	$R_\theta \cong 400$	x-array	1.7	1.7	236
Willmarth and Sharma (1984)	$R_\theta = 9{,}840$	$\partial u/\partial y$	0.35	1.6	28,015
Balint et al. (1987a)	$R_\theta = 2{,}100$	9-wire probe	2.3	8.9	913
Present	$R_\theta = 1{,}010$	ω_z	1.95	1.95	518
	$R_\theta = 2{,}870$		4.76	4.76	603
	$R_\theta = 4{,}850$		7.82	7.82	620

Table 2.1 Principal characteristics of the zero pressure gradient boundary layers of the present study; f_c = low-pass cut-off frequency; f_s = sampling frequency.

R_θ	U_∞(m/s)	δ_{99}(mm)	θ(mm)	H	u_τ(m/s)	C_f	f_c(hz)	f_s(hz)
1,010	0.607	206	24.8	1.45	0.0282	0.00430	250	500
2,870	1.752	205	24.5	1.40	0.0707	0.00325	500	1,000
4,850	2.981	199	24.3	1.38	0.1125	0.00285	1,000	2,000

Table 2.2 Summary information concerning the wall-flow investigation data presented in Figure 2.8a,b. Note that R_θ indicates boundary layer flow, and $R_{d/2}$ indicates channel flow. Also note that the probe scale given is computed using the largest dimension necessary to measure (compute) v.

Studies(s)	S(v) at $y^+ \cong 20$	Reynolds number	Probe type	Probe scale in viscous units	Type of facility	Tunnel inlet contraction?	If a boundary layer flow does it develop along the tunnel wall?
Andreopoulos et al. (1984)	0.20	R_θ=3,624	temp. wake sensor	20.9	closed	yes	no
Gupta and Kaplan (1972)	0.23 0.50	R_θ=1,900 R_θ=6,500	x-array	2.8 10.8	open	yes	no
Present	0.18 0.10 0.20	R_θ=1,010 R_θ=2,870 R_θ=4,850	x-array	1.95 4.76 7.82	closed	no	yes
Balint et al. (1987a)	-0.40	R_θ=2,100	9-wire probe	8.9	closed	yes	yes
Barlow and Johnston (1985)	-0.25	R_θ=1,140	LDA	3.0	closed	yes	yes
Wei (1987)	-0.30 -0.05 0.13 0.69	$R_{d/2}$=2,970 $R_{d/2}$=14,914 $R_{d/2}$=22,776 $R_{d/2}$=39,580	LDA	0.66 2.76 3.94 6.43	closed	yes	---
Kreplin and Eckelmann (1979)	0.15	$R_{d/2}$=3,850	x-array	1.75	closed	no	---
Kastrinakis and Eckelmann (1983)	0.48	$R_{d/2}$=12,000	4-wire probe	11.5	open	yes	---
Kim et al. (1987)	-0.25	$R_{d/2}$=3,300	direct N. S. comp.	12.0	periodic boundary conditions	no	---

Table 2.3 Normalized spanwise vorticity probe dimensions; $\eta^+ = \eta u_\tau/\nu$; η_{min} and η_{max} refer to minimum and maximum measured Kolmogoroff scales found in each R_θ distribution (η estimated by using ϵ from equation 2.5). The individual wire length and x-array spacing are also equal to Δy.

R_θ	η^+_{min}	η^+_{max}	$\Delta y/\eta_{min}$	$\Delta y/\eta_{max}$	$\Delta z/\eta_{min}$	$\Delta z/\eta_{max}$
1,010	1.3	3.2	1.5	0.6	5.0	2.0
2,870	1.4	5.3	3.4	0.9	11.1	3.0
4,850	1.7	7.0	4.6	1.1	15.6	3.8

Table 2.4 Summary information concerning other wall-flow investigation data presented in Chapter 2 (except Figure 2.8a,b). Note that R_θ indicates boundary layer flow, and $R_{d/2}$ indicates channel flow. See Table 2.3 for information pertaining to the present probe dimensions.

Studies(s)	Figure(s) [2.*]	Symbol	Reynolds number	Probe type	Probe scale in viscous units
Ueda and	5,6,7	◫ △	R_θ=1,244	single	2.7
Hinze (1975)	5,6,7	◫	R_θ=4,248	wire	6.7
Andreopoulos	5,6	▽	R_θ=3,624	single	20.9
et al. (1984)	5,6	▽	R_θ=5,535	wire	33.4
Purtell et al.	5,6	✳	R_θ= 465	single	8.0
(1981)	5,6	✳	R_θ=1,340	wire	8.2
	5,6	✳	R_θ=1,840		10.9
	5,6	✳	R_θ=3,480		20.4
	5,6	✳	R_θ=5,100		29.9
Wallace et al. (1977)	7	✡	$R_{d/2}$=3,850	x-array	1.9
Johansson and	5	○	$R_{d/2}$=25,000	single	4,14,21,32
Alfredsson (1983)	6	○ ●	$R_{d/2}$=25,000	wire	14,32
Ligrani and Bradshaw (1987)	5	▼	R_θ=2,620	single wire	3.3,34
Wei (1987)	5,6	□	$R_{d/2}$=2,970	LDA	0.66
	5,6,18,19	□	$R_{d/2}$=14,914		2.76
	4,5	□	$R_{d/2}$=39,580		6.43
Balint et al. (1987a)	14,15,22	✡	R_θ=2,100	9-wire probe	9.5
Kim et al. (1987)	14	⌘	$R_{d/2}$=3,300	direct N. S. comp.	*

* $\Delta y^+_{min} \cong 0.05$, $\Delta y^+_{max} \cong 4.4$, $\Delta z^+ \cong 7.0$, $\Delta x^+ \cong 12.0$

Table 2.5 General criteria to ensure the convergence of statistics up to 4th order moments in boundary layer flows for the range $1{,}000 < R_\theta < 5{,}000$.

	average	r.m.s.	skewness	kurtosis
	to ensure ±3% accuracy	to ensure ±3% accuracy	to ensure ±5% accuracy	to ensure ±5% accuracy
velocity and velocity-velocity products	$1{,}000U_\infty/\delta$	$1{,}000U_\infty/\delta$	$4{,}000U_\infty/\delta$	$2{,}500U_\infty/\delta$
velocity gradients and vorticity	----	$1{,}000U_\infty/\delta$	$3{,}500U_\infty/\delta$	$2{,}000U_\infty/\delta$
velocity-vorticity products	$3{,}000U_\infty/\delta$	$1{,}000U_\infty/\delta$	$6{,}000U_\infty/\delta$	$5{,}000U_\infty/\delta$

Table 3.1 Summary information concerning other wall-flow investigation data presented and referenced in Chapter 3. Note that R_θ indicates boundary layer flow, and $R_{d/2}$ indicates channel flow. See Table 2.3 for information pertaining to the present probe dimensions.

Studies(s)	Figure(s) [3.*]	Symbol	Reynolds number	Probe type(s)	Probe scale in viscous units
Alfredsson et al. (1988)	6b,7b	△	$R_\theta \cong 2{,}800$	SWP	8.0
	1,6b,7b	▽	$R_{d/2}=3{,}850$	SFP	≅2.0
Andreopoulos et al. (1984)	2a,3,8	O	$R_\theta=3{,}624$	SWP	20.9
	6b,7b	O	$R_\theta=3{,}624$	TWS	≅20.9
Balint et al. (1987a)	13b,14,15	✡	$R_\theta=2{,}100$	9WP	9.5
Barlow and Johnston (1985)	6b,7b	●	$R_\theta=1{,}140$	LDA	$\Delta y^+ \cong 1.5$ $\Delta z^+ \cong 3.0$
Erm et al.(1985)	---		$617 \le R_\theta \le 5{,}010$	SWP	24-51
Gupta and Kaplan (1972)	8,11	⊡	$R_\theta=1{,}900$	XWP	3.9
	11	⊙	$R_\theta=6{,}500$	XWP	14.2
Kim et al. (1987)	6b,11,13b	⋊	$R_{d/2}=3{,}300$	DNS	*
Kreplin and Eckelmann (1979)	6b	⧖	$R_{d/2}=3{,}850$	SFP	≅2.0
Ligrani and Bradshaw (1987)	1,6b,7b	▼	$R_\theta=2{,}620$	SWP	3.3
Murlis et al. (1982)	---		$791 \le R_\theta \le 4{,}750$	XWP	25-30
Perry and Abell (1975)	---		$40{,}000 \le R_{d/2} \le 130{,}000$	XWP	36-140
Purtell et al. (1981)	1	✳	$R_\theta=1{,}340$	SWP	8.2
Spalart (1988)	13b	←	$300 \le R_\theta \le 1{,}410$	DNS	#
Wei (1987)	2b,5,11	△	$R_{d/2}=2{,}970$	LDA	0.66
	2b,3,5,6b,7b,9 11,12	□	$R_{d/2}=14{,}914$		2.76
	5	◊	$R_{d/2}=22{,}776$		3.94
	2b	◊	$R_{d/2}=39{,}580$		6.43

SWP: single wire probe, SFP: single film probe
XWP: x-wire probe, XFP: x-film probe
TWS: temperature wake sensor
LDA: laser Doppler anemometer
DNS: direct Navier-Stokes simulation
9WP: nine wire probe

* $\Delta y^+_{min} \cong 0.05$, $\Delta y^+_{max} \cong 4.4$, $\Delta z^+ \cong 7.0$, $\Delta x^+ \cong 12.0$

$\Delta z^+ \cong 6.7$, $\Delta x^+ \cong 20.0$, for Δy^+ information see Chapter 2.1

Table 4.1 Summary of two point ω_z-ω_z correlation experiments.

A: Experiments with probe separations in the direction normal to the wall.

Stationary Probe Positions

	Fig. 4.10	Fig. 4.11	Fig. 4.12	Fig 4.13
R_θ = 1,010	y^+=100.5	y^+=29.5	y^+=13.4	y^+=7.5
R_θ = 2,870	y^+=102.7	y^+=32.4	y^+=16.2	

B: Experiments with probe separations in the spanwise direction.

Stationary Probe Positions

	Fig. 4.15	Fig. 4.16	Fig. 4.17
R_θ = 1,010	$y^+\cong$33.5 (2)	y^+=15.3	y^+=6.7
R_θ = 2,870	y^+=33.6	y^+=20.4	

FIGURES

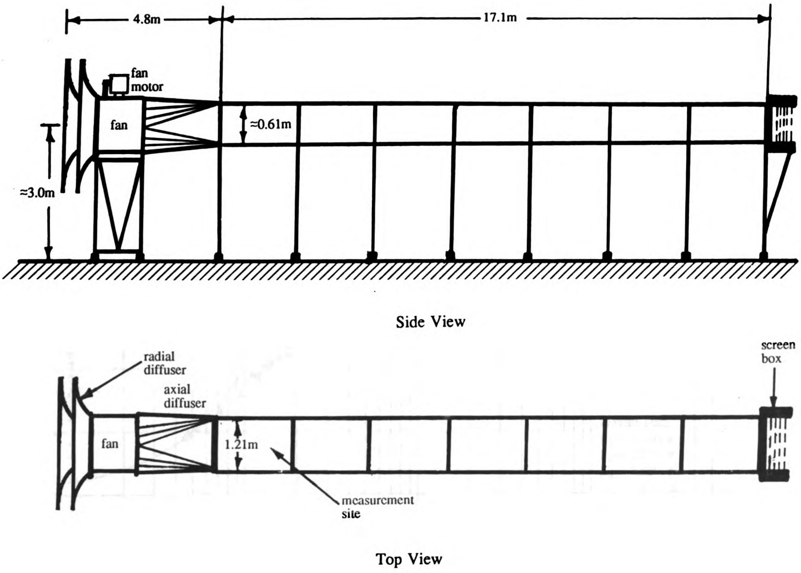

Figure 2.1 Schematic of the 17 meter low speed tunnel.

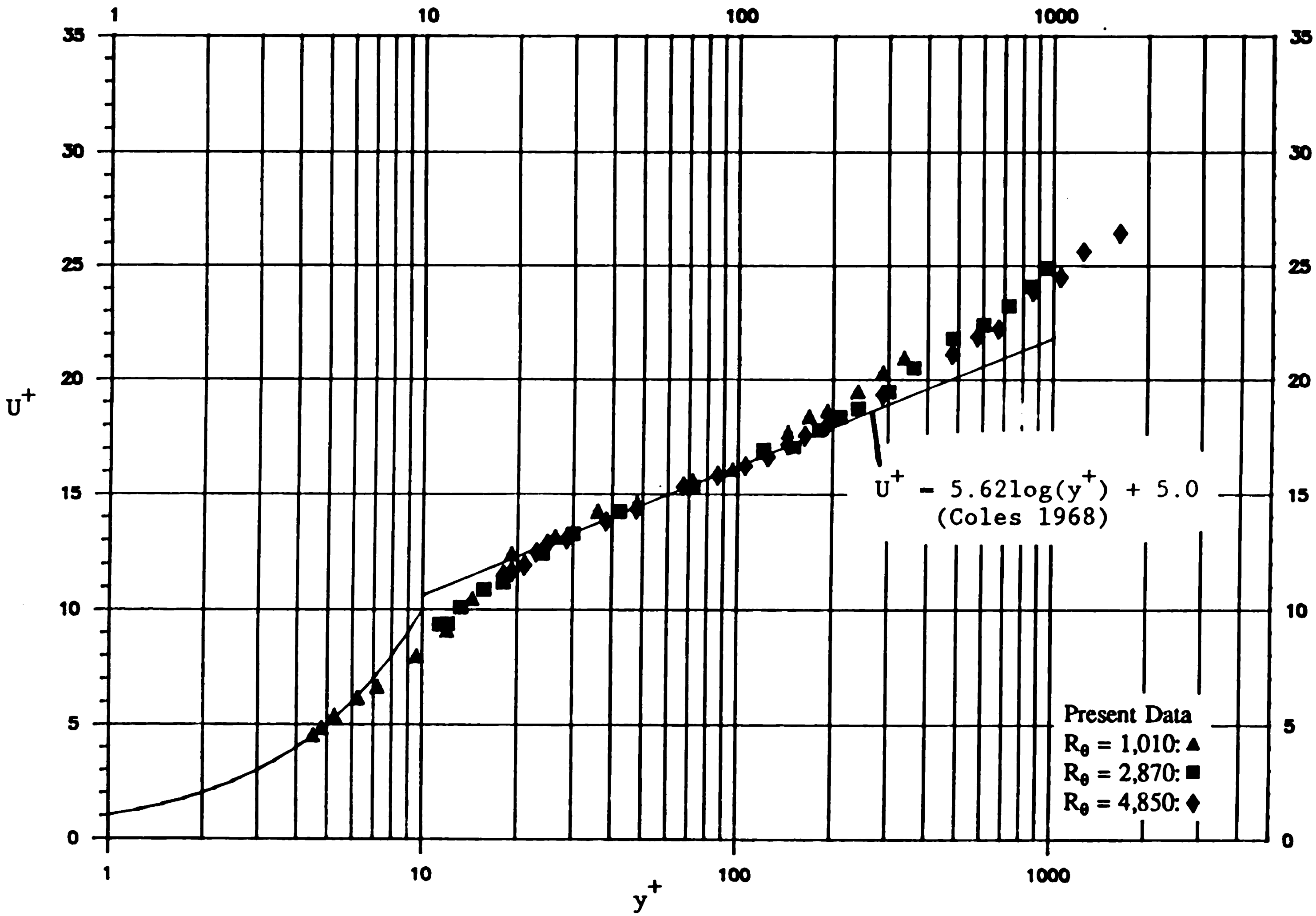

Figure 2.2 Logarithmic mean velocity profiles.

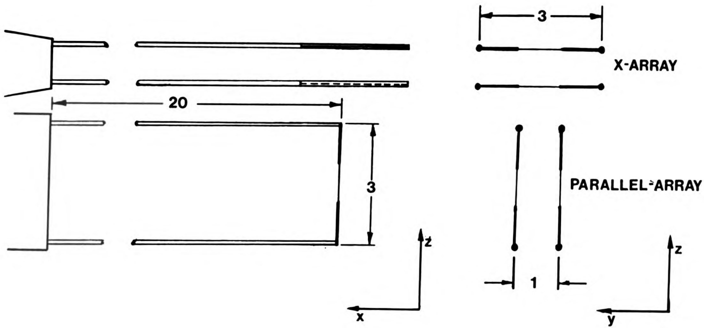

Figure 2.3 The spanwise vorticity probe.

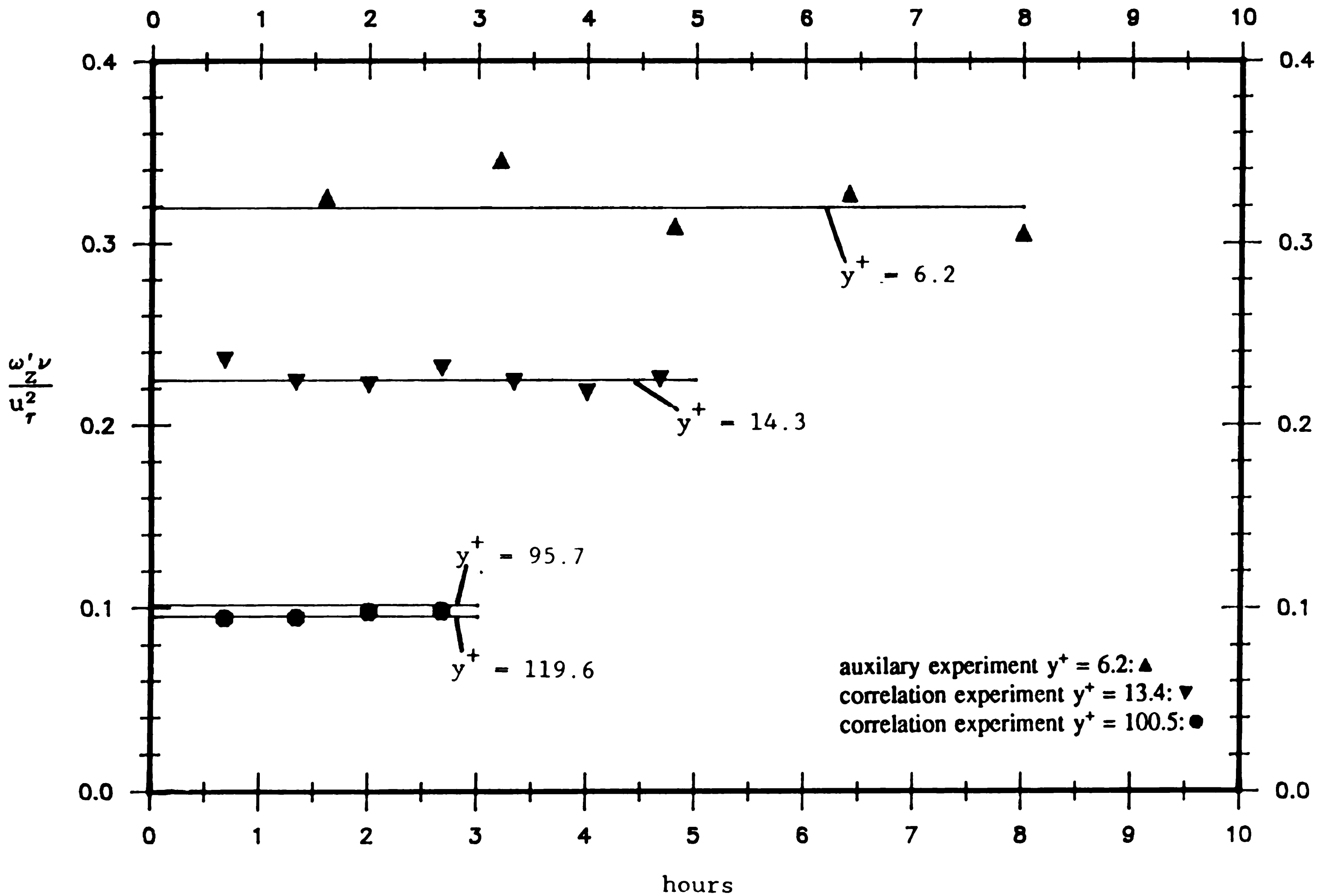

Figure 2.4 Measured $\omega_z'\nu/u_\tau^2$ values at different locations in the R_θ = 1,010 boundary layer as a function of experiment time. Solid lines represent values from the R_θ = 1,010 distribution of Figure 2.14 at the y^+ values indicated.

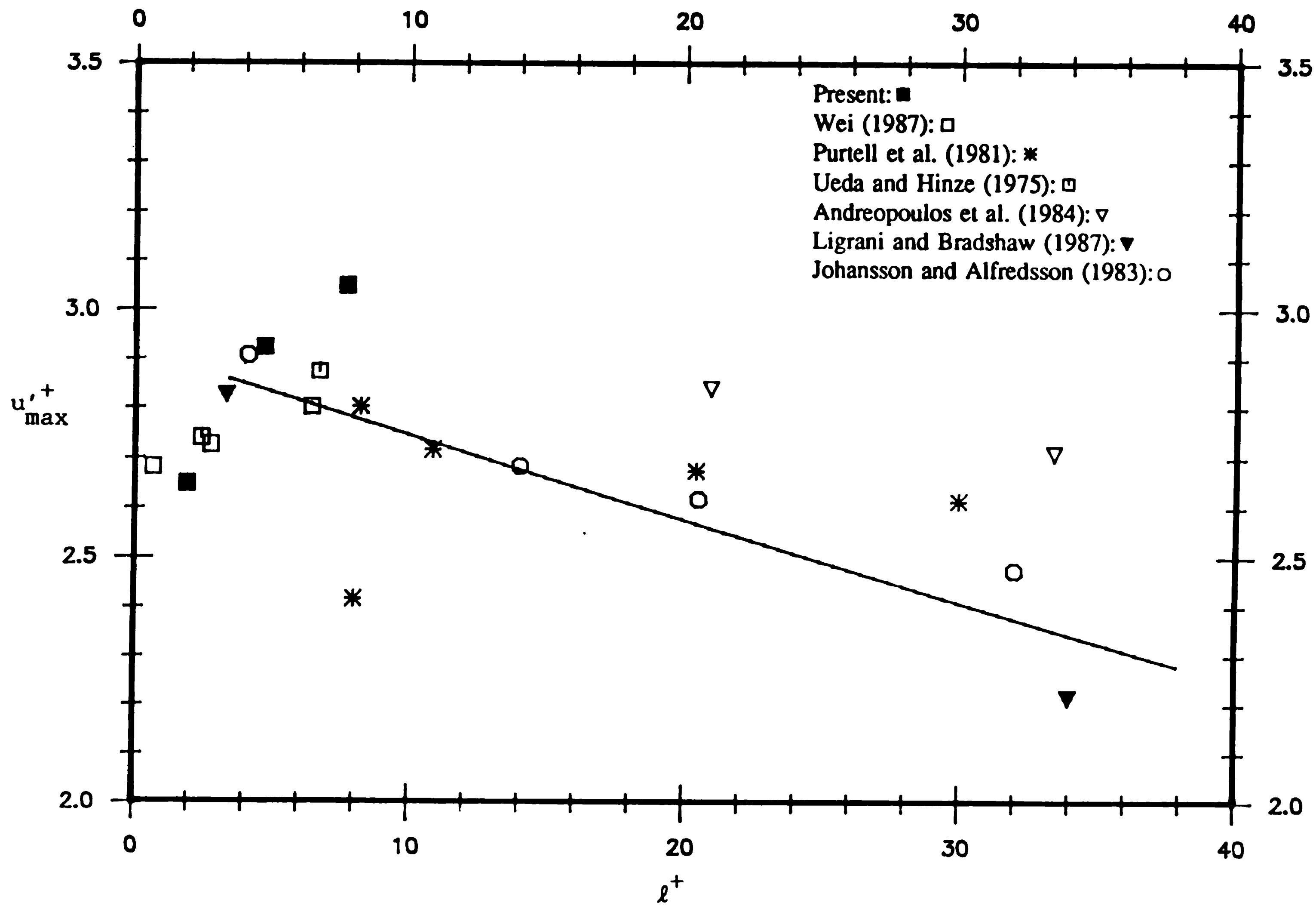

Figure 2.5 The maximum non-dimensional axial intensity as a function of sensor length in viscous units. The curve-fit of the Ligrani and Bradshaw, and Johansson and Alfredsson data is given by, $2.859 - 0.0175\ell^{+} + 0.0000175\ell^{+2}$, $3.3 \leq \ell^{+} \leq 34$. Note that a curve fit of the Johansson and Alfredsson data alone (not shown) is given by, $3.002 - 0.0253\ell^{+} + 0.00028\ell^{+2}$, $4 \leq \ell^{+} \leq 32$. Details pertaining to the other researcher's data are given in Table 2.4.

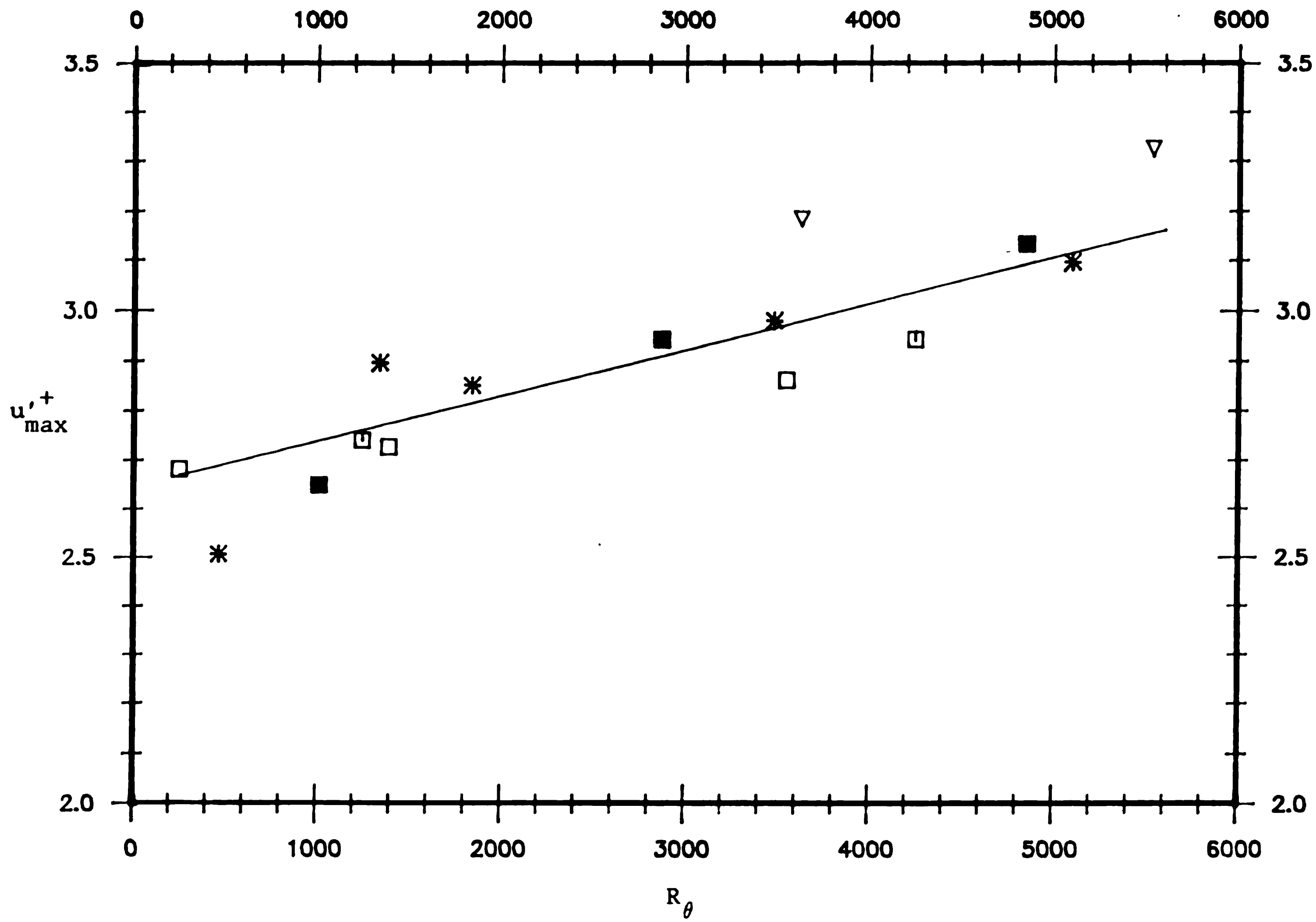

Figure 2.6 The maximum non-dimensional axial intensity as a function of R_θ. Symbols same as in Figure 2.5, and the solid line represents a linear least squares curve fit given by $(u'/u_\tau)_{max} = 2.616 + (0.000092)R_\theta$.

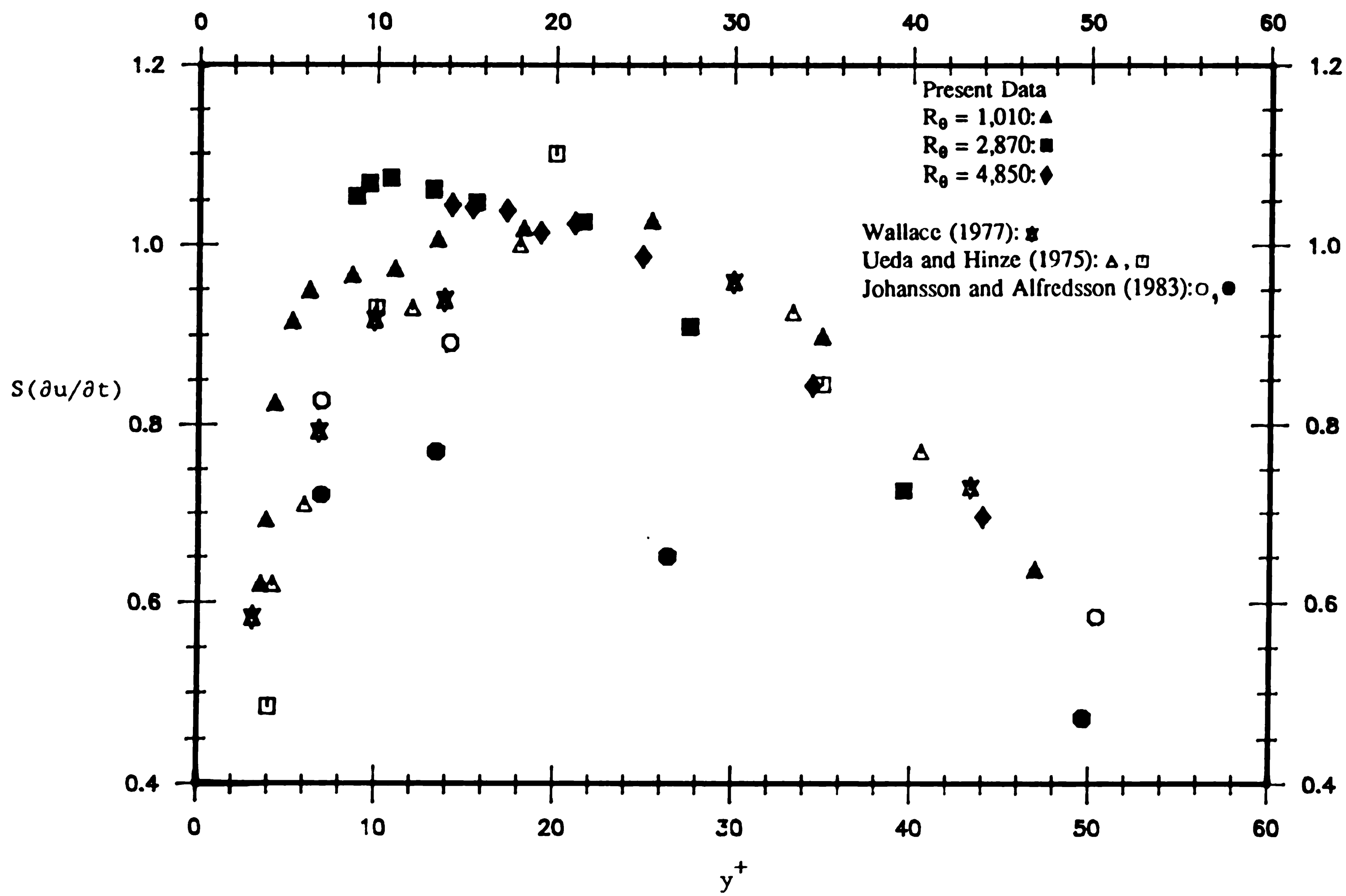

Figure 2.7 Near wall distributions of the skewness of $\partial u/\partial t$.
For probe scale information and Reynolds numbers of other researchers see Table 2.4.

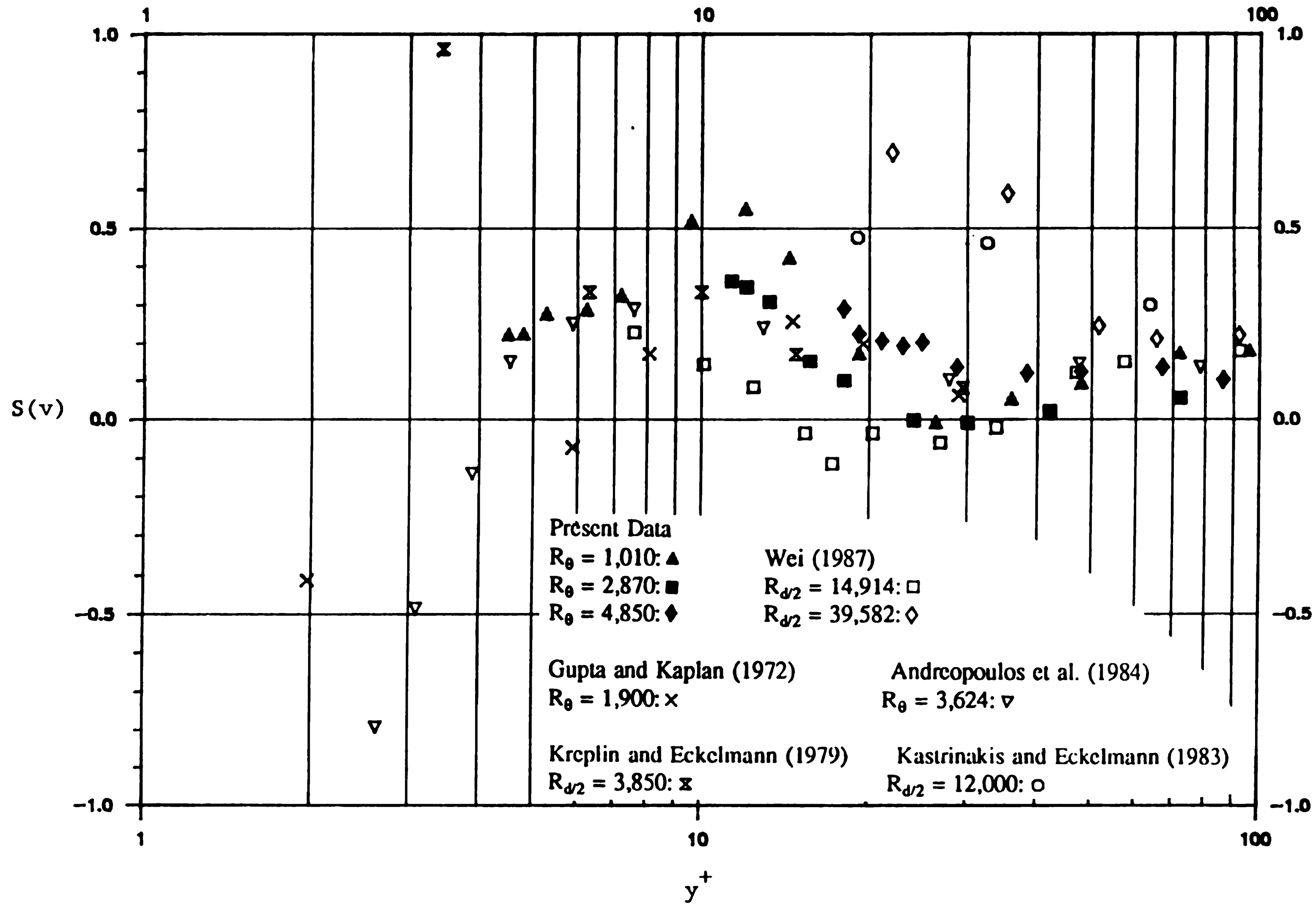

Figure 2.8 Near wall distributions of the skewness of the v component velocity fluctuations (also see Table 2.2).

a) Distributions which are positive in the range $5 \le y^+ \le 30$.

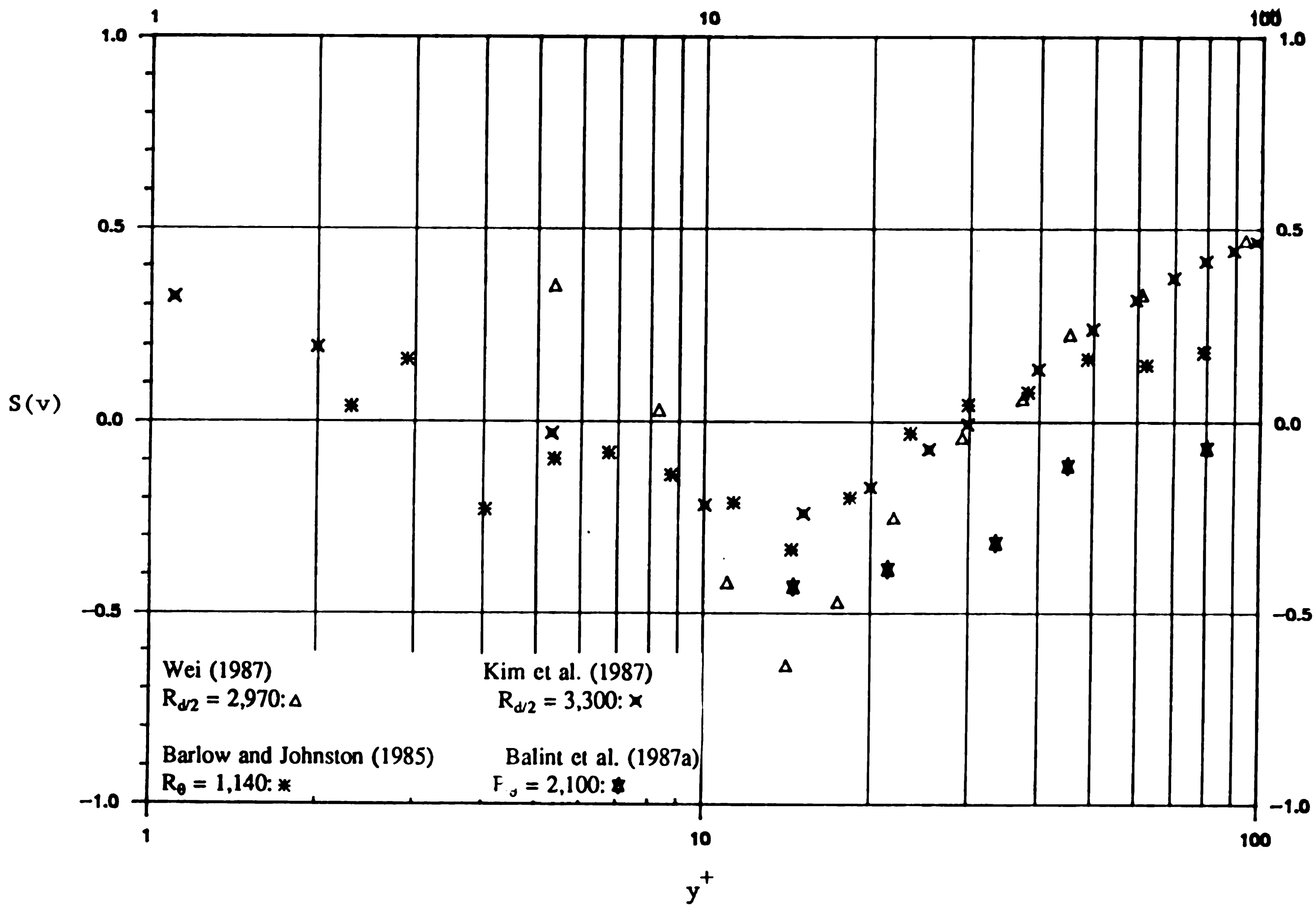

Figure 2.8 Near wall distributions of the skewness of the v component velocity fluctuations (also see Table 2.2).

b) Distributions which are negative in the range $5 \le y^+ \le 30$

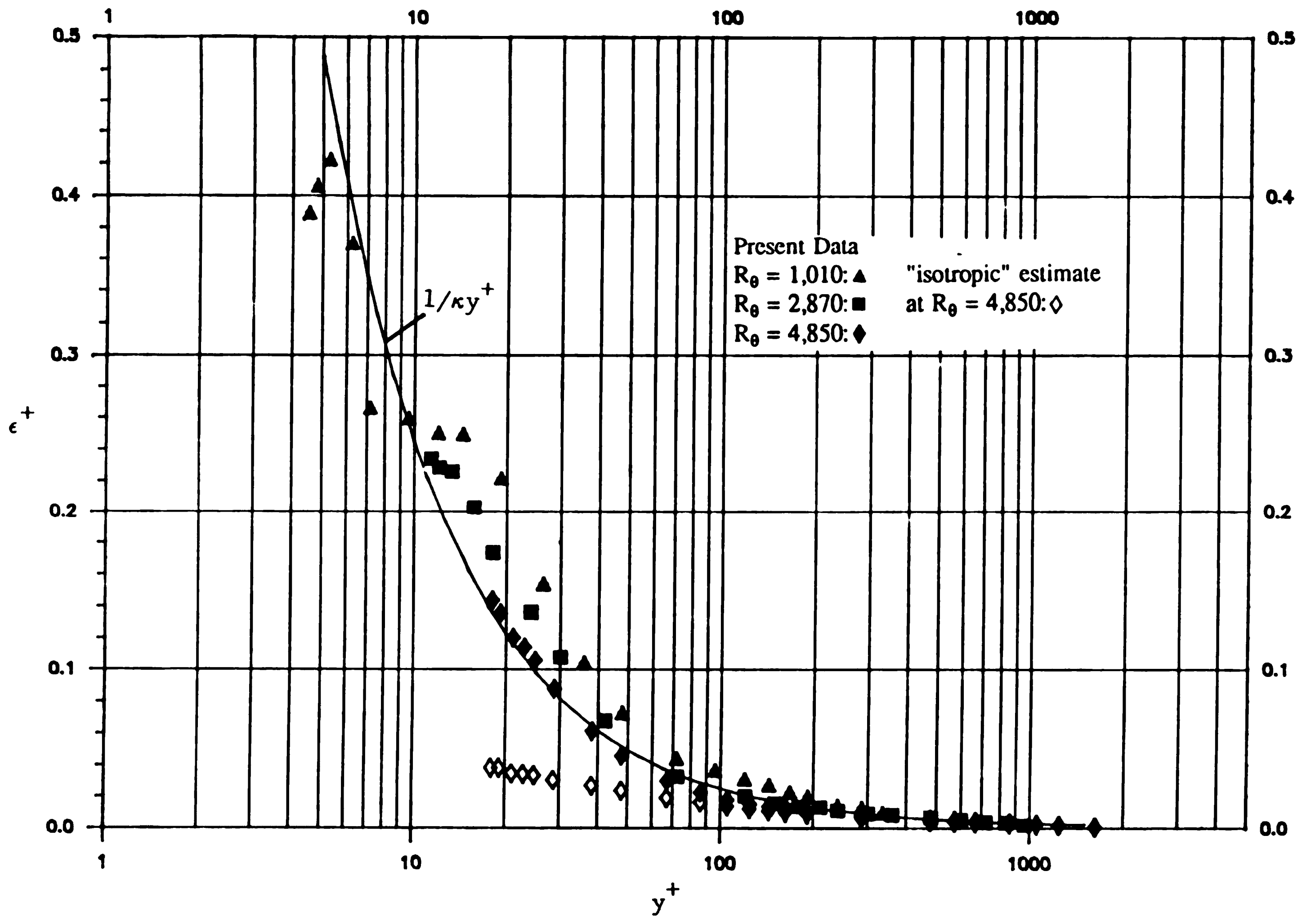

Figure 2.9 Present turbulent dissipation rate estimates as given by equation 2.5 and normalized by inner variables. The solid line = $1/\kappa y^+$, where $\kappa = 0.41$.

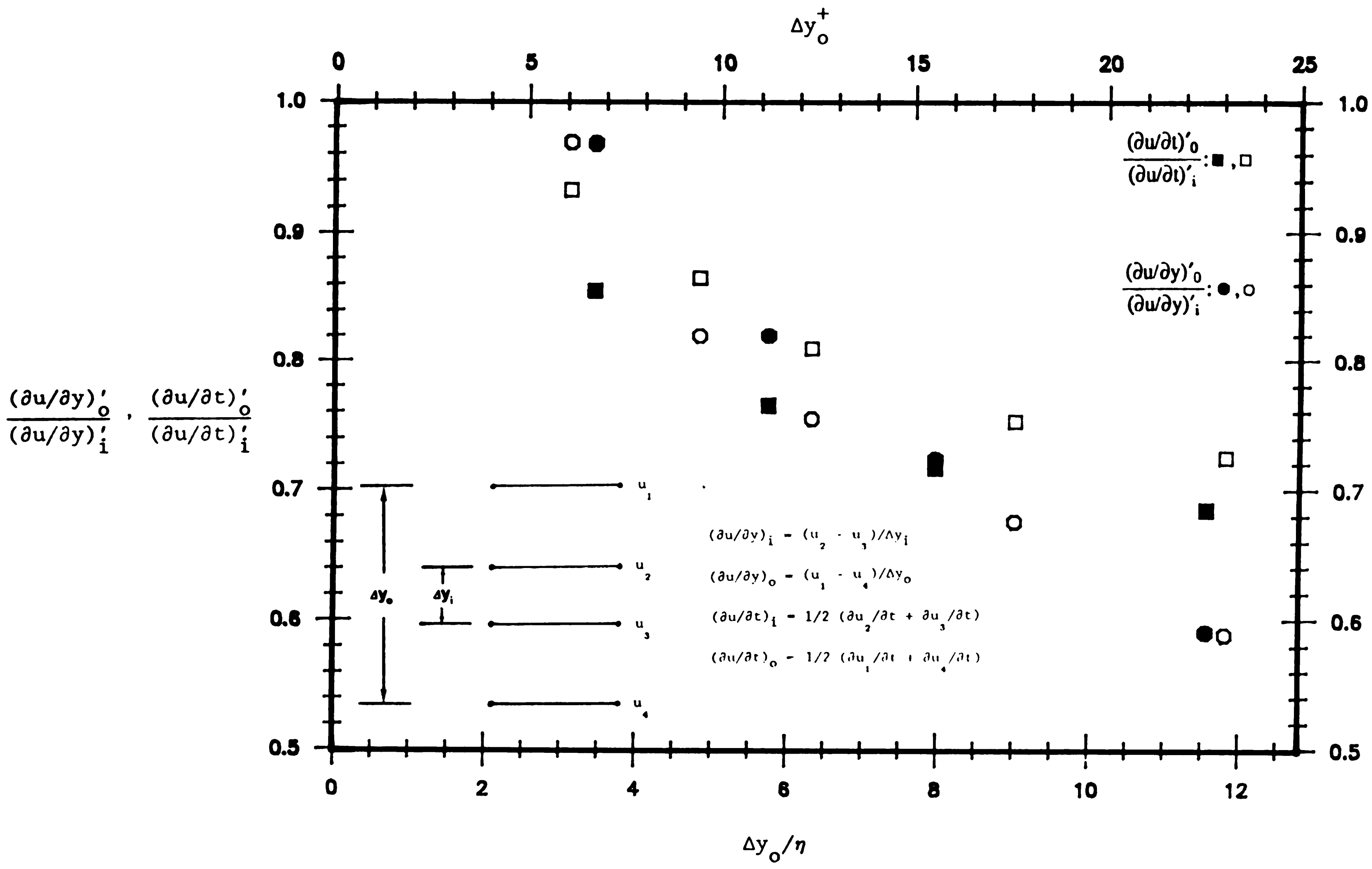

Figure 2.10 Attenuation of gradient intensity ratios as a function of the non-dimensional outer array wire separation (see insert) in the $R_\theta = 1,010$ boundary layer. Solid symbols give results at $y^+ \cong 38$. Open symbols give results at $y^+ \cong 53$.

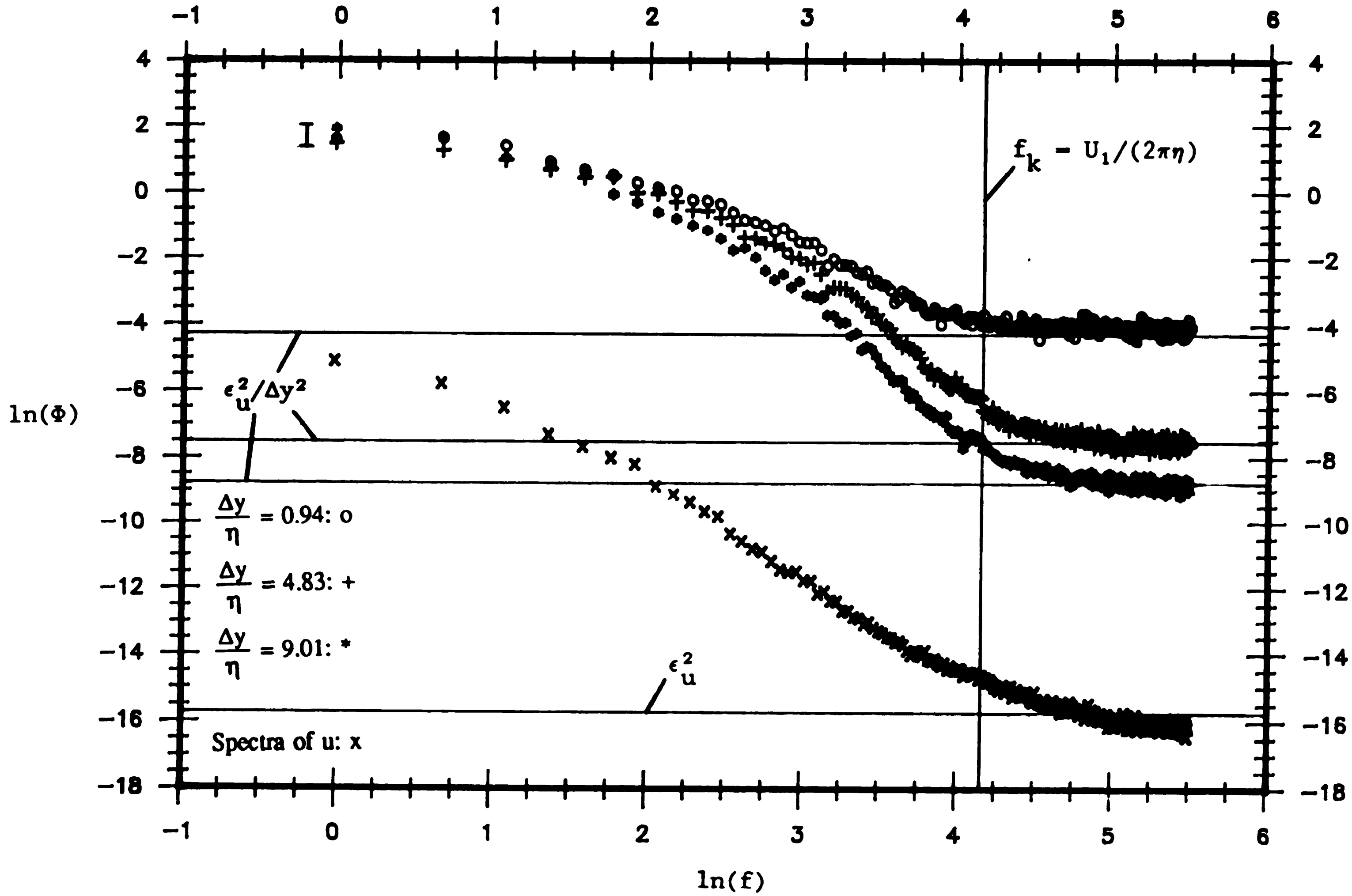

Figure 2.11 Frequency spectra of $\partial u/\partial y$ at $y^+ \cong 53$ in the $R_\theta = 1,010$ boundary layer for different Δy spacings. The horizontal lines through the $\partial u/\partial y$ spectra are the electronic noise levels as predicted by $\Phi(\partial u/\partial y) = \epsilon_u{}^2/\Delta y^2$, where $\epsilon_u{}^2$ is the energy level of the electric noise in $\Phi(u)$.

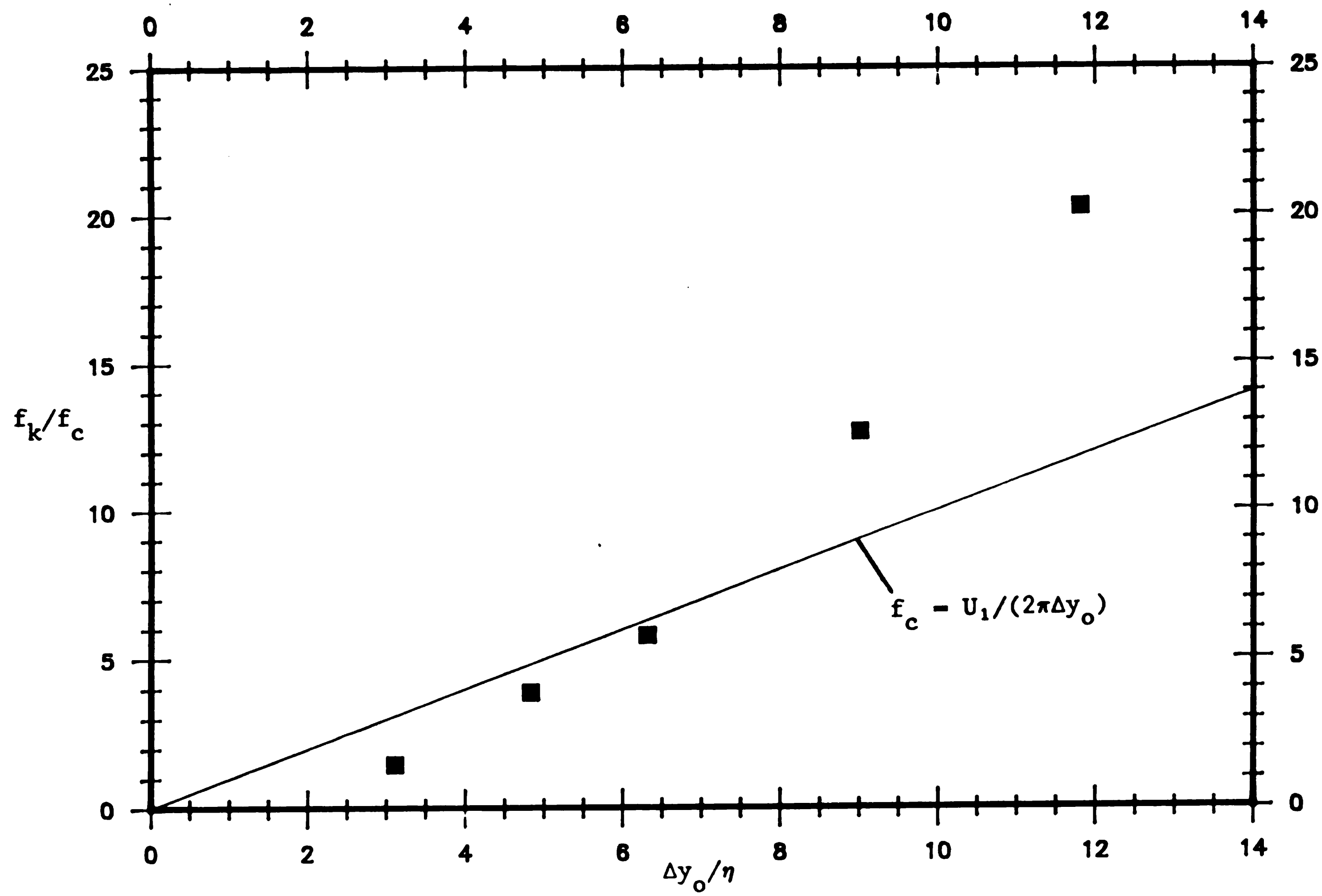

Figure 2.12 Approximate cut-off frequencies of $\Phi(\partial u/\partial y)$ due to the spatial filtering effect of finite wire separation (point of divergence with the $\Delta y/\eta = 0.94$ curve) as a function of non-dimensional wire spacing.

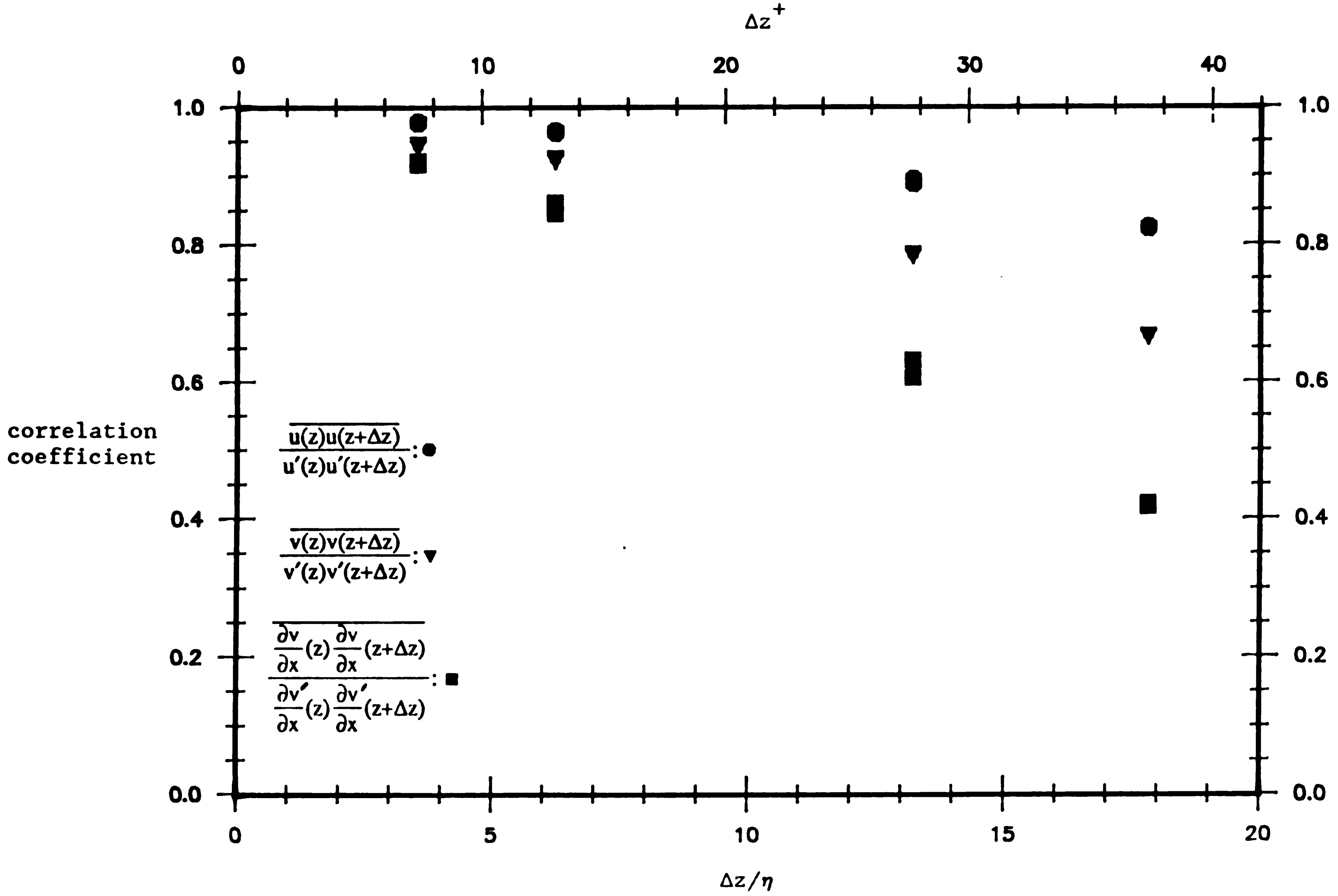

Figure 2.13 Correlation coefficients of u, v, and $\partial v/\partial x$ as a function of spanwise separation at $y^+ \cong 140$ in the $R_\theta = 1{,}010$ boundary layer.

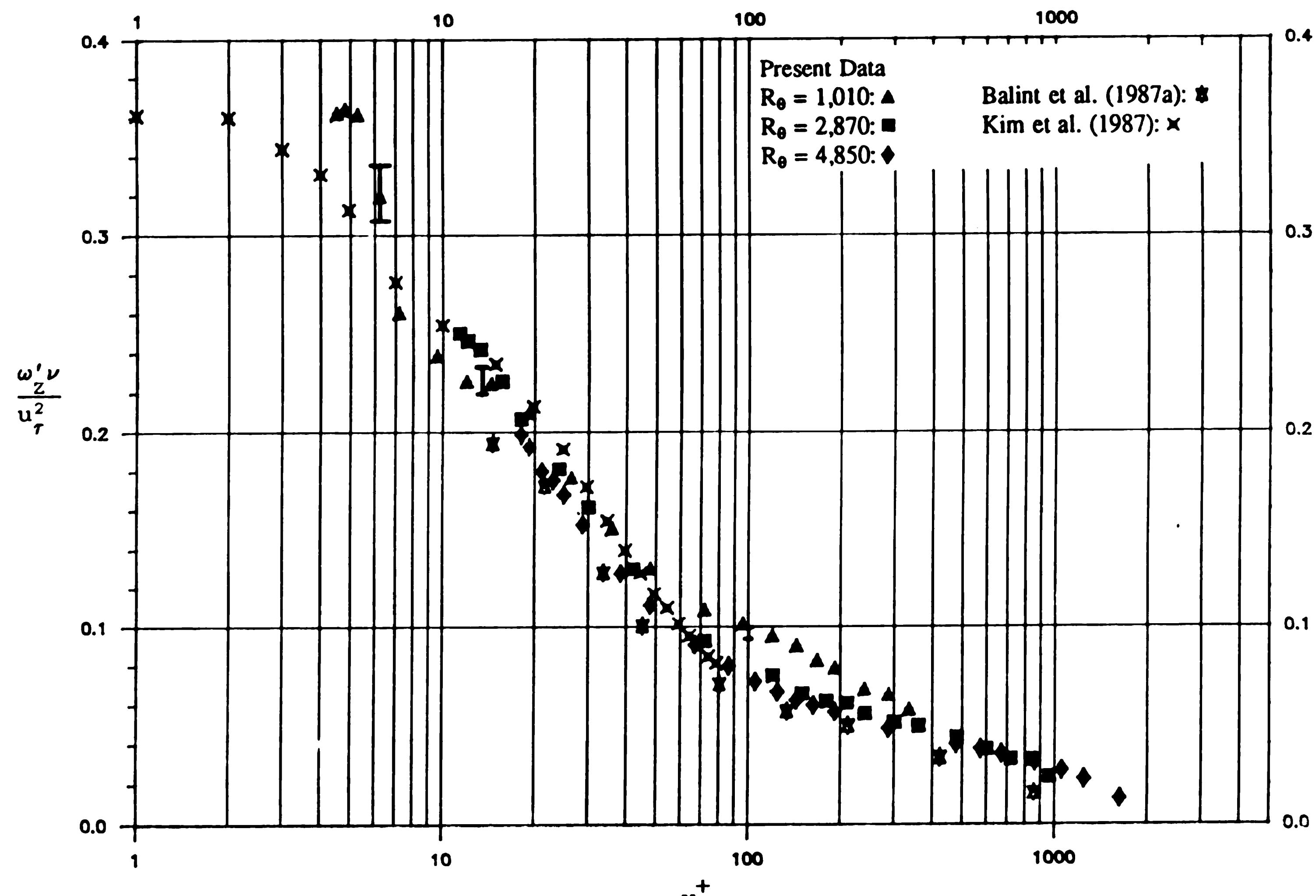

Figure 2.14 Inner variable non-dimensionalization of the rms spanwise vorticity distribution. The error bars at $y^+ = 6.2$, 13.4 and 100.5 are derived from the data of Figure 2.4.

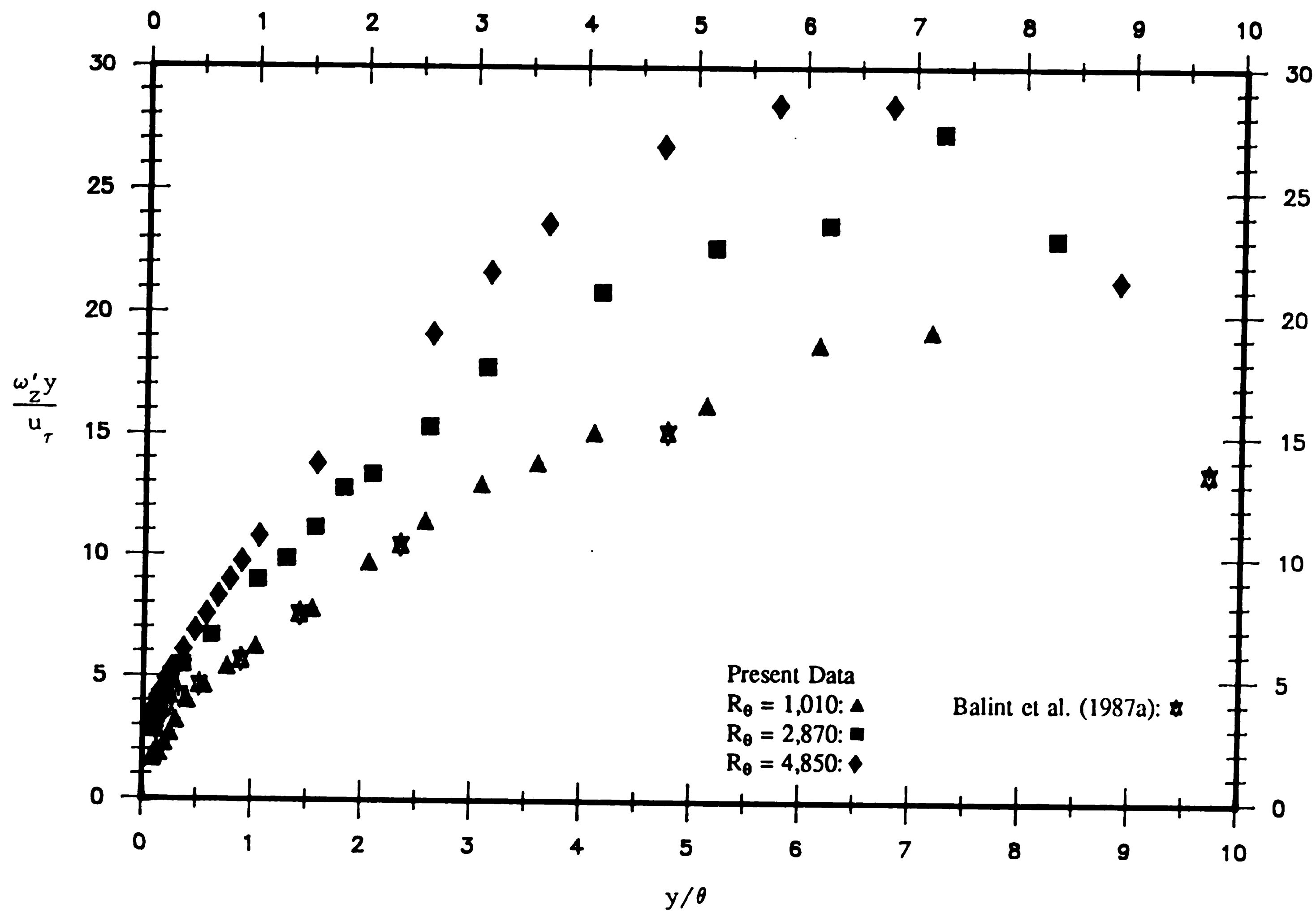

Figure 2.15 The r.m.s. spanwise vorticity distribution normalized by the function y/u_τ and plotted versus y/θ.

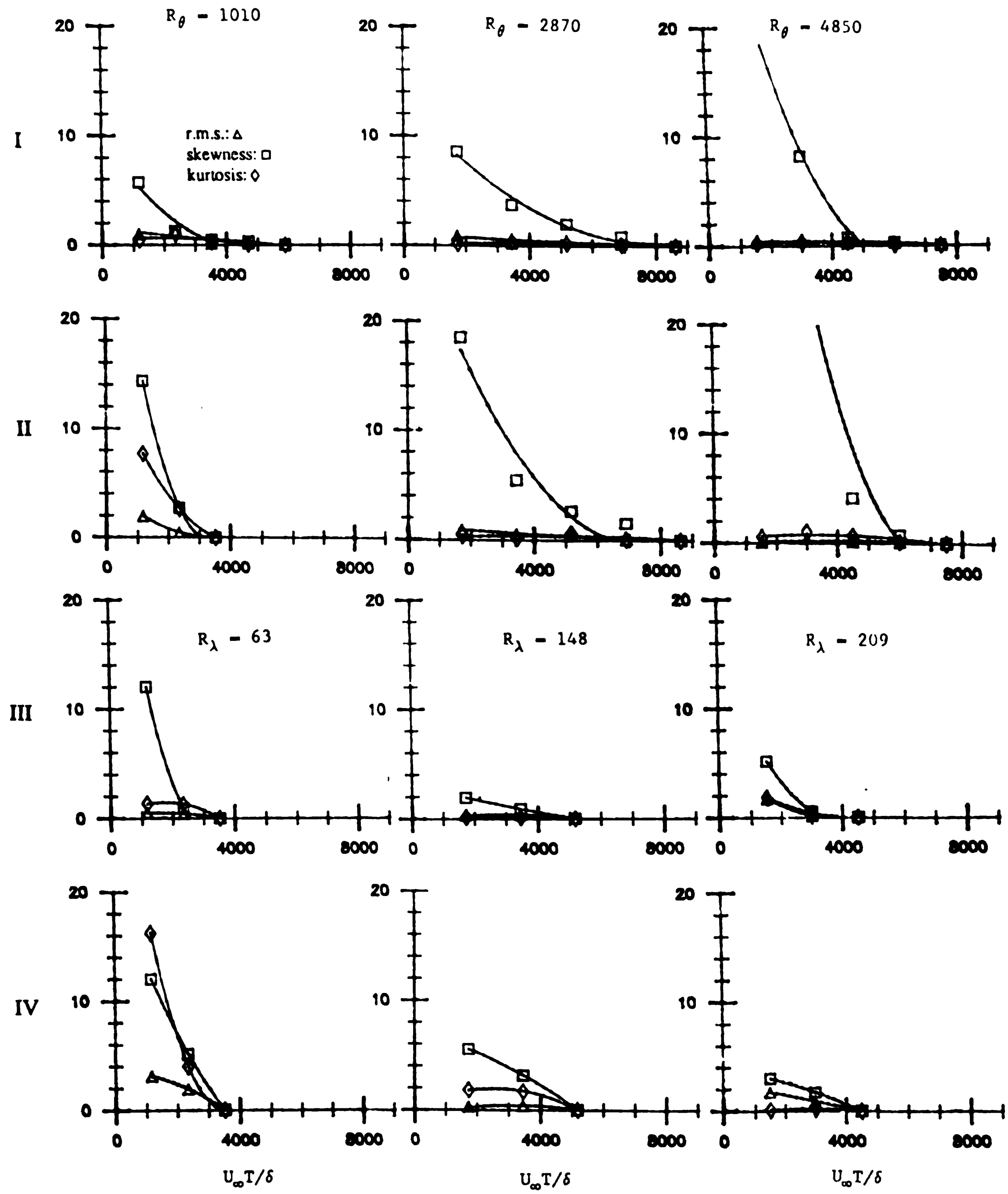

Figure 2.16 Convergence data for the u velocity statistics.

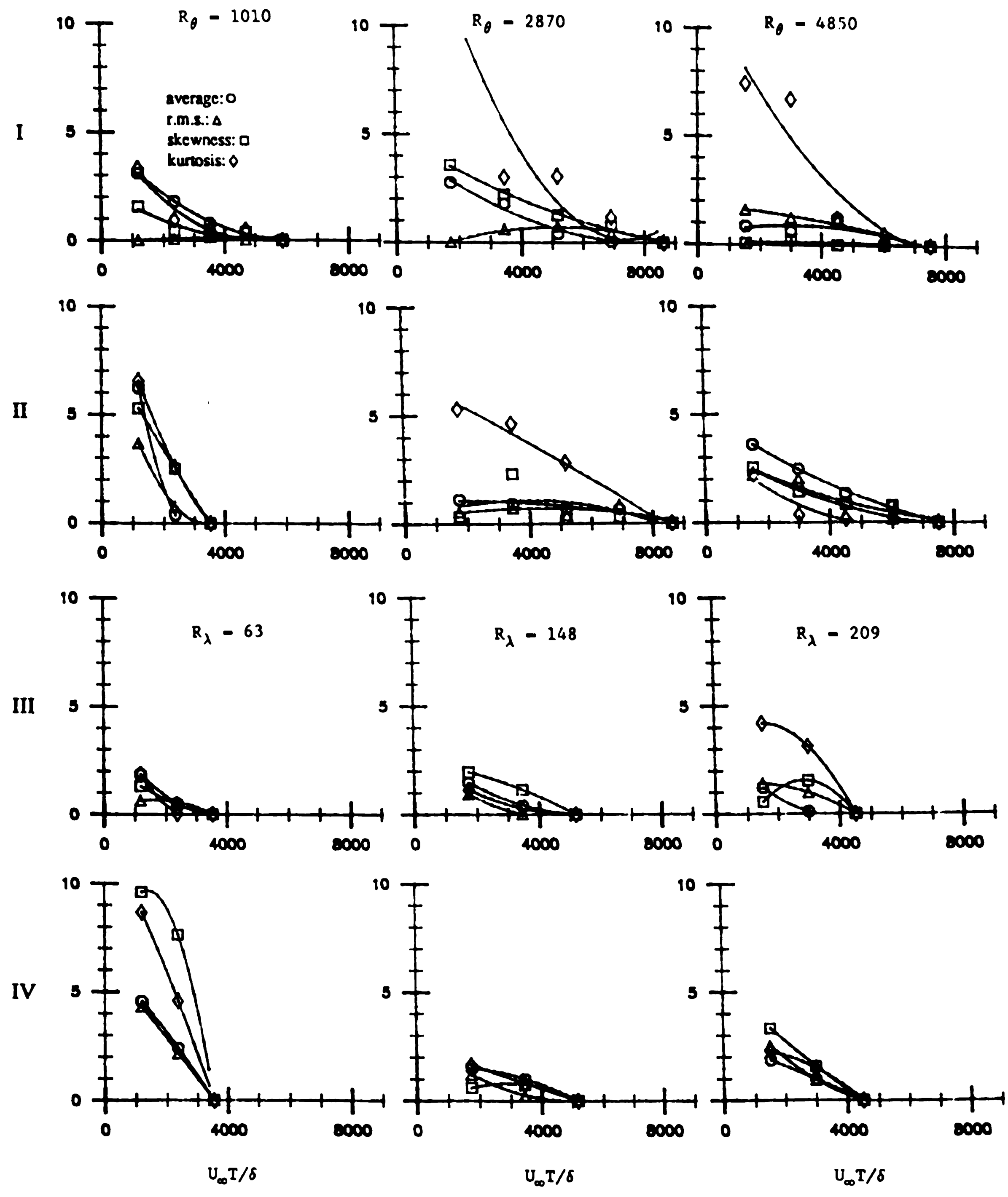

Figure 2.17 Convergence data for the uv statistics.

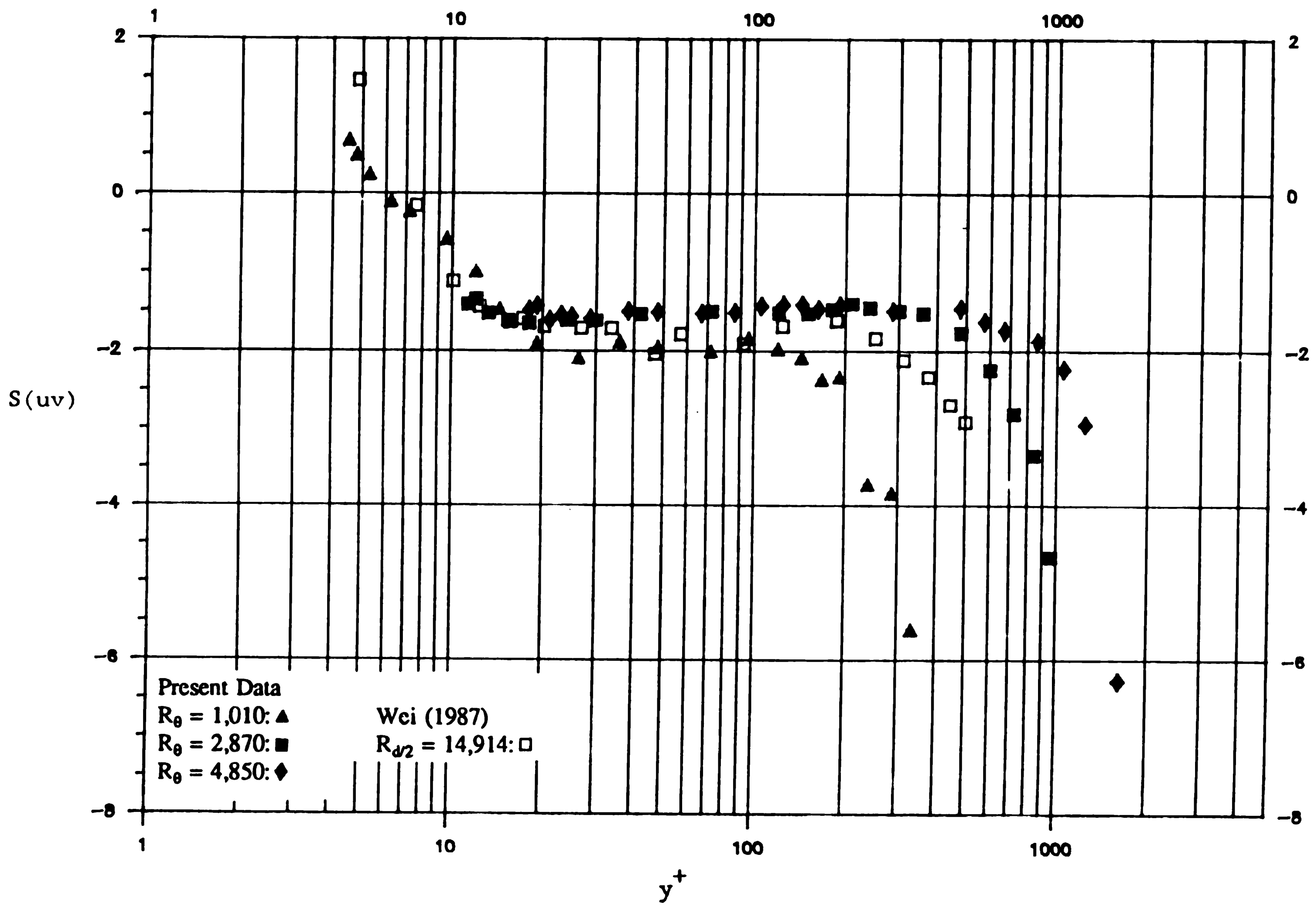

Figure 2.18 Skewness of uv distributions vs y^+.

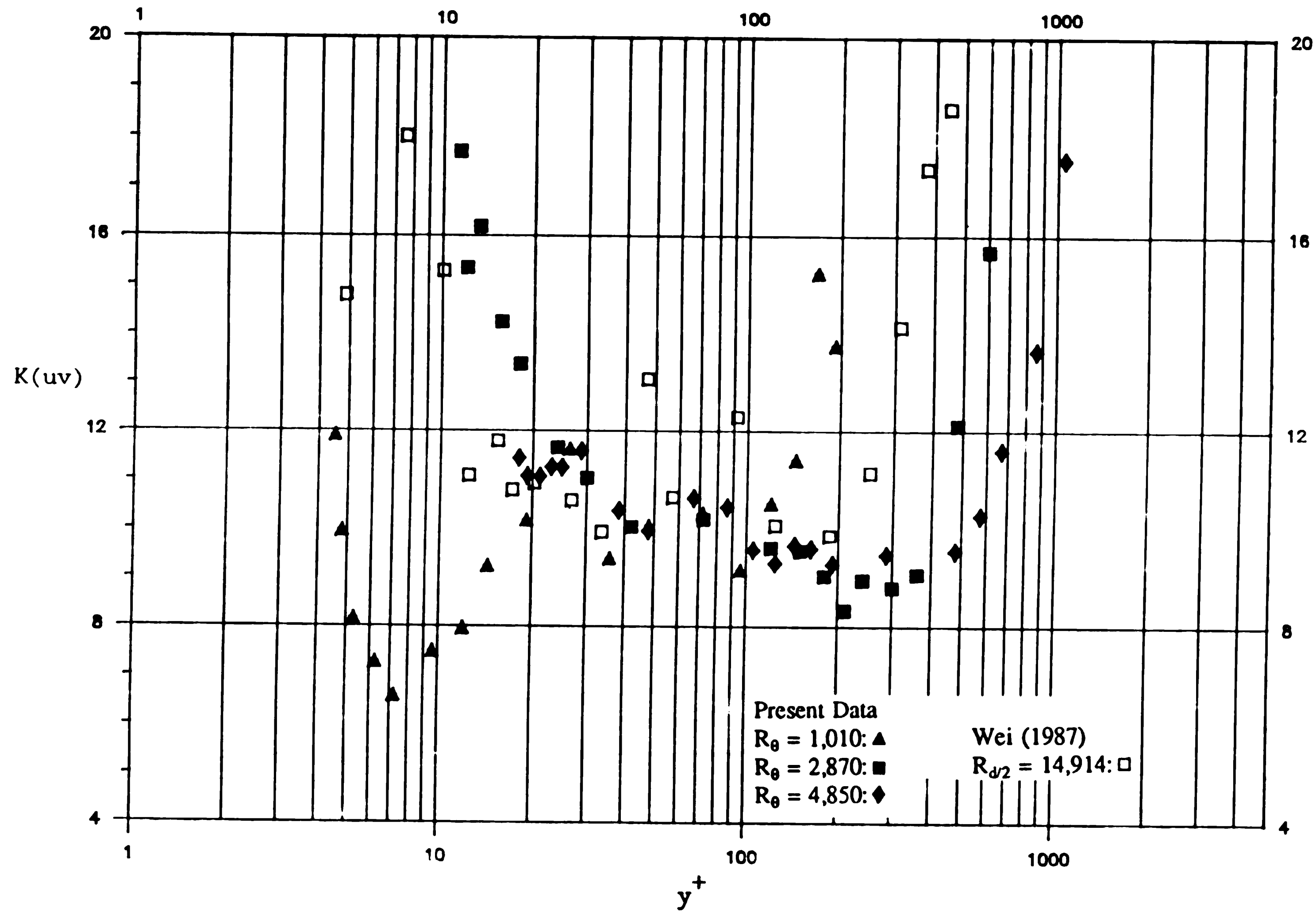

Figure 2.19 Kurtosis of uv distributions vs y^+.

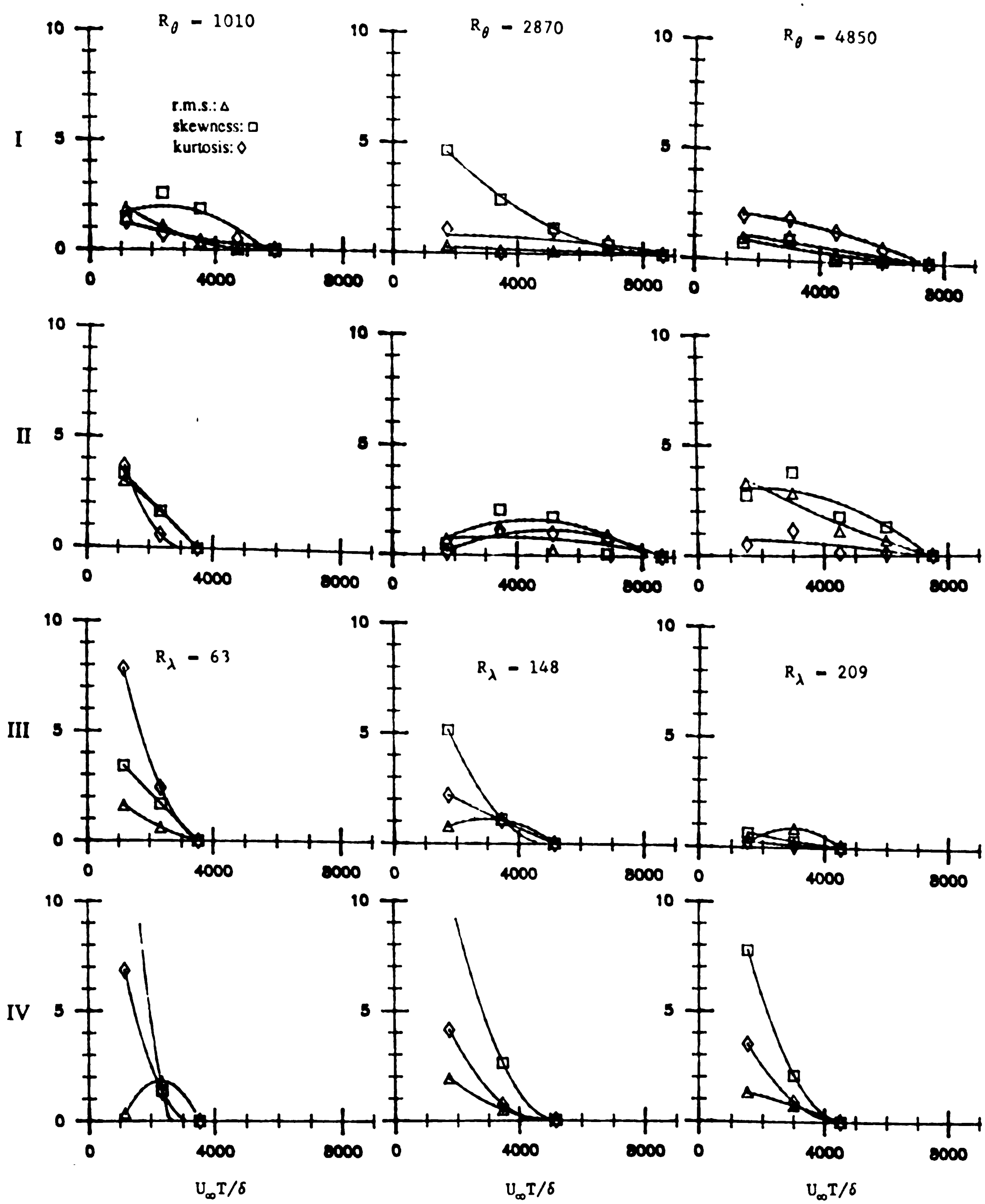

Figure 2.20 Convergence data for the $\partial u/\partial t$ statistics.

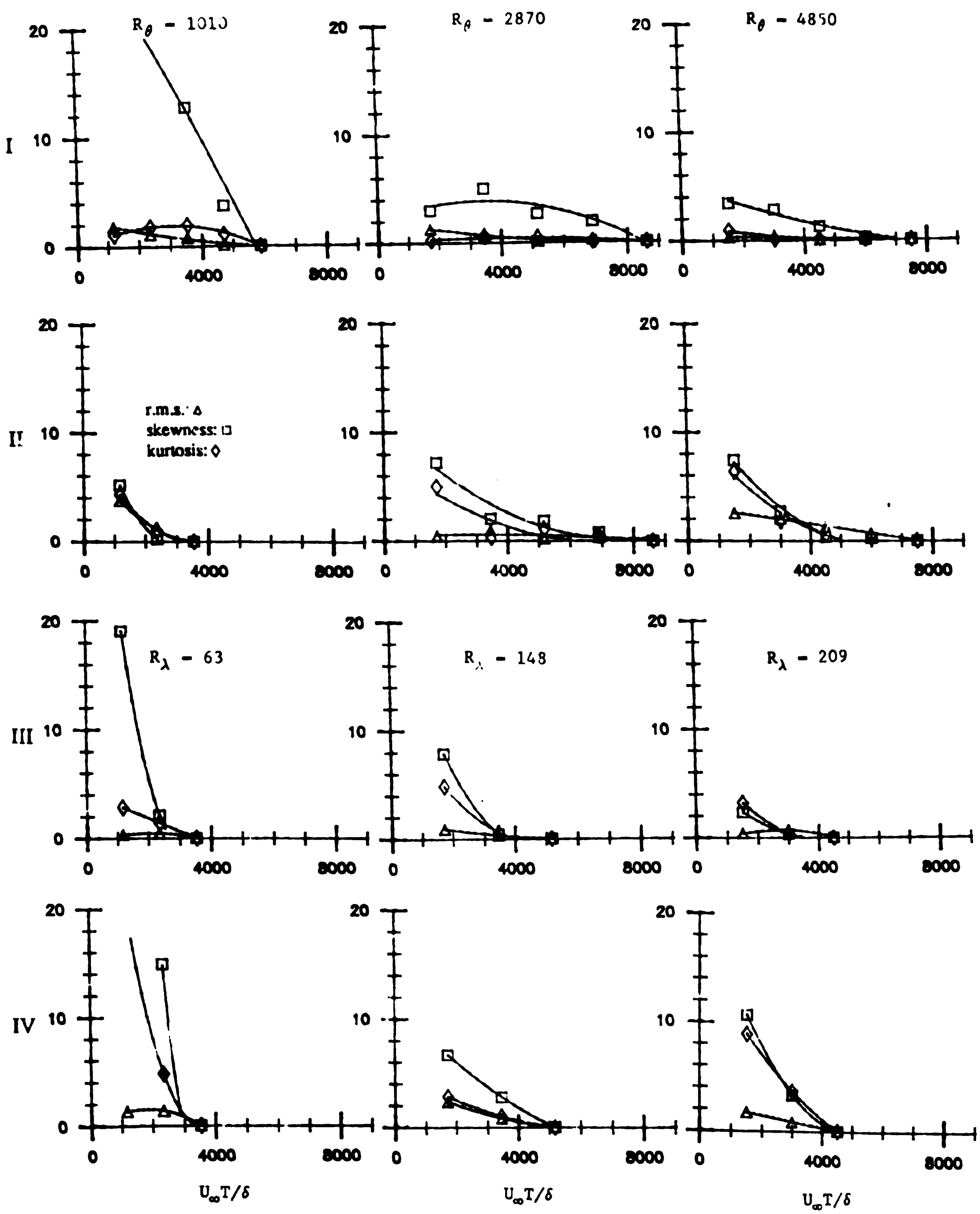

Figure 2.21 Convergence data for the ω_z statistics.

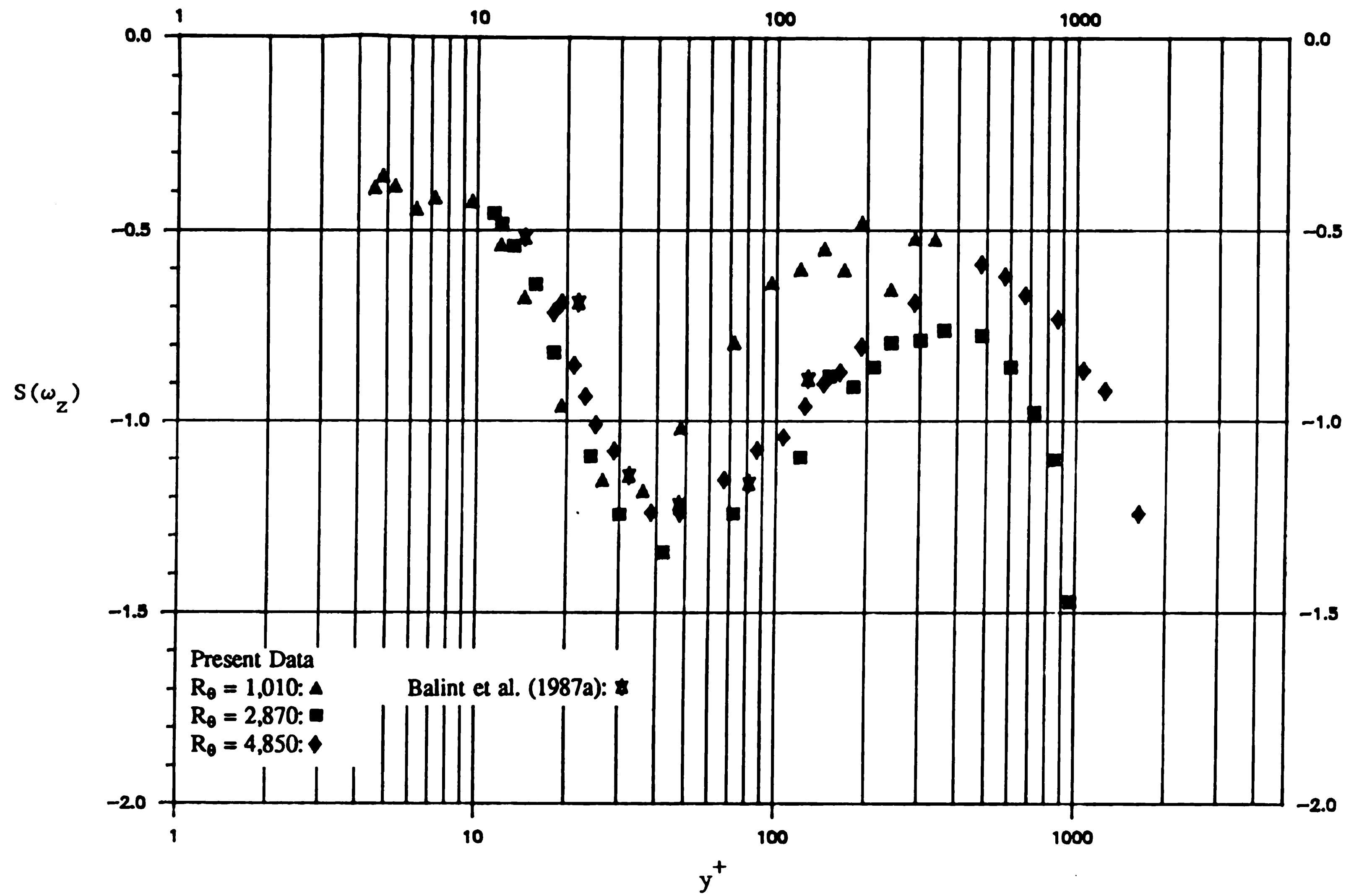

Figure 2.22 Skewness of ω_z distributions vs y^+.

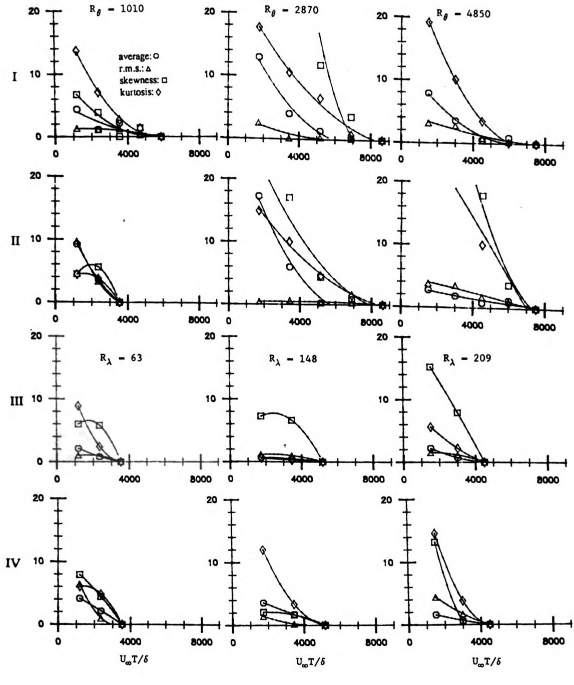

Figure 2.23 Convergence data for the $v\omega_z$ statistics.


1
10
100
1000
3.5

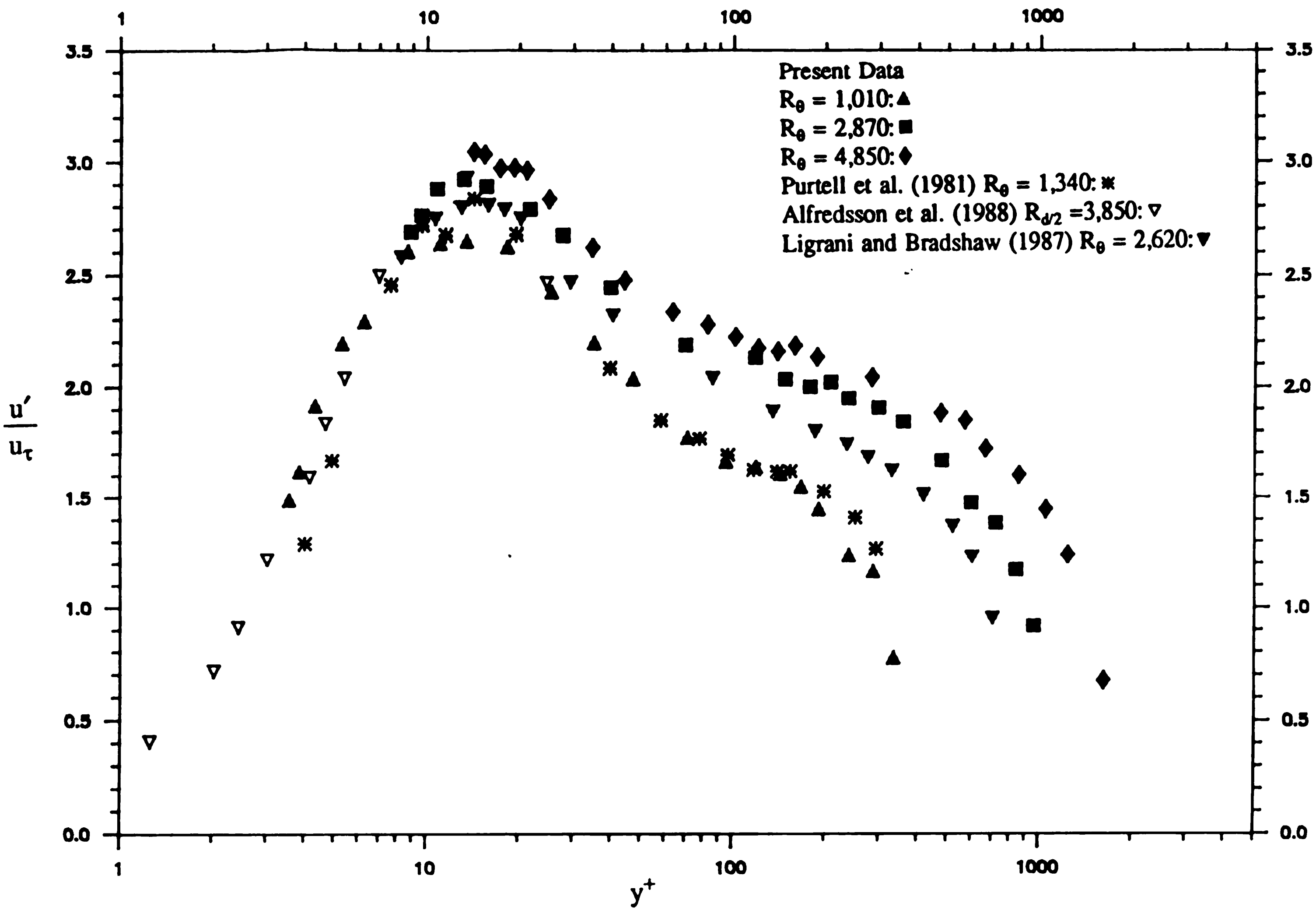

Figure 3.1 Inner variable normalized streamwise intensity profiles.

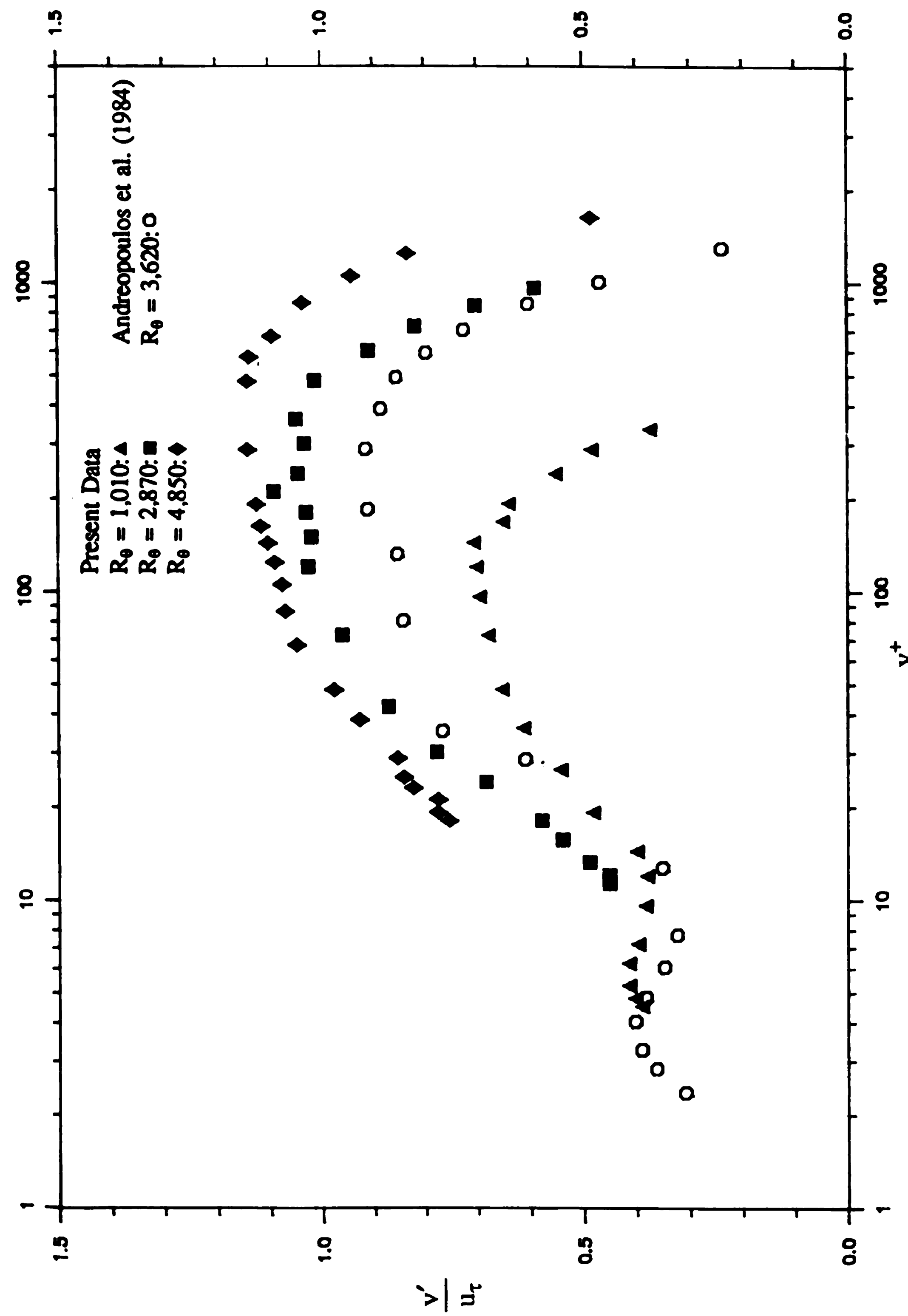

Figure 3.2 Inner variable normalized normal intensity profiles.
a) Present data.

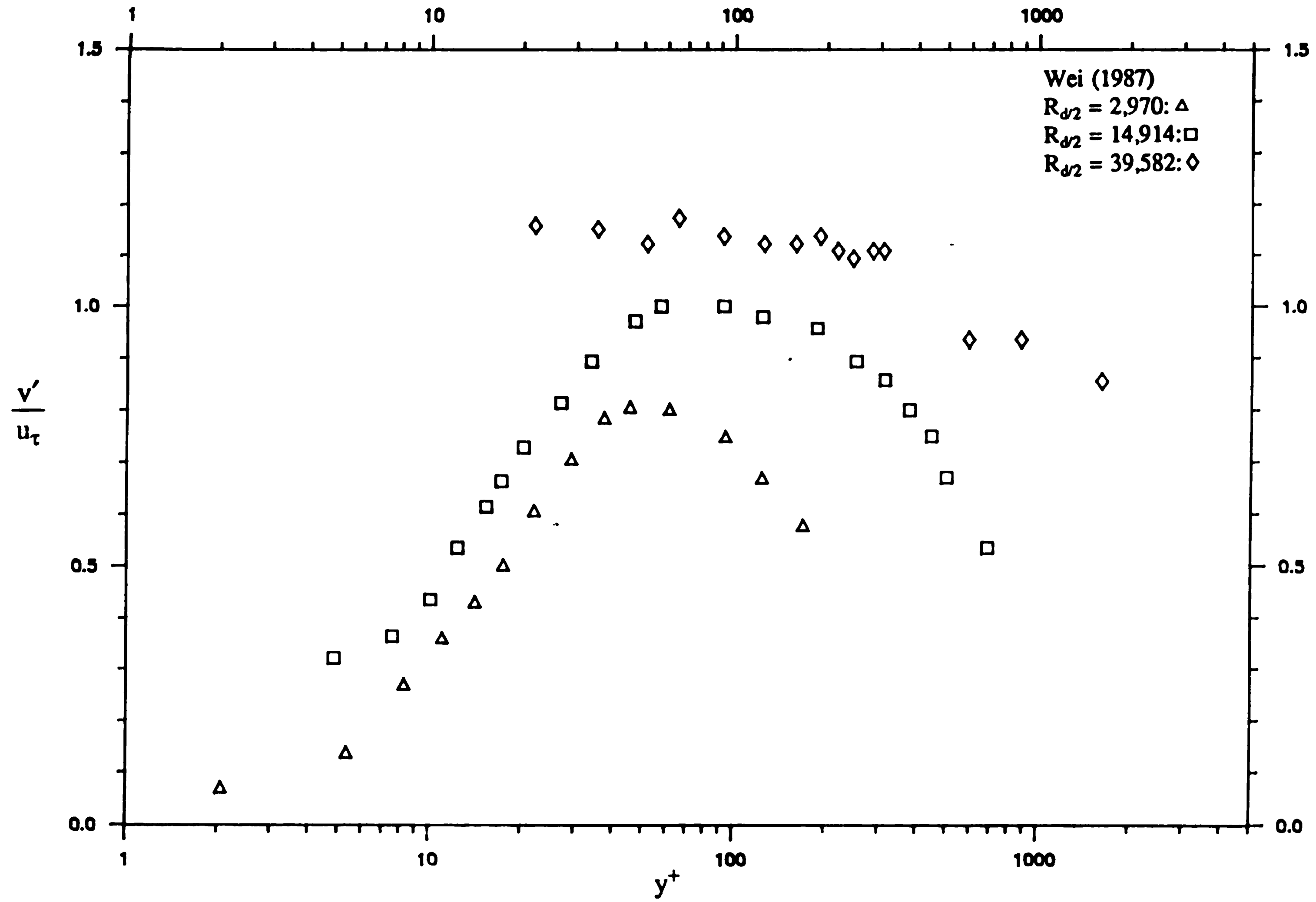

Figure 3.2 Inner variable normalized normal intensity profiles,
b) Data of Wei (1987).

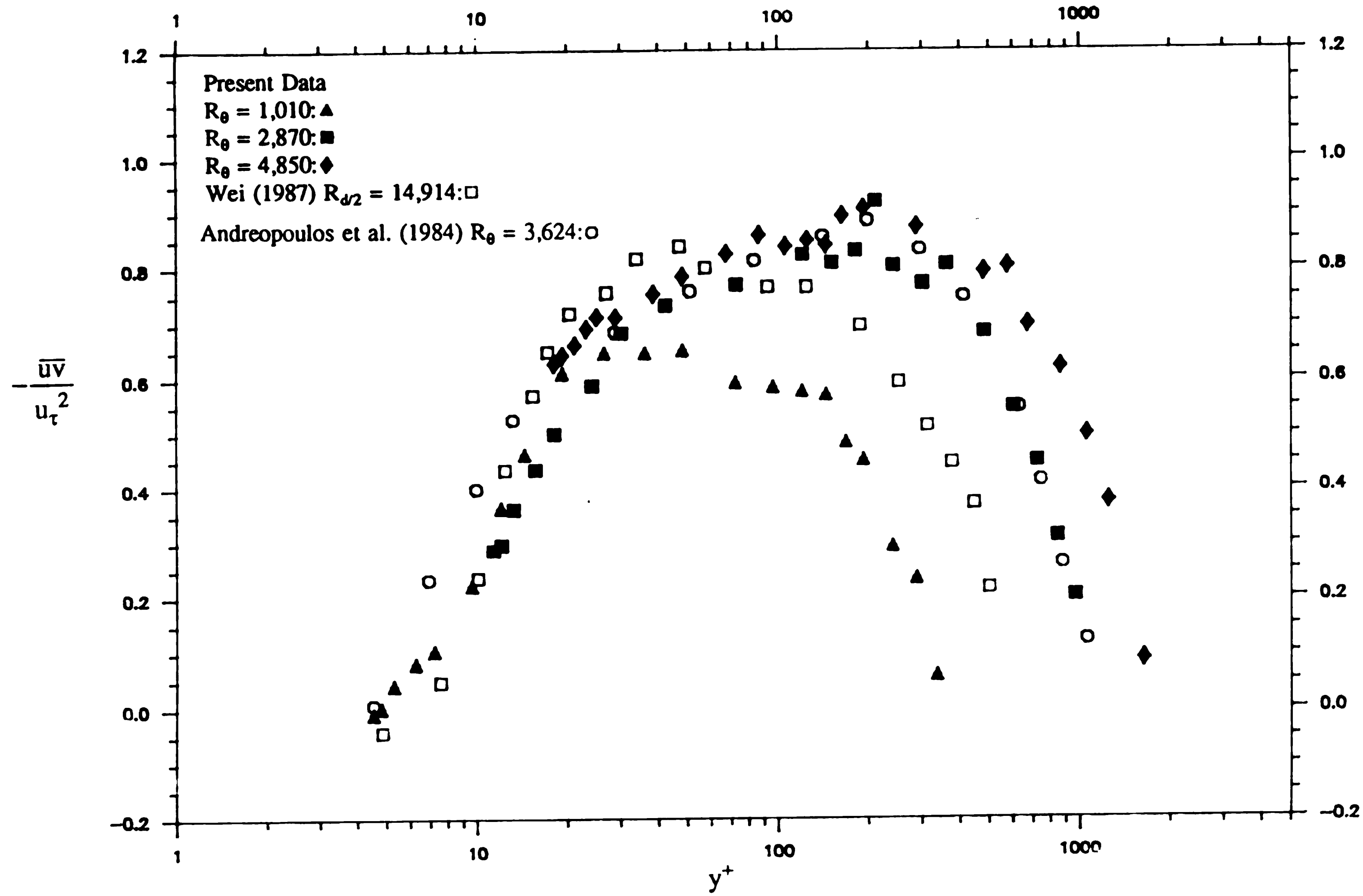

Figure 3.3 Inner variable normalized Reynolds stress profiles.

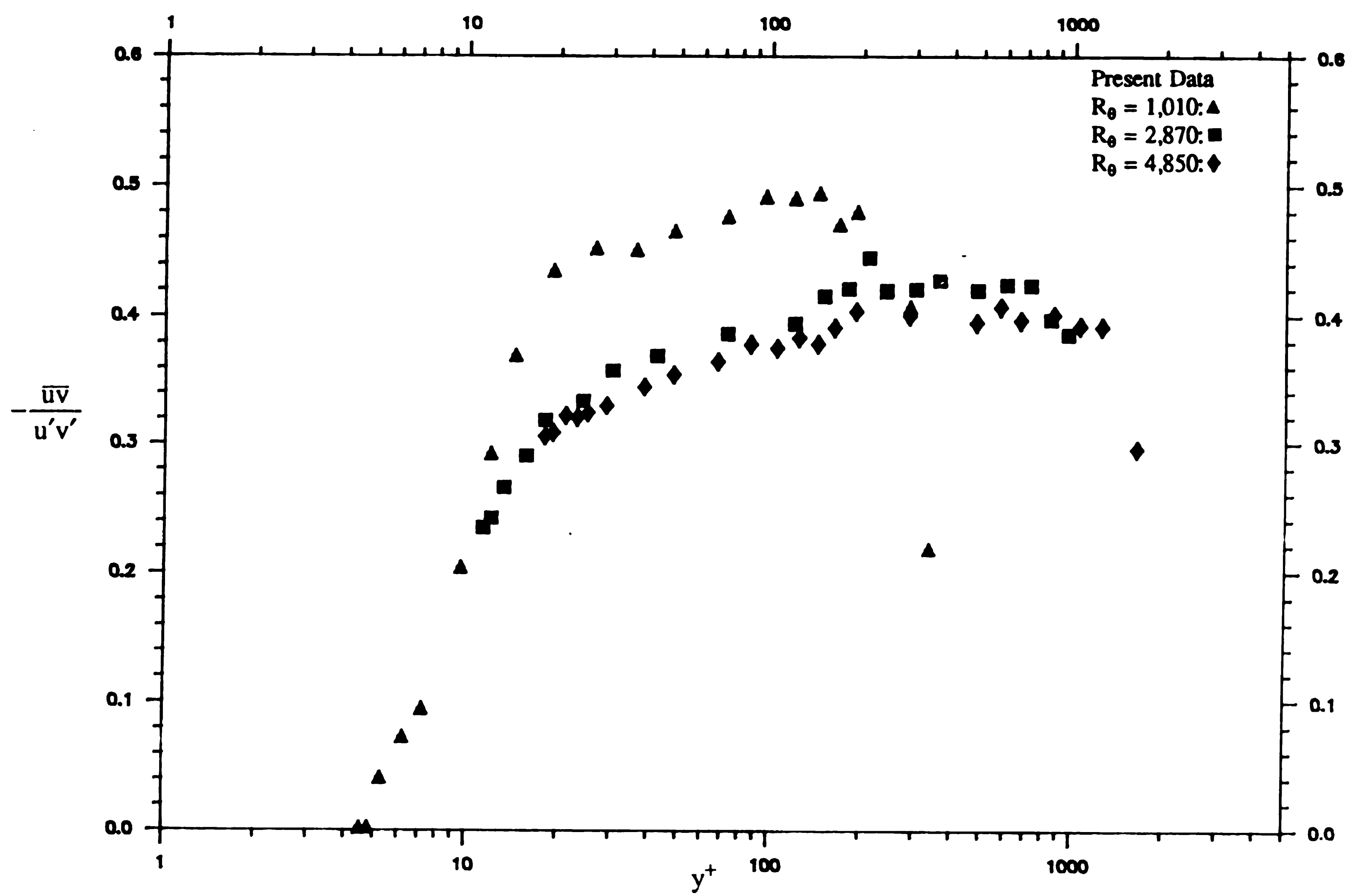

Figure 3.4 Reynolds stress correlation coefficient profiles versus y^+.

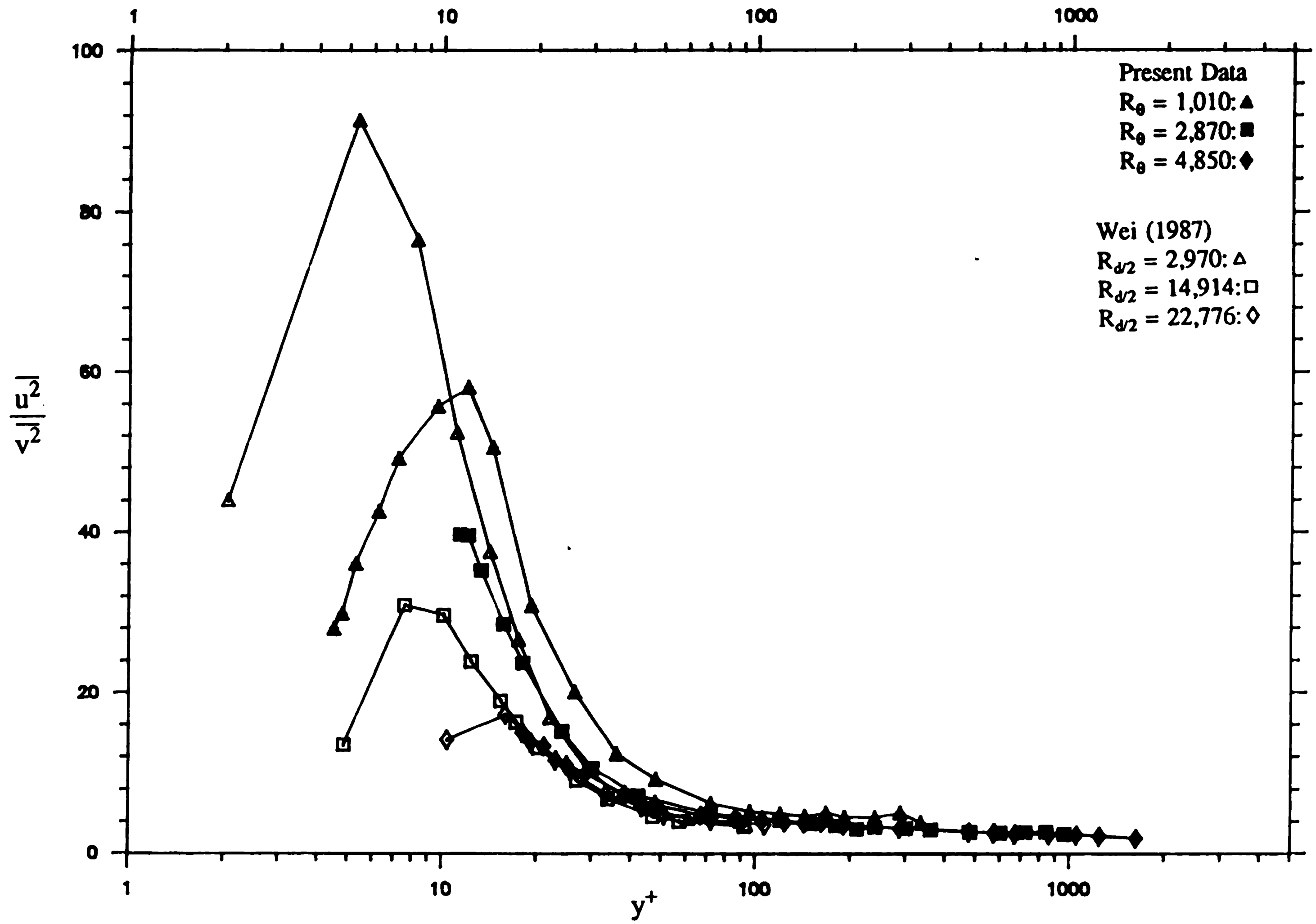

Figure 3.5 Velocity variance ratio profiles versus y^+.

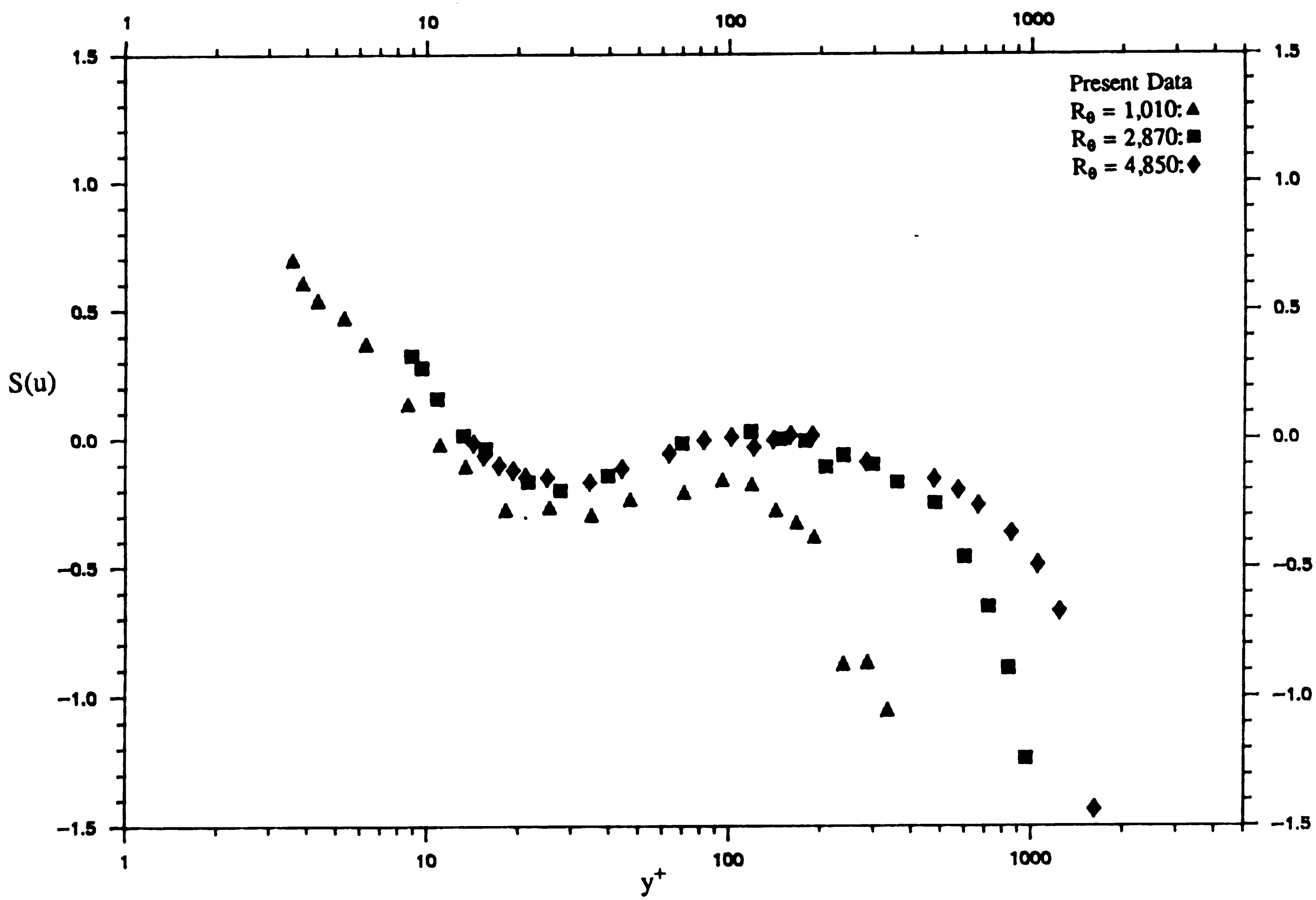

Figure 3.6 Streamwise velocity skewness profiles versus y^+,
a) Present data.

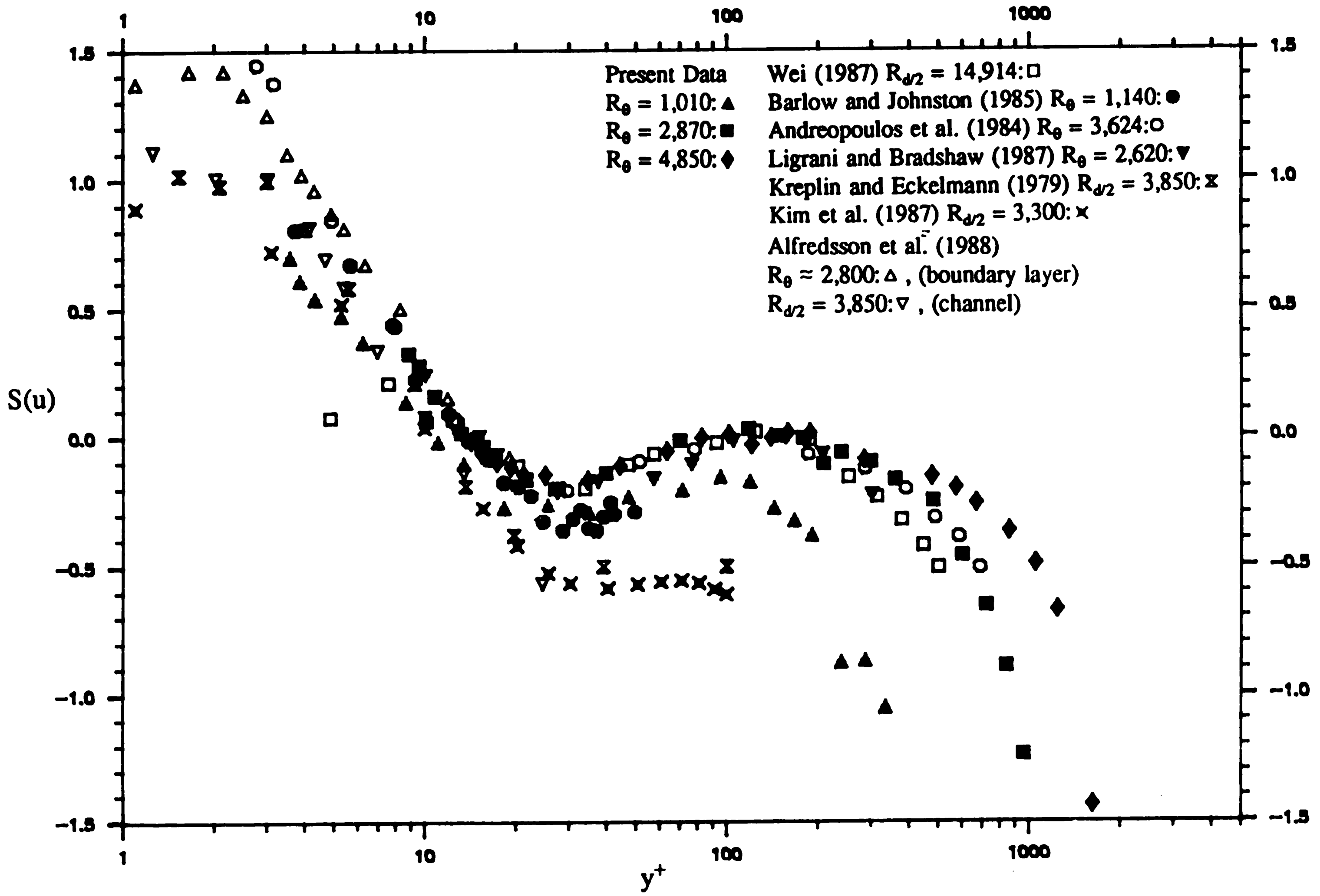

Figure 3.6 Streamwise velocity skewness profiles versus y^+,
b) Present data plus those of others.

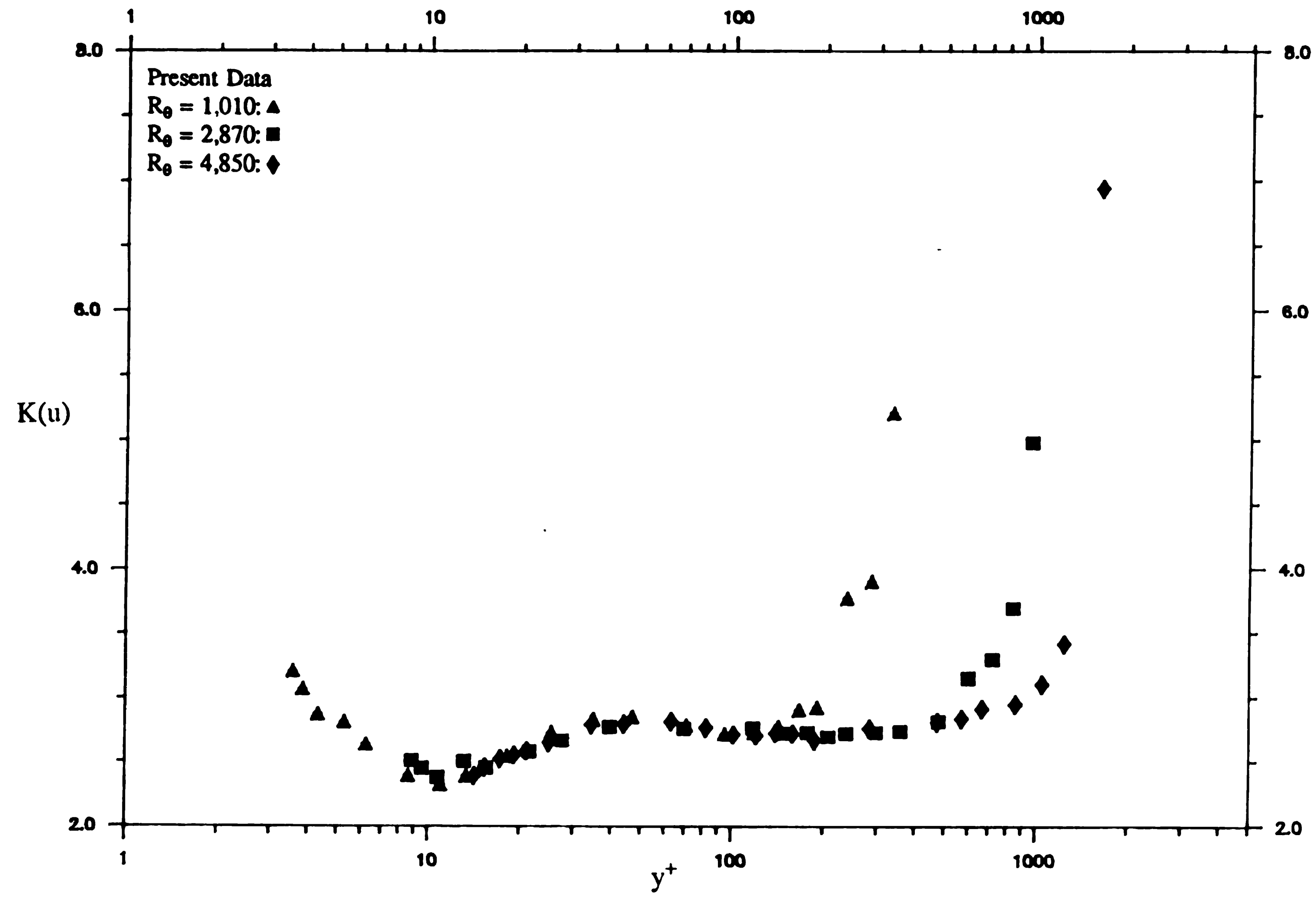

Figure 3.7 Streamwise velocity kurtosis profiles versus y^+,
a) Present data.

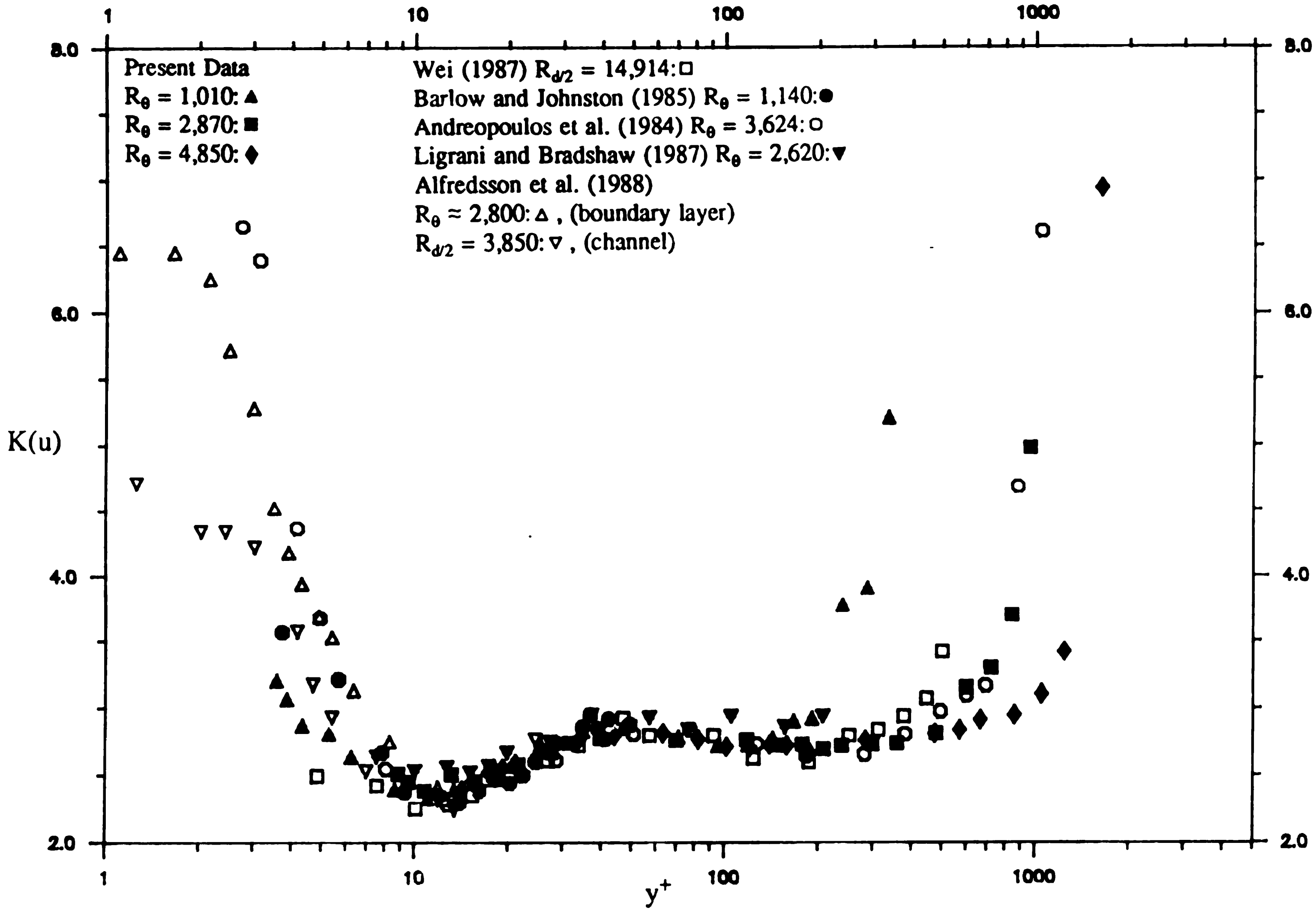

Figure 3.7 Streamwise velocity kurtosis profiles versus y^+,
b) Present data plus those of others.

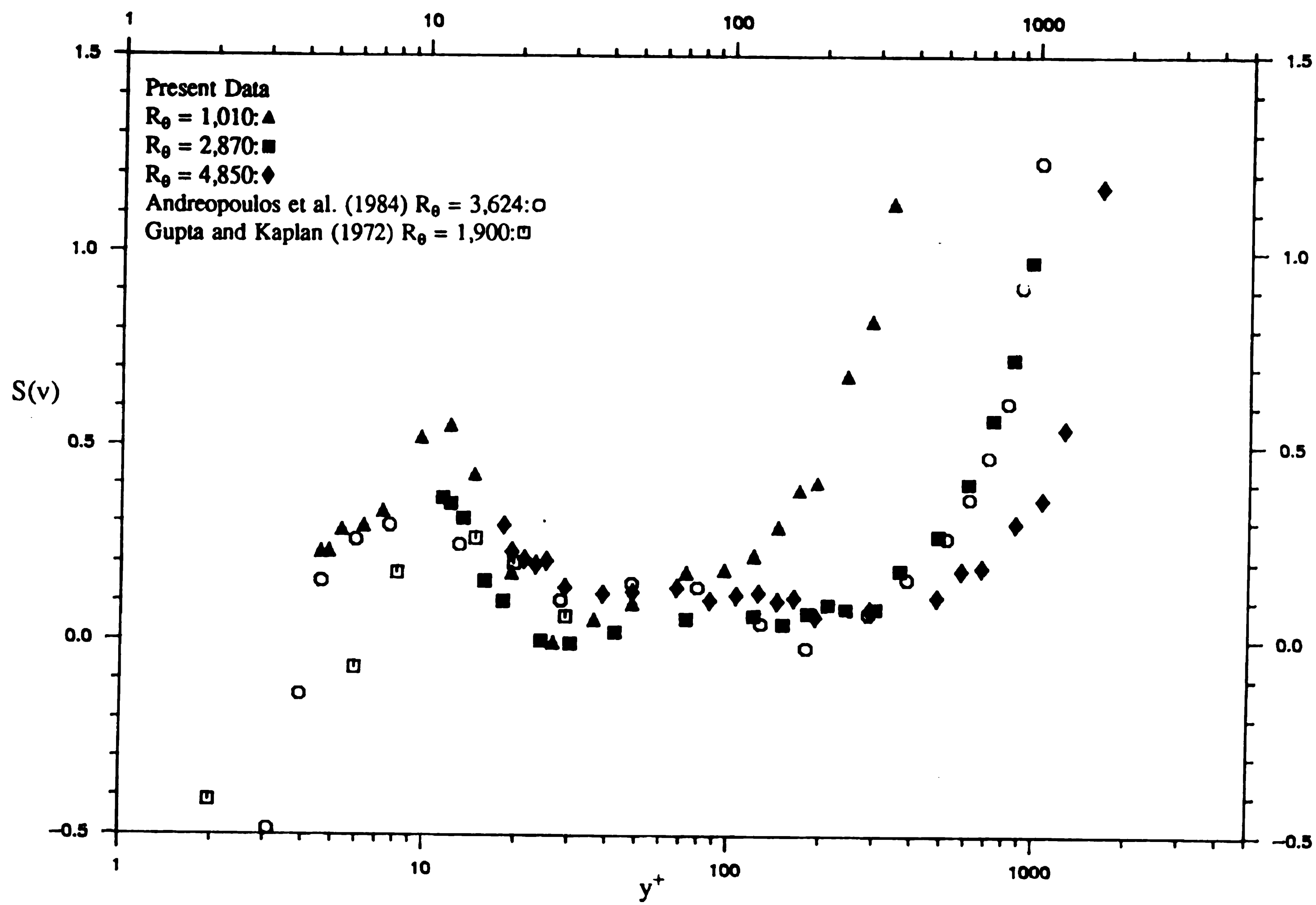

Figure 3.8 Normal velocity skewness profiles versus y^+.

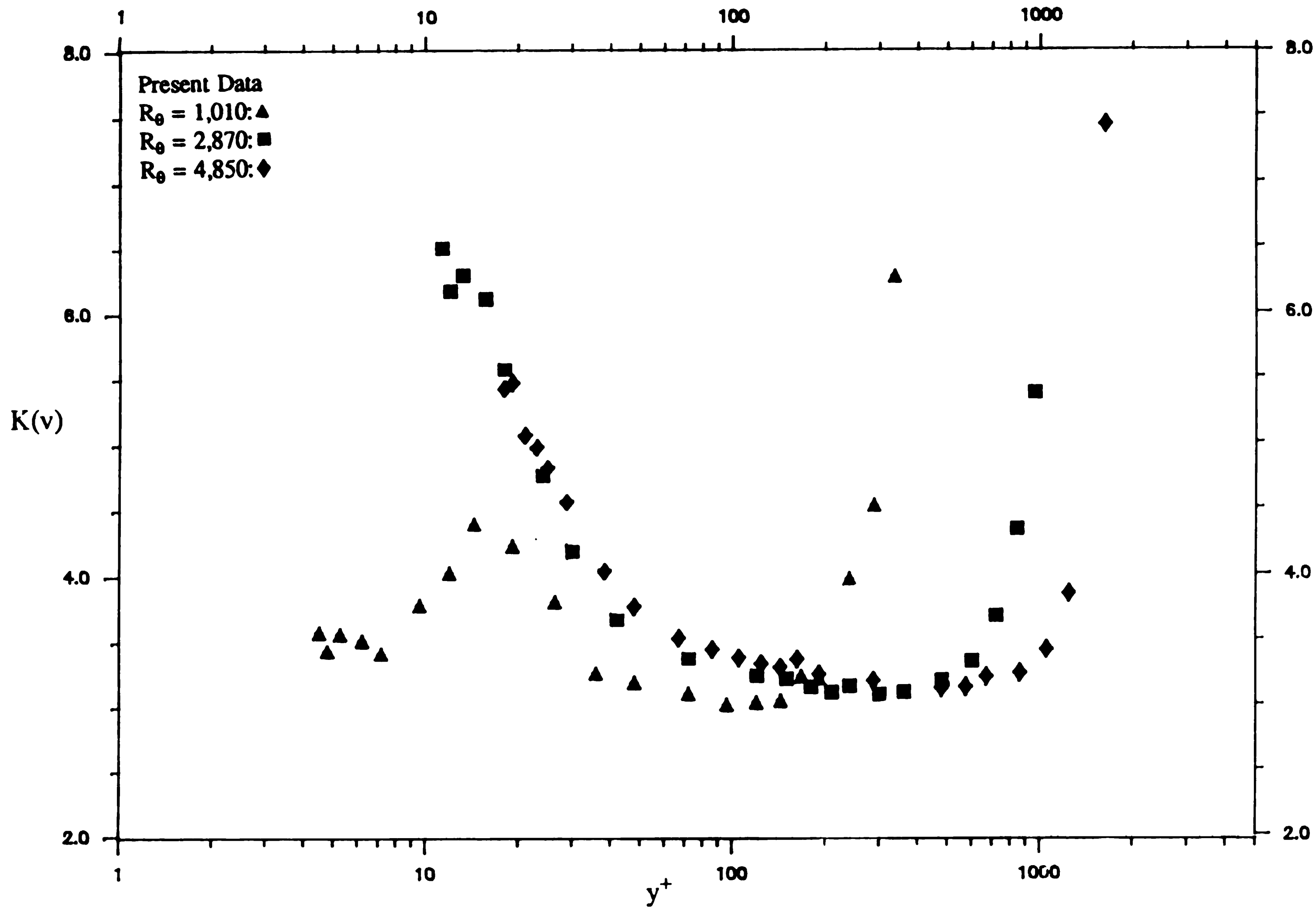

Figure 3.9 Normal velocity kurtosis profiles versus y^+.

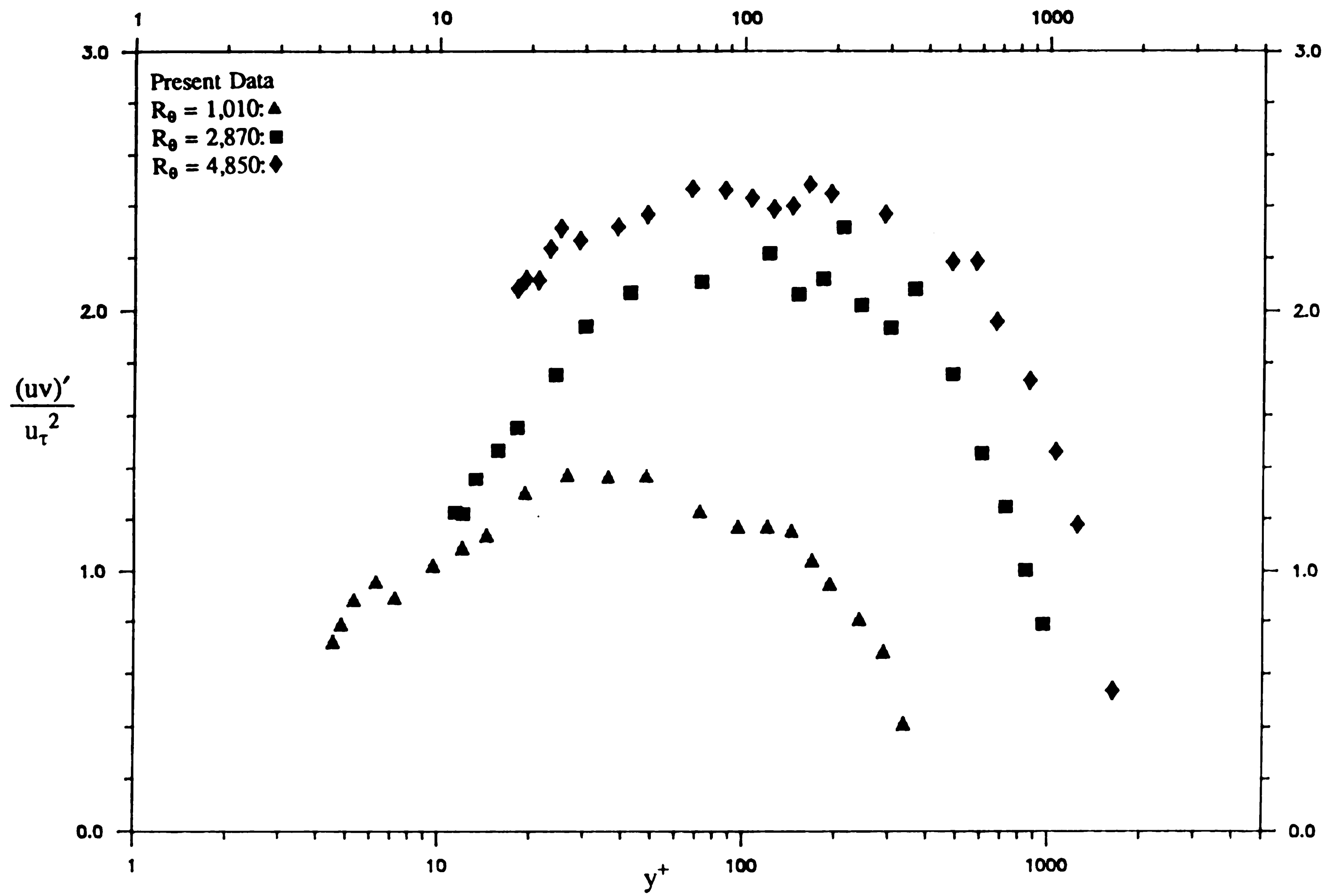

Figure 3.10 Inner variable normalized Reynolds stress intensity profiles.

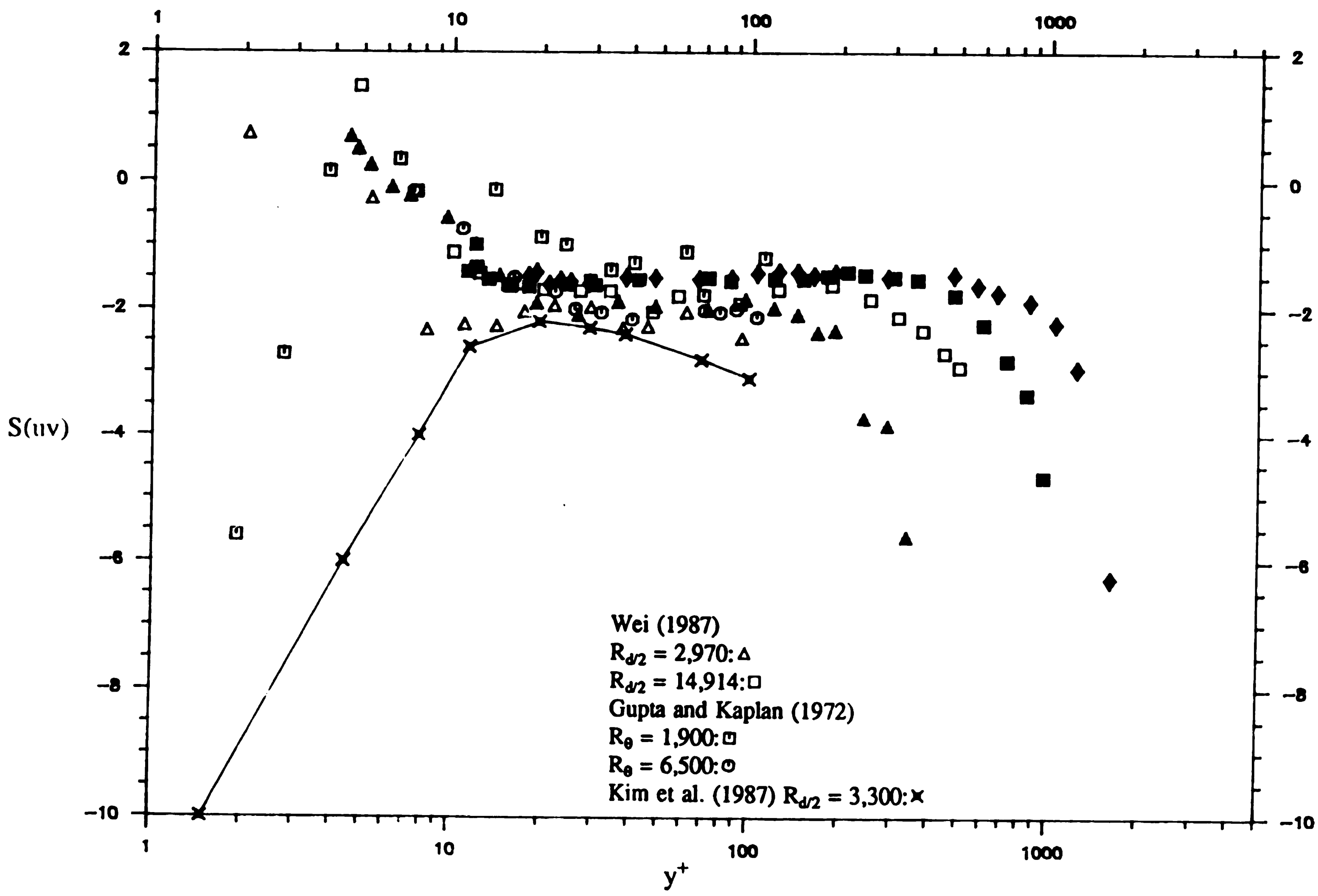

Figure 3.11 Reynolds stress skewness profiles versus y^+.

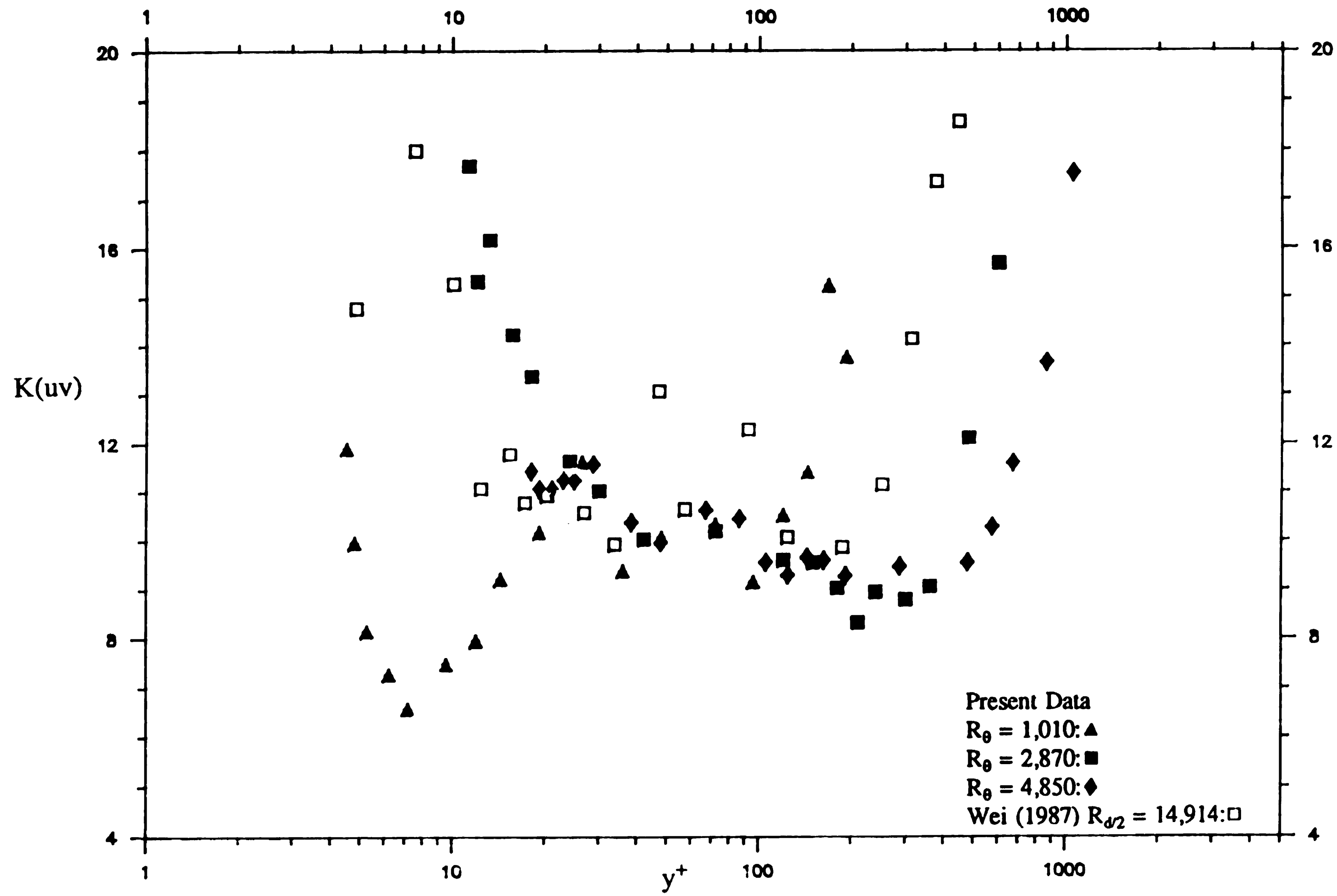

Figure 3.12 Reynolds stress kurtosis profiles versus y^+.

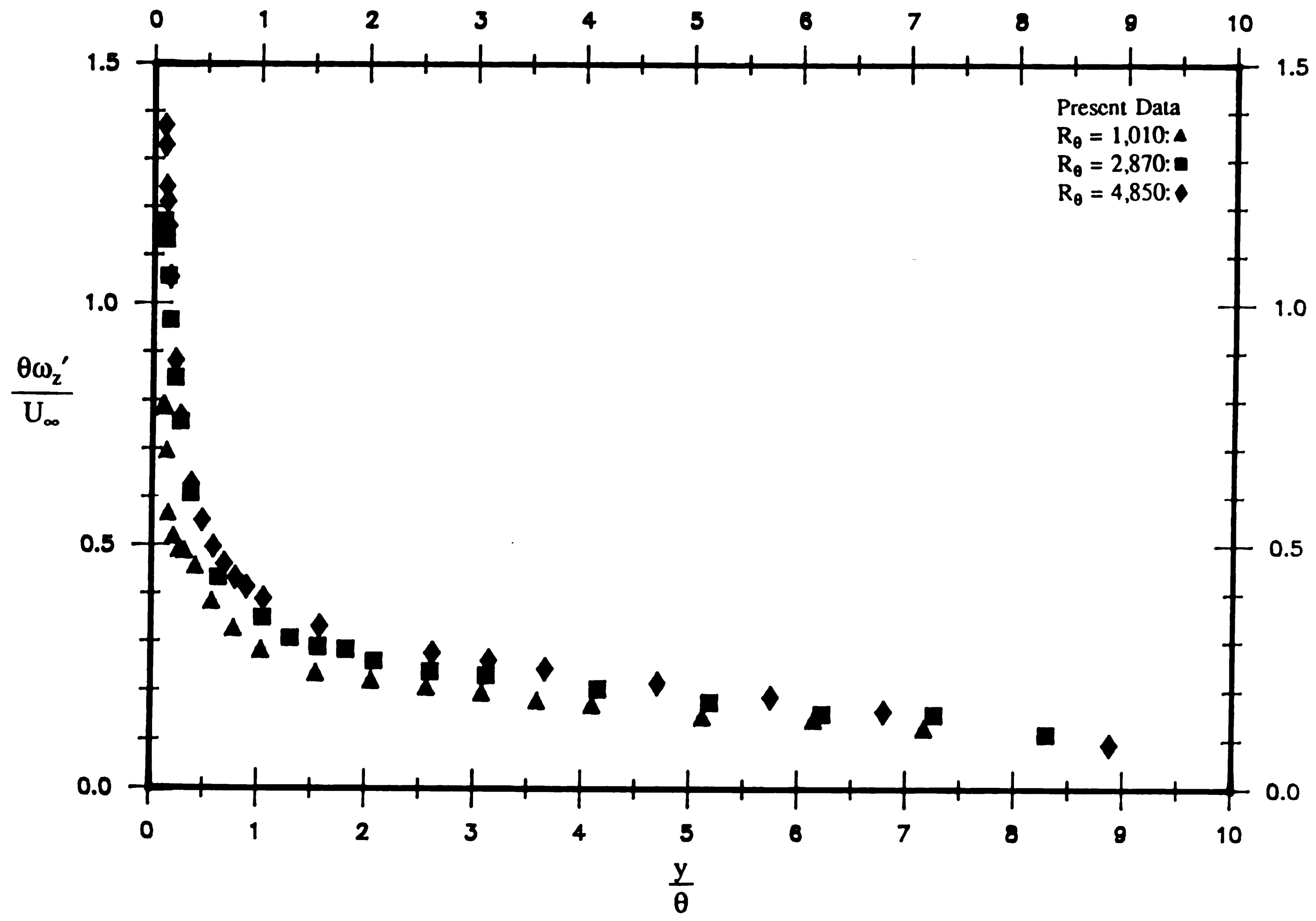

Figure 3.13 Spanwise vorticity intensity profiles,
a) Normalized by θ and U_∞ versus y/θ.

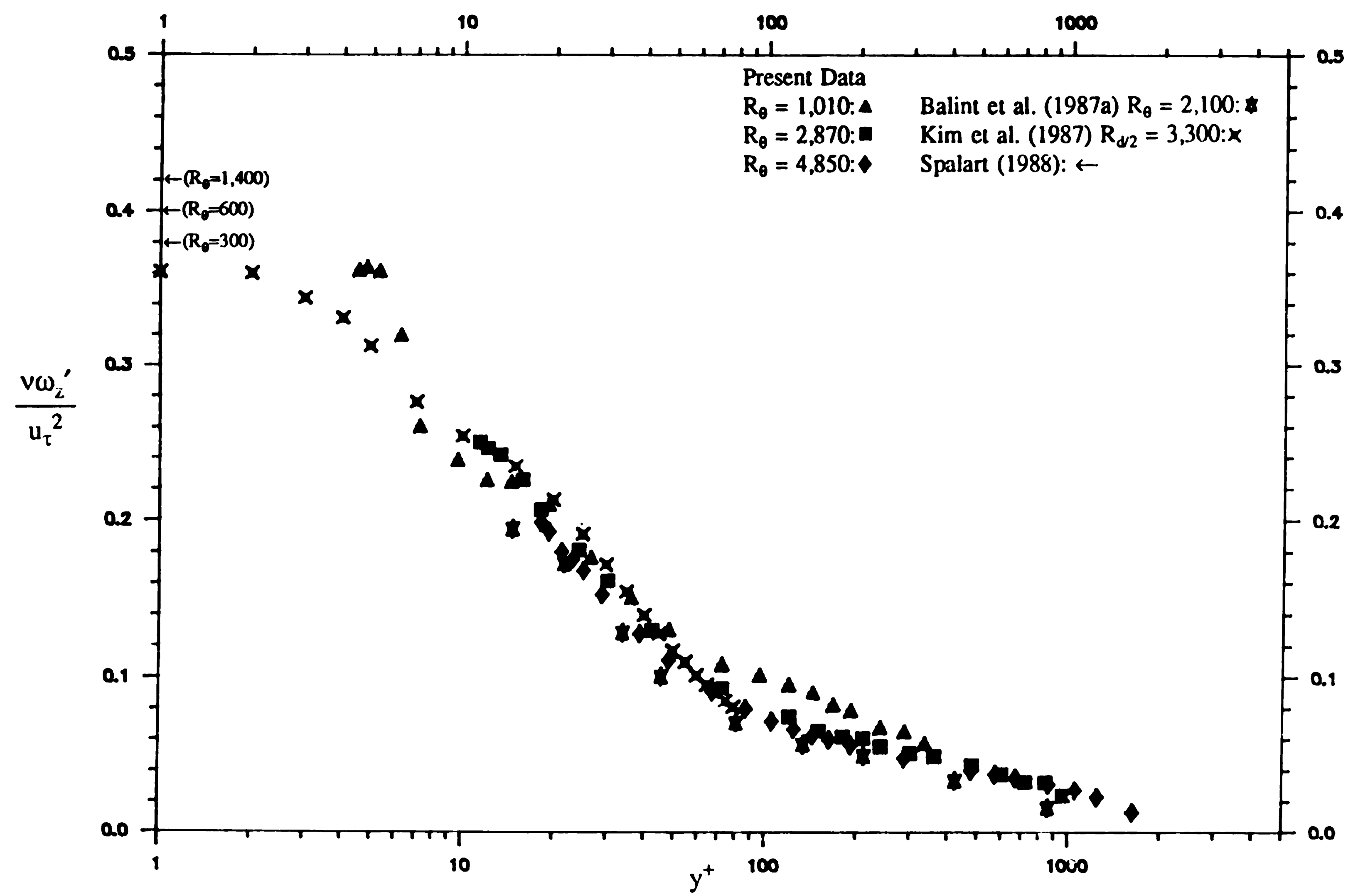

Figure 3.13 Spanwise vorticity intensity profiles,
b) Normalized by ν and u_τ versus y^+.

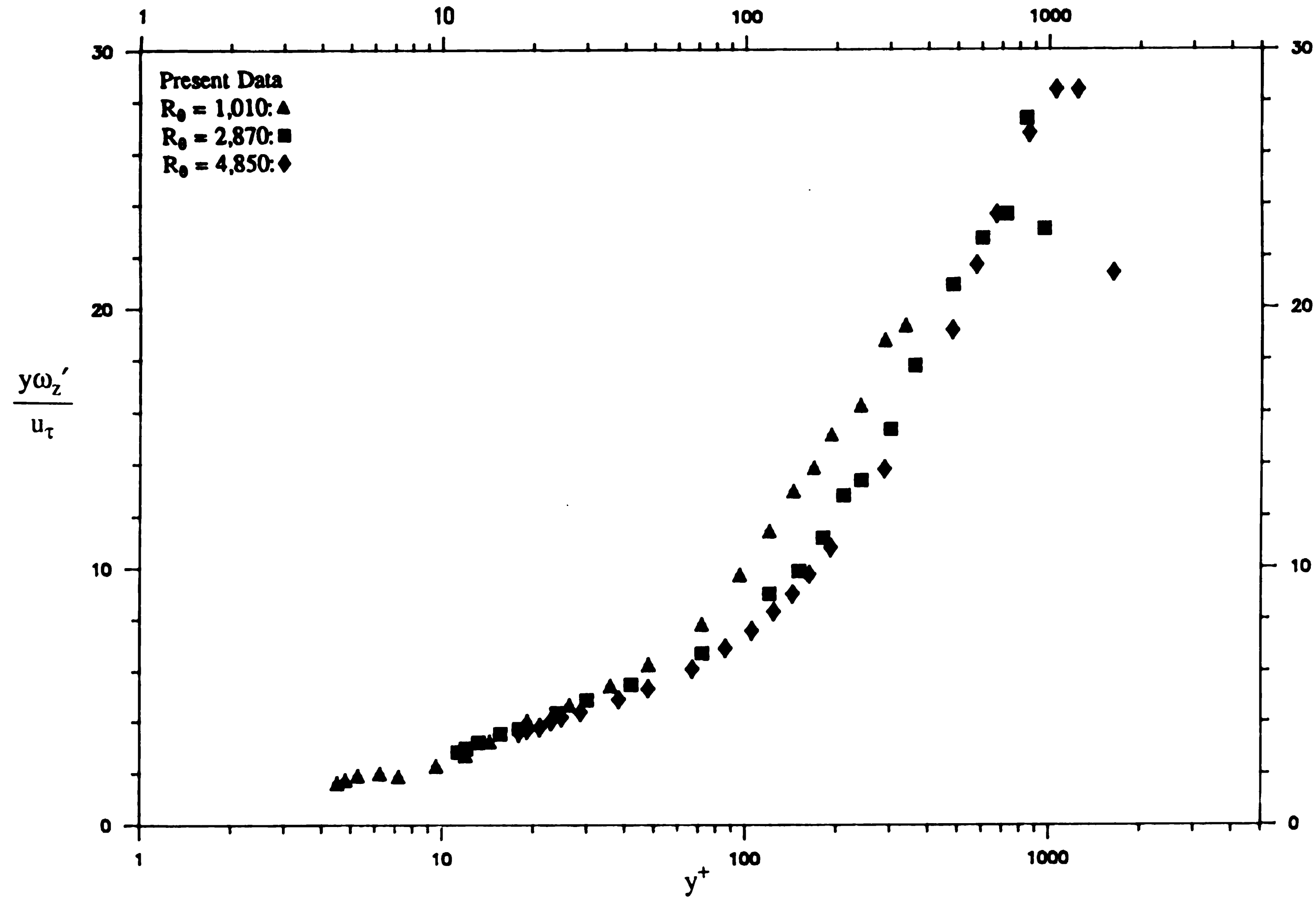

Figure 3.13 Spanwise vorticity intensity profiles,
c) Normalized by the function y/u_τ versus y^+.

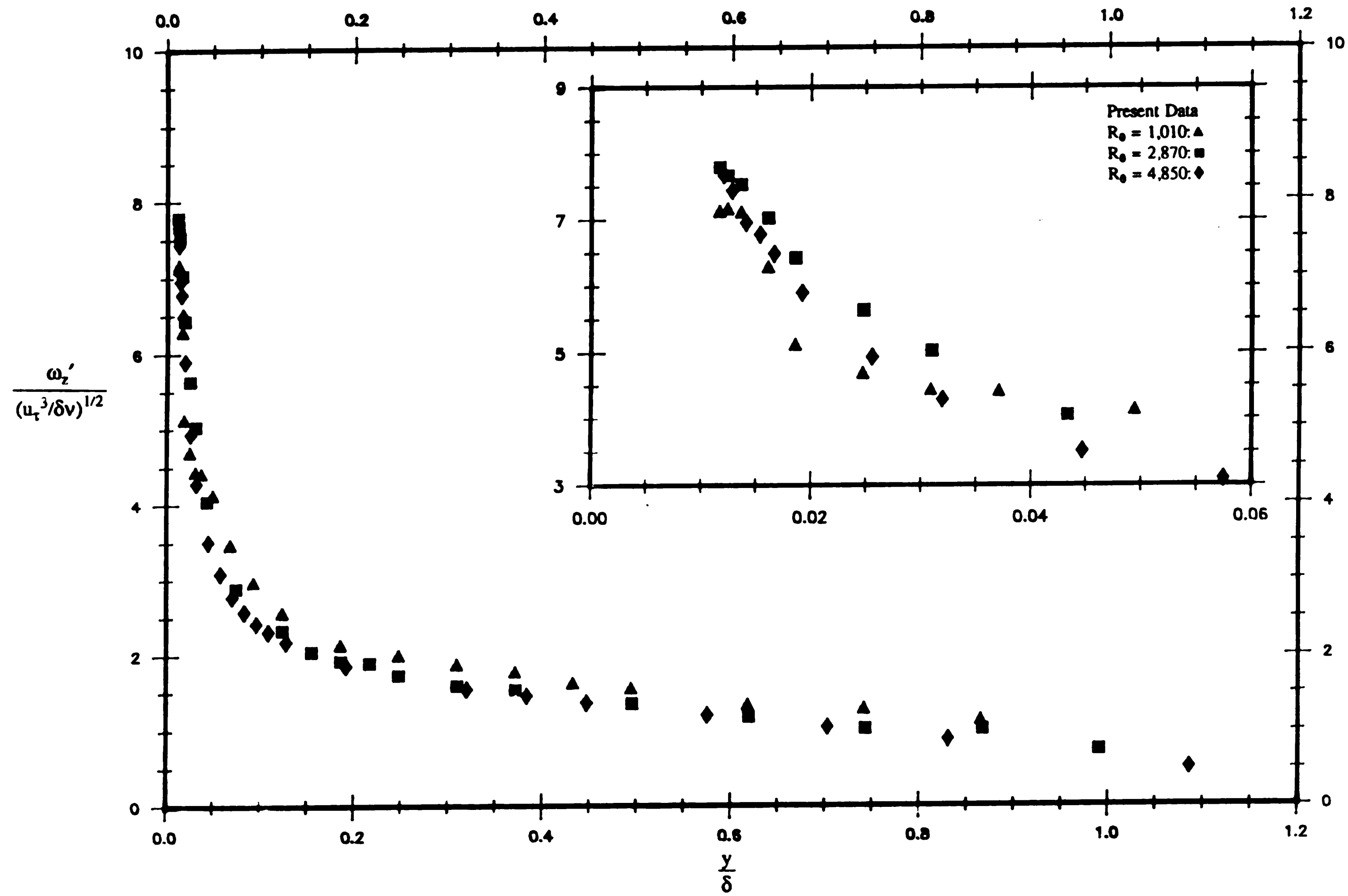

Figure 3.13 Spanwise vorticity intensity profiles,
d) Normalized by δ, ν and u_τ versus y/δ.

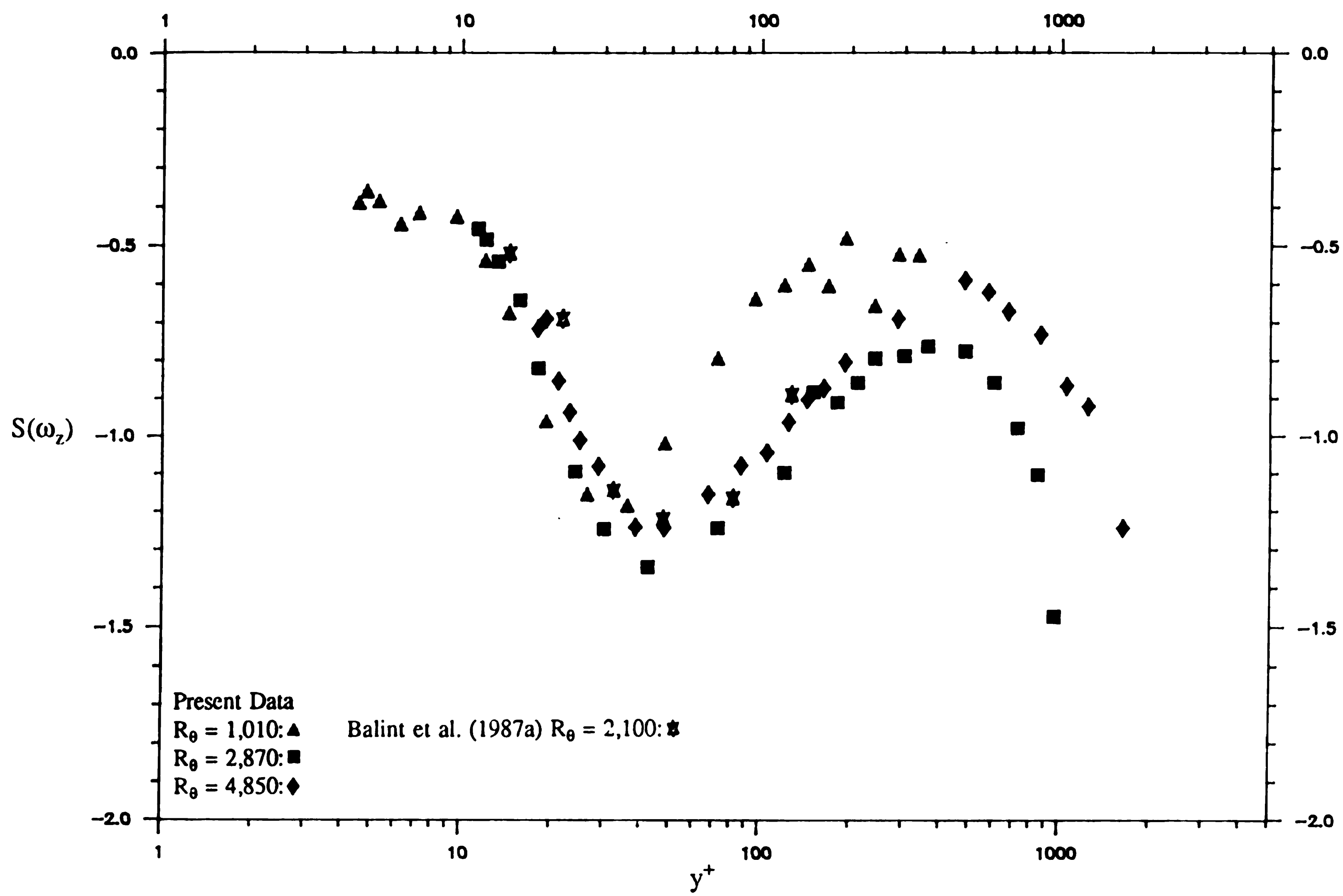

Figure 3.14 Spanwise vorticity skewness profiles versus y^+.

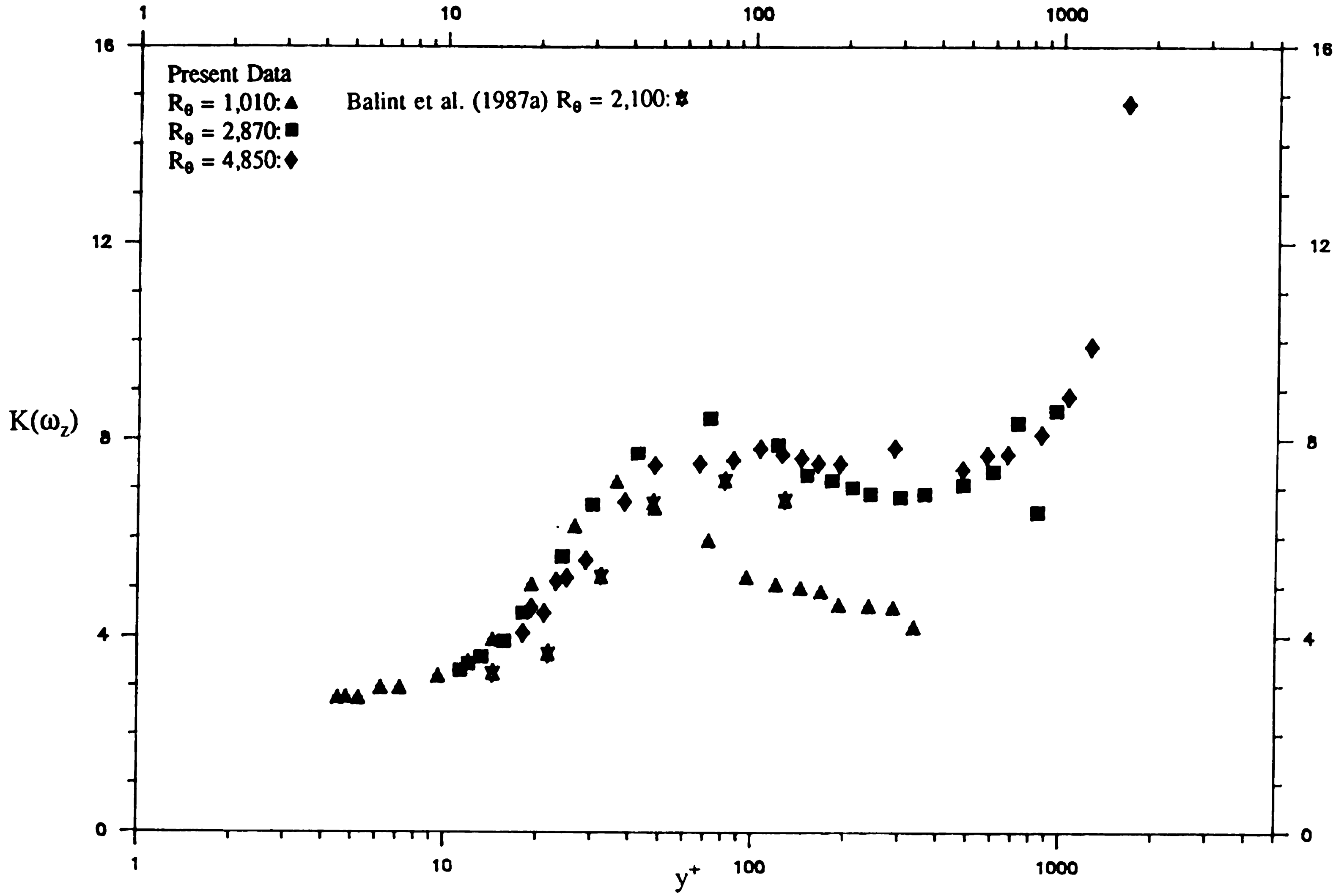

Figure 3.15 Spanwise vorticity kurtosis profiles versus y^+.

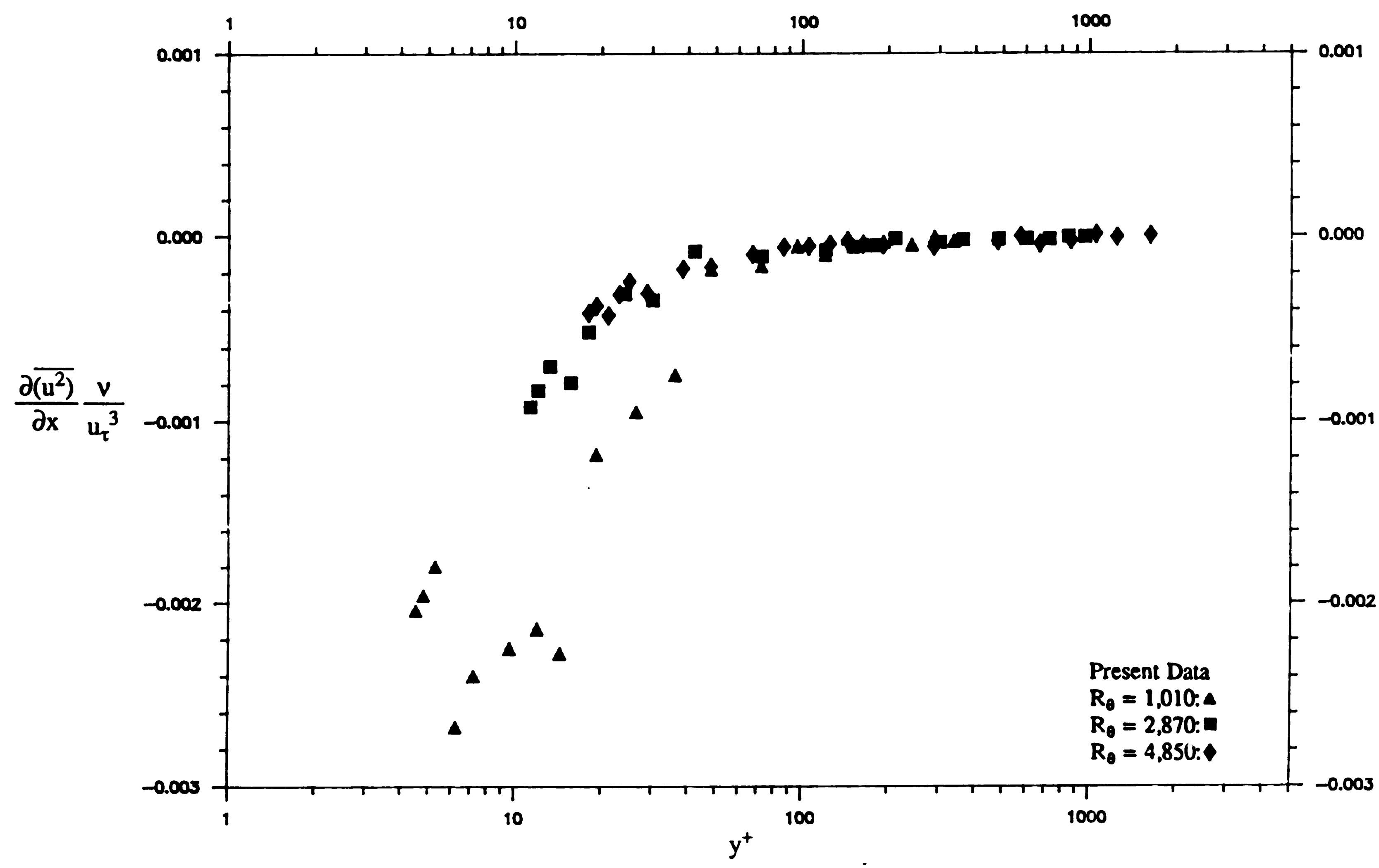

Figure 3.16 Profiles of the average streamwise gradient of the streamwise velocity variances under an inner variable normalization.

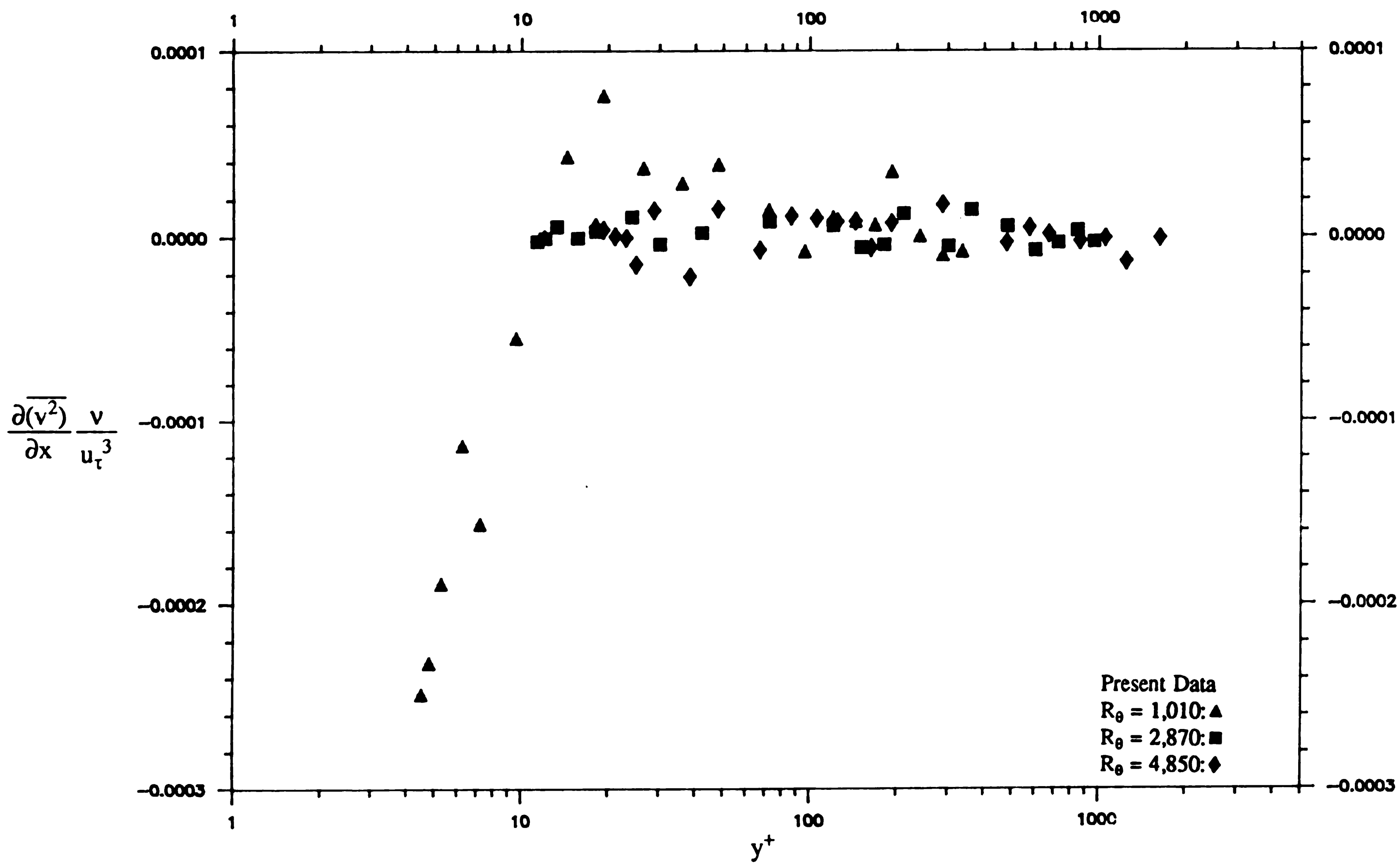

Figure 3.17 Profiles of the average streamwise gradient of the normal velocity variances under an inner variable normalization.

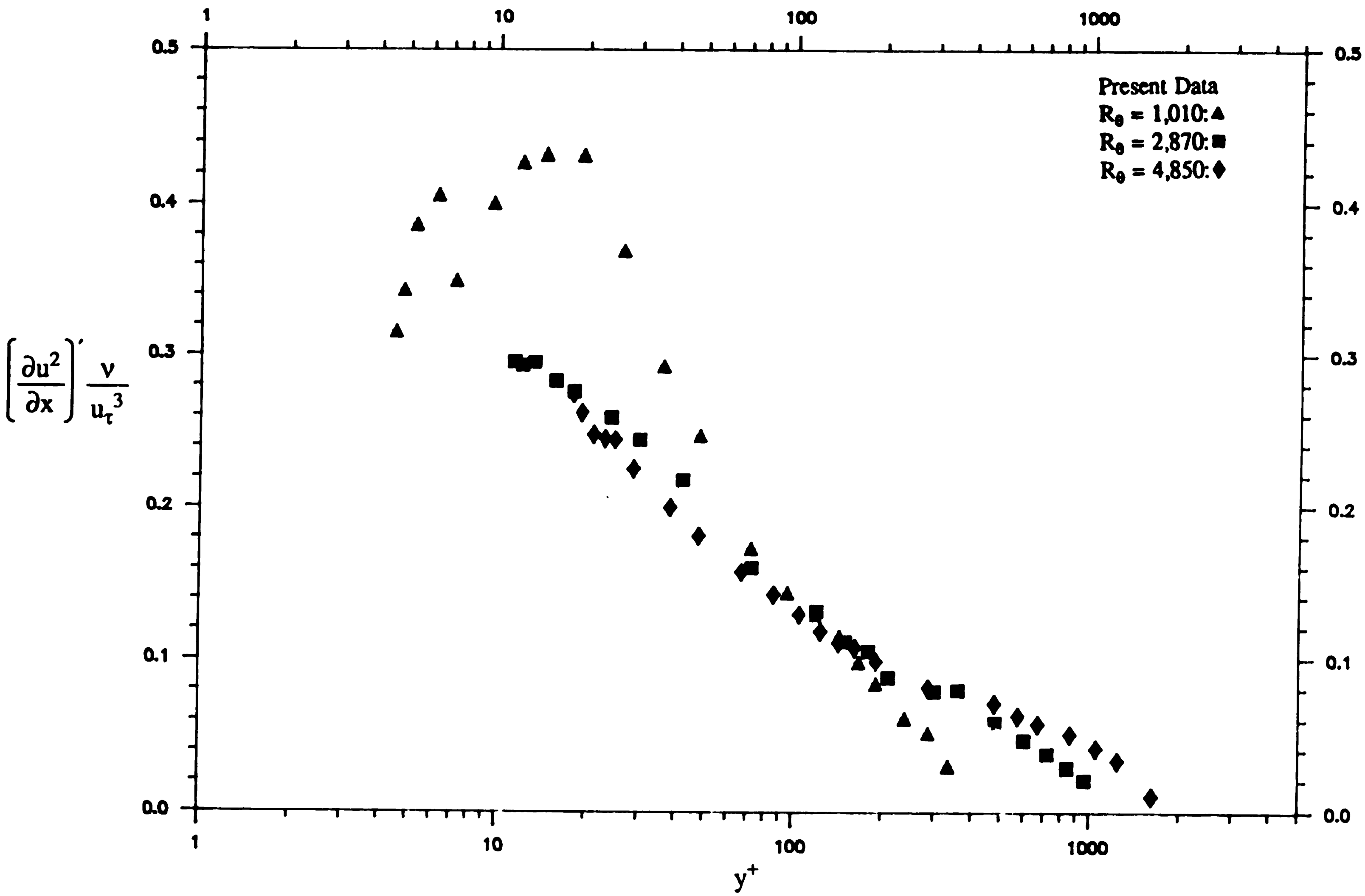

Figure 3.18 Profiles of the rms streamwise gradient of the streamwise velocity variances under an inner variable normalization.

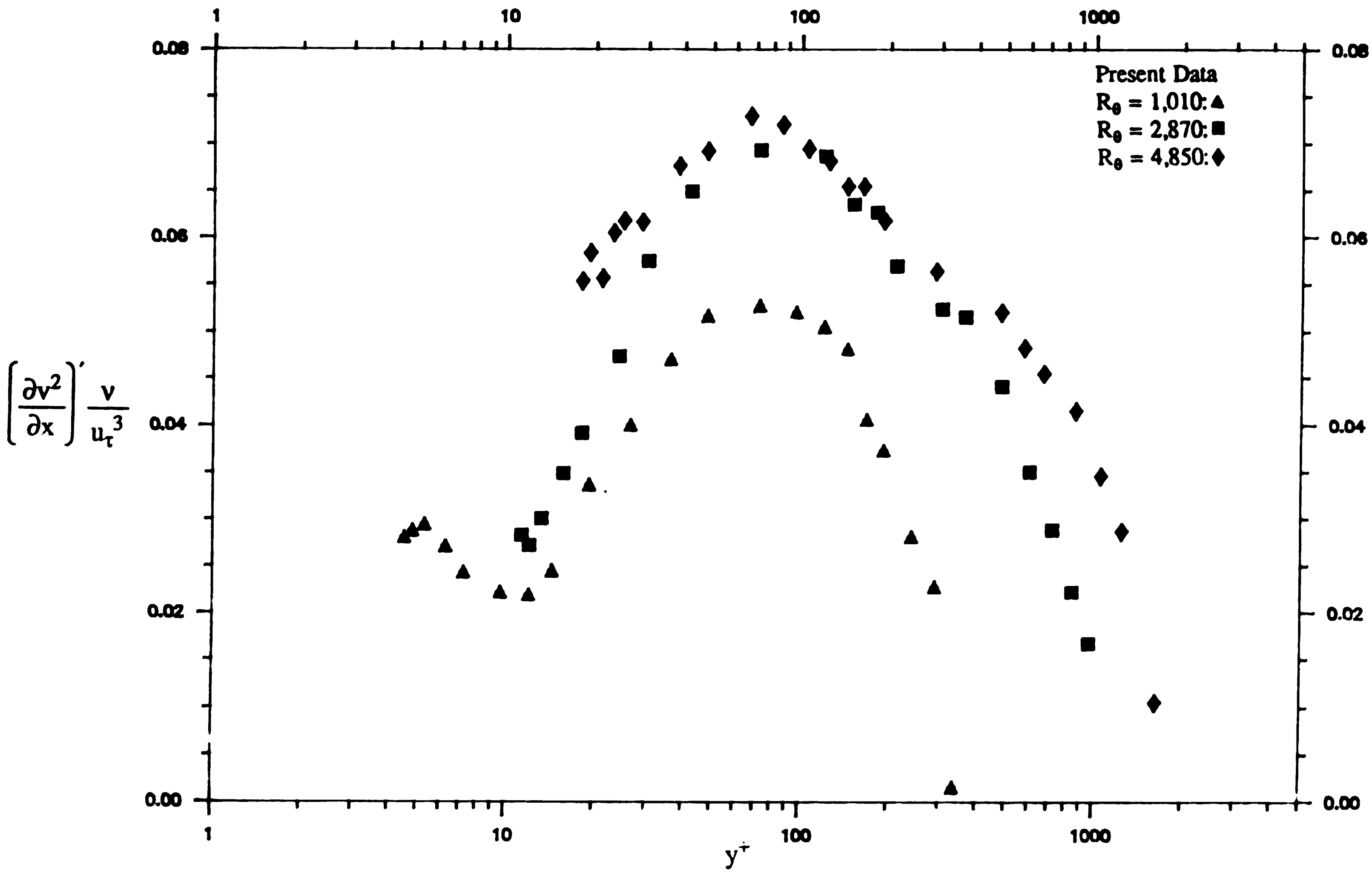

Figure 3.19 Profiles of the rms streamwise gradient of the normal velocity variances under an inner variable normalization.

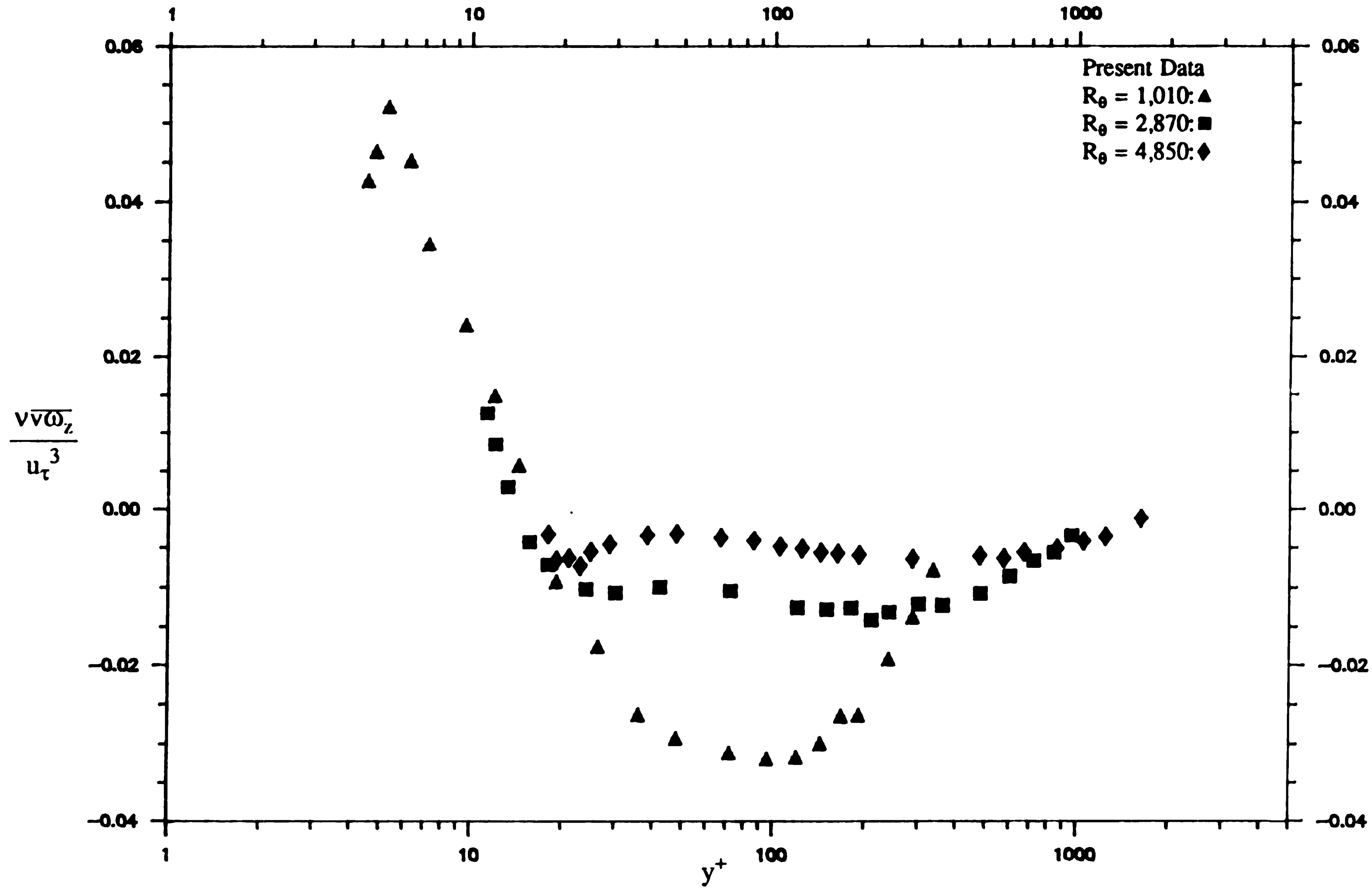

Figure 3.20 Inner variable normalized $\langle v\omega_z \rangle$ profiles.

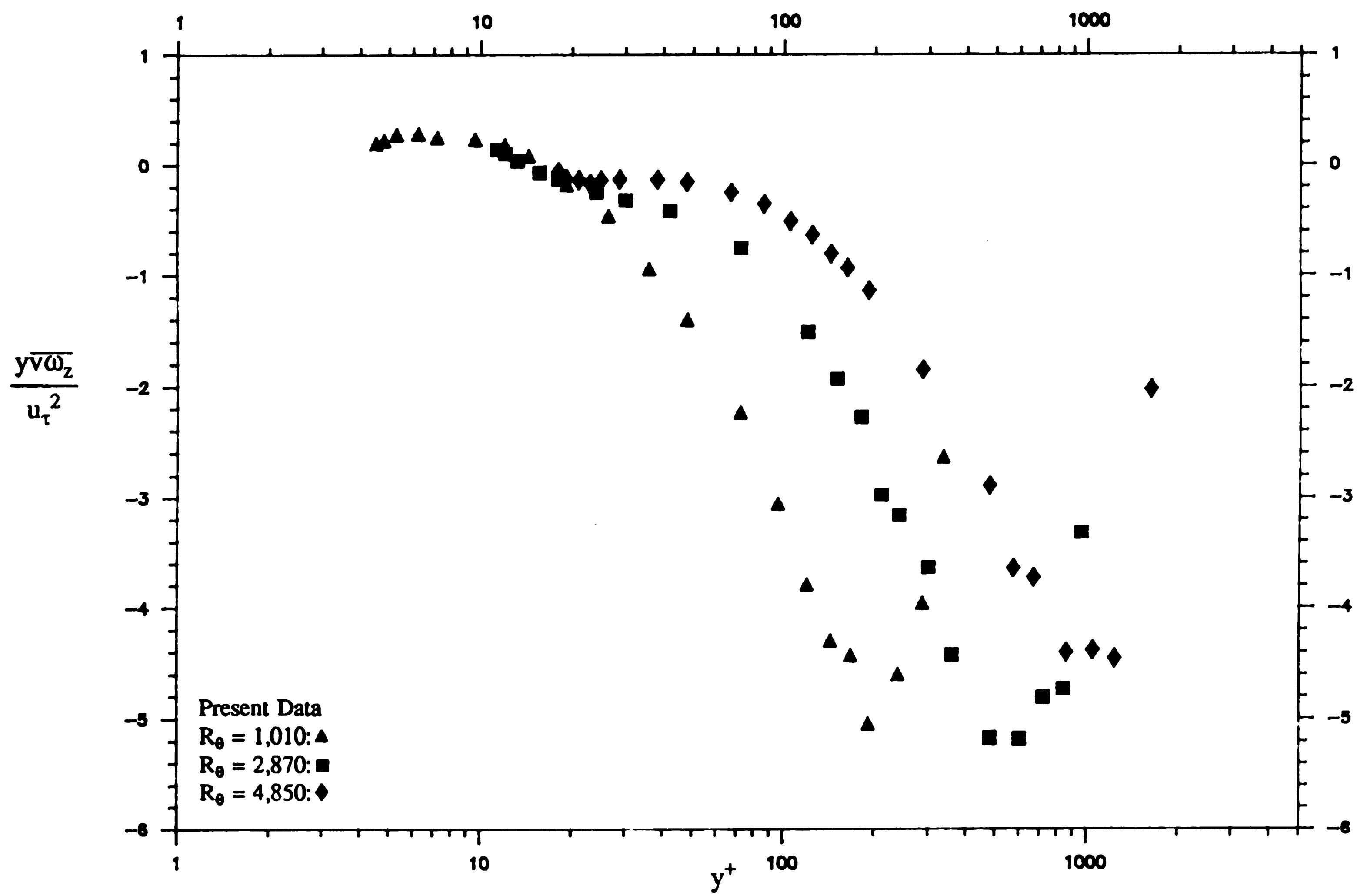

Figure 3.21 Normalization of the $<v\omega_z>$ profiles using the function y/u_τ^2.

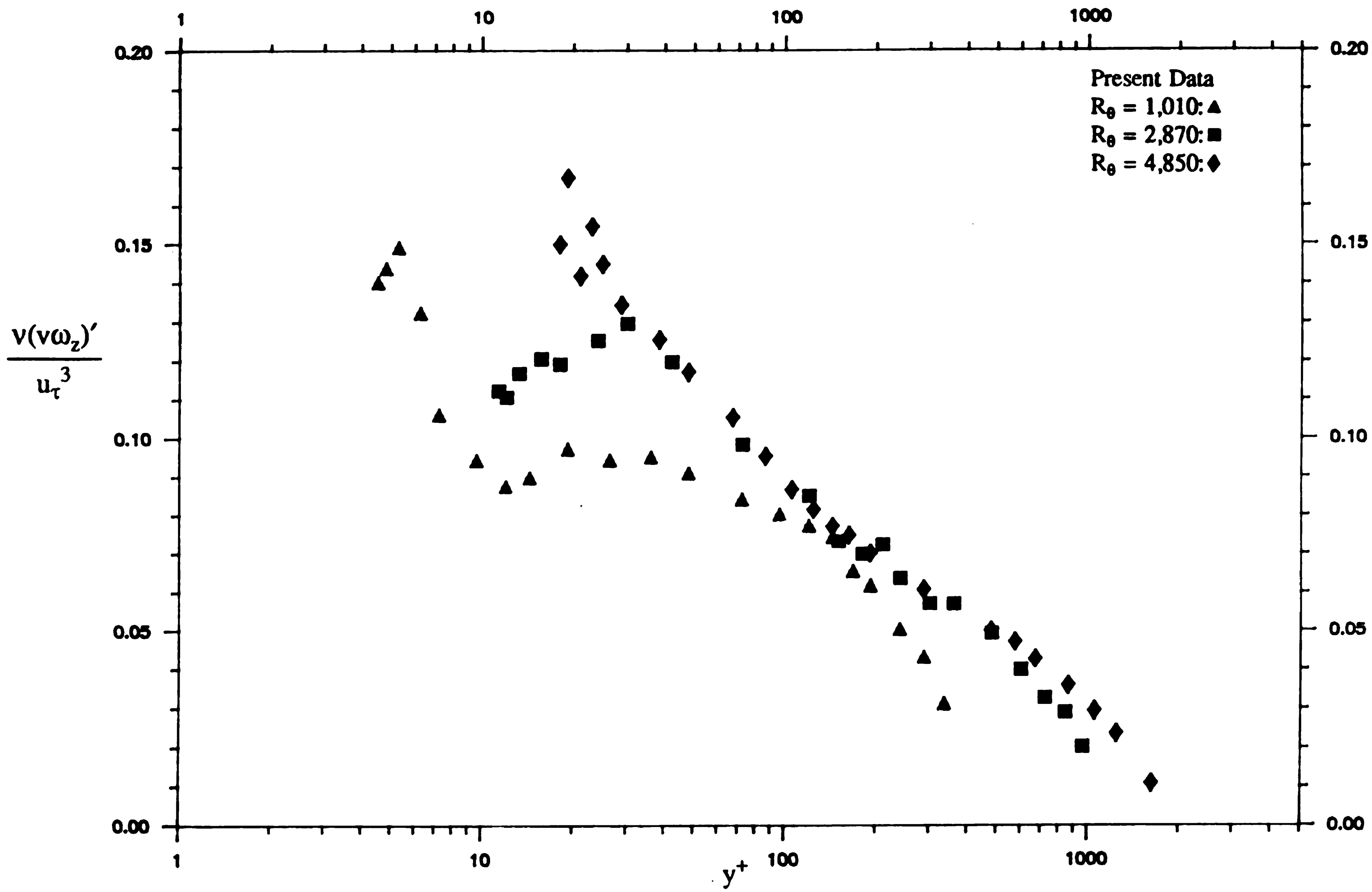

Figure 3.22 Inner variable normalized $(v\omega_z)'$ profiles.

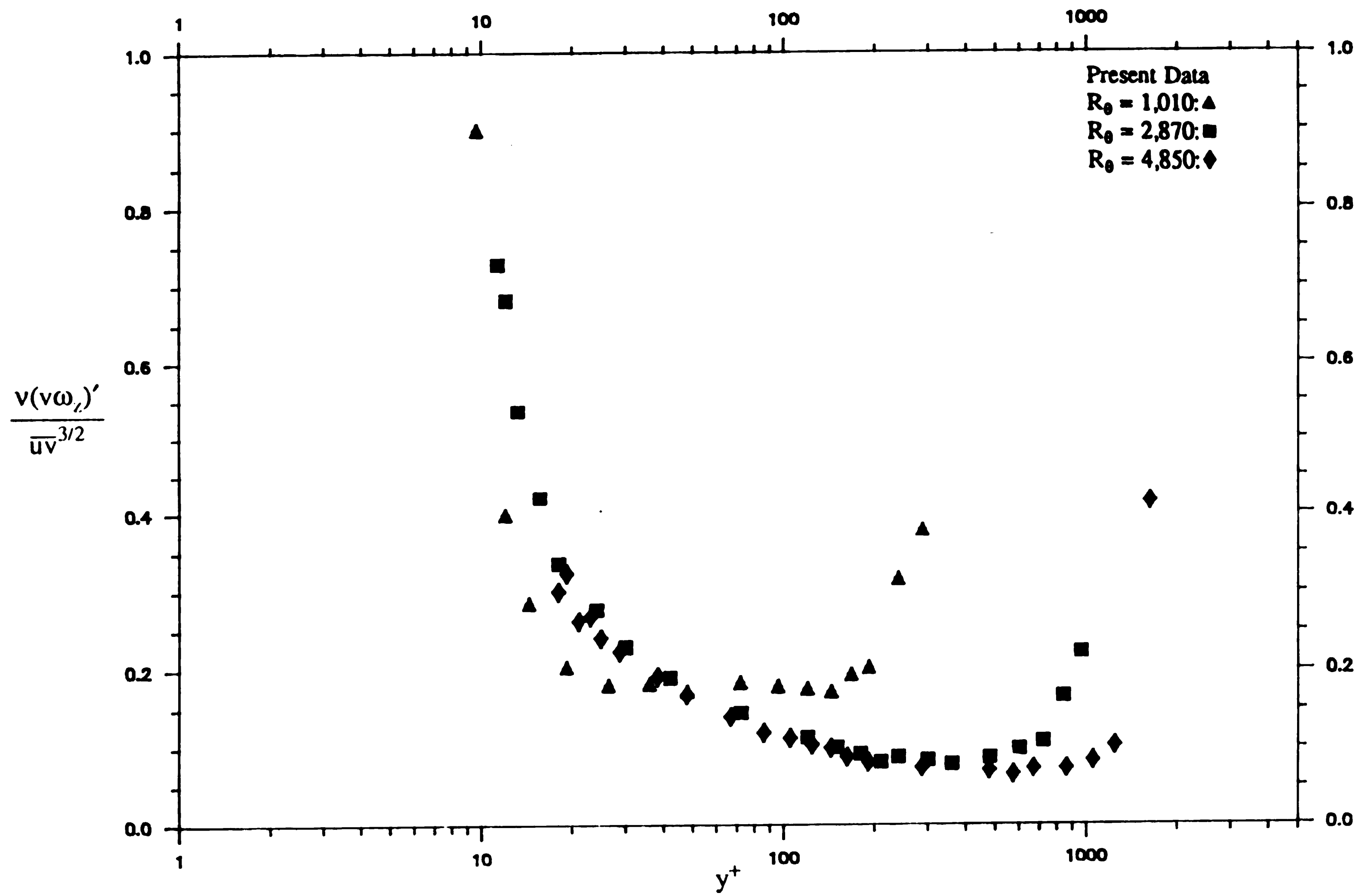

Figure 3.23 Normalization of the $(v\omega_z)'$ profiles using the function $\nu/\langle uv\rangle^{3/2}$.

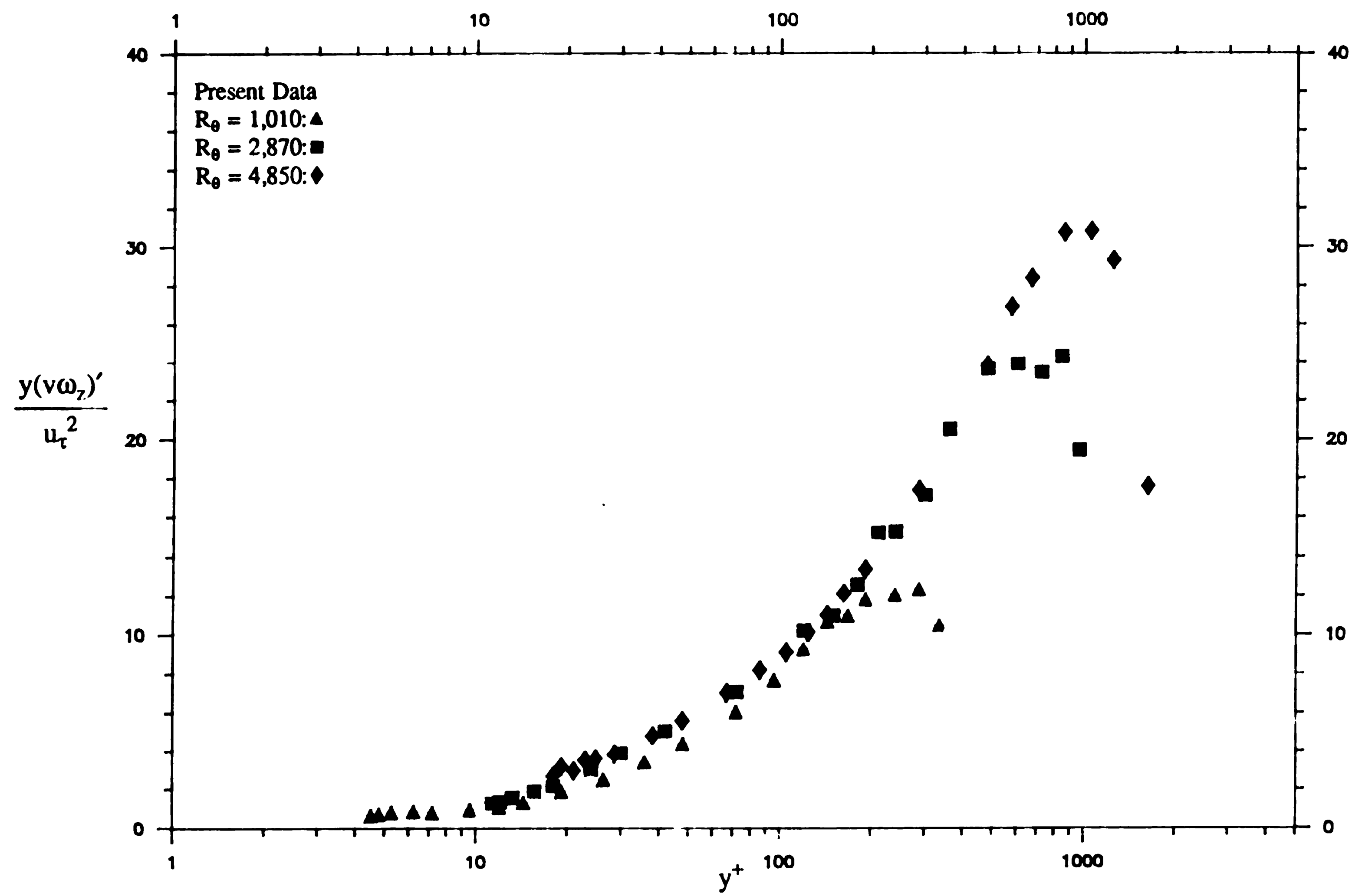

Figure 3.24 Normalization of the $(v\omega_z)'$ profiles using the function y/u_τ^2.

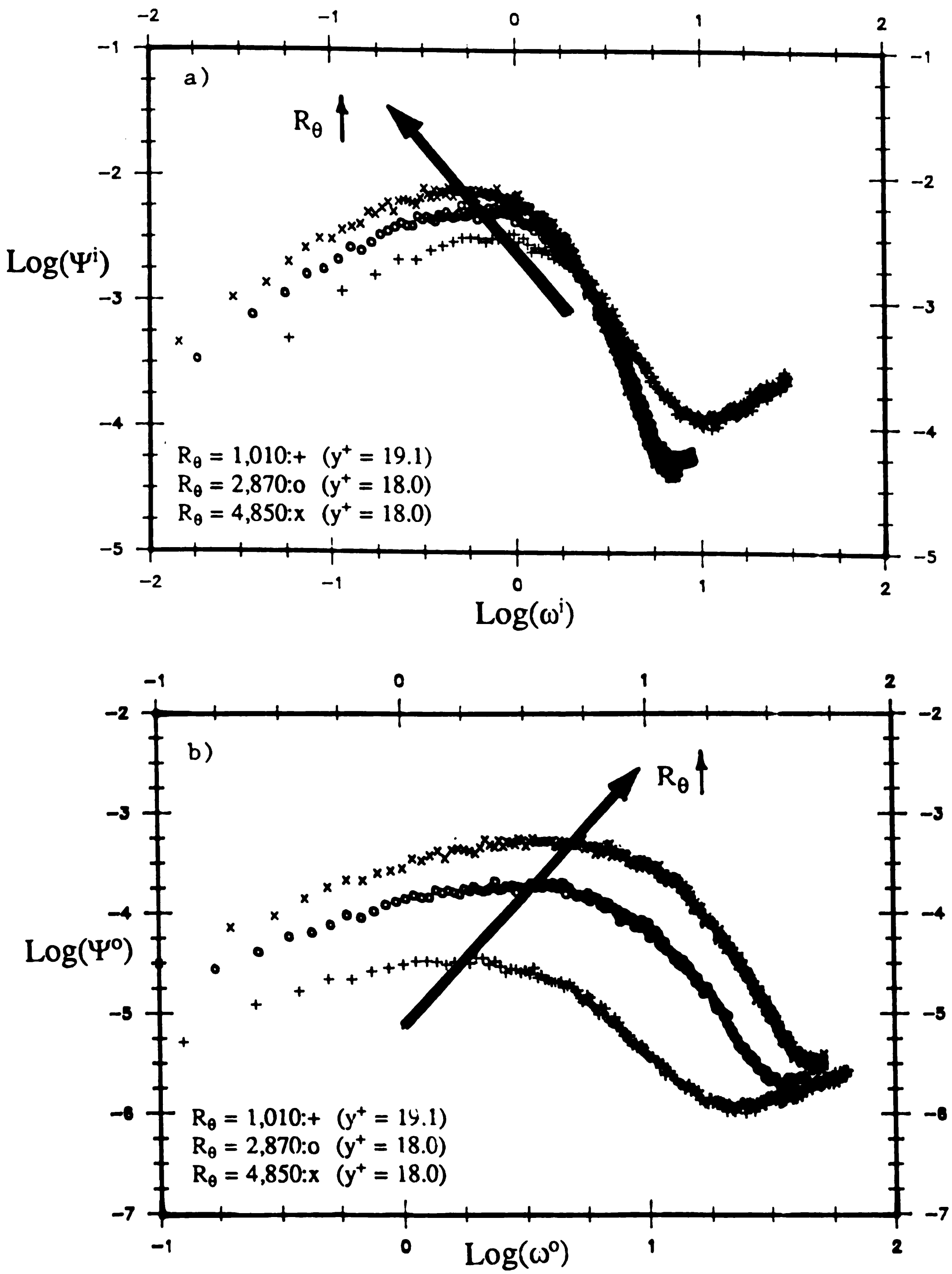

Figure 3.25 Spectral functions of $v\omega_z$ at $y^+ \cong 20$,
a) Inner normalization (see eq. 3.5)
b) Outer normalization (see eq. 3.6).

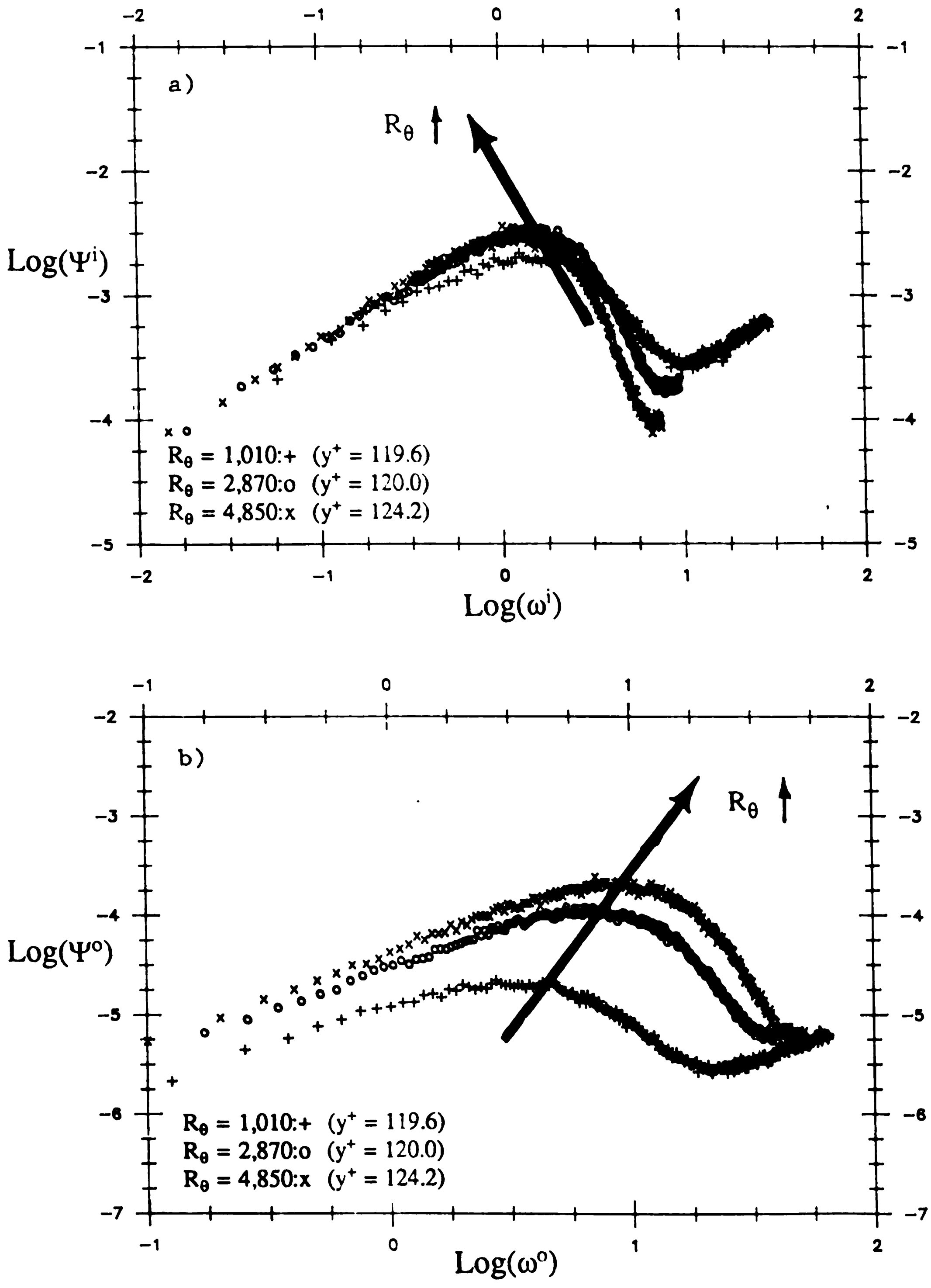

Figure 3.26 Spectral functions of $v\omega_z$ at $y^+ \cong 120$,
a) Inner normalization (see eq. 3.5)
b) Outer normalization (see eq. 3.6).

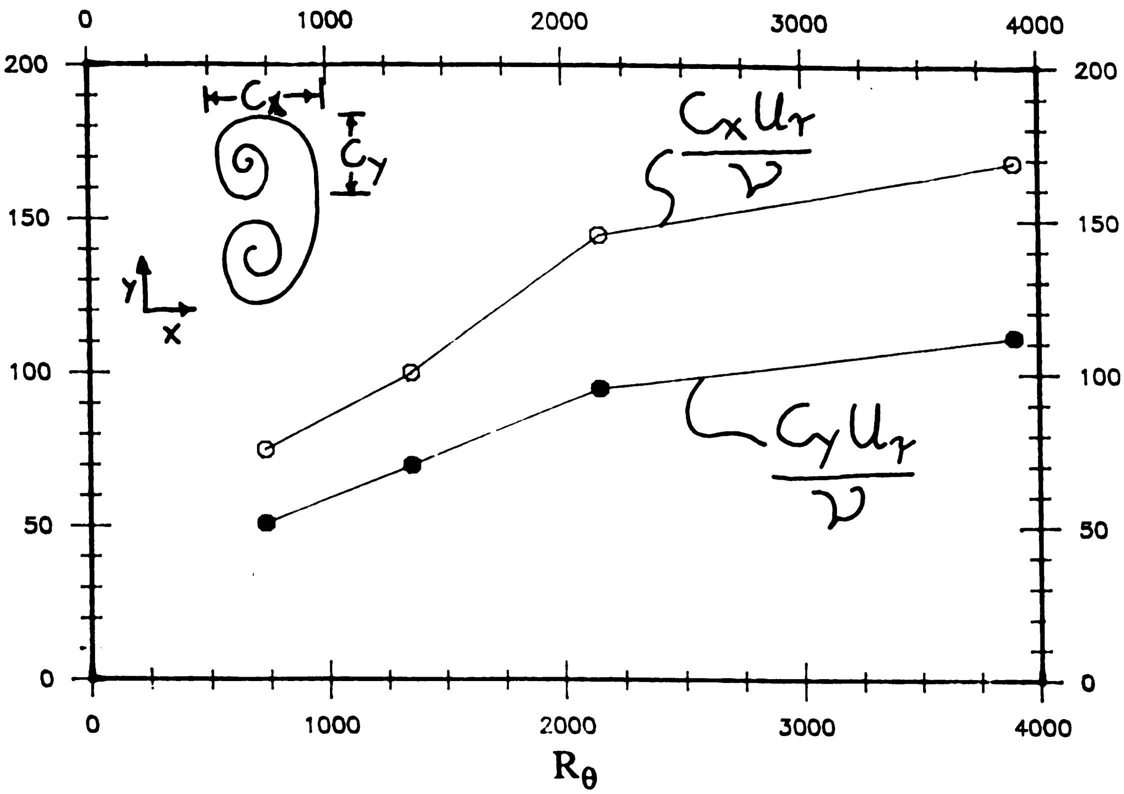

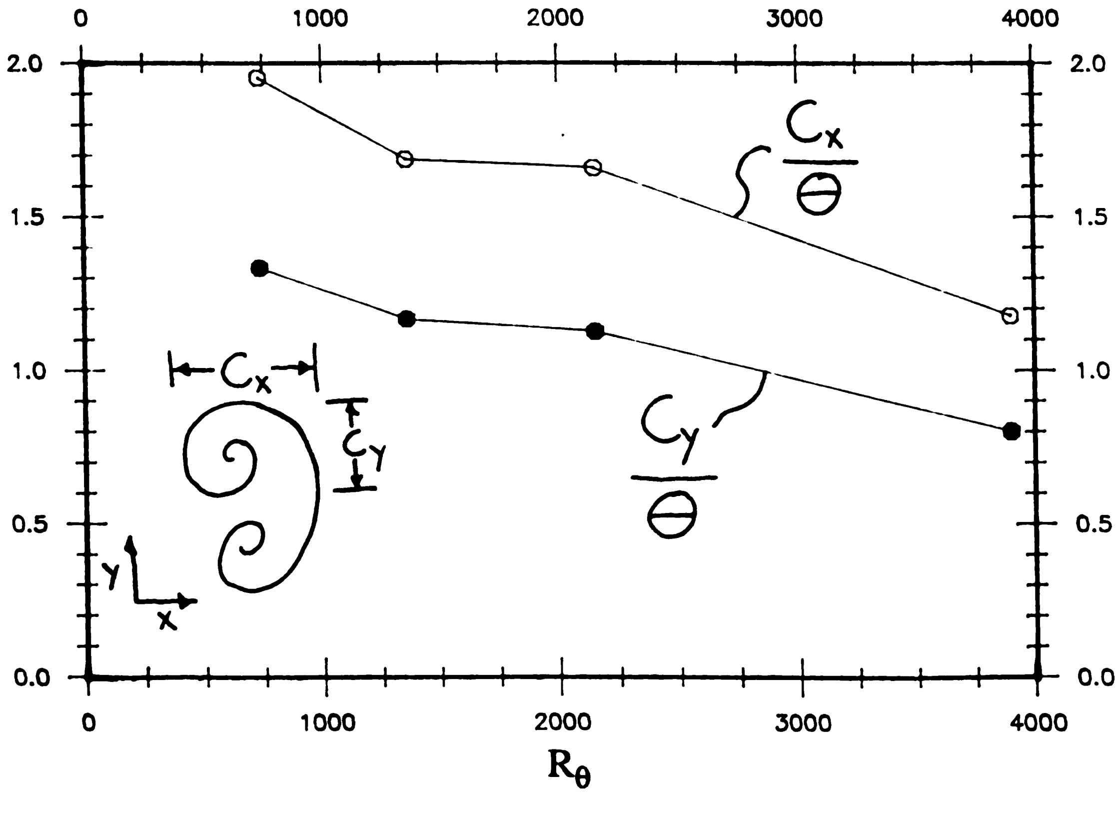

Figure 3.27 Reynolds number dependence of the vortex ring-like motions as measured by Falco (unpublished),
a) Inner normalization
b) Outer normalization.

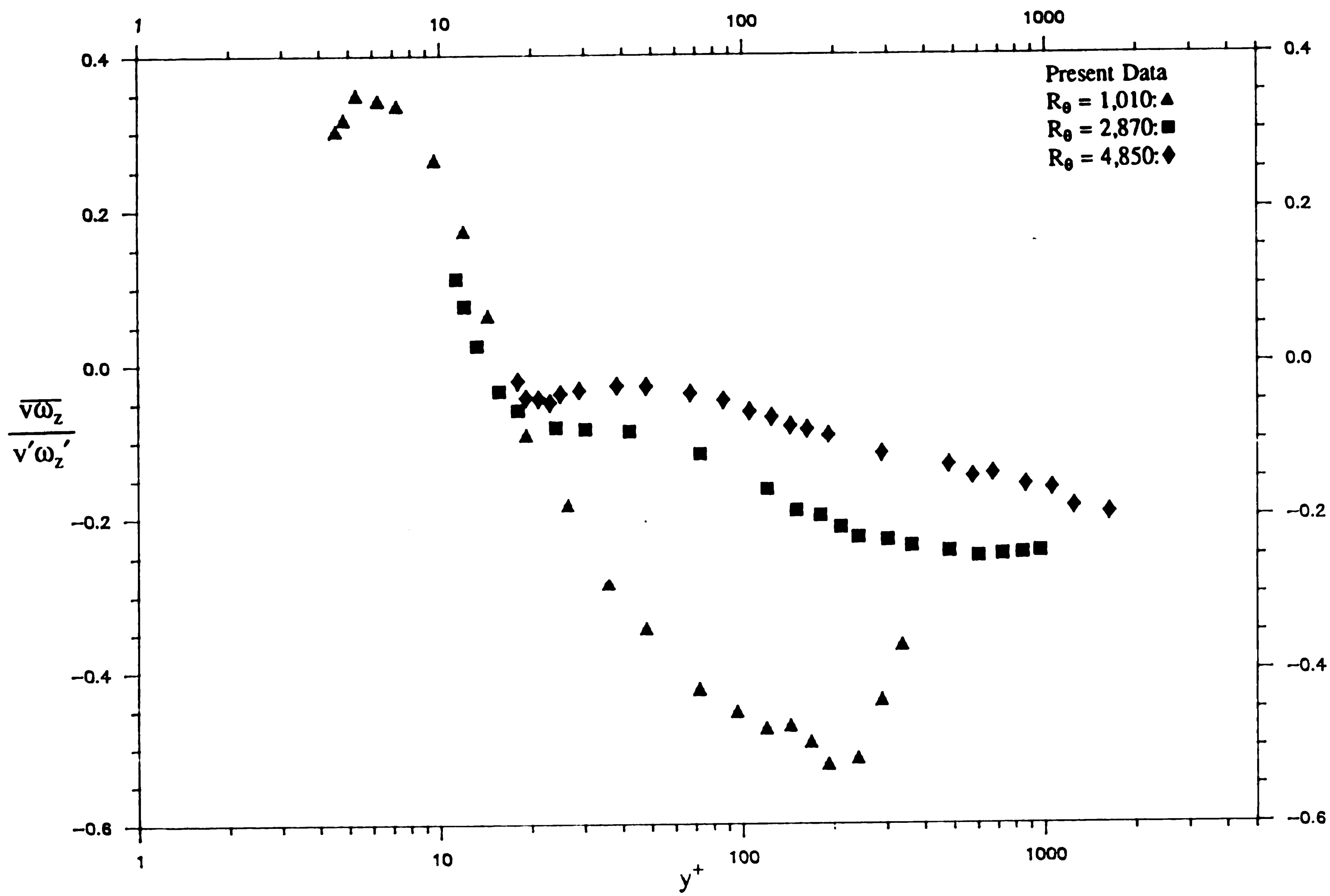

Figure 3.28 Correlation coefficient profiles of $v\omega_z$ versus y^+.

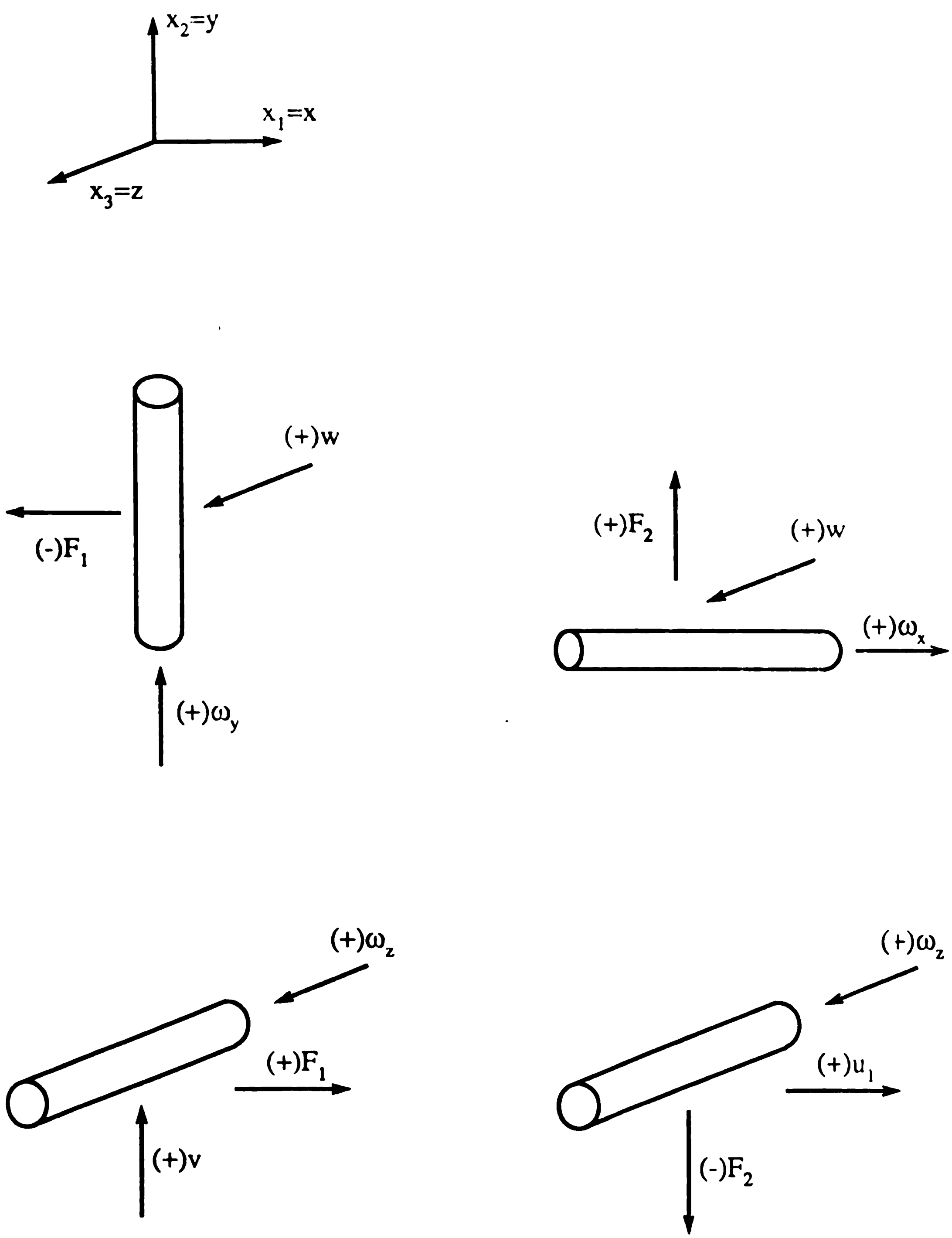

Figure 3.29 Vortex force directions for the given velocity vorticity products.

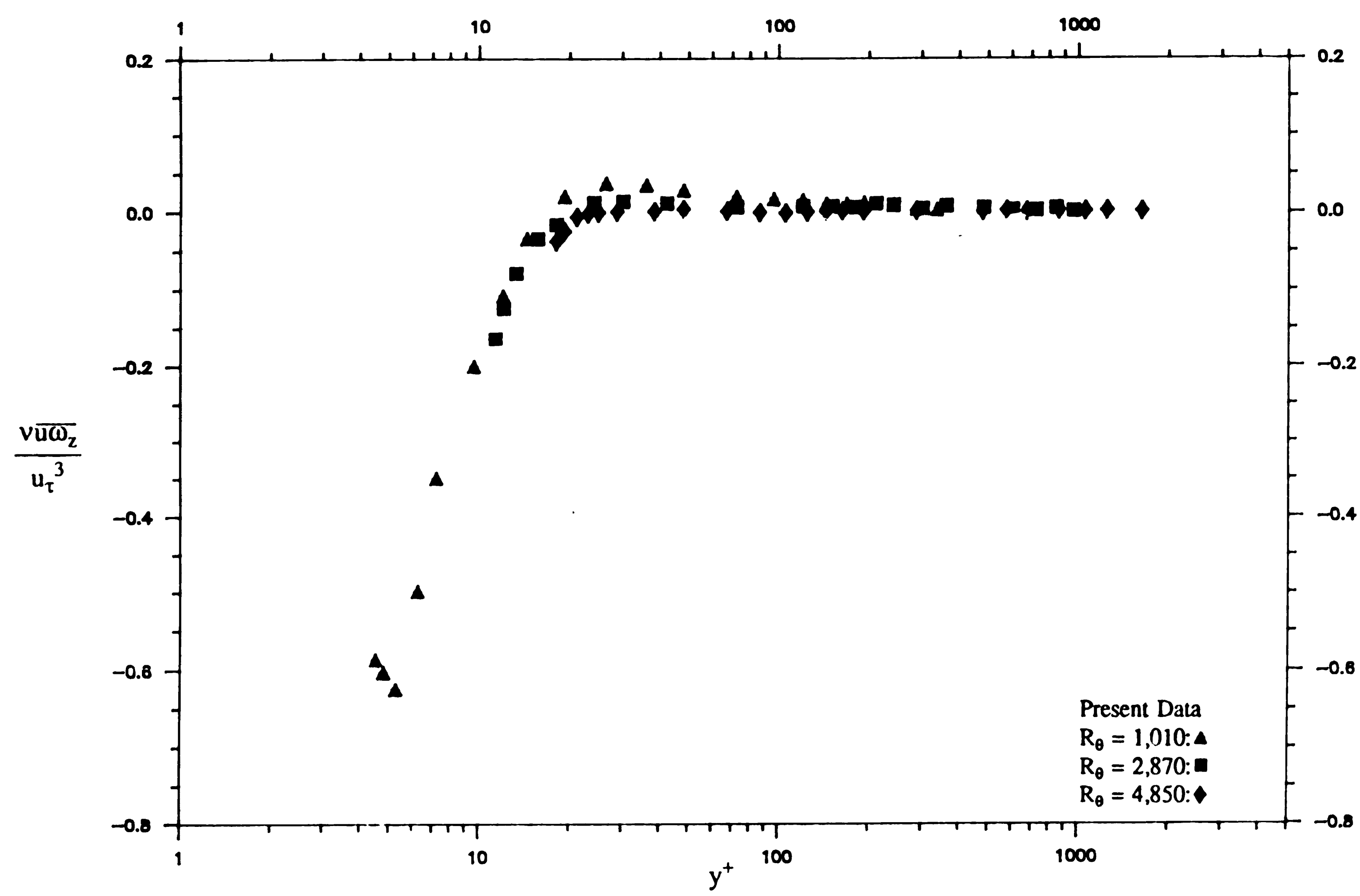

Figure 3.30 Inner variable normalized $<u\omega_z>$ profiles.

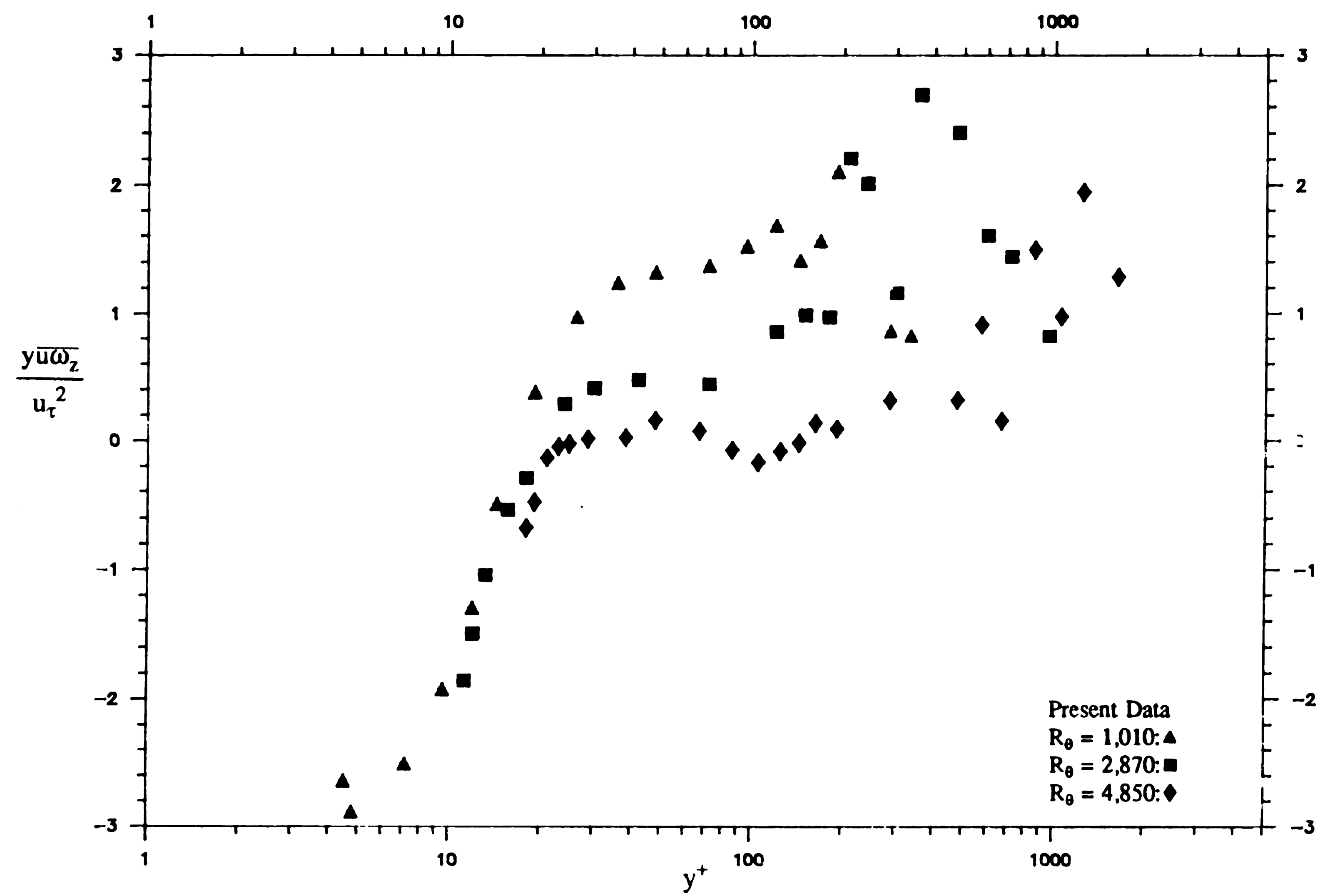

Figure 3.31 Normalization of the $<u\omega_z>$ profiles using the function y/u_τ^2.

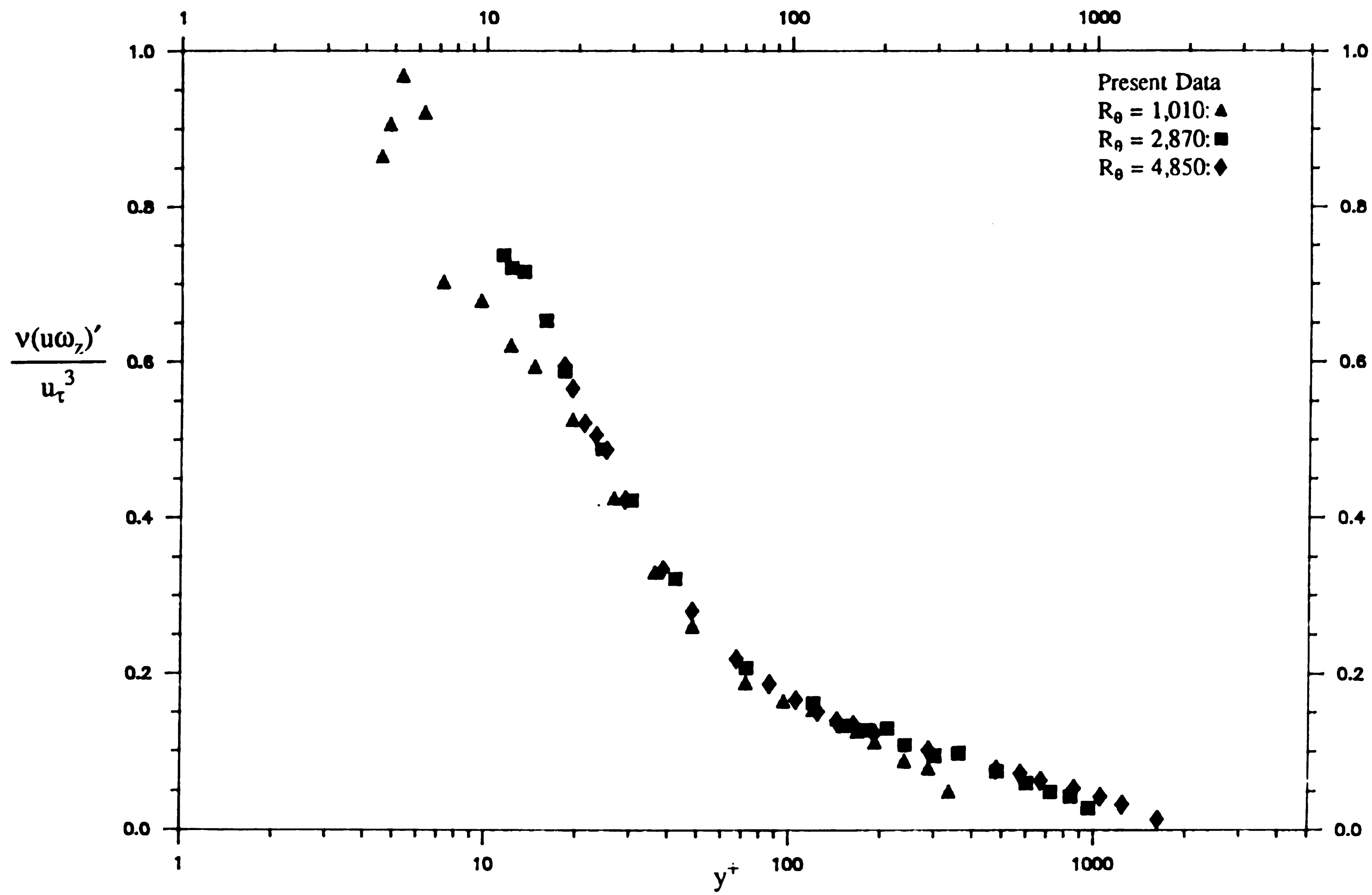

Figure 3.32 Inner variable normalized $(u\omega_z)'$ profiles.

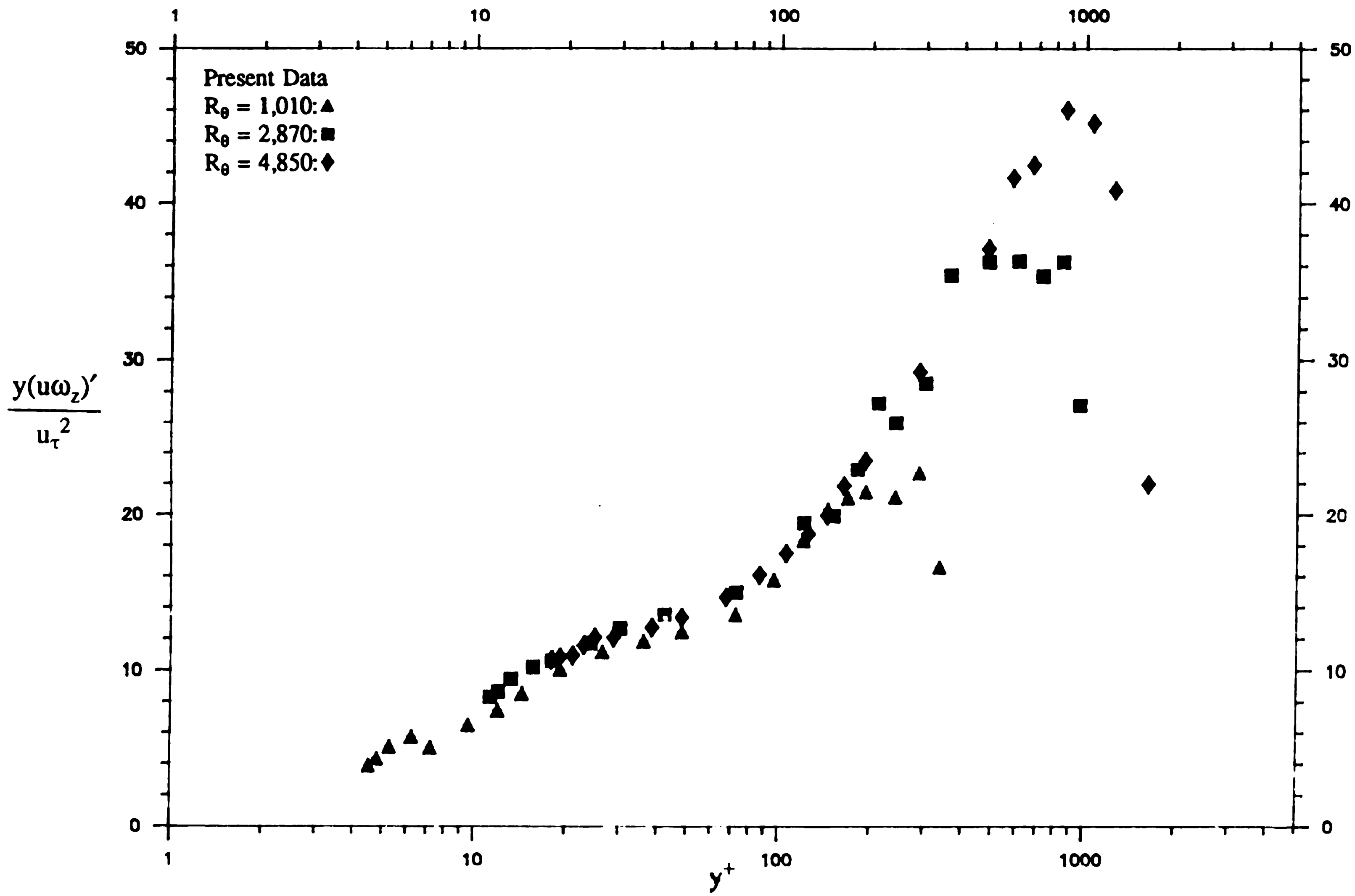

Figure 3.33 Normalization of the $(u\omega_z)'$ profiles using the function y/u_τ^2.

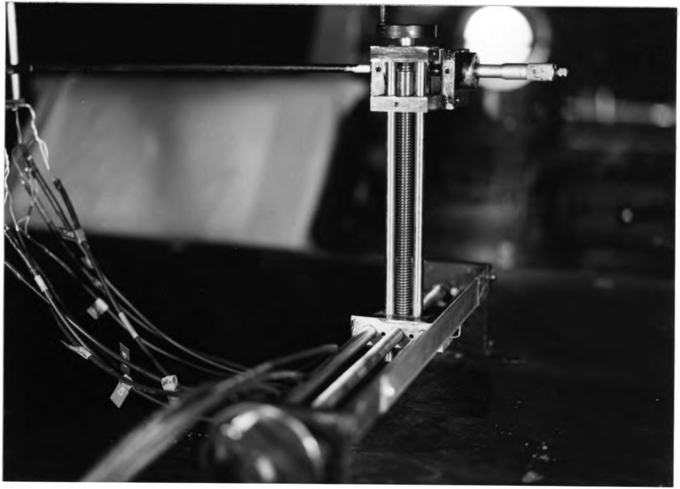

Figure 4.1 Traverse mechanism used in the Δz probe separation correlation experiments.

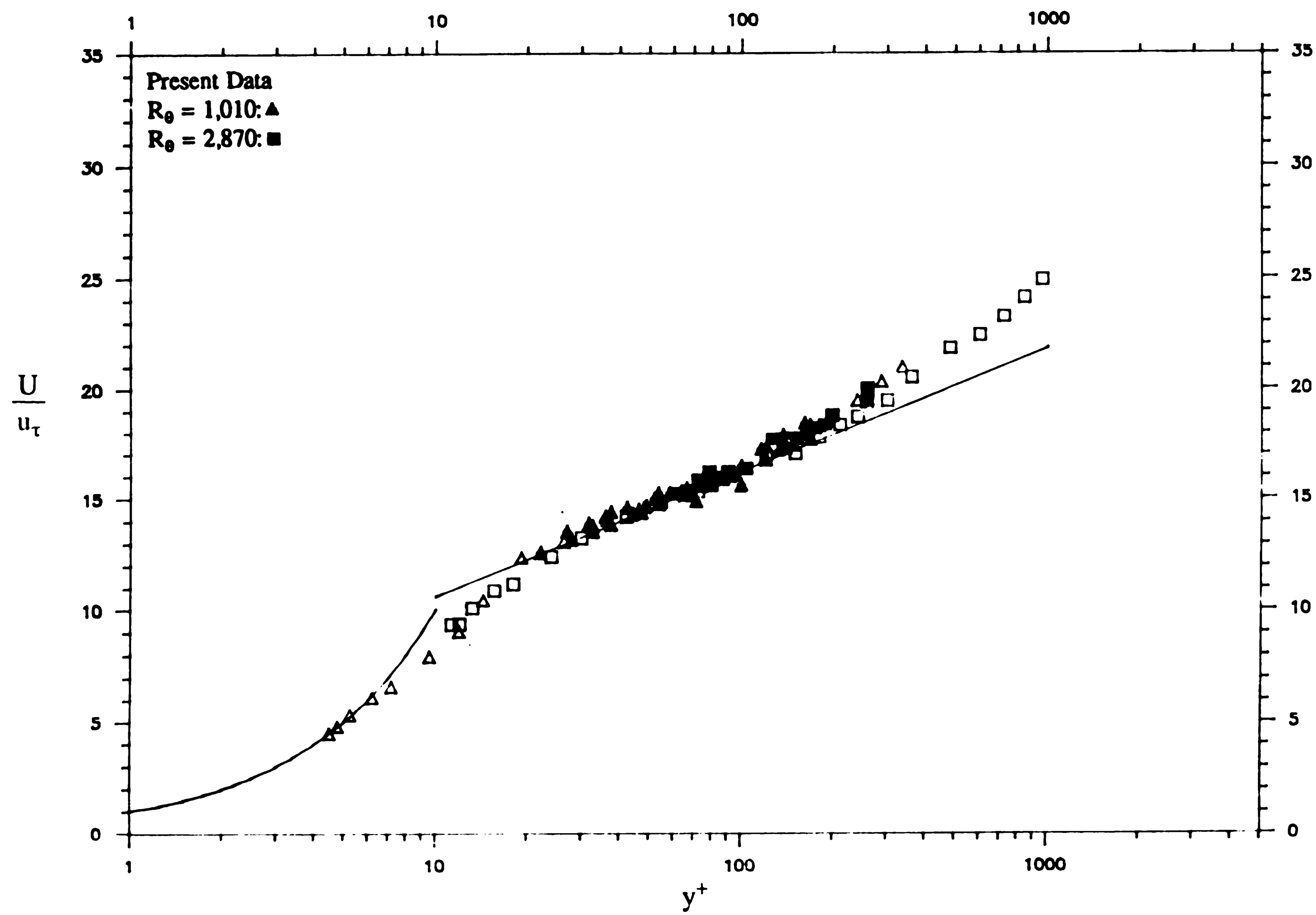

Figure 4.2 Mean velocity measurements from the moving probe of the Δy correlation experiments as normalized by the friction velocities in Table 2.1 and overlaid on the single probe profiles of Figure 2.2.

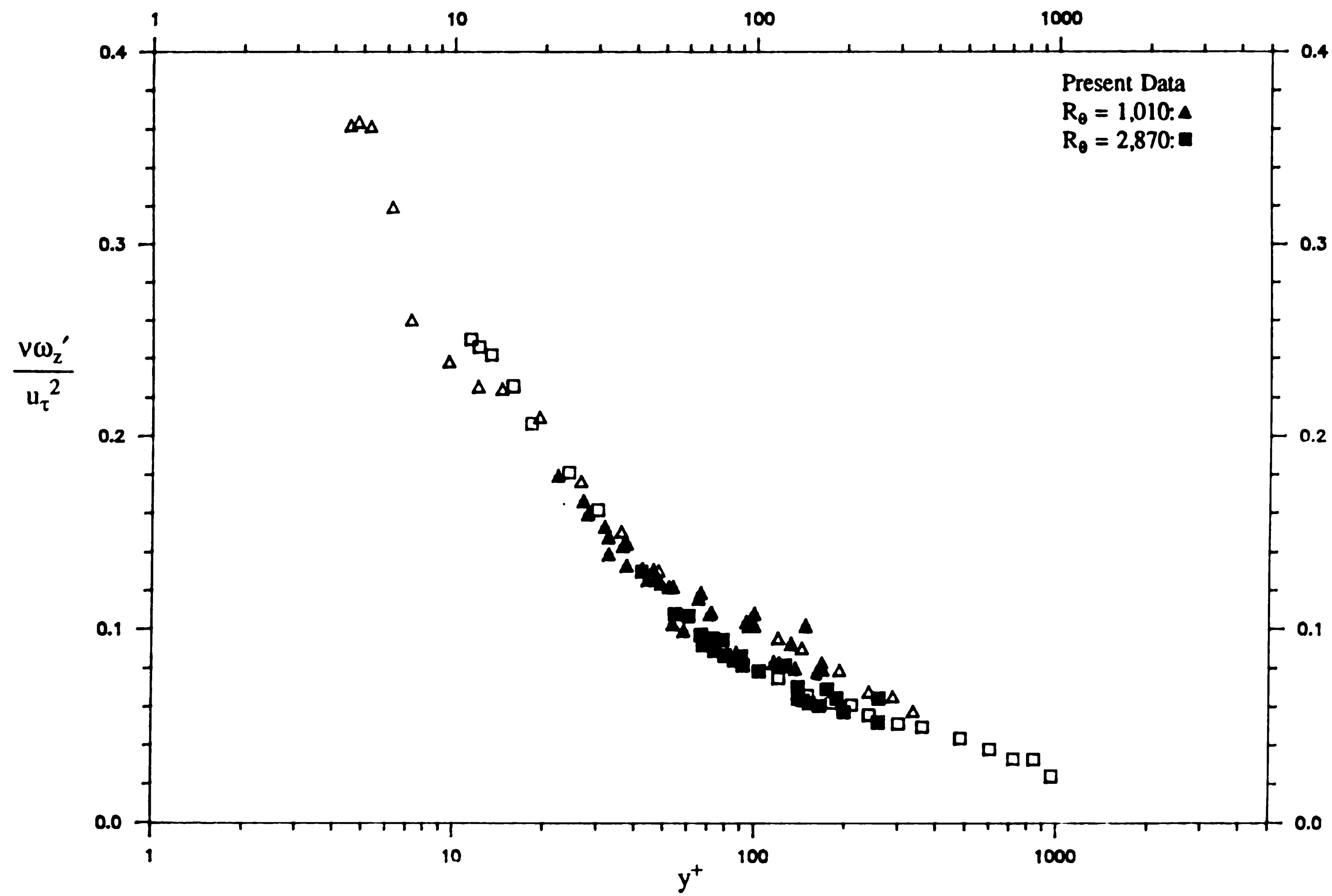

Figure 4.3 Spanwise vorticity intensity measurements from the moving probe of the Δy correlation experiments as normalized by the friction velocities in Table 2.1 and overlaid on the single probe profiles of Figure 2.14.

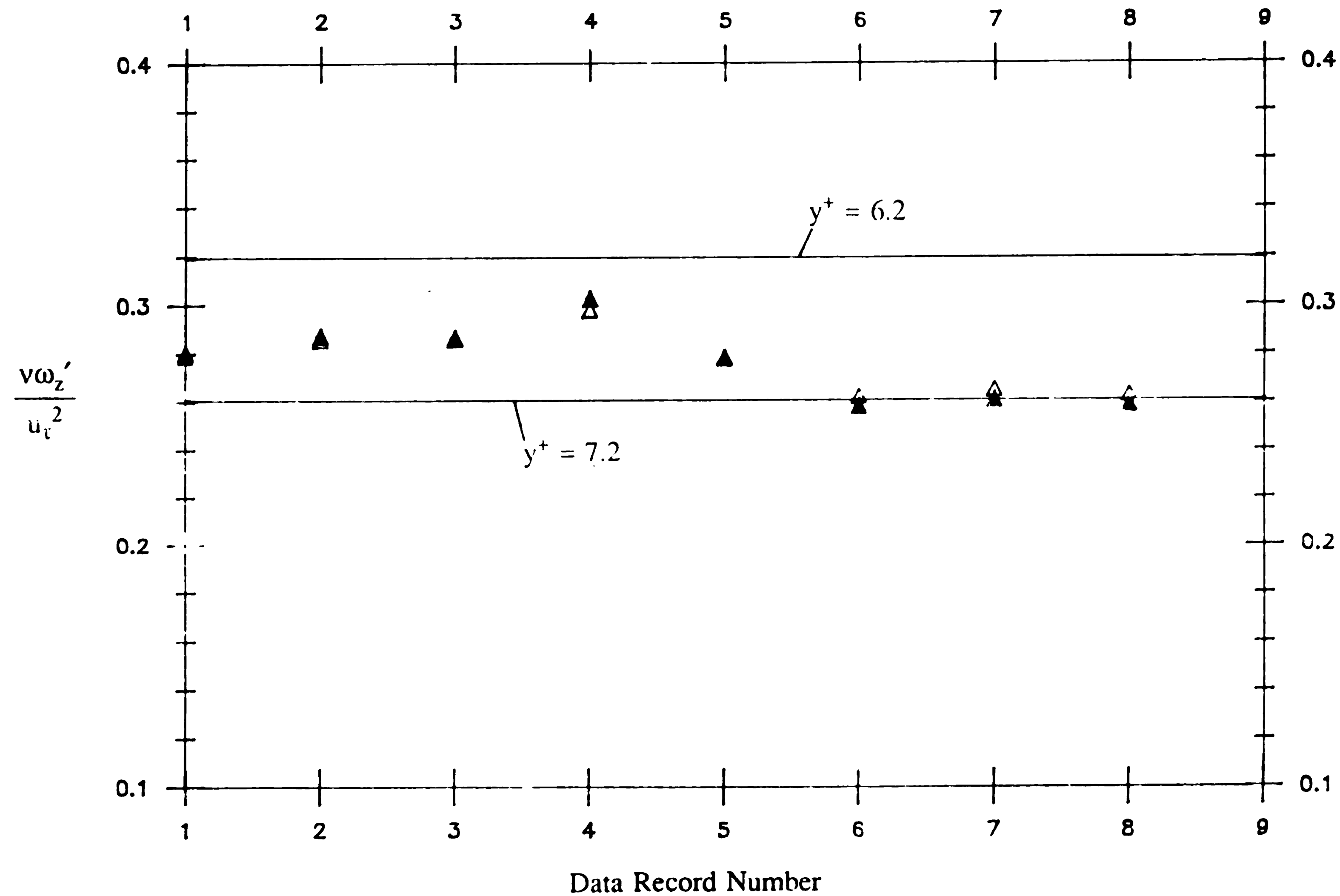

Figure 4.4 Spanwise vorticity intensity measurements from the $R_\theta \cong 1{,}010$ Δz probe separation experiments at $y^+ = 6.7$ as normalized by the friction velocity in Table 2.1 and compared with the relevant values of Figure 2.14, open symbols -- stationary probe, solid symbols -- moving probe.

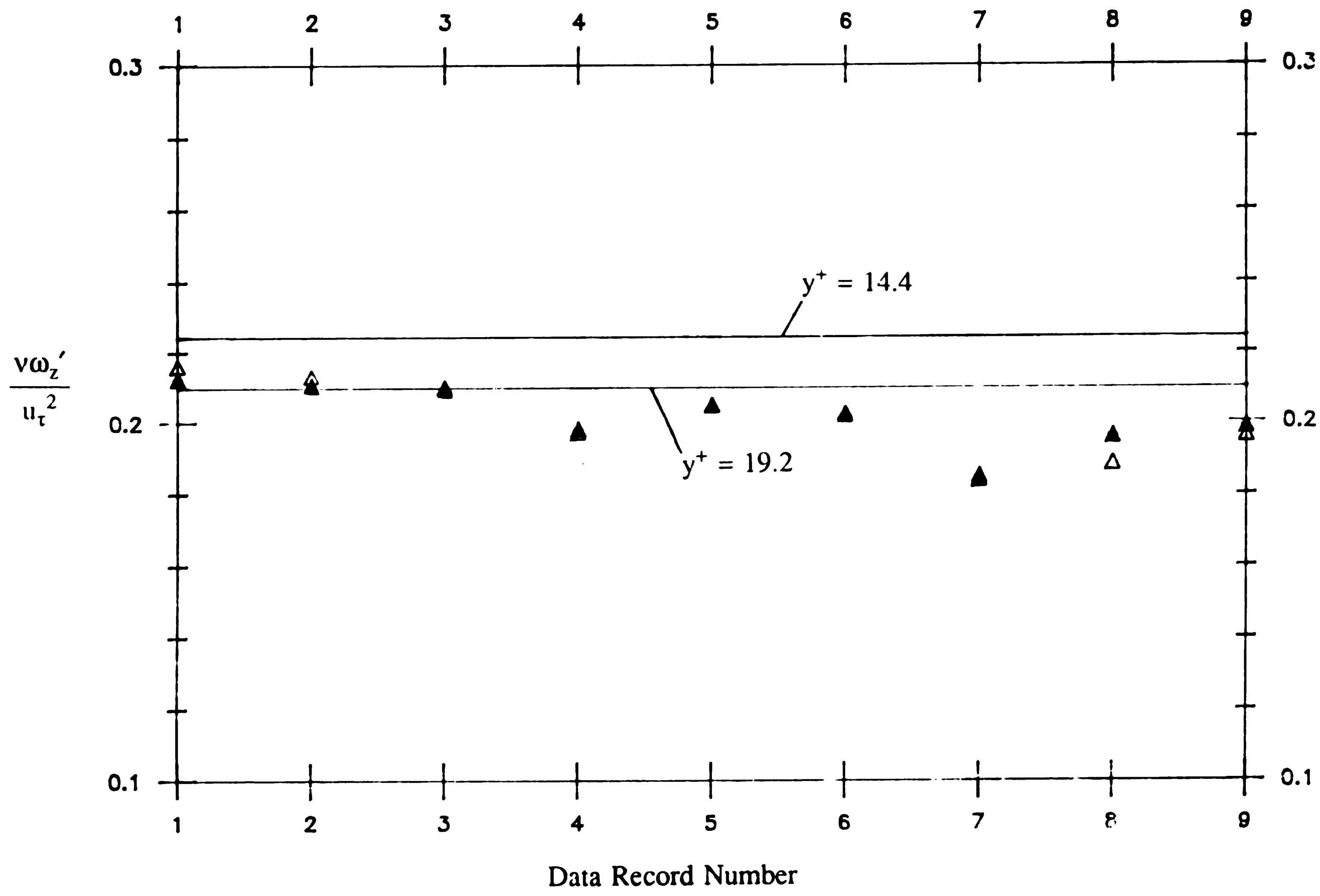

Figure 4.5 Spanwise vorticity intensity measurements from the $R_\theta \cong 1{,}010$ Δz probe separation experiments at $y^+ = 15.3$ as normalized by the friction velocity in Table 2.1 and compared with the relevant values of Figure 2.14, open symbols -- stationary probe, solid symbols -- moving probe.

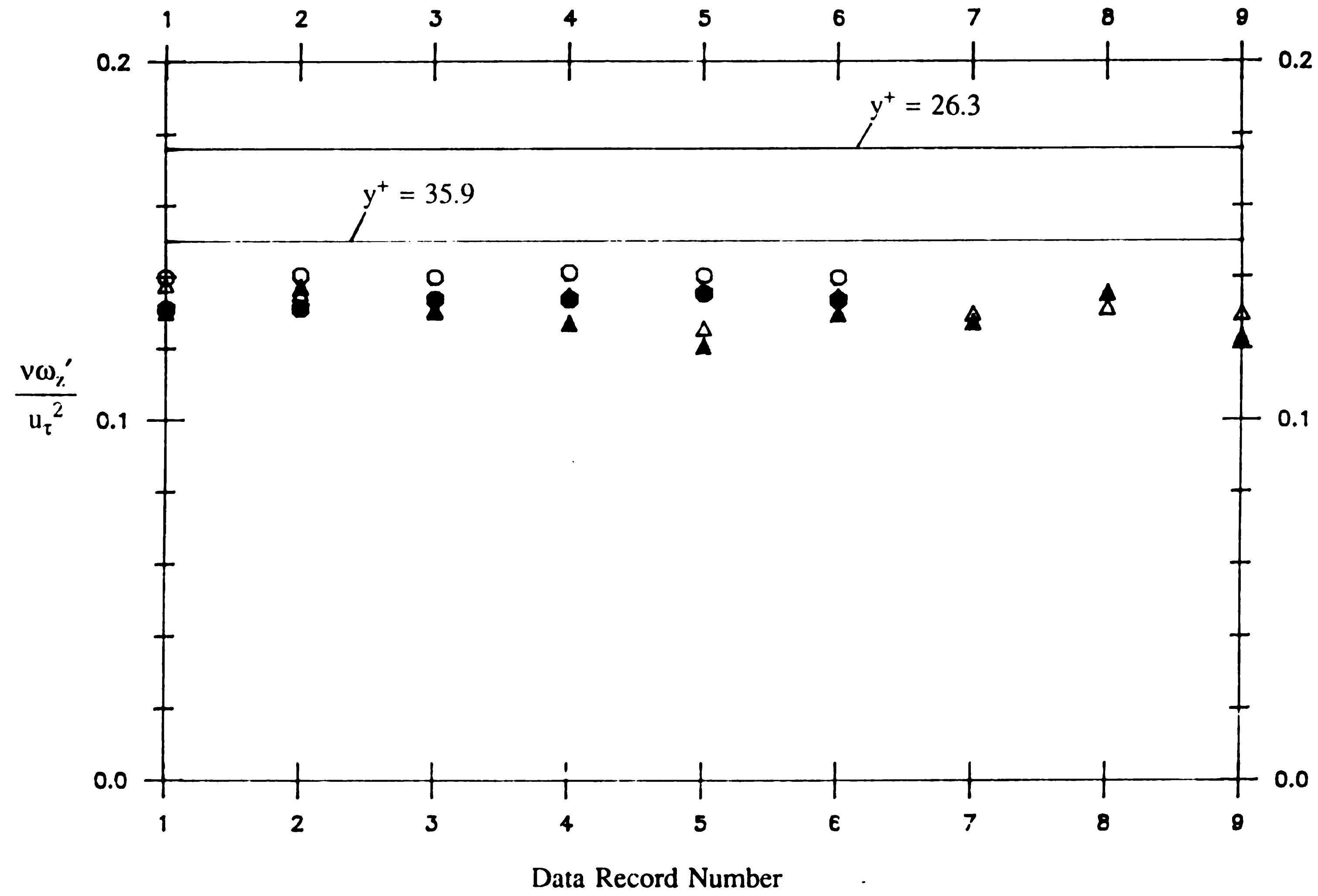

Figure 4.6 Spanwise vorticity intensity measurements from the $R_\theta \cong 1{,}010$ Δz probe separation experiments at $y^+ = 33.5$ as normalized by the friction velocity in Table 2.1 and compared with the relevant values of Figure 2.14, open symbols -- stationary probe, solid symbols -- moving probe.

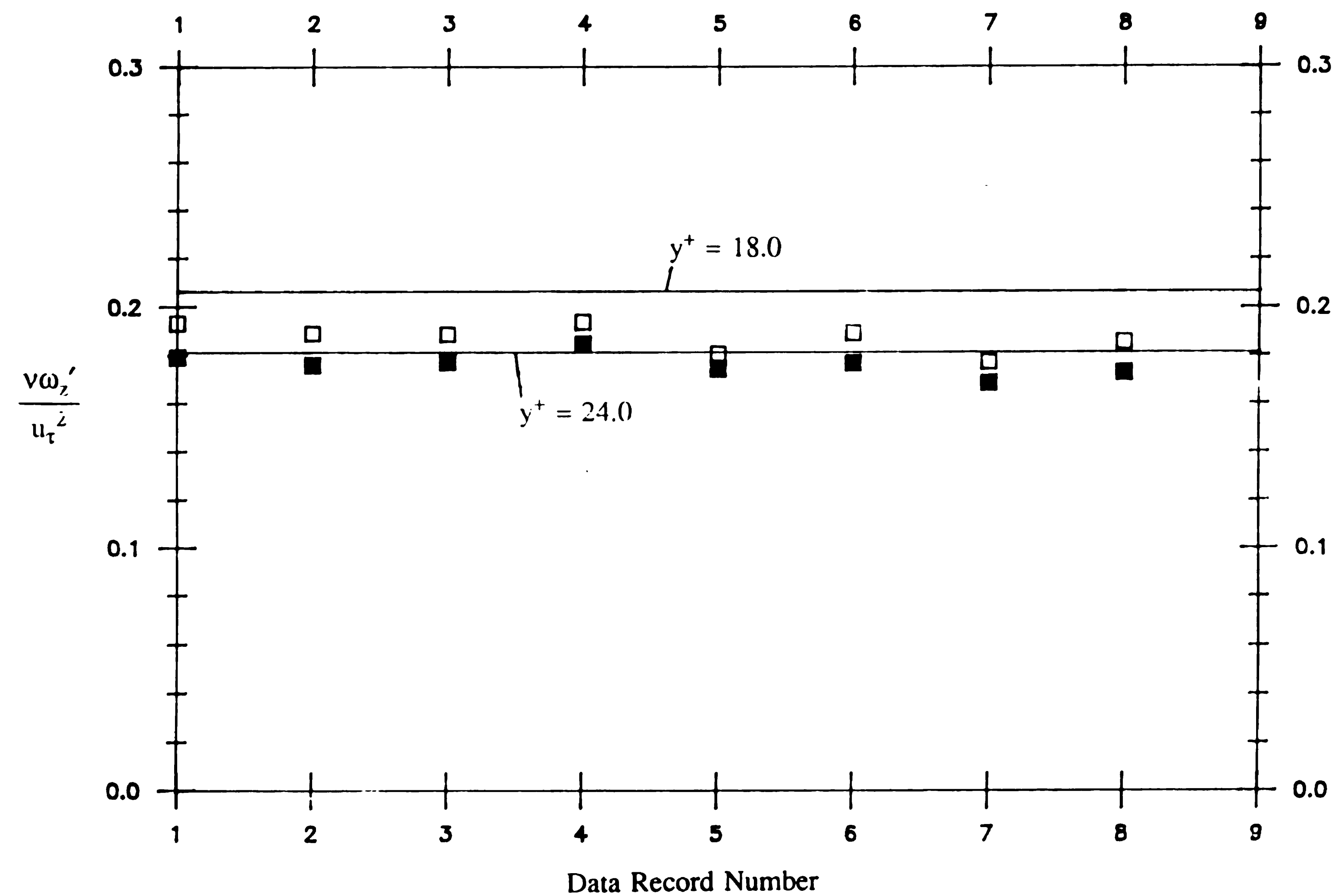

Figure 4.7 Spanwise vorticity intensity measurements from the $R_\theta \cong 2,870$ Δz probe separation experiments at $y^+ = 20.4$ as normalized by the friction velocity in Table 2.1 and compared with the relevant values of Figure 2.14, open symbols -- stationary probe, solid symbols -- moving probe.

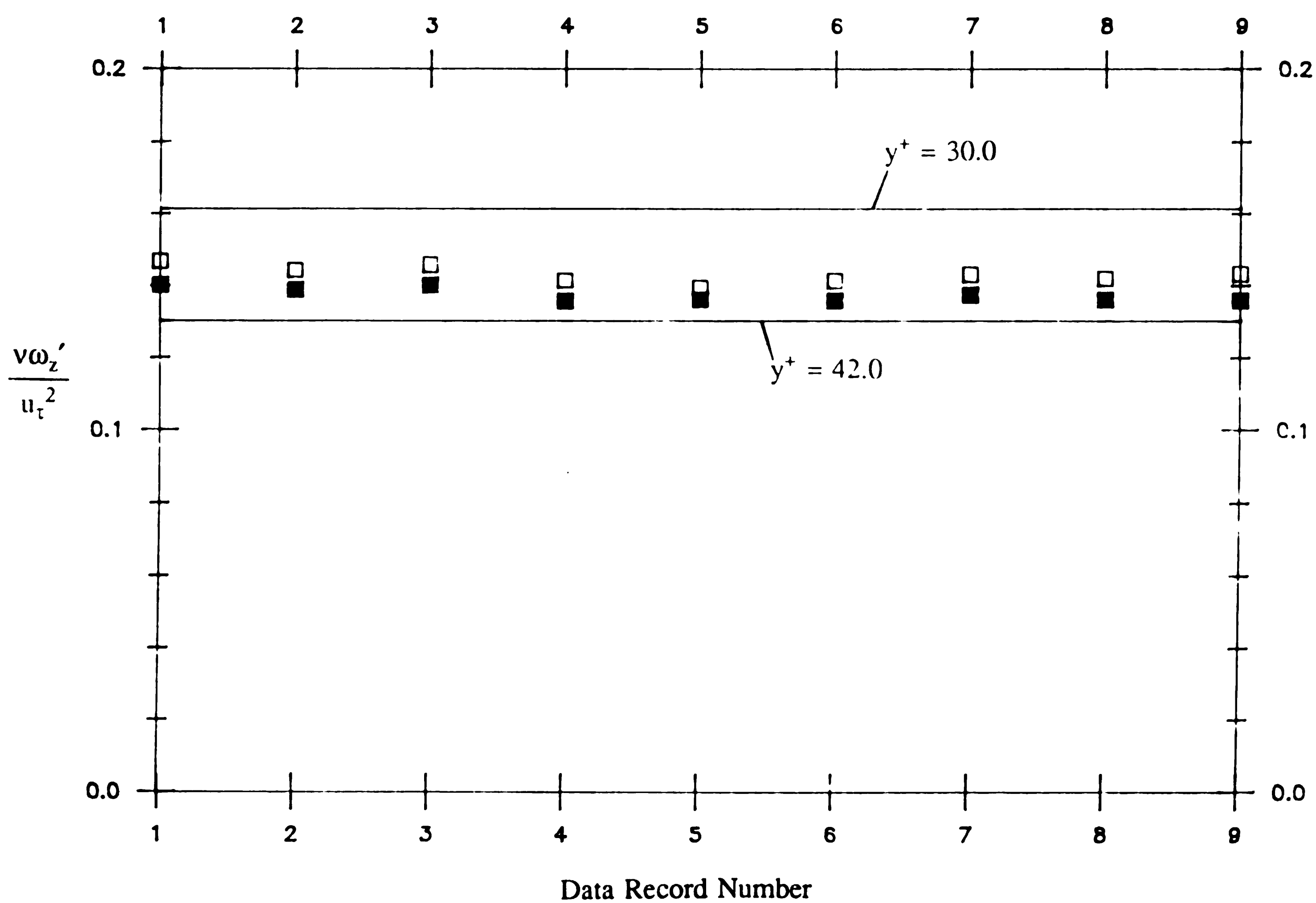

Figure 4.8 Spanwise vorticity intensity measurements from the $R_\theta \cong 2,870$ Δz probe separation experiments at $y^+ = 33.6$ as normalized by the friction velocity in Table 2.1 and compared with the relevant values of Figure 2.14, open symbols -- stationary probe, solid symbols -- moving probe.

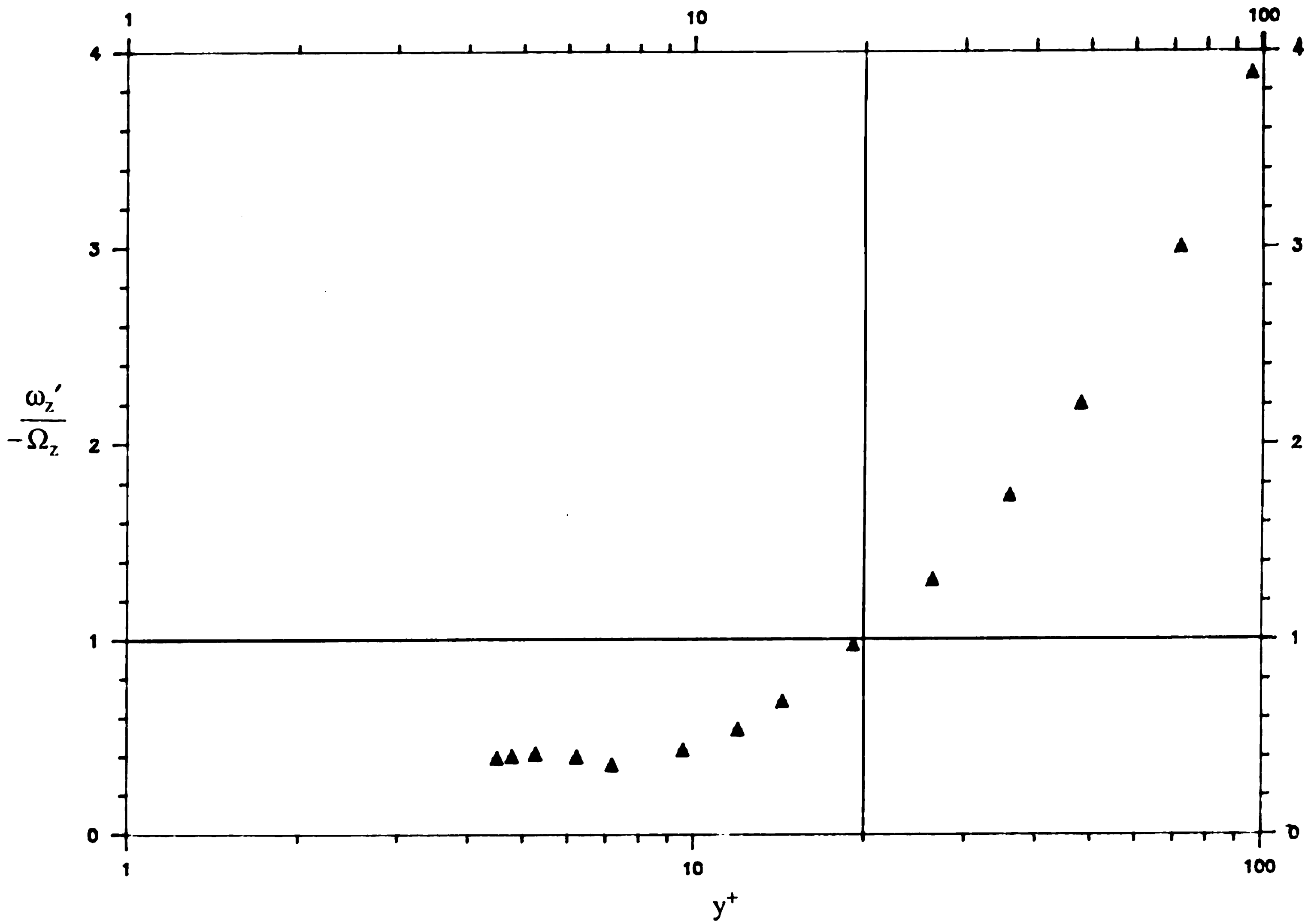

Figure 4.9 Ratio of the present spanwise vorticity intensity profile at $R_\theta = 1{,}010$ to the mean vorticity profile, $\Omega_z \cong -\partial U/\partial y$, of Van Driest (1956) as given in Figure A2.3.1.

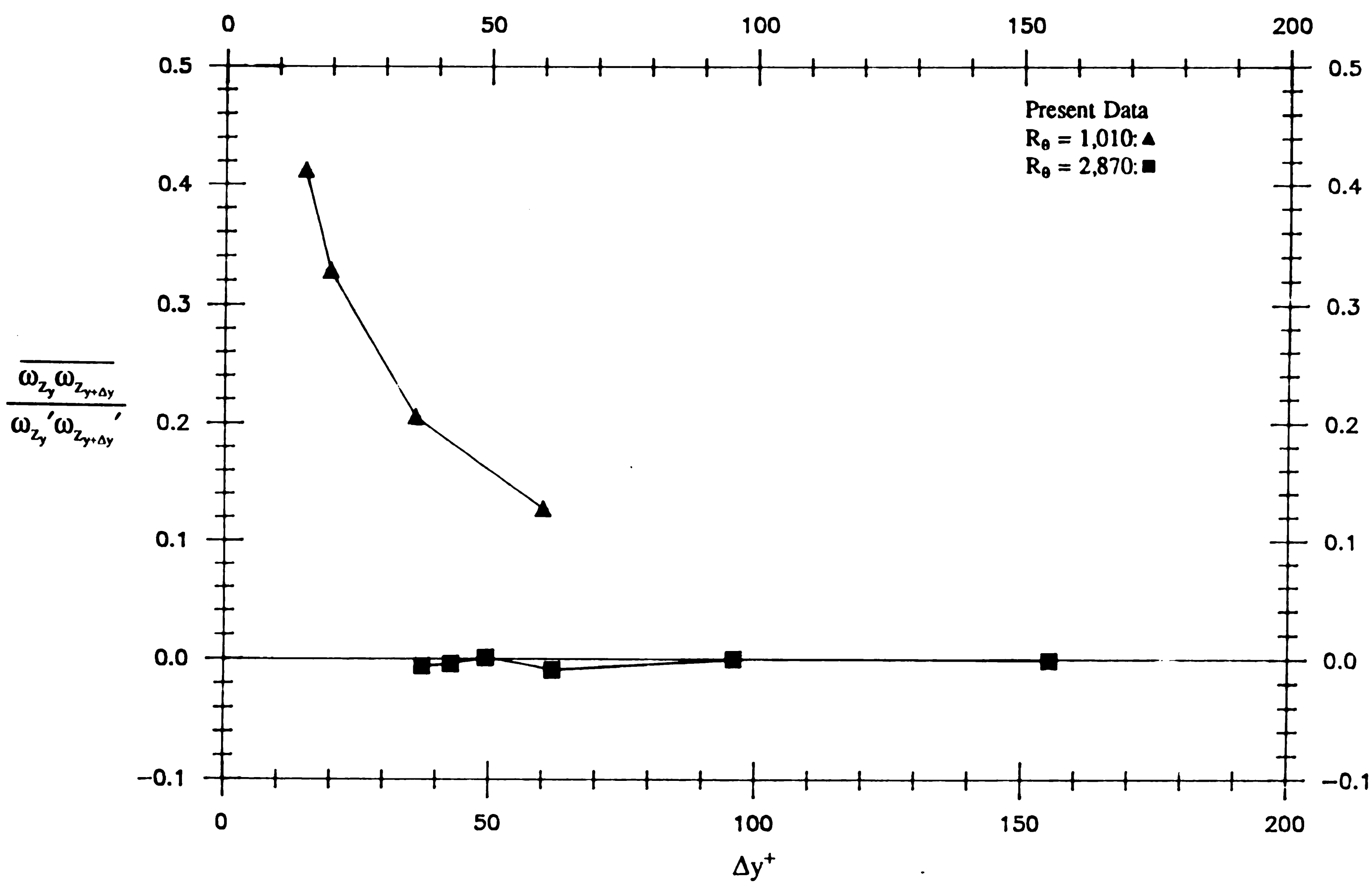

Figure 4.10 Results of the ω_z-ω_z correlations for positive Δy separations and the stationary probe positioned at $y^+ \cong 100$.

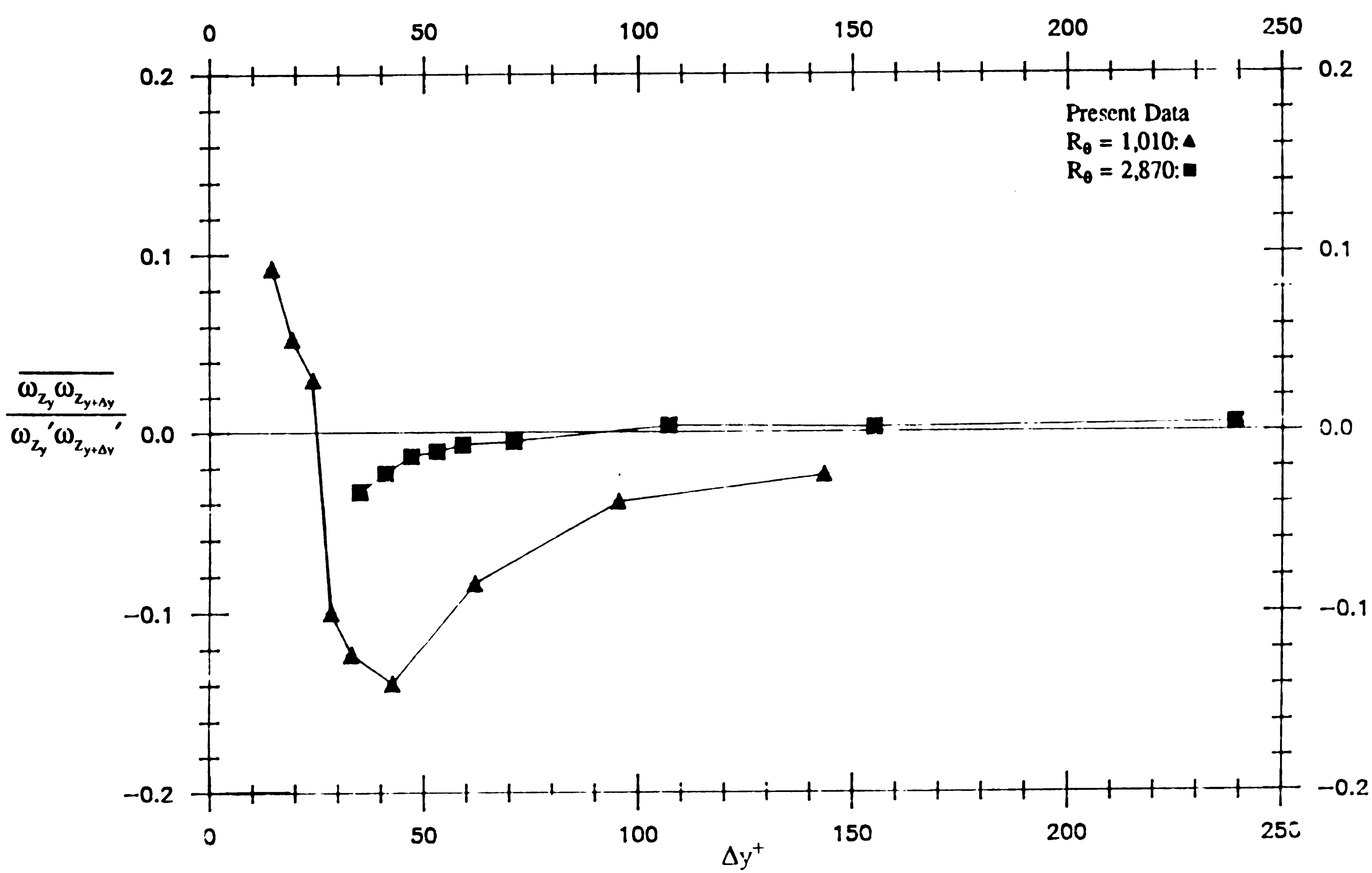

Figure 4.11 Results of the ω_z-ω_z correlations for positive Δy separations and the stationary probe positioned at $y^+ \cong 30$.

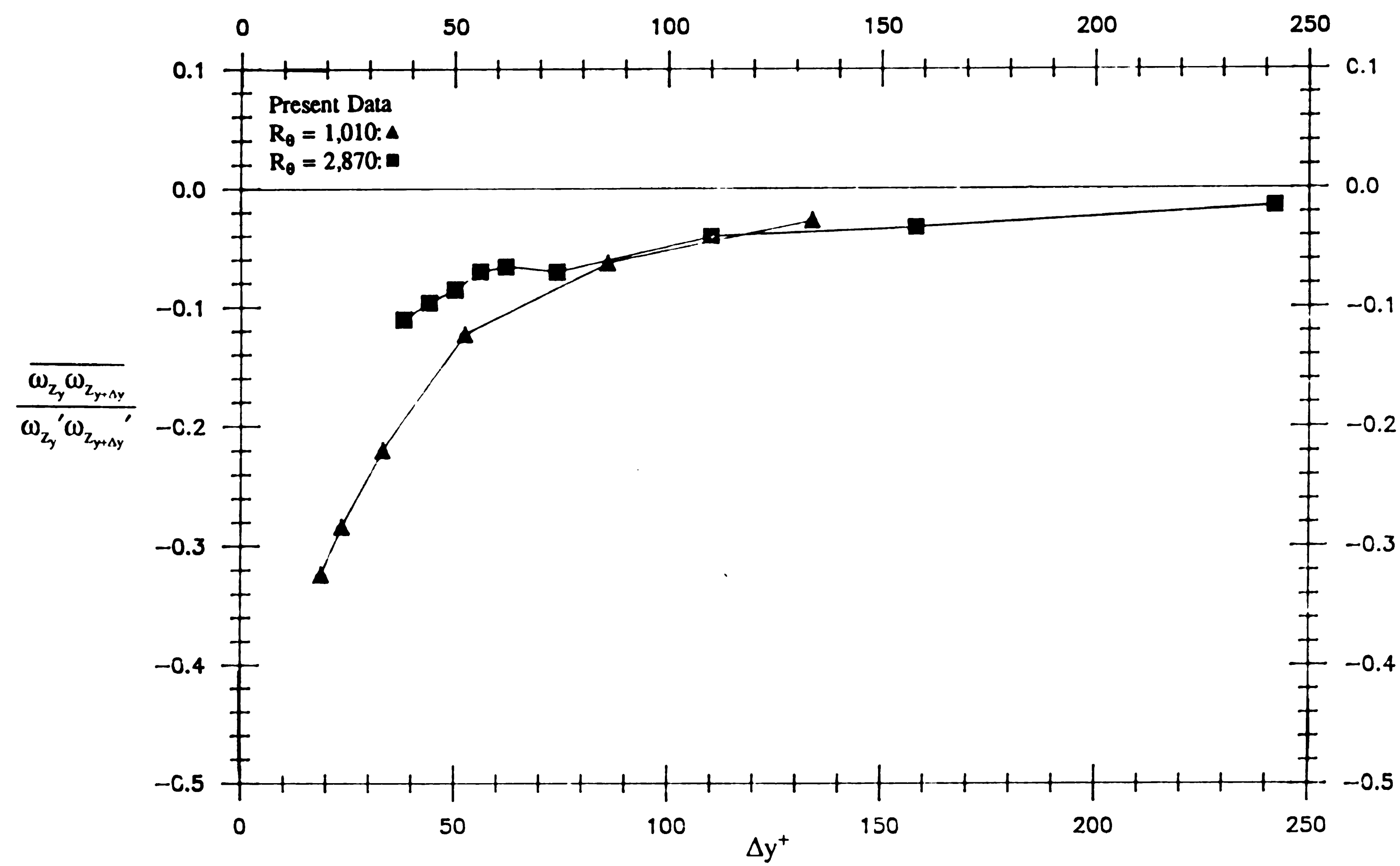

Figure 4.12 Results of the ω_z-ω_z correlations for positive Δy separations and the stationary probe positioned at $y^+ \cong 15$.

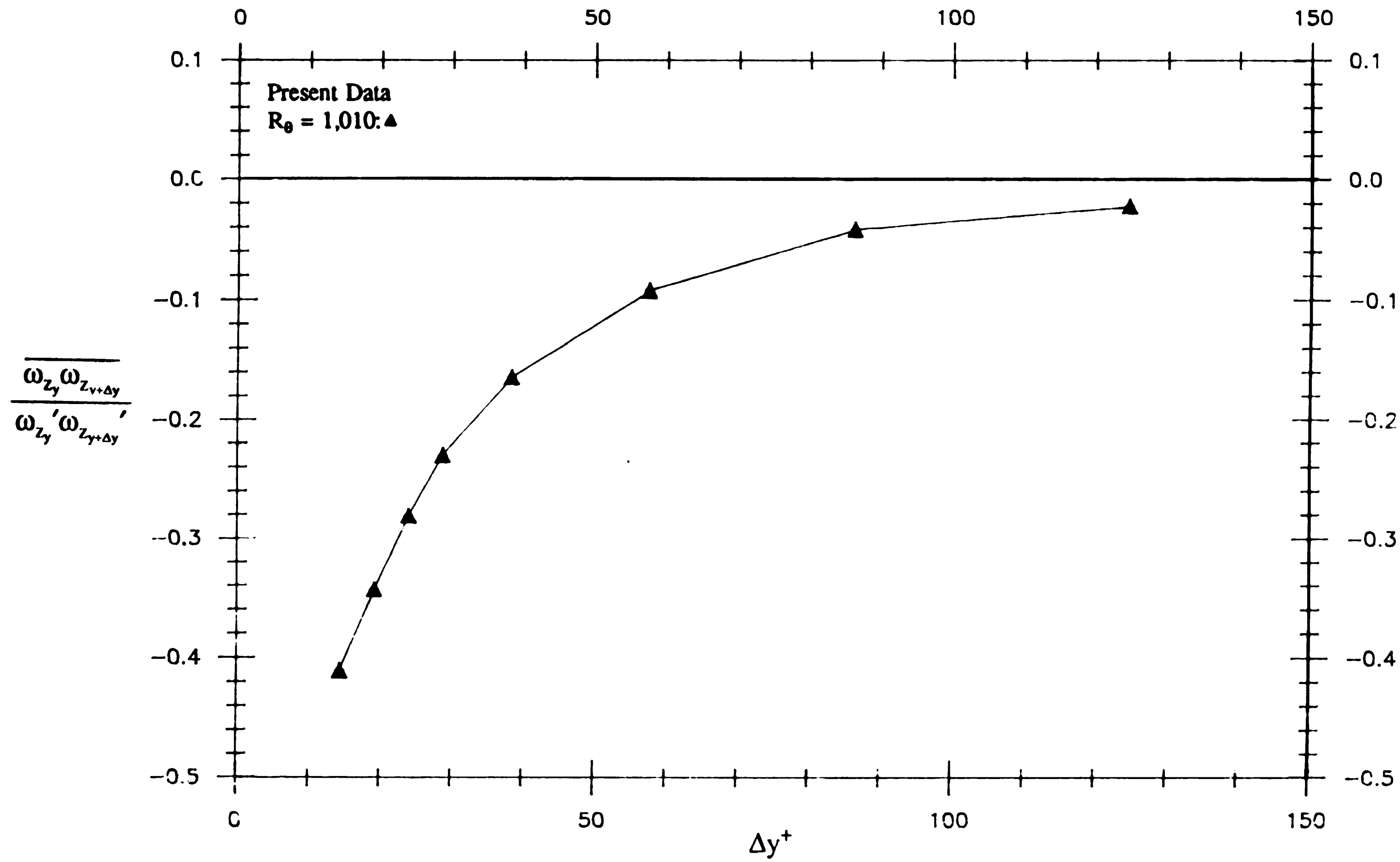

Figure 4.13 Results of the ω_z-ω_z correlations for positive Δy separations and the stationary probe positioned at $y^+ = 7.5$ ($R_\theta = 1{,}010$ only).

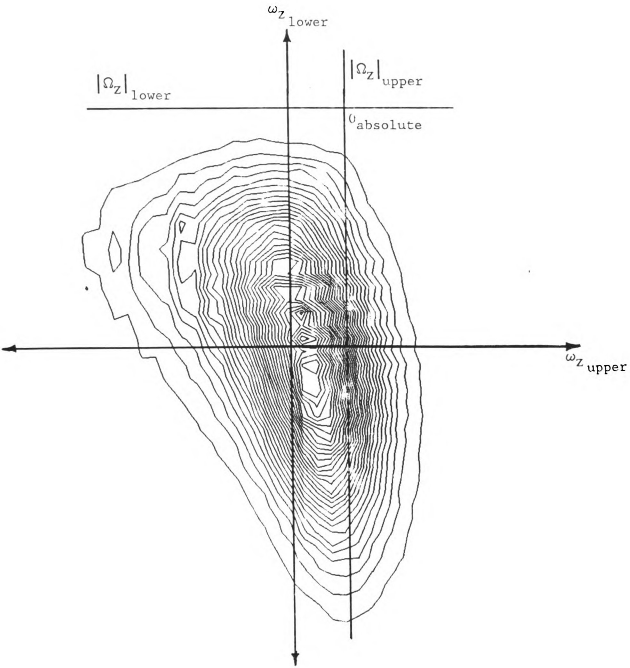

Figure 4.14 Two dimensional probability contour map as derived from the fluctuating spanwise vorticity signals contributing to the data point of closest separation in Figure 4.13.

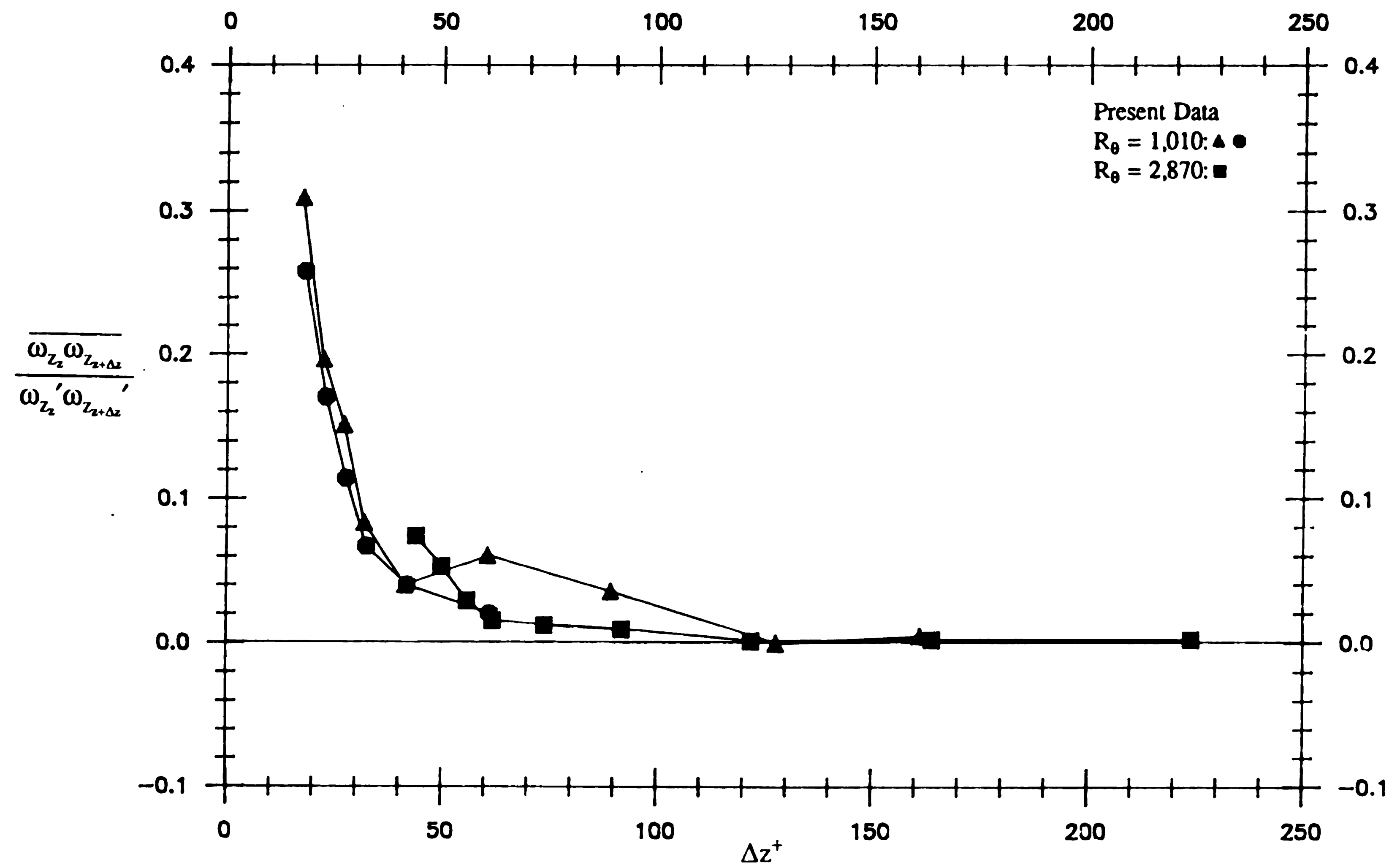

Figure 4.15 Results of the ω_z-ω_z correlations for Δz separations and the probes positioned at $y^+ \cong 30$.

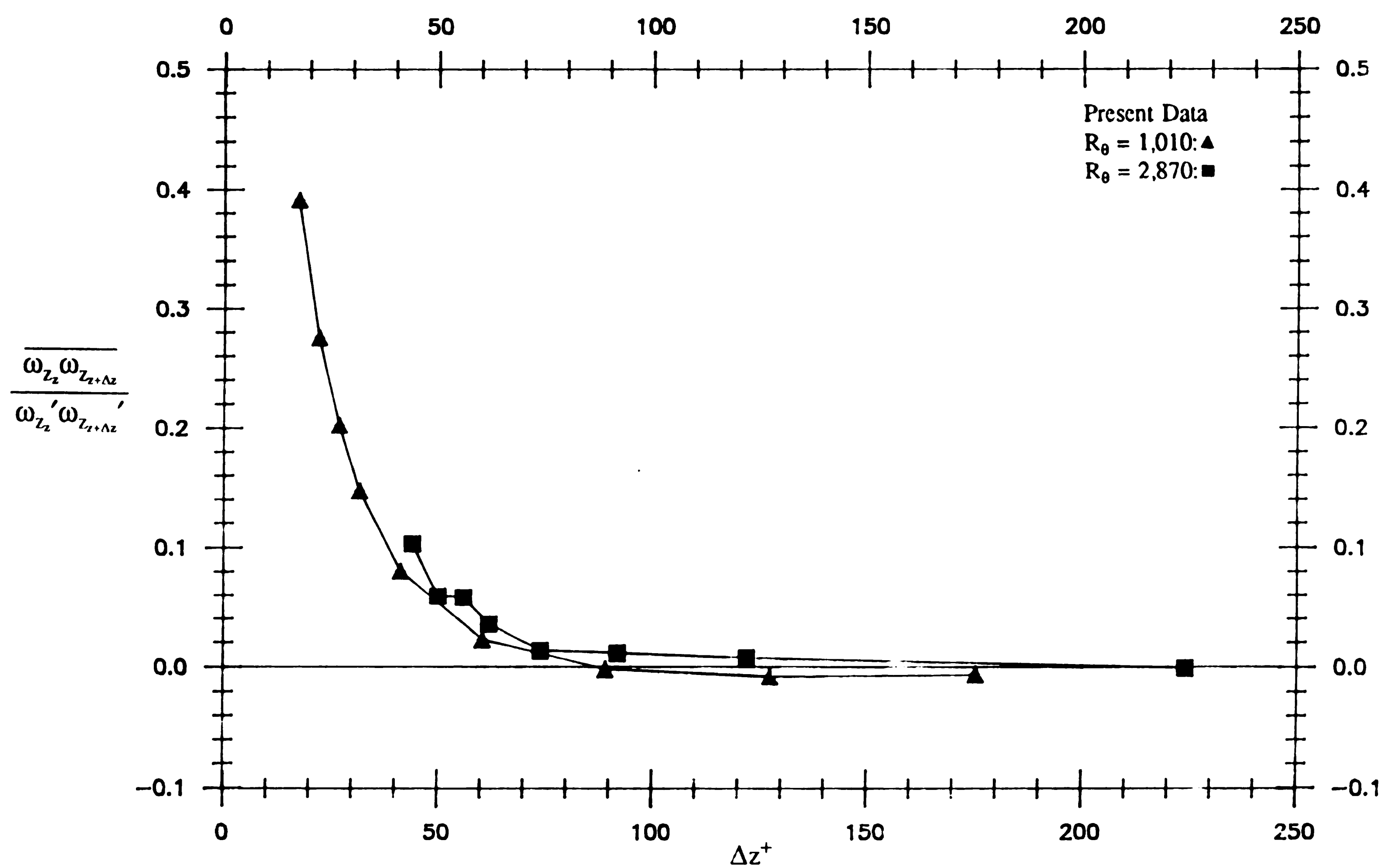

Figure 4.16 Results of the ω_z-ω_z correlations for Δz separations and the probes positioned at $y^+ = 15.3$ at $R_\theta = 1,010$ and $y^+ = 20.4$ at $R_\theta = 2,870$.

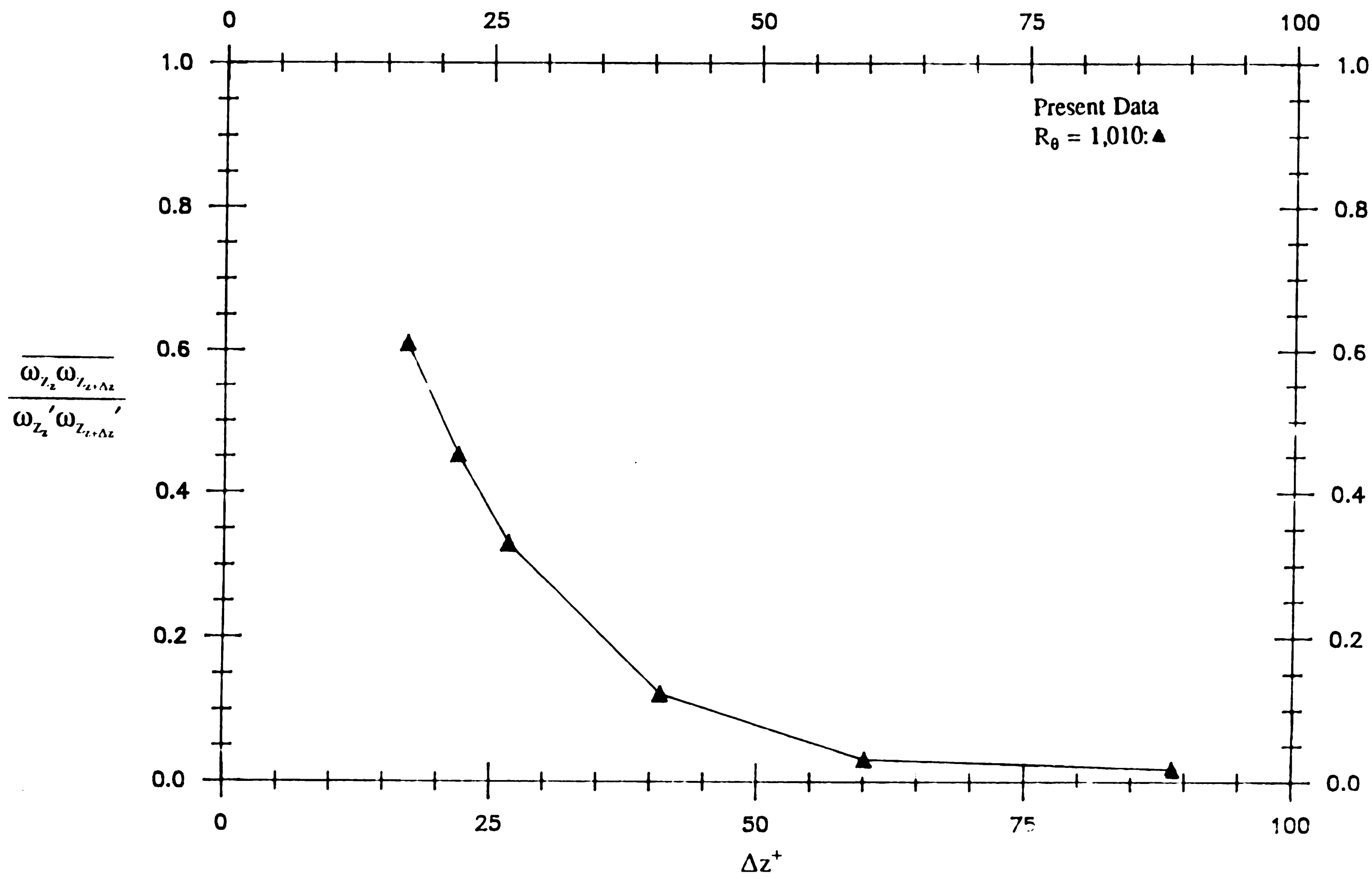

Figure 4.17 Results of the ω_z-ω_z correlations for Δz separations and the probes positioned at $y^+ = 6.7$ ($R_\theta = 1,010$ only).

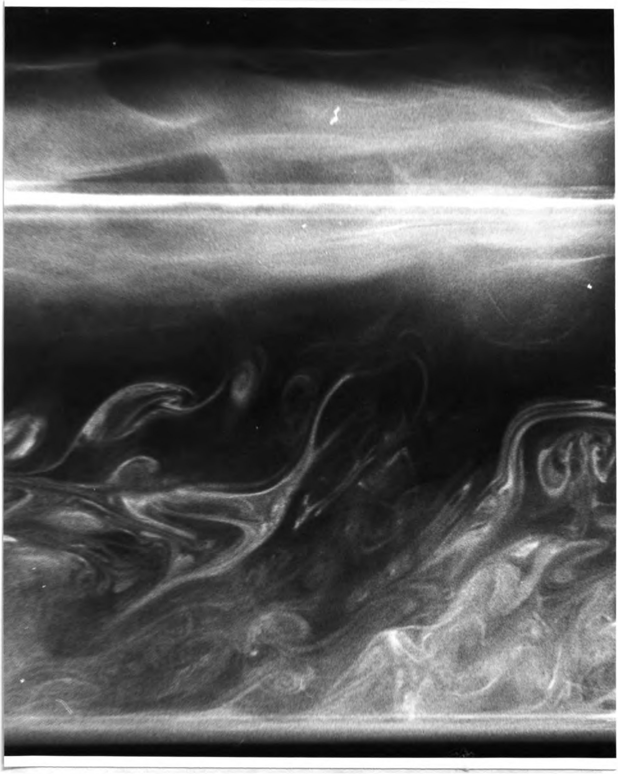

Figure 5.1a Example of the more probable high angle small scale lifting sublayer motion (early in its evolution).

Figure 5.1b Example of the more probable high angle small scale lifting sublayer motion (later in its evolution).

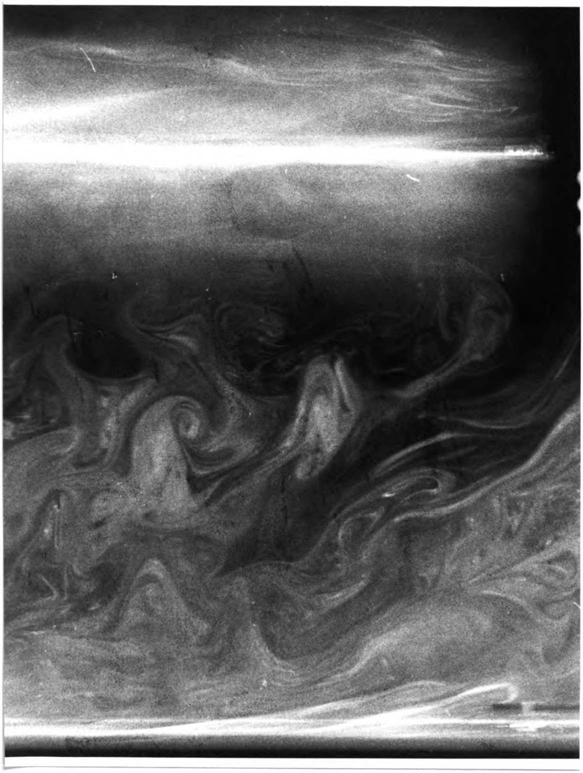

Figure 5.2 Example of the less probable low angle large scale lifting sublayer motion.

APPENDICES

APPENDIX 2.1 ON COMPUTING STREAMWISE DERIVATIVES

In their study Subramanian et al. (1985) derive the following expression for a streamwise derivative with ϵ_u percent error in the measured values of u.

$$<(\partial u/\partial x)^2> = <\Delta u/\Delta x>^2 + <2u\epsilon_u>/\Delta x^2 + <0(\epsilon_u)^2>$$

This expression shows that provided the ϵ_u are correlated with u the error in $(\partial u/\partial x)^2$ as computed by a finite difference approach becomes quite significant as the equivalent Δx under Taylor's hypothesis becomes small. Subramanian et al. further show, using grid flow measurements, that the minimum Δx for which the above error term is negligible is $\cong$ 3.8 mm (for the given ϵ_u of their experiment). In this appendix a quantitative example is given showing that the least squares method of computing streamwise derivatives of the present study is superior to a finite difference approach in that it allows for a much smaller Δx without sacrificing accuracy, and is more robust in the presence of noise.

In this example estimates of $<(\partial u/\partial x)^2>$ as computed by both methods are compared for various Δx separations and noise levels for a known function u with correlated errors ϵ_u. For the function we choose $u = \cos 2\pi x + \epsilon_u$ with $\epsilon_u = AUu$, where U represents random selections from uniformly distributed numbers between 0 and 1, and A is small. Using this function, the "true" mean square derivative is:

$$<(\partial u/\partial x)^2> = (4\pi^2/T)\int_0^T \sin^2 2\pi x dx = 2\pi^2. \qquad \text{(A2.1.1)}$$

The comparisons in Figures A2.1.1 and A2.1.2 are made between the central difference approximation

$$(\partial u/\partial x)_3 = (-u_5 + 8u_4 - 8u_2 + u_1)/(12\Delta x) + O(\Delta x^2) \qquad \text{(A2.1.2)}$$

and the derivative of a local 5 point least squares fit to the model

$$u = X + Yx + Zx^2$$

i.e

$$(\partial u/\partial x)_3 = Y + 2Zx_3, \qquad \text{(A2.1.3)}$$

where the subscripts in the above relations refer to the point within the 5 point window at which the derivative is evaluated (i.e. point 3 is the center point). The comparisons presented are representative of the phenomena observed for numerous reasonable Δx separations and noise levels. Figure A2.1.1 shows the effect of decreasing Δx for a given noise level and Figure A2.1.2 shows the effect of increasing the noise level for a given Δx. In both of these figures the straight line indicates the "true" value of $2\pi^2 \cong 19.74$. Figure A2.1.1, for small Δx, shows results similar to that of the grid flow data of Subramanian et al. If these results are representative of what happens in turbulence data reduction, then by using the least squares method one can expect to be able to decrease the minimum allowable Δx approximately 2.5 times the value permitted by the finite difference method. In any case, under the conditions presented in Figures A2.1.1 and A2.1.2, the least squares method clearly out-performs the finite difference method.

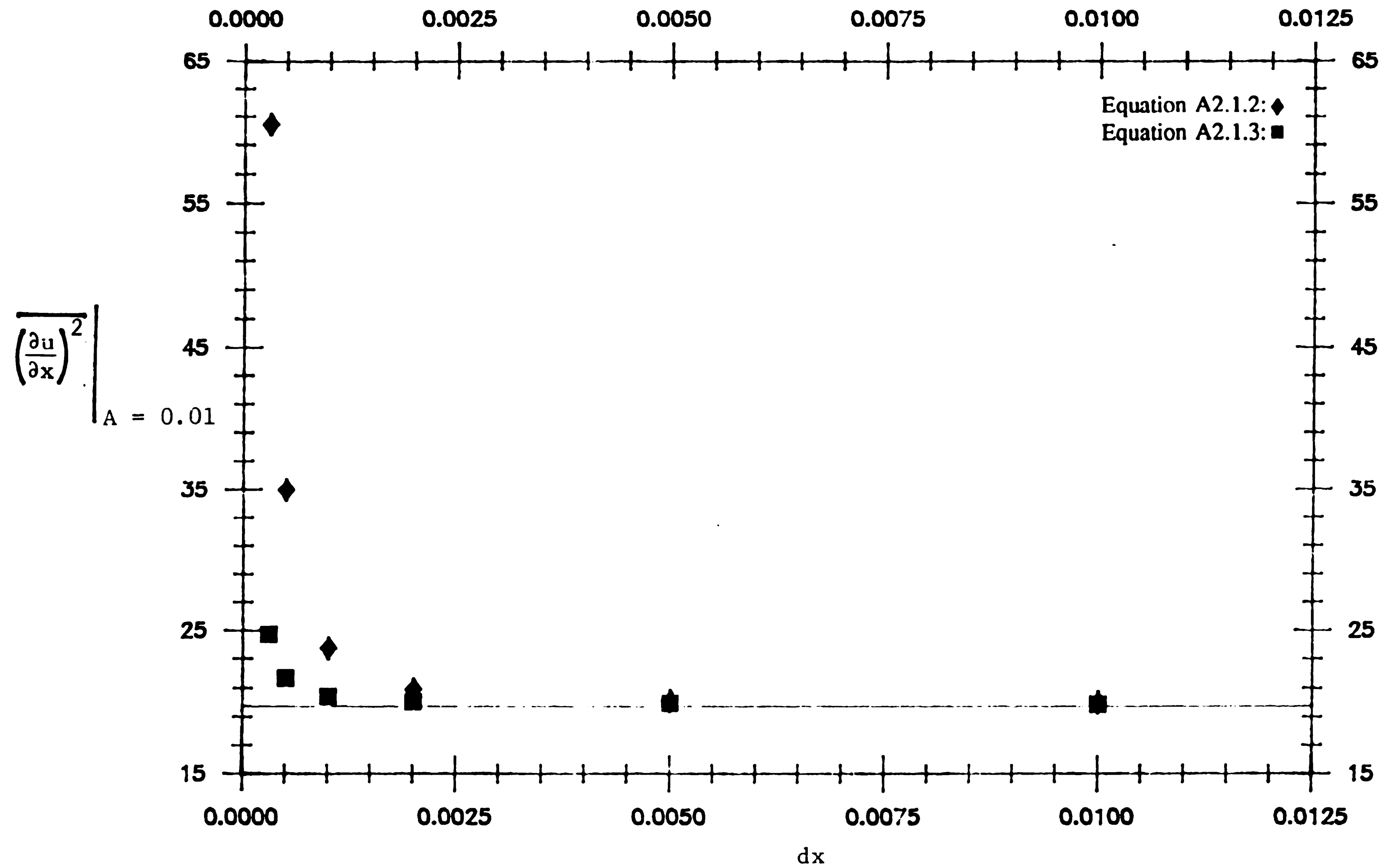

Figure A2.1.1 Comparison of "$(\partial u/\partial x)^2$" as estimated by equation A2.1.2 with as estimated by equation A2.1.3 as a function of Δx and for a given noise level.

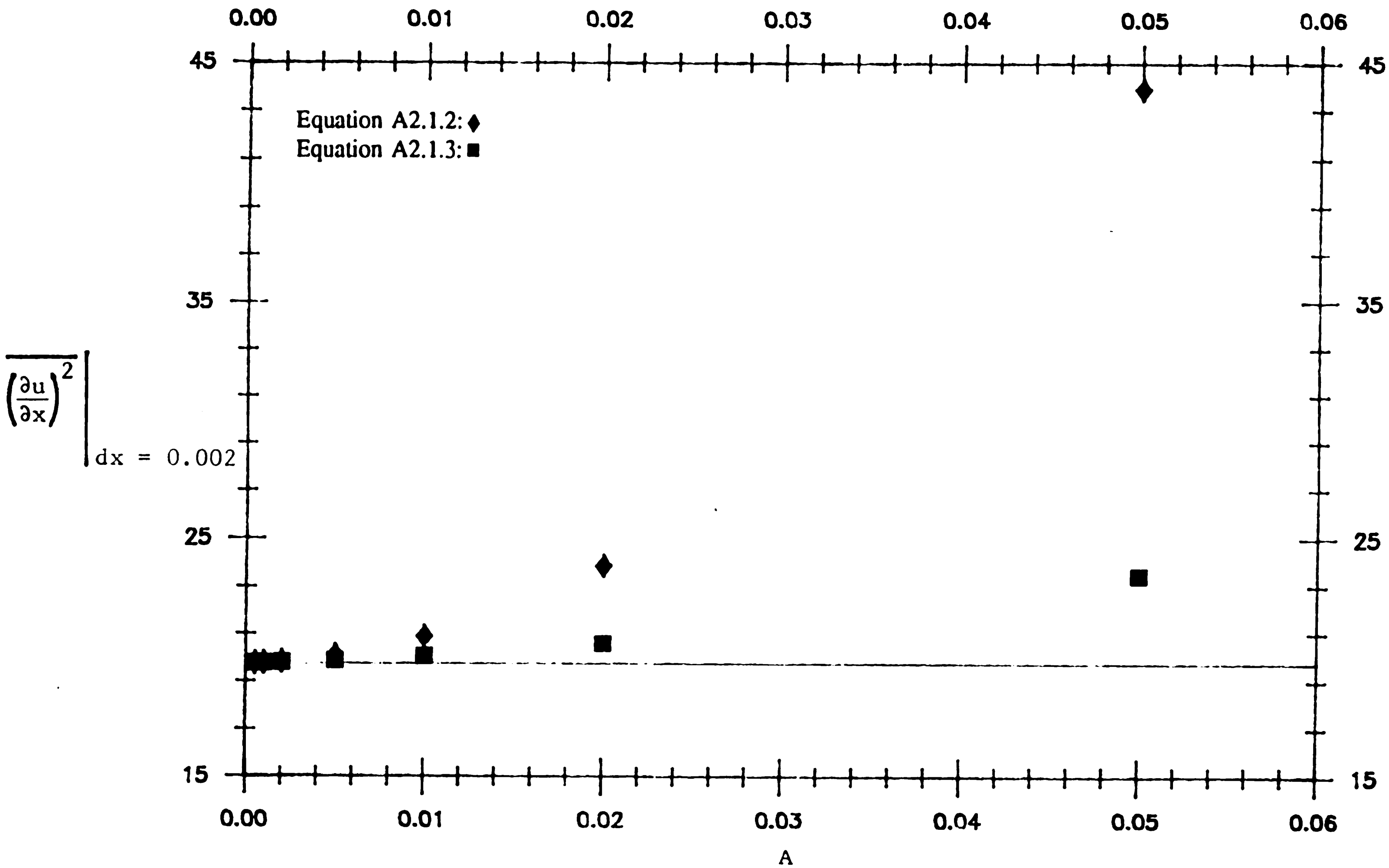

Figure A2.1.2 Comparison of "$(\partial u/\partial x)^2$" as estimated by equation A2.1.2 with as estimated by equation A2.1.3 as a function of noise level for a given Δx.

APPENDIX 2.2 DATA SMOOTHING PROCEDURE

As discussed in Chapter 2.4.5 a point-to-point check of all of the velocity records was made prior to computing the velocity derivatives and ω_z. This procedure was used to reduce the singular-like phenomena that spurious isolated data points could have on derivative quantities. This testing procedure and the corrections used once a spurious datum is found, are described in this appendix.

The voltage to velocity conversion process was broken up into a 100 point buffering procedure in which the hot-wire voltages are initially converted via the calibration equations into uncorrected velocities. An rms is then computed based upon this 100 point buffer of velocities. For a given file conversion the user selects the number of these rms levels to be used as the smoothing criterion. Selecting a greater number of these rms levels will cause less smoothing. During highly turbulent times the criterion will accordingly increase, whereas during quiescent times the criterion decreases. Thus care had to be taken in selecting an overall criterion (i.e. appropriate for an entire data set) that worked well in the intermittent regions very near and very far from the wall.

A failure is defined to occur when the absolute difference between any two adjacent points is greater than the given criterion. Three basic failure types/corrections were defined. A type 1 failure (isolated point) occurs when point I+1 fails in relation to both points I and I+2, and points I and I+2 do not fail. The corrective measure taken for a type 1 failure was to replace point I+1 with the average of points I and I+2. A type 2 failure (double point) occurs when points I and I+1 and points I and I+2 fail, but points I+1 and I+2 do not fail. The corrective measure in this case was to adjust point I+1 such that it is 1/2 a criteria from point I (+ or - such that they maintain their original orientation), and to move point I+2 such that it maintains its relationship with point I+1. A type 3 failure (multi-point) occurs when points I and I+1, I and I+2, and I+1 and I+2 all fail. The highly arbitrary correction in the case was to set all of the points equal to the value of point I.

The philosophy behind this smoothing procedure was to eliminate possible non-flow generated data without removing any information provided by the turbulence. Using this as a goal, it was assumed that (since electronic phenomena typically occurs at much higher frequencies than found naturally in the present turbulent flows) the generic failure type was the isolated point (type 1). Confidence was gained in this assumption in that for any given file one could increase the criterion until virtually all of the detected failures were type 1. Output from the smoothing subroutine included reference to the failed points, their original and corrected values and the failure type. By iterating through numerous files covering the various regions of the boundary layer it was found that a criterion of three rms levels worked well in recognizing the maximum number of type 1 failures relative to types 2 and 3 (for the three single probe experiments described in chapter 2). This optimal criterion undoubtedly depends upon the given flow, as well as the particular data acquisition equipment being used. An example of the smoothing subroutine output is given in Table A2.1.1.

Table A2.2.1 Sample output from the velocity data smoothing subroutine.

BAD POINT SUMMARY

TOTAL NUMBER OF SMOOTHED POINTS = 27

BAD VAL	NEW VAL	ROW	COL	FTYP	CRIT
5.094	5.588	5708.000	1.000	1.100	0.452
5.305	5.744	5708.000	3.000	1.100	0.362
5.409	5.914	5708.000	4.000	1.100	0.498
5.493	5.146	64095.000	1.000	1.100	0.306
5.698	5.158	64095.000	3.000	1.100	0.404
5.673	5.153	64095.000	4.000	1.100	0.495
5.069	5.398	70603.000	1.000	1.100	0.288
4.872	5.334	70603.000	3.000	1.100	0.346
5.768	5.278	88519.000	1.000	1.100	0.342
5.648	5.297	88519.000	2.000	1.100	0.338
5.514	5.129	88519.000	3.000	1.100	0.341
5.584	5.845	88520.000	4.000	2.100	0.507
5.584	5.845	88521.000	4.000	2.200	0.507
4.890	5.186	89019.000	1.000	1.100	0.357
4.872	5.246	89019.000	3.000	1.100	0.357
6.173	5.575	254438.000	3.000	1.100	0.506
4.872	5.173	268546.000	3.000	1.100	0.263
5.278	4.839	344154.000	1.000	1.100	0.311
5.203	4.826	344154.000	2.000	1.100	0.289
4.715	5.160	372486.000	1.000	1.100	0.402
4.489	5.129	390338.000	3.000	1.100	0.678
4.592	4.881	398457.000	1.000	1.100	0.484
5.424	5.100	433225.000	3.000	1.100	0.297
5.545	5.086	451783.000	3.000	1.100	0.404
4.789	5.394	471184.000	3.000	1.100	0.485
5.454	5.096	493986.000	3.000	1.100	0.283
4.624	5.231	510121.000	3.000	1.100	0.475

APPENDIX 2.3 ON MEASURING THE MEAN VELOCITY GRADIENT

An alternate means of assessing the accuracy of the present spanwise vorticity probe gradient measurements is to compare the derivative of the mean velocity profile with the average of the instantaneous $\partial U/\partial y$ measurement deduced from the parallel-array contained in the ω_z probe. According to the study of Bottcher and Eckelmann (1985), probe interference effects may be compensated for in velocity measurements during the calibration procedure, but in order to obtain accurate gradient measurements the parallel array must be calibrated in a gradient field. This conclusion inherently assumes that the construction of the parallel-array is such that the flow field seen by one wire is altered by presence of the other wire.

Before proceeding to an examination of the present $\partial U/\partial y$ measurements it is useful to note some of the differences between this study and that of Bottcher and Eckelmann. The two most important of these differences have to do with the probe construction. In their study, a TSI 1244-20W parallel array was employed. This hot-film array has 1mm long films attached to 12.7mm long prongs which are attached to a blunt-end 3.2mm diameter probe body. This results in the ratio of the prong length to frontal diameter (pertinent to flow blockage) to be equal to about 4. In contrast, the parallel-array of the present study has 3mm long wires (in which only the center millimeter is active -- thus serving to isolate the active sensor from the prongs) supported on 20mm long prongs which are attached to a tapered head with a frontal diameter (again pertinent to flow blockage) of about 2.5mm. This results in a prong length to frontal diameter of about 8. It is presently believed that these differences greatly reduce the effect of blockage effects on the present $\partial U/\partial y$ measurements.

Comparisons were made between $\partial U/\partial y$ estimates as deduced from the mean profile, and those deduced from the average $\partial U/\partial y$ of the parallel array, $\partial U/\partial y|_p$. However, the scatter in the $\partial U/\partial y$ data inferred from finite differencing the mean velocity profile was great enough that it made for an inconclusive assessment of the performance of the parallel-array. Thus it was decided to instead compare $\partial U/\partial y|_p$ with the semi-empirical curve-fit of Van Driest (1956), $\partial U/\partial y|_v$. Note that the use of other curve-fits such as Spalding (1961) yield essentially identical results. This comparison for the three Reynolds numbers of the present study is made in Figure A2.3.1 for $y^+ \leq 50$. As can be seen, in general, the present results agree quite well with each other, but all of the data under-predict the semi-empirical based result.

This trend appears consistent with the results of Bottcher and Eckelmann (in that probe interference effects generally result in an under-estimation of the gradient -- except for very low probe Reynolds numbers, see below), and thus suggests that probe interference effects may have influenced the present measurements. To further examine this possibility, these differences were analyzed in the same manner suggested by Figure 7 of Bottcher and Eckelmann. Figure A2.3.2 plots the relative systematic error, E,

$$E = \frac{\partial U/\partial y|_p - \partial U/\partial y|_v}{\partial U/\partial y|_v}$$

times the wire separation ($\Delta y = 0.98$mm) versus the two different probe

Reynolds numbers; using the mean velocity, the probe support-rod diameter, and the tapered-head diameter, R_p and R_h respectively. When the differences with the Van Driest model are examined in this way, the trends in the data are seen to be significantly different from those predicted by the Bottcher and Eckelmann study. In their study they found that for probe Reynolds numbers greater than about 23 the quantity $\Delta y \bullet E$ started out negative and (on average) steadily increased with increasing probe Reynolds number to a limiting value of about -0.2. As can be seen for the present two lowest Reynolds number flows (which fall within the range of probe Reynolds numbers investigated in the Bottcher and Eckelmann study) this is not the case. In these two flows the lowest probe Reynolds number data clearly have the smallest (rather than the largest) error.

In interpreting results presented in the form of Figure A2.3.2 one must also consider the fact that at $y^+ = 50$ the mean gradient is only about 5% of the value at the wall. Therefore, any small additive bias (in terms of $u_\tau{}^2/\nu$) has an amplified affect as the distance from the wall increases. To illustrate this point, consider "correcting" the two lower Reynolds number profiles such that each value in the distribution is altered by an additive constant equal to the amount that makes the point representing the smallest $\Delta y \bullet E$ values of Figure A2.3.2 have essentially zero error. For the $R_\theta = 1{,}010$ and 2,870 distributions this means adding 2.75 s^{-1} and 7.5 s^{-1} to each point respectively (or about 5.2% and 2.2% of $u_\tau{}^2/\nu$ respectively). The "corrected" distributions are shown in Figure A2.3.3. These distributions show that a constant additive error model does very well in explaining the deviations from the semi-empirical result (especially for the $R_\theta = 2{,}870$ flow). Figure A2.3.4 further supports this conclusion in that it shows that the $\Delta y \bullet E$ values for the R_θ

= 1,010 distribution are about equally spread around zero, and the R_θ =2,870 $\Delta y \bullet E$ curve is nearly a horizontal line.

Thus, while there are differences between the present $\partial U/\partial y|_p$ distributions and that given by Van Driest, these differences seem to be best described by an additive systematic error model, not a proportional error model. This point is important since probe interference errors should be proportional to value of the mean gradient -- as shown by Bottcher and Eckelmann. Somewhat unfortunately, this finding also excludes other proportional error sources such as the measurement of the wire separation and/or u_τ. Interestingly enough however, the ratio of the absolute "corrections" discussed above are nearly proportional to the friction velocities of the two flows (i.e 2.75/7.5 $\cong u_\tau|_{1010}/u_\tau|_{2870} \cong$ 0.39). This may be a clue regarding the source of the small differences between the two $\partial U^+/\partial y^+$ distributions. At this time it appears that a plausible explanation might be some small additive bias in the matching calibration procedure described in Chapter 2. However, it is not certain that the present results are statistically significant. Furthermore, given the relatively small absolute "errors" involved, the association of these "errors" with a single source presents a formidable task. Finally, it should be noted that very little explicit data on $\partial U/\partial y$ is in the literature, and thus the low Reynolds number deviations from the semi-empirical equation used for comparison (which is largely derived from high Reynolds number velocity profile data) may be a true Reynolds number dependence.

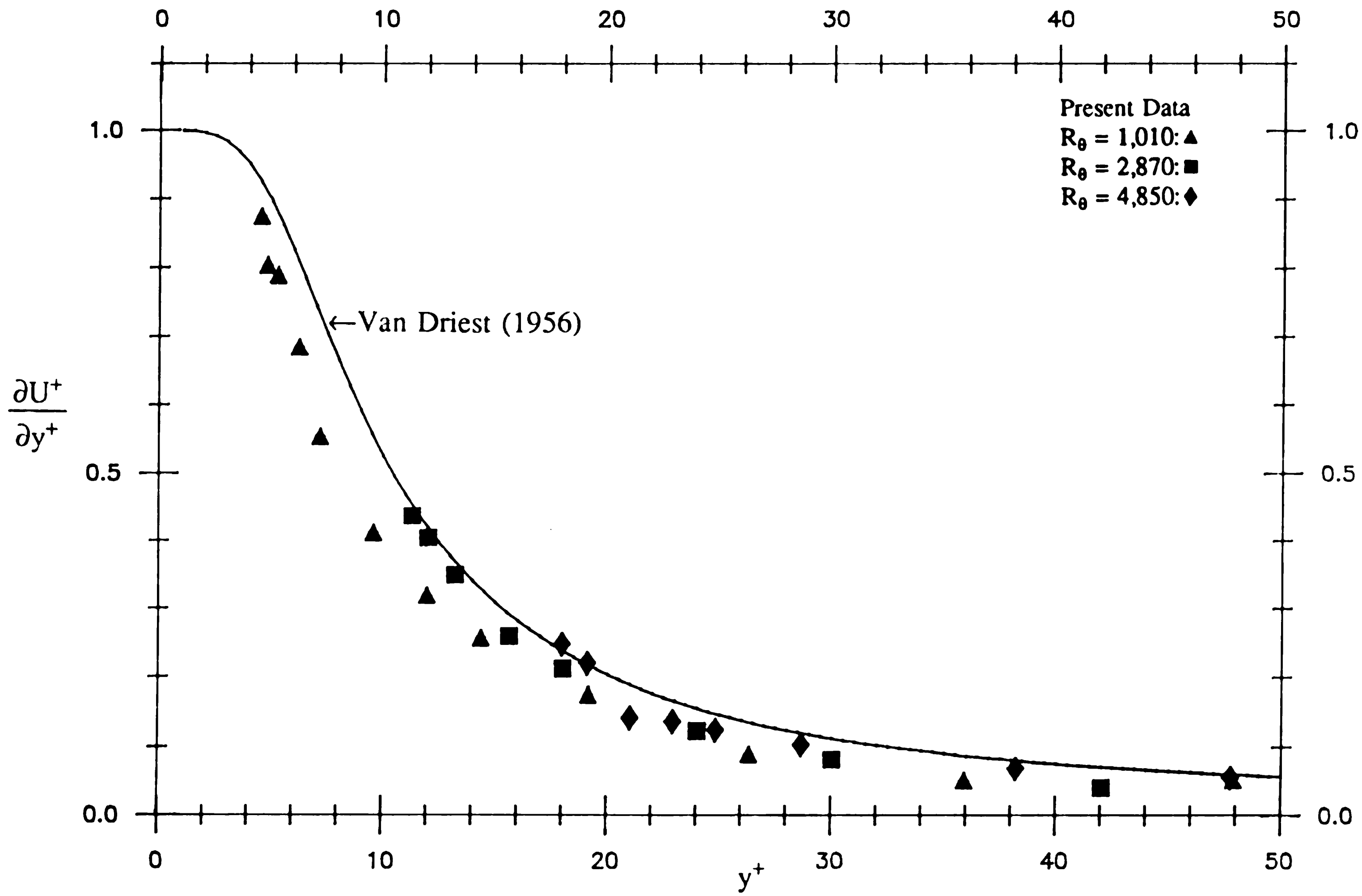

Figure A2.3.1 Near-wall mean velocity gradient profiles as computed by finite differencing the mean velocities measured from the parallel-array element contained within the spanwise vorticity probe.

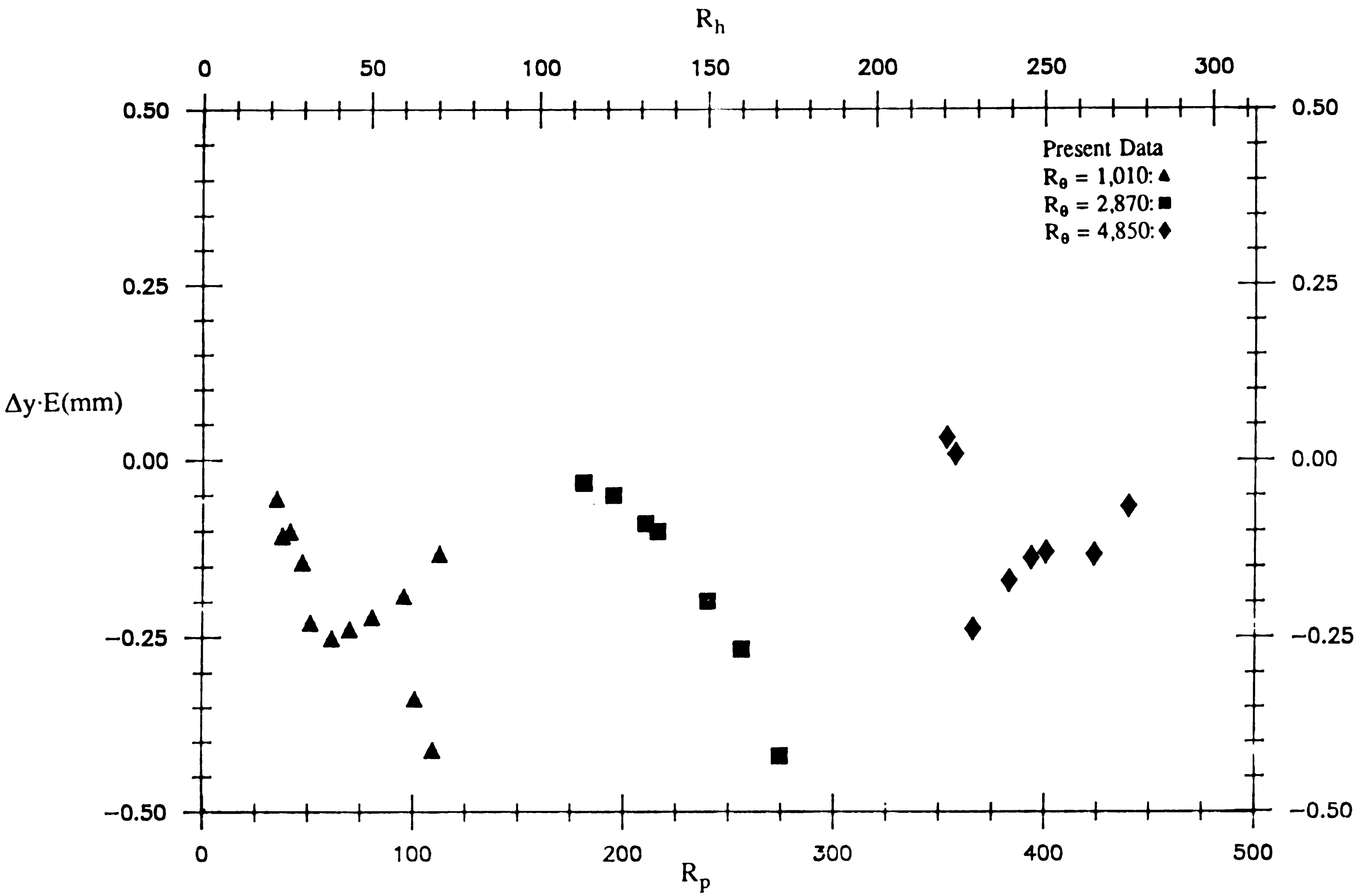

Figure A2.3.2 Product of the relative systematic error of the gradient, E, and the sensor separation, Δy, as a function of probe body and probe tapered head diameter Reynolds numbers (R_p and R_h respectively).

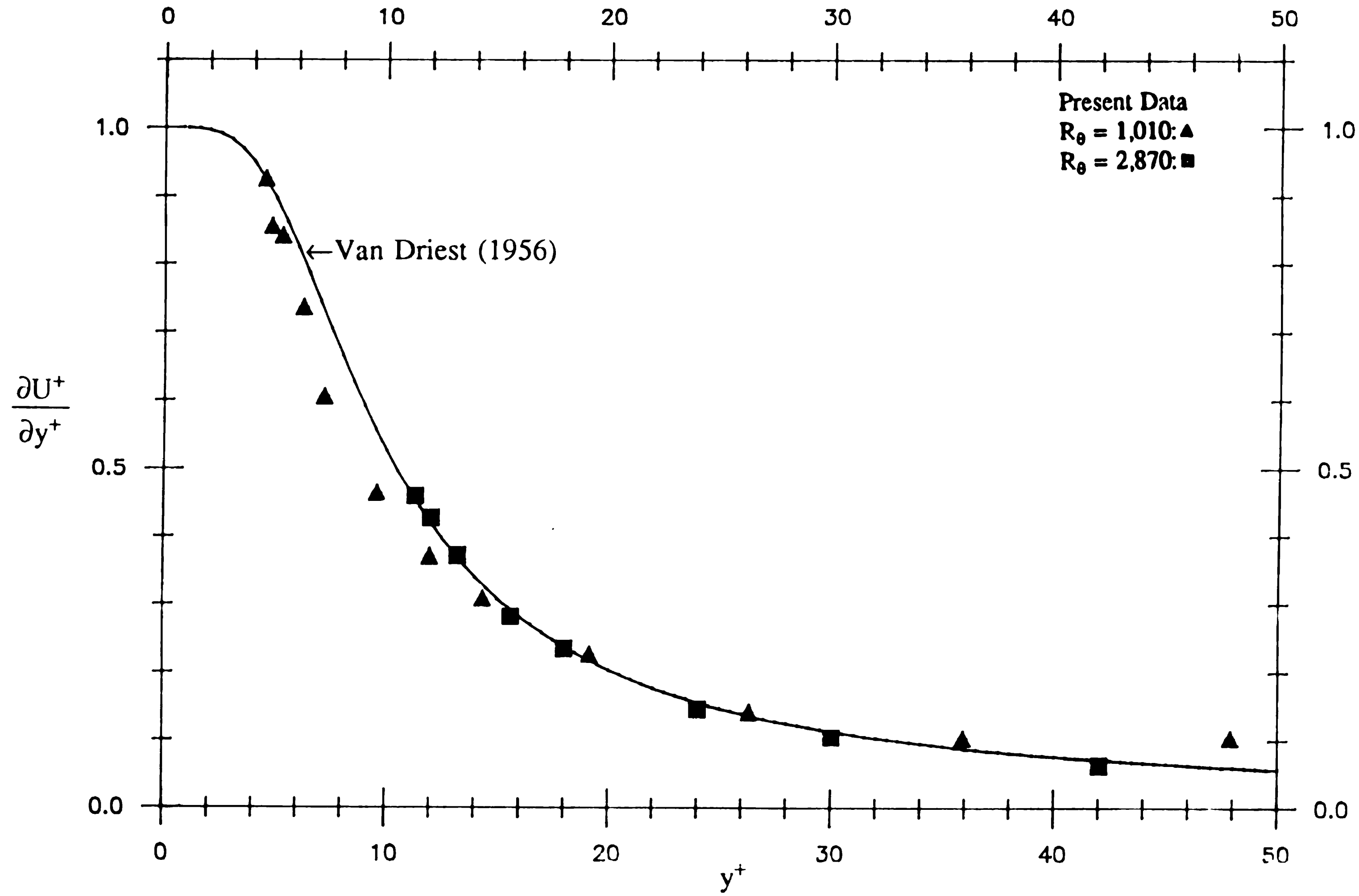

Figure A2.3.3 Near-wall mean velocity gradient profiles for the two lower Reynolds numbers shown in Figure A2.3.1 as "corrected" under the assumption of a constant additive error.

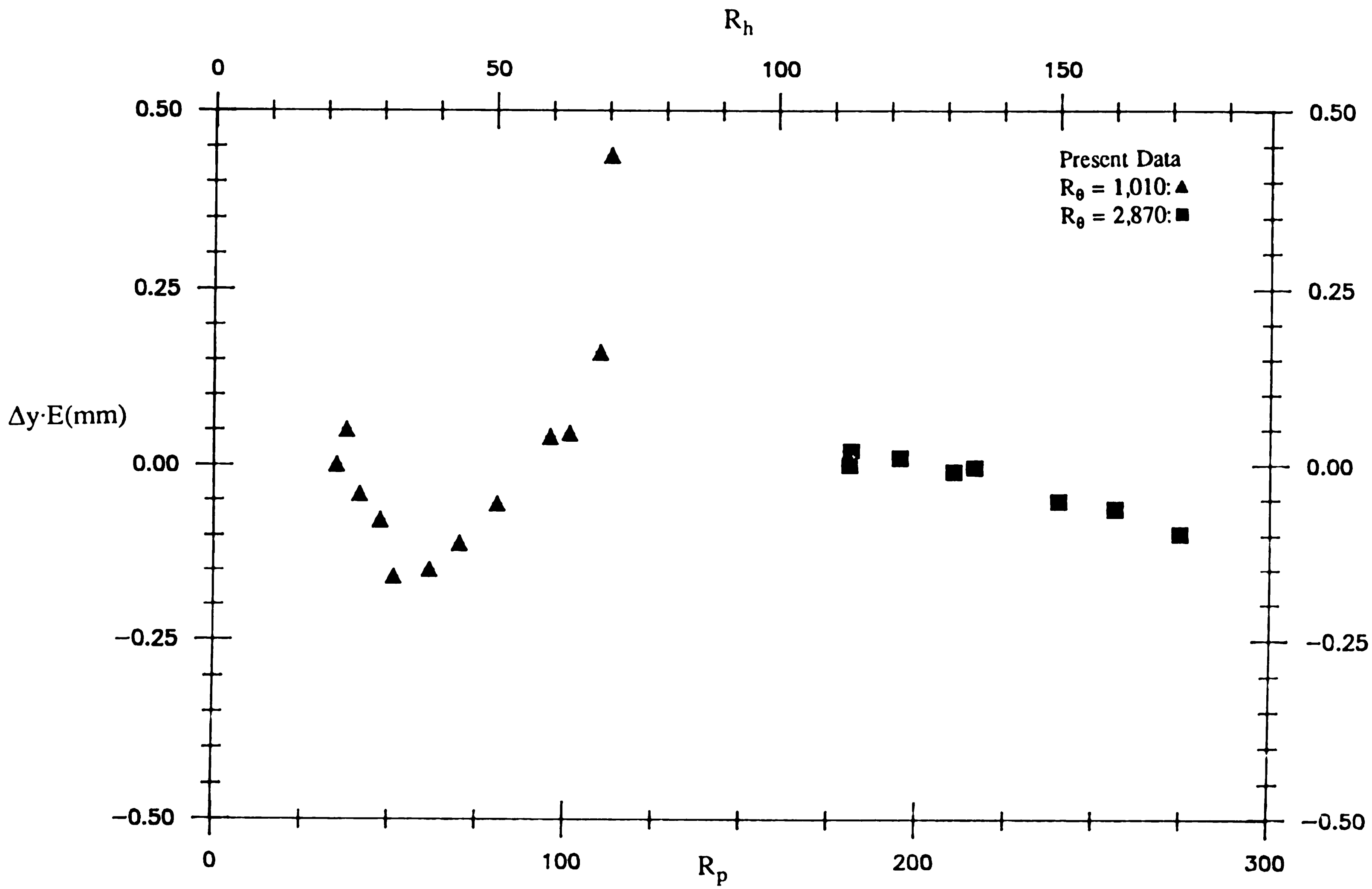

Figure A2.3.4 The product of the relative systematic error of the gradient, E, and the sensor separation, Δy, as a function of probe body and probe tapered head diameter Reynolds numbers (R_p and R_h respectively) for the "corrected" data of Figure A2.3.3.

APPENDIX 3.1 VELOCITY-VORTICITY CORRELATIONS RELATED TO THE GRADIENTS OF THE REYNOLDS STRESSES IN PARALLEL TURBULENT WALL FLOWS

This appendix describes, in general, how velocity vorticity correlations are related to the gradients of the Reynolds stresses in wall bounded turbulent flows that are (nearly) homogeneous in planes parallel to the wall. These relations are derived both from a tensor identity, and directly from the equations for the mean flow. Furthermore, using the velocity vorticity correlations measured in the present experiments and approximate analytical relations, unmeasured velocity vorticity correlation profiles are deduced.

The contents of this appendix have been accepted for publication as a "Brief Communication" in the Physics of Fluids A.

VELOCITY–VORTICITY CORRELATIONS RELATED TO THE GRADIENTS OF THE REYNOLDS STRESSES IN PARALLEL TURBULENT WALL FLOWS

J. C. Klewicki
Department of Mechanical Engineering
Michigan State University, East Lansing, Michigan, U.S.A.

ABSTRACT

By using the momentum equations in "vorticity" form, relations between velocity-vorticity correlations and gradients of the Reynolds stresses are established for a two dimensional turbulent channel flow. Employing these relations, the approximate formulas of Phillips [Phys. Fluids **30** 1987] and recently obtained experimental data allows for unmeasured velocity-vorticity correlation profiles to be deduced. The results herein indicate that the contributions to the gradients of the diagonal stresses are dominated by the correlation involving the spanwise vorticity component, while the contributions to the off-diagonal stresses are shared almost equally between the correlations involving the spanwise and normal vorticity components.

It can be shown[1] that the gradients of the Reynolds stresses in an incompressible turbulent flow are related to velocity-vorticity correlations via the following relation.

$$\frac{\partial}{\partial x_j}(\overline{u_j u_i}) = -\varepsilon_{ijk}\overline{u_j \omega_k} + \frac{1}{2}\frac{\partial}{\partial x_i}(\overline{u_j u_j}). \tag{1}$$

In that many investigators[2-5] feel that the most promising approach to understanding turbulent flows is through the study of the vorticity field, Eq. (1) is important because it relates the mean transport of the Reynolds stresses to the vorticity field through the indicated velocity-vorticity correlations. By setting i = 1 and applying Eq. (1) to a fully developed, plane turbulent channel flow it may be readily shown that the gradient of the 1-2 component may expressed as

$$\frac{d}{dy}(\overline{uv}) = \overline{w\omega_y} - \overline{v\omega_z}, \tag{2}$$

where u, v and w are the fluctuating velocity components in the streamwise, x, the direction normal to the wall, y, and the spanwise direction, z, and ω_k is the fluctuating vorticity component in the k direction. Thus Eq. (2) specifically shows how the gradient of the component of the Reynolds stress tensor that appears in the equation for the mean velocity is related to the fluctuating vorticity field. In this Brief Communication it is shown that Eq. (2), as well as the relations between the y-gradients of the diagonal terms of the stress tensor represented by setting i = 2 in Eq. (1), are not only derivable via Eq (1) but may also be derived directly from the equations for the mean flow.

This Brief Communication begins by presenting the relevant time-averaged momentum equations in "velocity" form for a plane turbulent channel flow.

Examination of these equations (along with Eq. (2)) indicates that the mean velocity, U, is dependent on the above velocity-vorticitv correlations. Then by re-deriving the appropriate momentum equations in "vorticity" form, the same identities involving velocity-vorticity correlations found by setting i = 2 and 3 in Eq. (1) are deduced. Pertaining to the i = 1 and i = 2 relations from Eq. (1), $\overline{v\omega_z}$ and $\overline{u\omega_z}$ data are provided from the recent high resolution measurements of Klewicki and Falco[6]. Then, by using $\partial(\overline{uv})/\partial y$ data, and the approximate asymptotic results of Phillips[7] for the gradients of the pertinent Reynolds stresses, approximate profiles for the unmeasured terms, $\overline{w\omega_y}$ and $\overline{w\omega_x}$, are deduced. A brief discussion concerning the physical interpretation of these terms, and their possible Reynolds number dependence follows. A much more complete discussion of these results, and their relationship to other structural features of turbulent wall-flows is given in Klewicki and Falco[8].

The pertinent time-averaged x and y momentum equations (the z equation is identically zero) in "velocity" form for a steady, fully developed, incompressible, plane turbulent channel flow can be readily found in many books on fluid mechanics (cf. Arpaci and Larsen[9]) and are given by

$$\frac{\partial}{\partial x}\left[\frac{P}{\rho}\right] = \frac{d}{dy}\left[\nu\frac{dU}{dy} - \overline{uv}\right] \tag{3}$$

and

$$\frac{\partial}{\partial y}\left[\frac{P}{\rho}\right] = -\frac{d}{dy}(\overline{v^2}), \tag{4}$$

where lower case letters denote fluctuating quantities and upper case letters denote mean quantities. Examination of Eq.s (2) and (3) indicates that Eq. (3) may be rewritten as

$$\frac{\partial}{\partial x}\left[\frac{P}{\rho}\right] = \nu\frac{d^2U}{dy^2} - (\overline{w\omega_y} - \overline{v\omega_z}). \tag{5}$$

Thus Eq. (5) explicitly shows that the equation for the mean velocity depends on the velocity vorticity-correlations appearing in Eq. (2).

The momentum equation in "vorticity" form is given by,

$$\frac{\partial \tilde{\mathbf{u}}}{\partial t} + \nabla\left[\frac{\tilde{\mathbf{u}}^2}{2}\right] - \tilde{\mathbf{u}}\times\tilde{\boldsymbol{\omega}} = -\nabla\left[\frac{\tilde{p}}{\rho}\right] + \nu\nabla^2\tilde{\mathbf{u}}, \tag{6}$$

where a tilde denotes a total quantity. By letting $\tilde{\mathbf{u}} = \mathbf{U} + \mathbf{u}$, $\tilde{p} = P + p$, and $\tilde{\boldsymbol{\omega}} = \boldsymbol{\Omega} + \boldsymbol{\omega}$, expanding Eq. (6) into its component equations, time averaging, and noting that for the given flow that:

- $\partial(\ )/\partial x = \partial(\ )/\partial z \equiv 0$, except for P (due to homogeneity),
- $V = W = \Omega_x = \Omega_y \equiv 0$,
- $\Omega_z \equiv -dU/dy$, and that
- $1/2d/dy(U^2) = -U\Omega_z$,

one arrives at the following equations.

$$\overline{v\omega_z} - \overline{w\omega_y} = -\frac{\partial}{\partial x}\left[\frac{P}{\rho}\right] + \nu\frac{d^2U}{dy^2} \tag{7}$$

$$\frac{1}{2}\frac{\partial}{\partial y}(\overline{u^2} + \overline{v^2} + \overline{w^2}) + \overline{u\omega_z} - \overline{w\omega_x} = -\frac{\partial}{\partial y}\left[\frac{P}{\rho}\right] \tag{8}$$

$$\overline{v\omega_x} - \overline{u\omega_y} = 0 \tag{9}$$

Examination of Eq. (7) indicates that the "vorticity" form of the momentum equation contains the relation between the mean velocity and the velocity-vorticity correlations given in Eq. (5). Comparison of Eq.s (8) and (4) reveals that there are additional terms in the "vorticity" form of the y momentum equation. By subtracting Eq. (4) from Eq. (8) and setting the difference equal to zero (which it must be since both forms of the y momentum equation are valid), one gets the i = 2 result from Eq. (1),

$$\frac{1}{2}\frac{\partial}{\partial y}(\overline{u^2} + \overline{w^2} - \overline{v^2}) + \overline{u\omega_z} - \overline{w\omega_x} = 0. \tag{10}$$

Finally, Eq. (9) presents a relation between velocity-vorticity correlations that is not made apparent if one only examines the "velocity" form of the momentum equation.

The $\nu\overline{v\omega_z}/u_\tau^3$, and $\nu\overline{u\omega_z}/u_\tau^3$ profiles of figures 1 and 2 are derived from the four-wire spanwise vorticity probe measurements of Klewicki and Falco[6] which were made in a very thick zero pressure gradient turbulent boundary layer. In the profiles of figure 2 one will notice the data point at $y^+ = 1$. This data point was derived by placing a u-measuring probe at $y^+ = 2$ (in a $R_\theta \approx 1{,}000$ flow, see Klewicki[10]) and using the relation

$$\frac{\nu\overline{u\omega_z}}{u_\tau^3}(y = 0) \approx \frac{1}{2u_\tau}\left[\frac{\overline{u^2}}{U}\right]_{y\to 0},$$

which can be derived via a Taylor series about y = 0. (Note that a similar relation incorporating the limiting value of $\overline{w^2}$ may be used to deduce the limiting value of $\nu\overline{w\omega_x}/u_\tau^3$, see below). As can be seen, the $\nu\overline{v\omega_z}/u_\tau^3$ profiles show a much greater relative variation with Reynolds number in the log-region than do the $\nu\overline{u\omega_z}/u_\tau^3$ profiles. Also it is readily apparent that the $\nu\overline{u\omega_z}/u_\tau^3$ profiles are about an order of magnitude larger at their peak value. Near the wall (say for $y^+ < 20$) both figures suggest that "wall variable" scaling causes a collapse of the data. Also, in both profiles the peak values are seen to occur near the edge of the sublayer. This should be expected however, since the mean Reynolds stress gradients are largest in this region of the flow.

In order to use the data of figure 1 and the gradient of the Reynolds stress to deduce the $v\overline{w\omega_y}/u_\tau^3$ profile as indicated by Eq. (2) one must first assess the validity of the parallel mean flow assumption implied by the form of Eq. (2). This has been done by Klewicki and Falco[11], in which it was demonstrated that the u and v streamwise gradient terms of the "boundary layer" form of Eq. (2),

$$\frac{\partial}{\partial y}(\overline{uv}) = \overline{w\omega_y} - \overline{v\omega_z} + \frac{1}{2}\frac{\partial}{\partial x}(\overline{v^2} + \overline{w^2} - \overline{u^2}),$$

are approximately two orders of magnitude smaller than the velocity-vorticity correlation terms for the given flow field. This approximate homogeneity in the streamwise direction also allows the data of figure 2 to be used in Eq. (10) to determine the $v\overline{w\omega_y}/u_\tau^3$ profile.

Using Eq. (2), the data of figure 1, and numerically differentiating the corresponding $\overline{uv}/u_\tau^2$ profiles at each R_θ allowed for the approximate $v\overline{w\omega_y}/u_\tau^3$ profiles given in figure 3 to be deduced. As one can see, away from the wall the deduced $v\overline{w\omega_y}/u_\tau^3$ profiles are very similar to the $v\overline{v\omega_z}/u_\tau^3$ profiles given in figure 1. The profiles of figures 1 and 3 indicate that the nearly zero mean transport of uv in the log-region is due to a balance of contributions rather than all terms being zero. Therefore, altering these correlations suggests the possibility for modifying momentum transport in the boundary layer. Nearer the wall the scatter in the $v\overline{w\omega_y}/u_\tau^3$ profiles is probably due to inaccuracies caused by numerically differentiating the $\overline{uv}/u_\tau^2$ profiles. This is felt to be the case due to the fact that both the $\overline{uv}/u_\tau^2$ profiles (not shown) and the $v\overline{v\omega_z}/u_\tau^3$ profiles given in figure 1 tend to exhibit a collapse for y^+ less than about 20, and thus so should the profiles of figure 3.

The fact that the profiles of figure 2 show very little variation with Reynolds number allows one to use the approximate high Reynolds number formulas of Phillips[7] for the y-gradients of the diagonal Reynolds stress terms of Eq. (10), and the R_θ = 1,010 data of figure 2 in order to obtain an approximate high Reynolds number $v\overline{w\omega_x}/u_\tau^3$ profile. The deduced $v\overline{w\omega_x}/u_\tau^3$ profile of figure 4 is considerably different from the $v\overline{u\omega_z}/u_\tau^3$ profiles of figure 2. In general the data shows that $v\overline{w\omega_x}/u_\tau^3$ exhibits less variation across the boundary layer than $v\overline{u\omega_z}/u_\tau^3$. An approximate error estimate on the deduced high Reynolds number $v\overline{w\omega_x}/u_\tau^3$ profile may be obtained by noticing that in this profile the value at $y^+ = 1$ is $\approx$ -0.04. Given that

$$\frac{v\overline{w\omega_x}}{u_\tau^3}(y = 0) \approx \frac{1}{2u_\tau}\left(\frac{\overline{w^2}}{U}\right)_{y\to 0},$$

the deduced negative value is clearly shown to be incorrect. Once again, based on the data of Klewicki[10] the actual value should be about +0.02. Thus an error estimate of $\approx$ $\pm$ 0.06 is obtained.

The results herein show that the contributions to the y gradient of $\overline{uv}$ are almost equally shared between $v\omega_z$ and $w\omega_y$, while the contributions to the normal stresses are dominated by the $u\omega_z$ term. Also, the fact that the measured $v\overline{u\omega_z}/u_\tau^3$ profiles show very little R_θ variation indicates that any R_θ variation in the $\overline{v^2}$ and $\overline{w^2}$ gradients of Eq. (10) are predominantly due to an R_θ variation in the correlation involving ω_x. This is in apparent agreement with the recent hypothesis of Wei[12], which associates the the nonuniversality of v'/u_τ with a relative increase in the creation of ω_x as the Reynolds number increases. This hypothesis, as well as other Reynolds number dependent features of boundary layer structure are further examined in Klewicki and Falco[8].

ACKNOWLEDGMENT

This work was supported by the Air Force Office of Scientific Research Contract No. 87-0047, contract monitor Dr. J. McMichael. The author also wants to thank professor R. E. Falco for his useful comments concerning this manuscript.

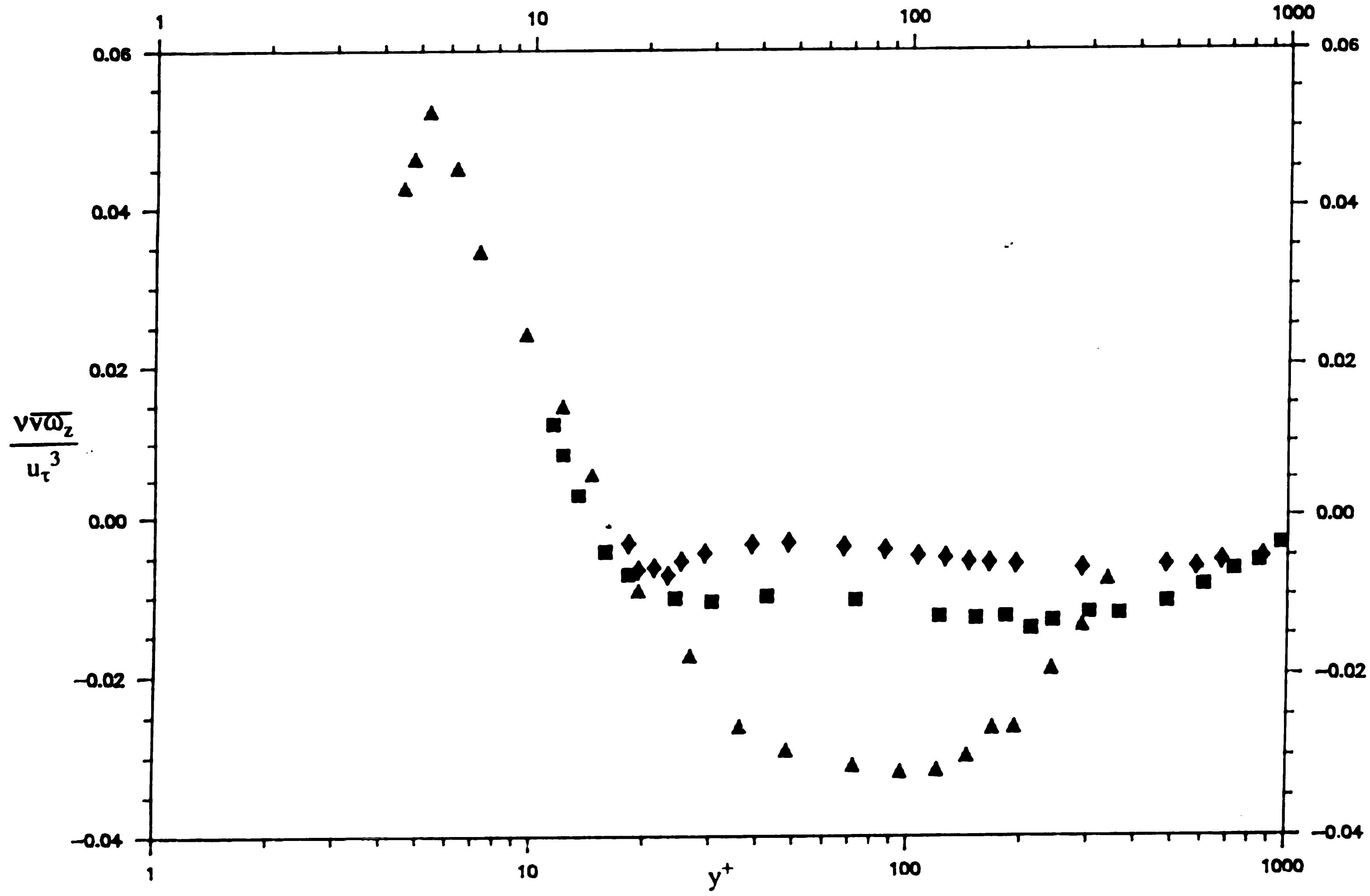

Figure A3.1.1 Figure 1: $v\overline{v\omega_z}/u_\tau^3$ profiles from the experimentally derived data base of Klewicki and Falco[6]; ▲ $R_\theta = 1{,}010$; ■ $R_\theta = 2{,}870$; ◆ $R_\theta = 4{,}850$

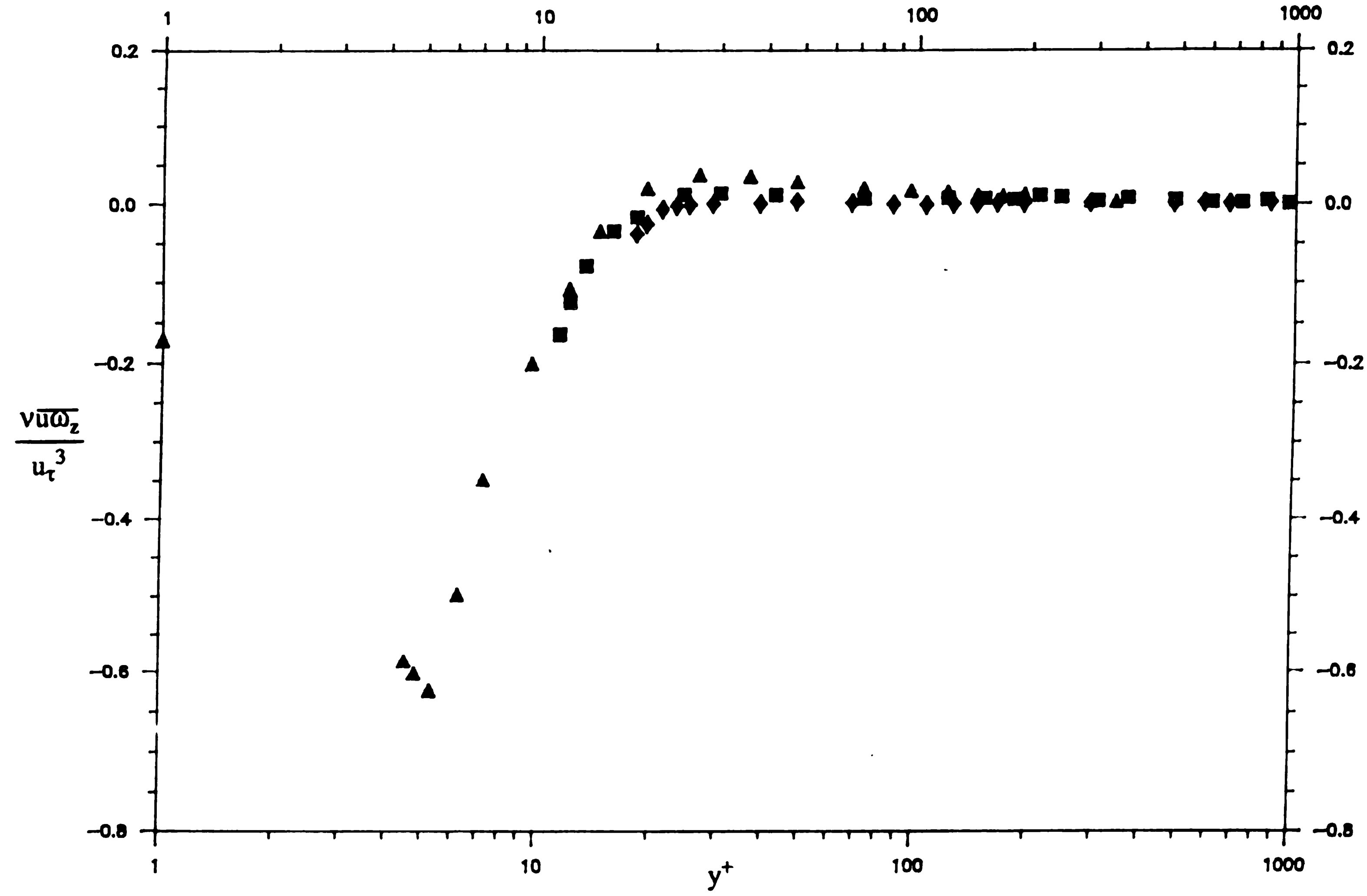

Figure A3.1.2 Figure 2: $\nu\overline{u\omega_z}/u_\tau^3$ profiles from the experimentally derived data base of Klewicki and Falco[6]; symbols same as in figure 1.

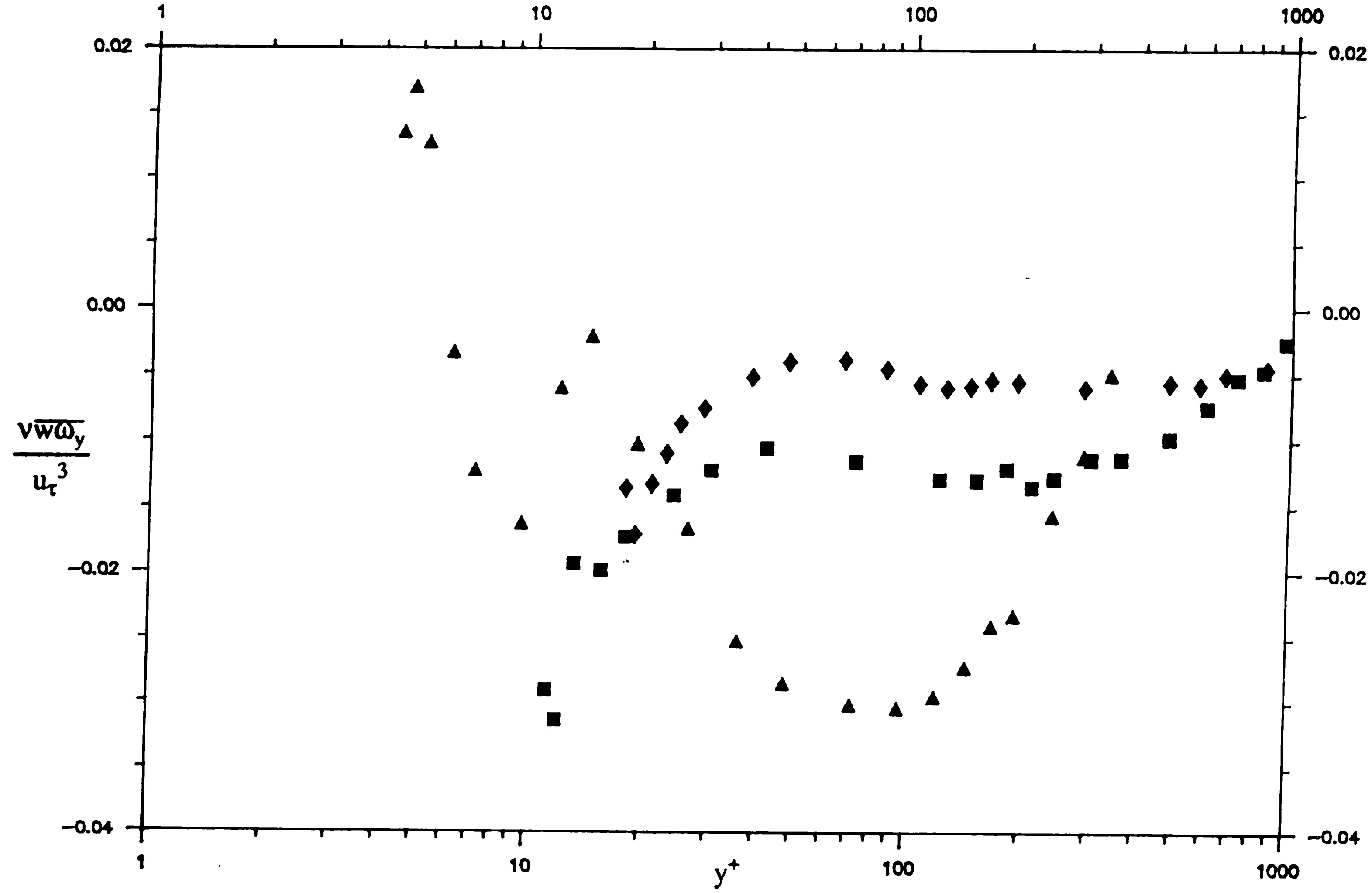

Figure A3.1.3 Figure 3: Deduced $v\overline{w\omega_y}/u_\tau^3$ profiles using the $\partial/\partial y(\overline{uv})$ data of Klewicki and Falco[6], the data of figure 1, and Eq. (2); symbols same as in figure 1.

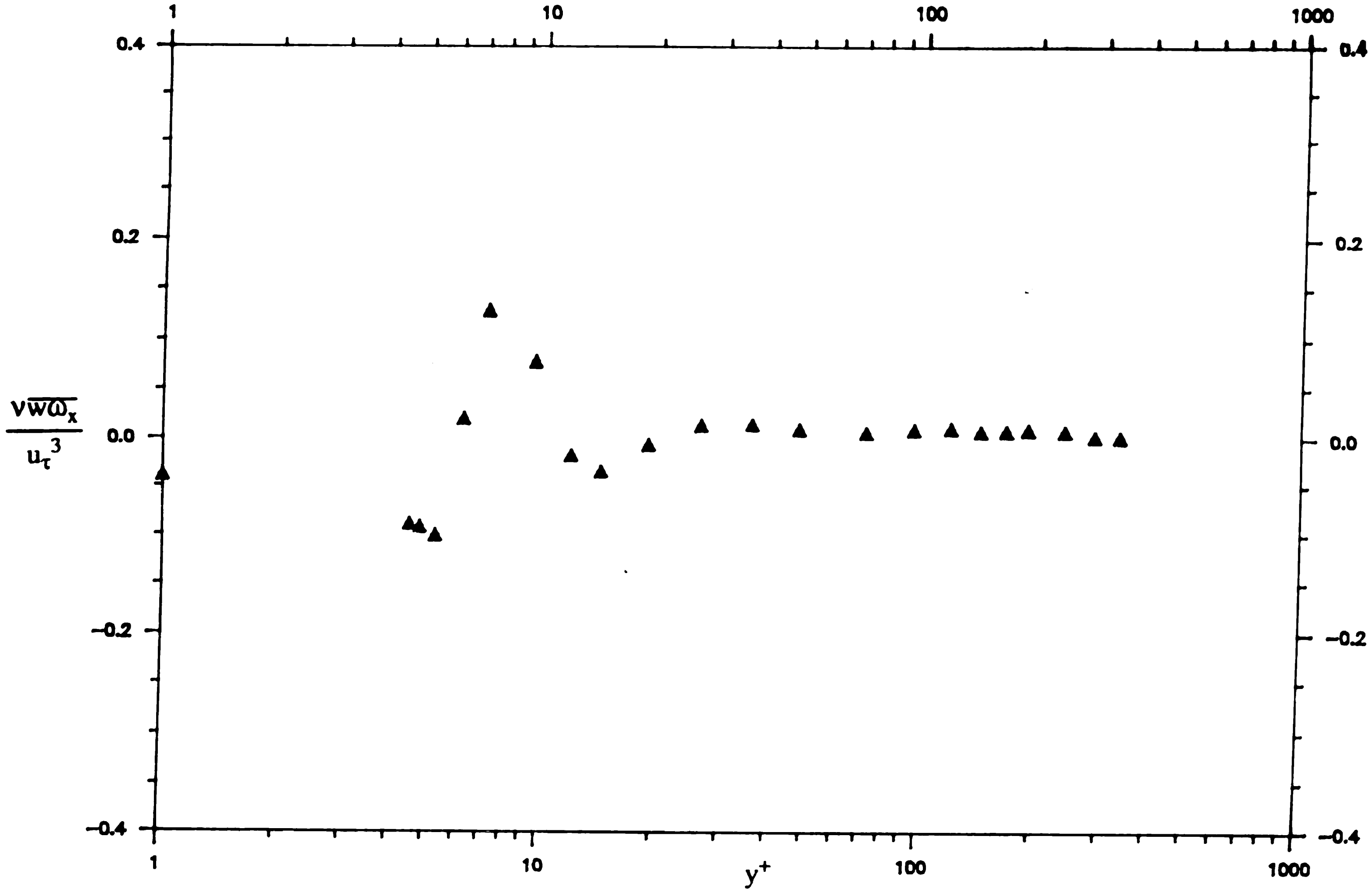

Figure A3.1.4 Figure 4: Approximate high Reynolds number $\nu\overline{w\omega_x}/u_\tau^3$ profiles deduced using the formulas of Phillips[7], the $R_\theta = 1{,}010$ data of figure 2, and Eq. (10); symbols same as in figure 1.

REFERENCES

[1]J. O. Hinze, *Turbulence* (McGraw-Hill, New York, 1975), 2nd ed.

[2]J. Laufer, *Ann. Rev. Fluid Mech.* **7**, 307 1975.

[3]W. W. Willmarth, in *Adv. in Appl. Mech.*, Vol. 15, edited by C. S. Yih (Academic Press, New York, 1975) p. 159.

[4]J. L. Balint, P. Vukoslavcevic, and J. M. Wallace, in *Advances in Turbulence*, eds. G. Comte-Bellot & J. Mathieu, (Springer-Verlag, Berlin, 1987) p. 456.

[5]J. F. Foss and J. M. Wallace, to appear in *Frontiers in Experimental Fluid Mechanics*, edited by M. Gad-el-Hak, (Springer-Verlag, Berlin, 1989).

[6]J. C. Klewicki and R. E. Falco, Rep. *TSL*–88–4, Michigan State University, 1988.

[7]W. R. C. Phillips, *Phys. Fluids* **30**, 2354 1987.

[8]J. C. Klewicki and R. E. Falco, to be submitted to *J. Fluid Mech.*.

[9]V. S. Arpaci and P. S. Larsen, *Convection Heat Transfer*, (Prentice-Hall, Englewood Cliffs, N.J., 1984).

[10]J. C. Klewicki, (unpublished) 1988.

[11]J. C. Klewicki and R. E. Falco, *Bull. Am. Phys. Soc.* **33**, 2286 1988.

[12]T. Wei, *Ph. D. dissertation*, University of Michigan, 1987.

APPENDIX 3.2 OUTER VARIABLE NORMALIZATIONS

This appendix gives outer variable normalizations of the present average and rms velocity, Reynolds stress and velocity vorticity correlation profiles. The presentation of these profiles allows for the interested reader to compare and contrast the outer variable normalizations of this appendix with the inner variable normalizations presented in Chapter 3. Specifically, the presentation of these data normalizations gives the reader the opportunity to make a more complete judgement concerning the validity of the conclusions and suggestions pertaining to flow physics made in Chapter 3.

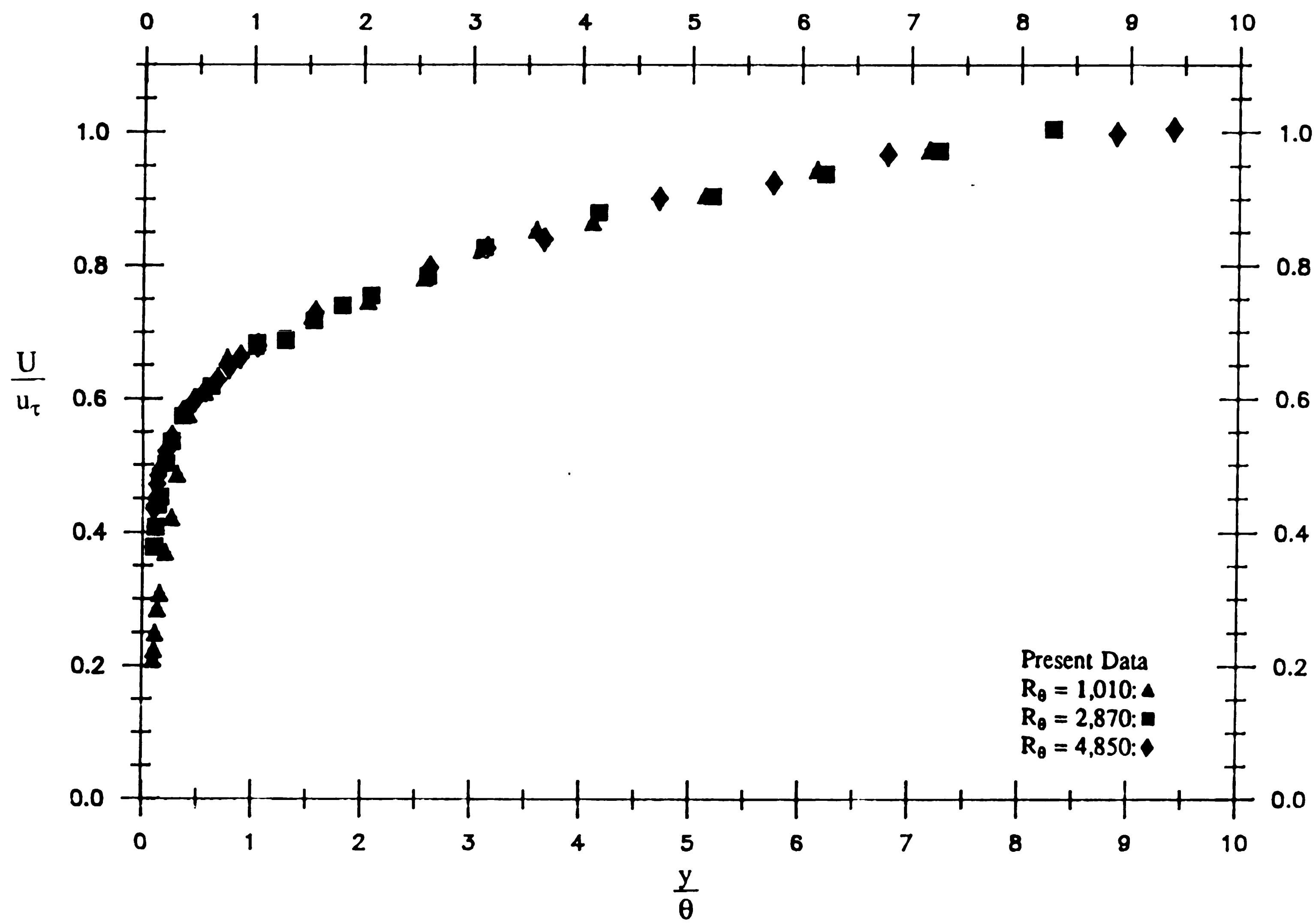

Figure A3.2.1 Mean velocity profiles normalized by u_τ and plotted versus y/θ.

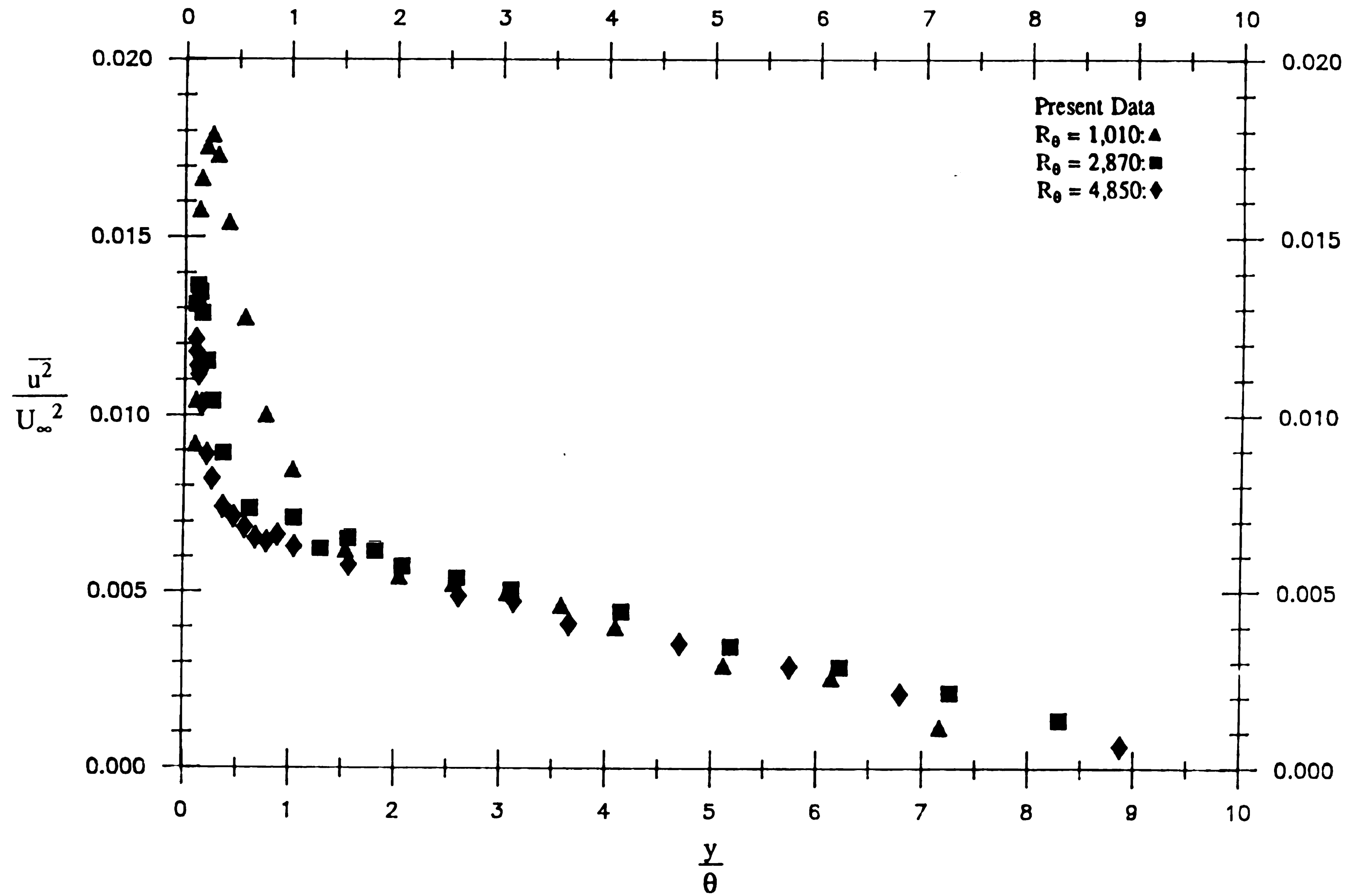

Figure A3.2.2 Streamwise fluctuating velocity variance profiles normalized by U_∞ and plotted versus y/θ.

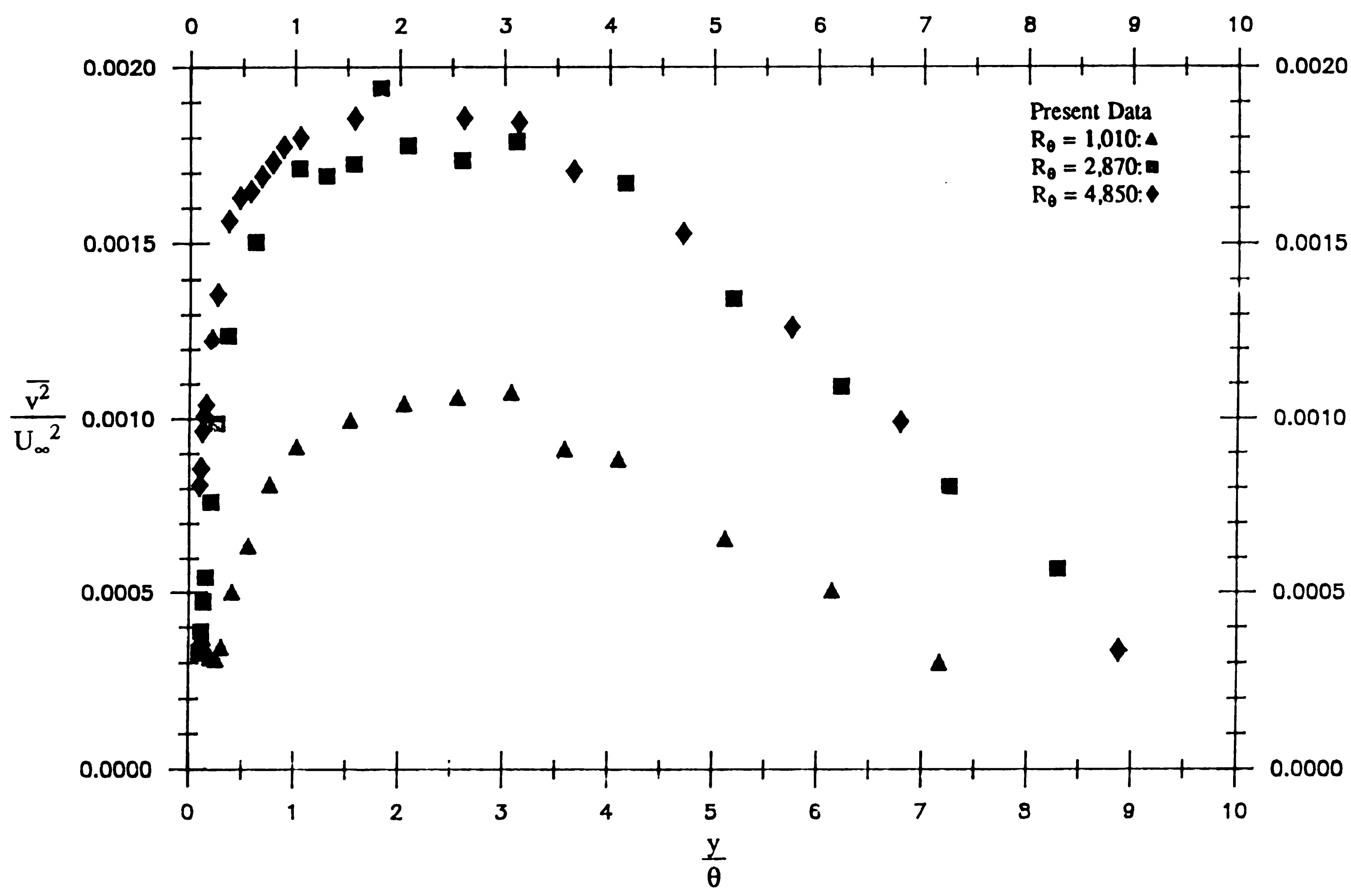

Figure A3.2.3 Normal fluctuating velocity variance profiles normalized by U_∞ and plotted versus y/θ.

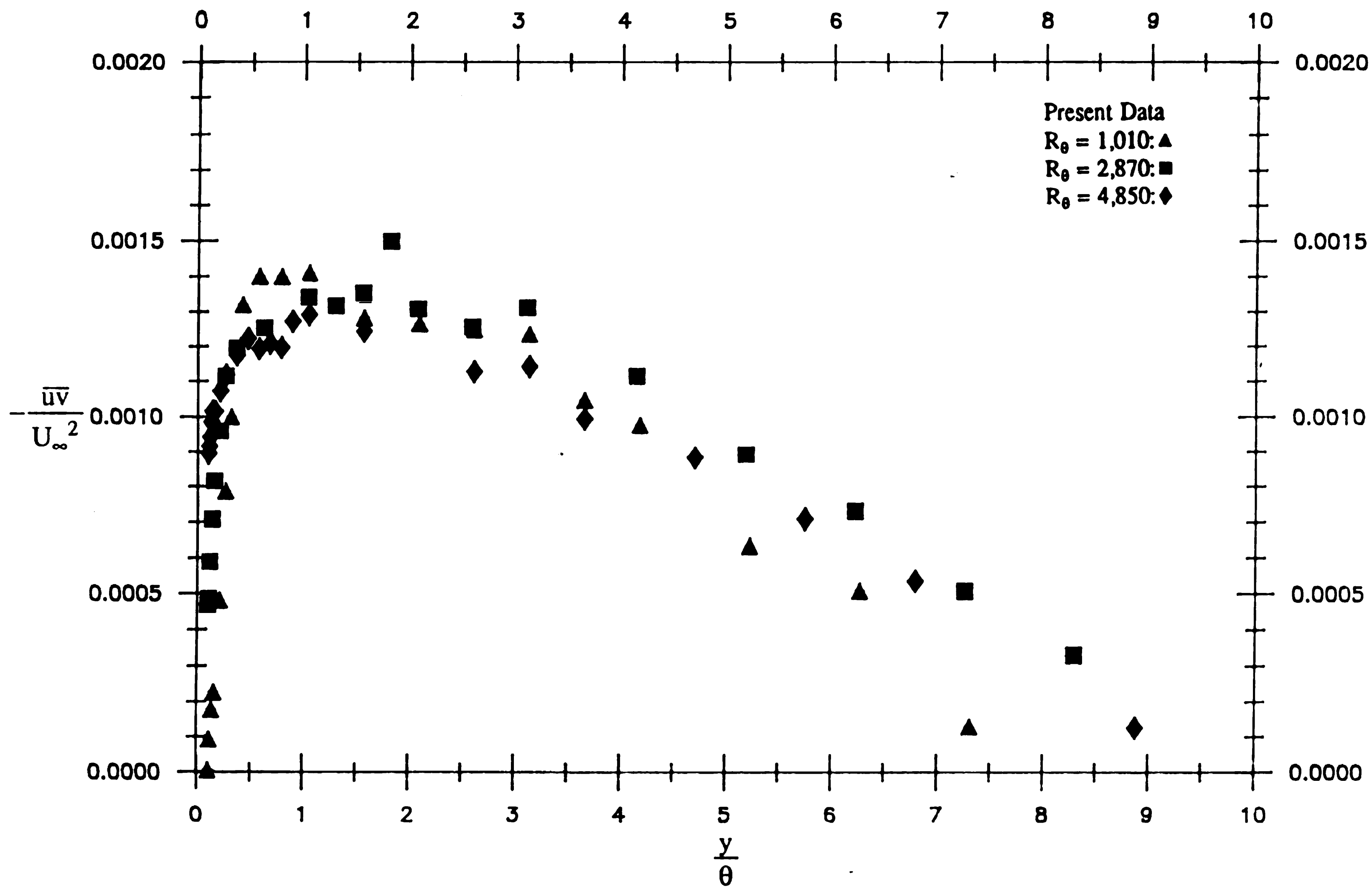

Figure A3.2.4 Reynolds stress profiles normalized by U_∞ and plotted versus y/θ.

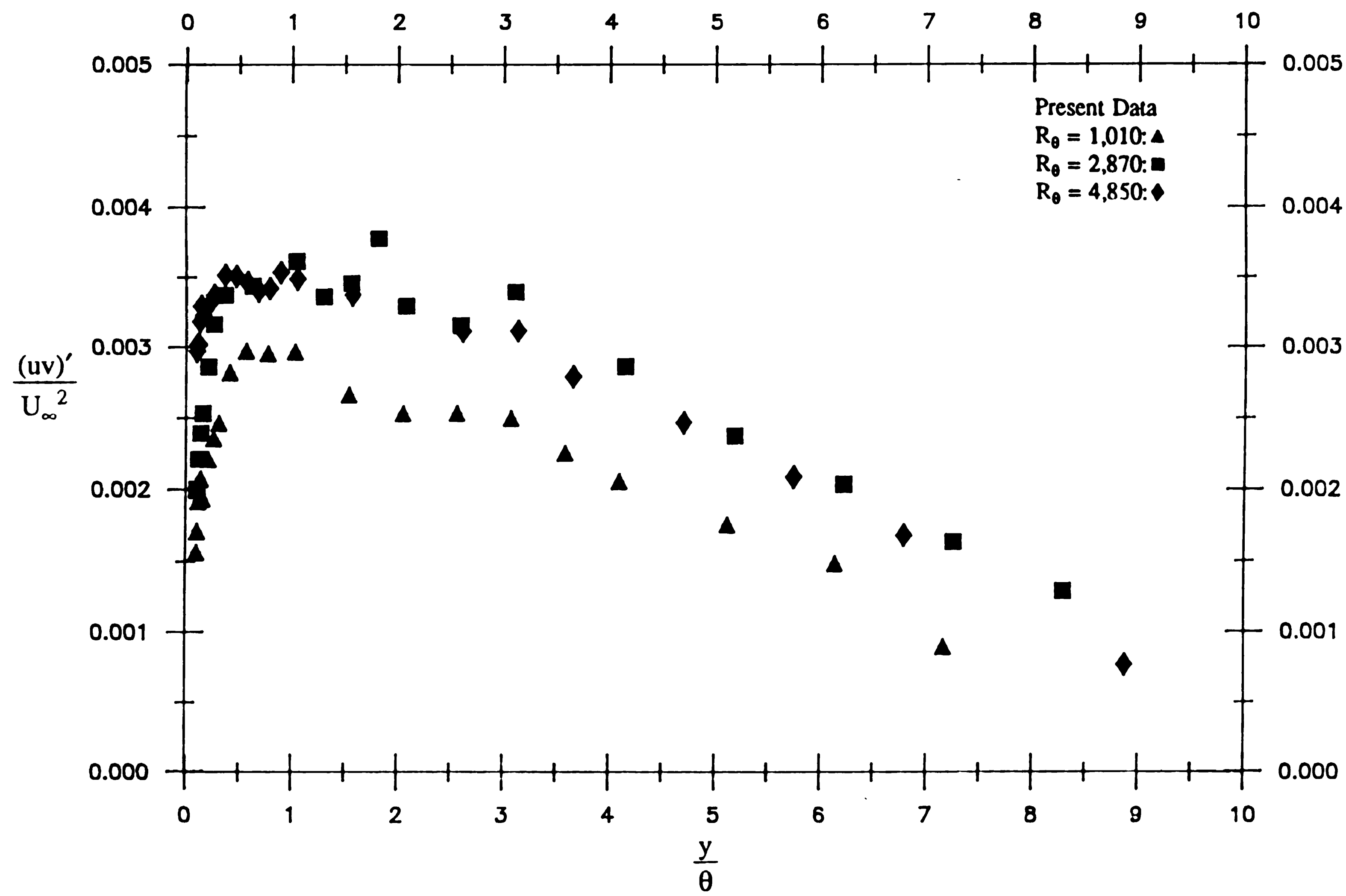

Figure A3.2.5 Reynolds stress rms profiles normalized by U_∞ and plotted versus y/θ.

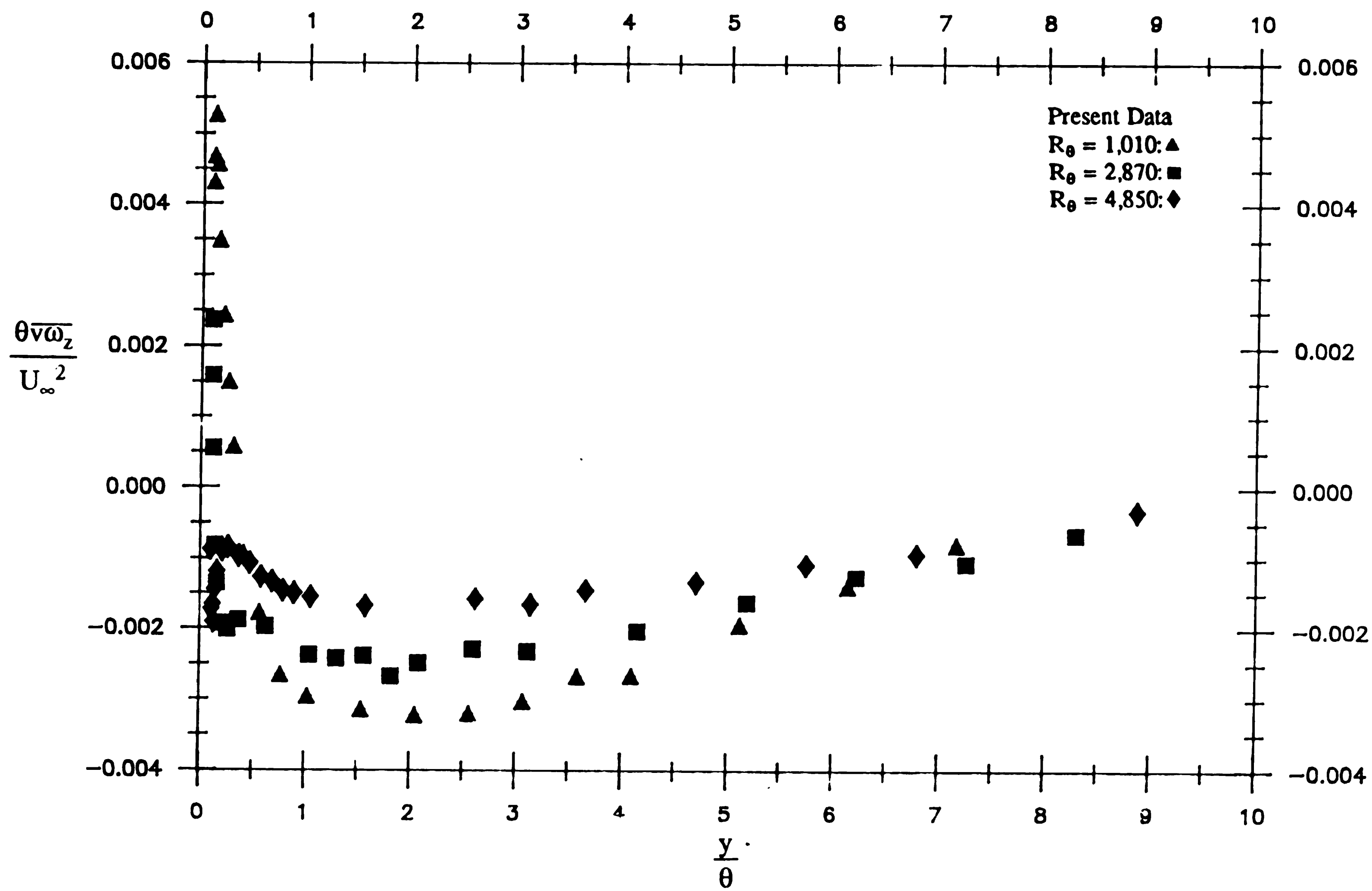

Figure A3.2.6 $\langle v\omega_z \rangle$ profiles normalized by θ and U_∞ and plotted versus y/θ.

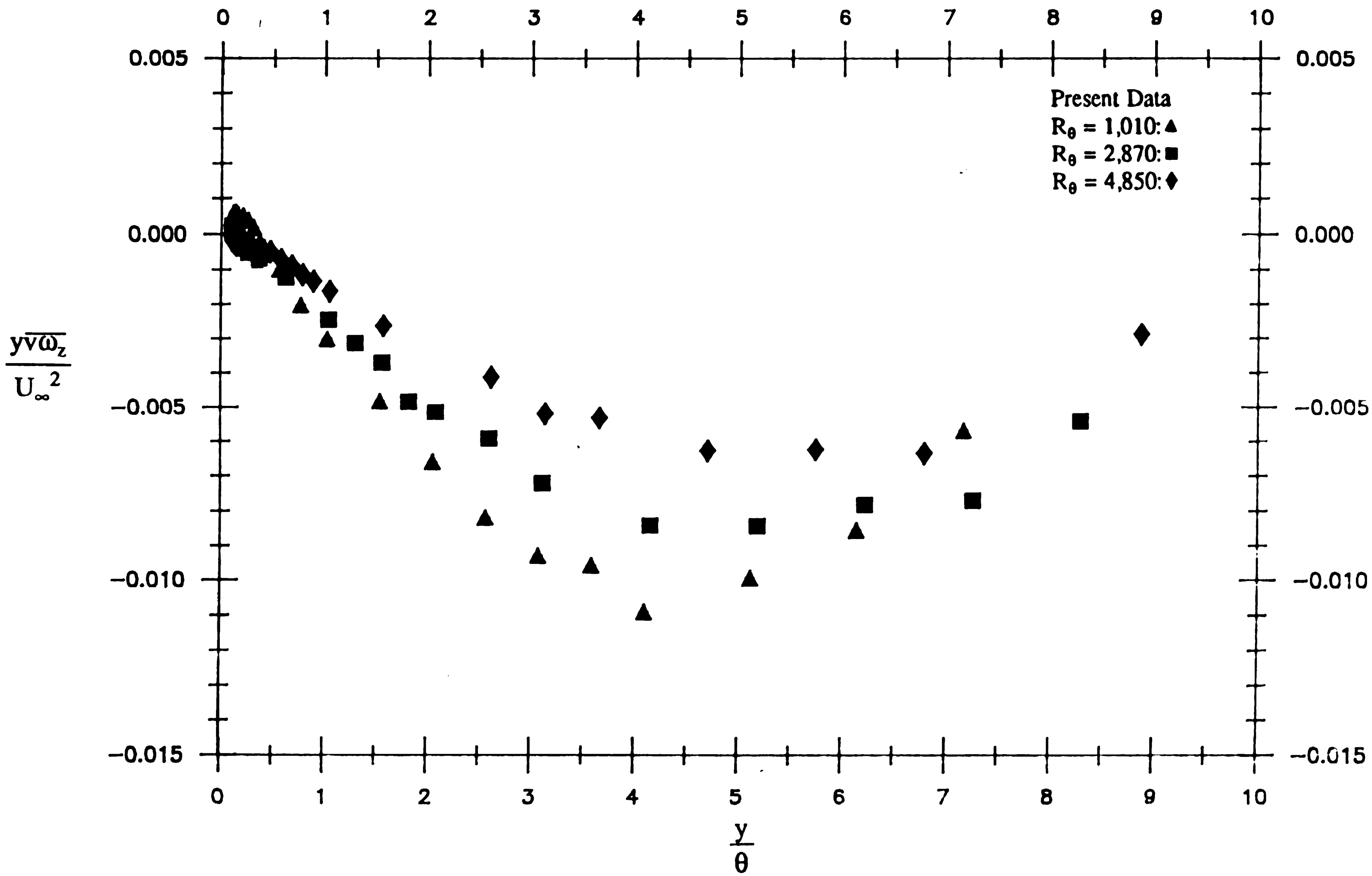

Figure A3.2.7 $<v\omega_z>$ profiles normalized by the function y/U_∞^2 and plotted versus y/θ.

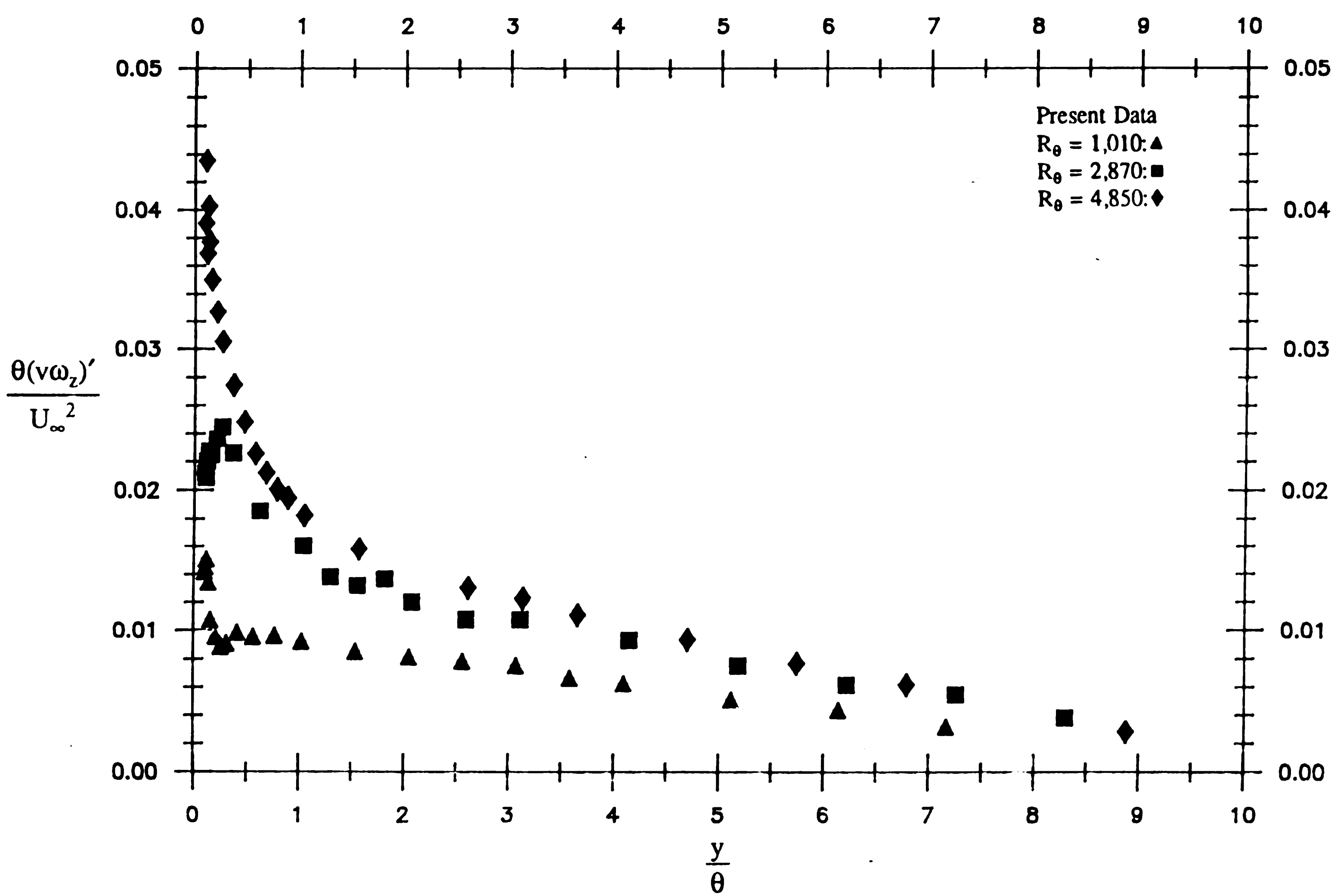

Figure A3.2.8 $(v\omega_z)'$profiles normalized by θ and U_∞ and plotted versus y/θ.

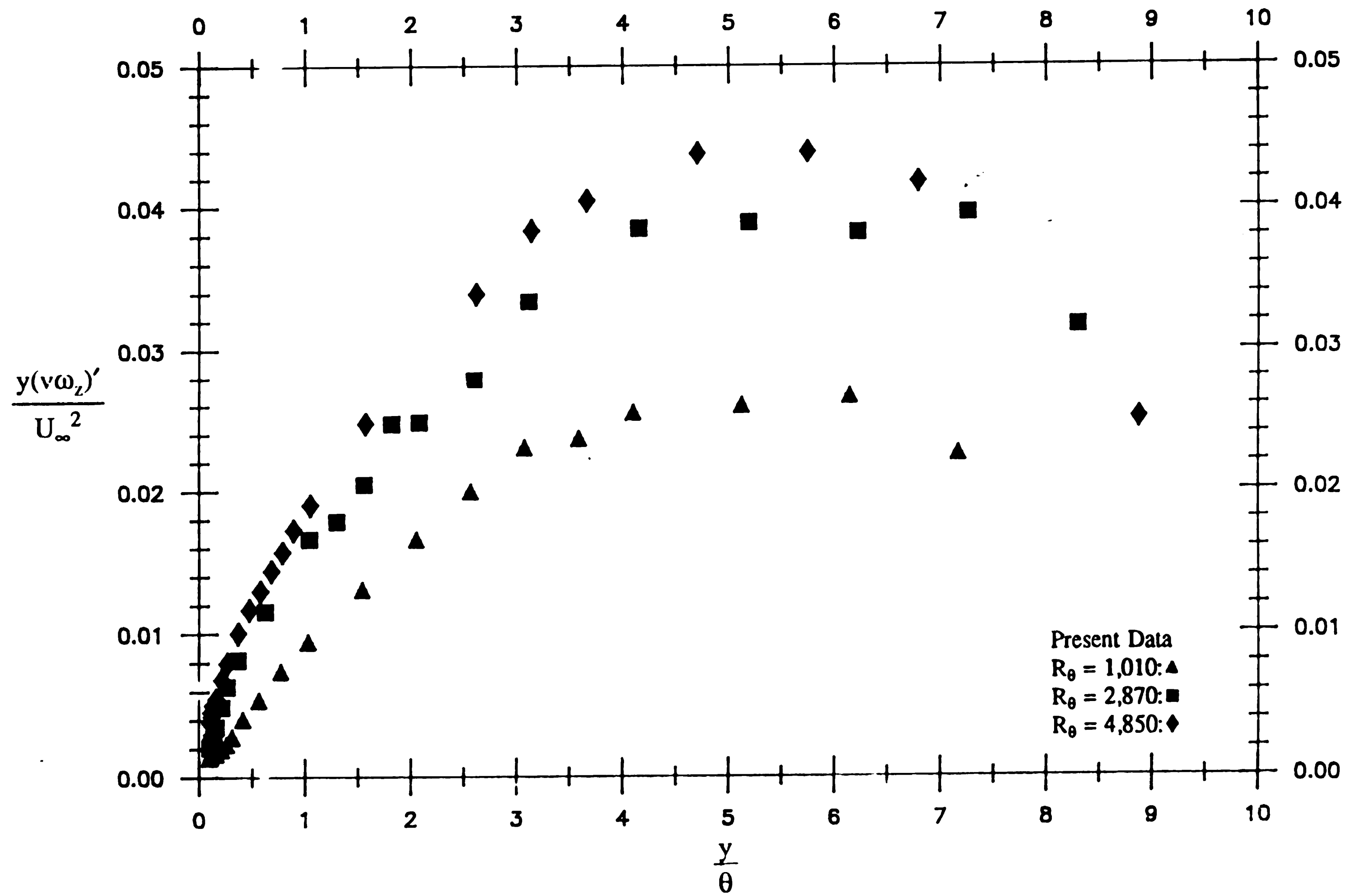

Figure A3.2.9 $(v\omega_z)'$ profiles normalized by the function y/U_∞^2 and plotted versus y/θ.

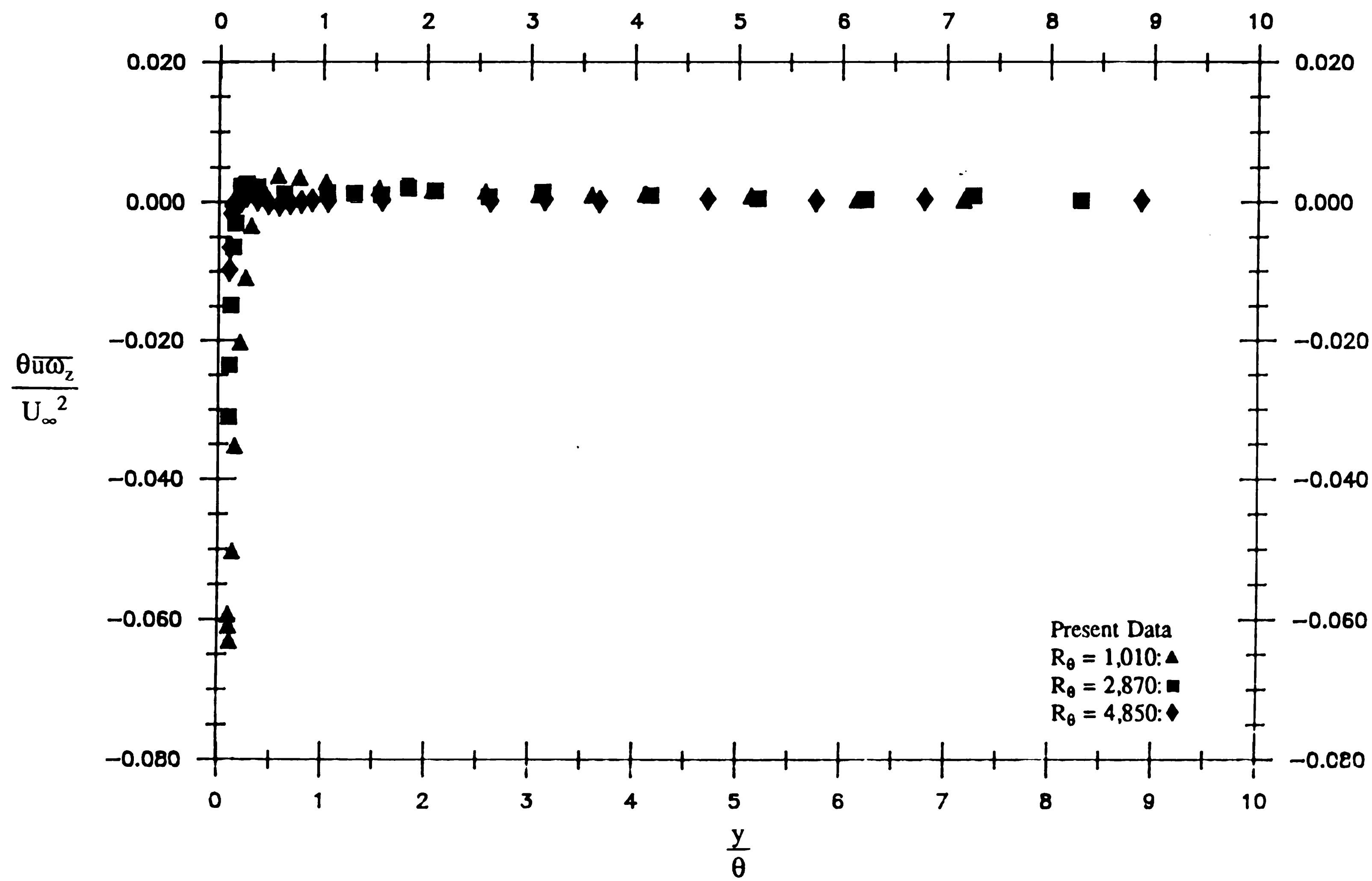

Figure A3.2.10 <$u\omega_z$> profiles normalized by θ and U_∞ and plotted versus y/θ.

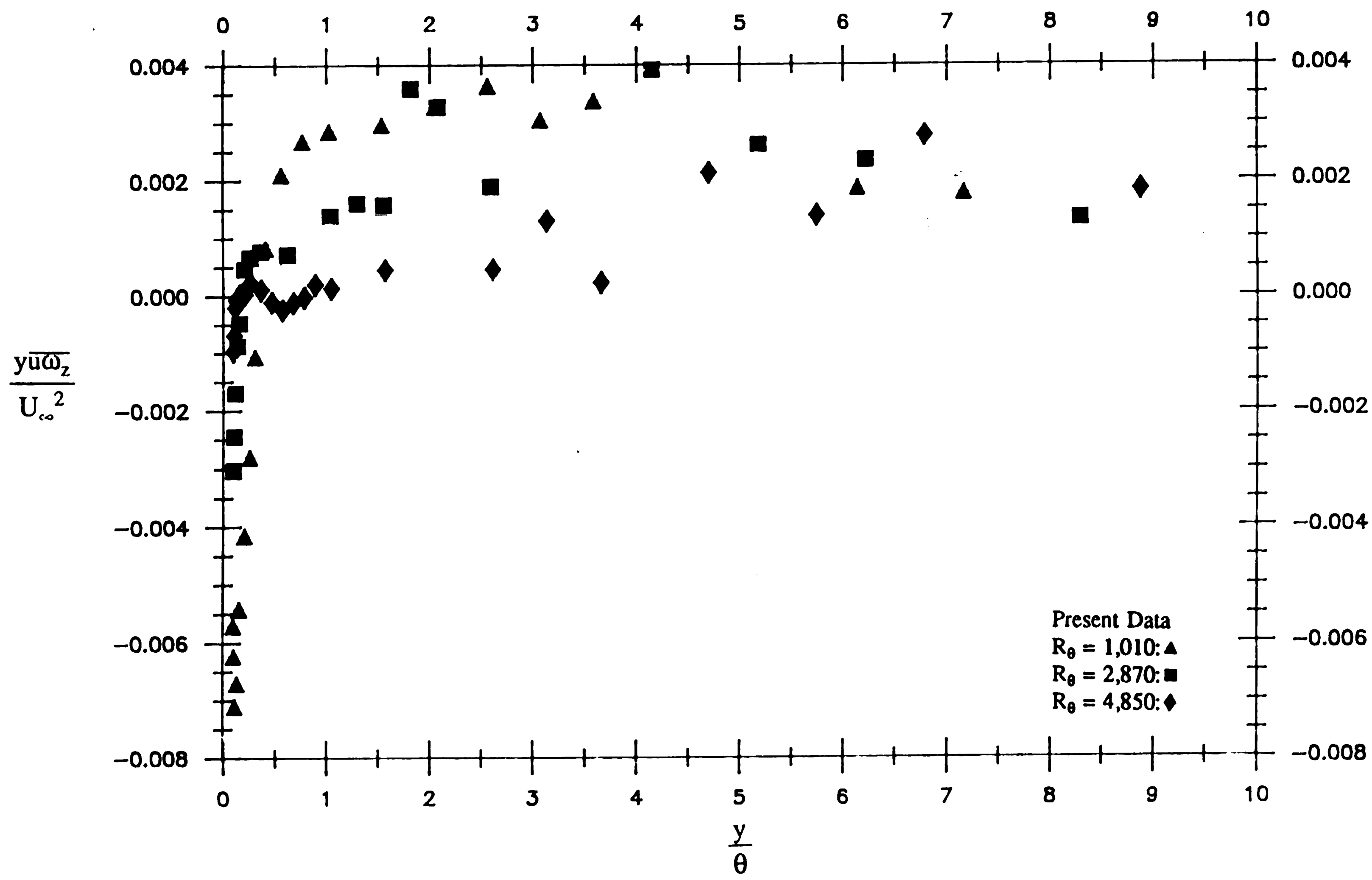

Figure A3.2.11 $<u\omega_z>$ profiles normalized by the function y/U_∞^2 and plotted versus y/θ.

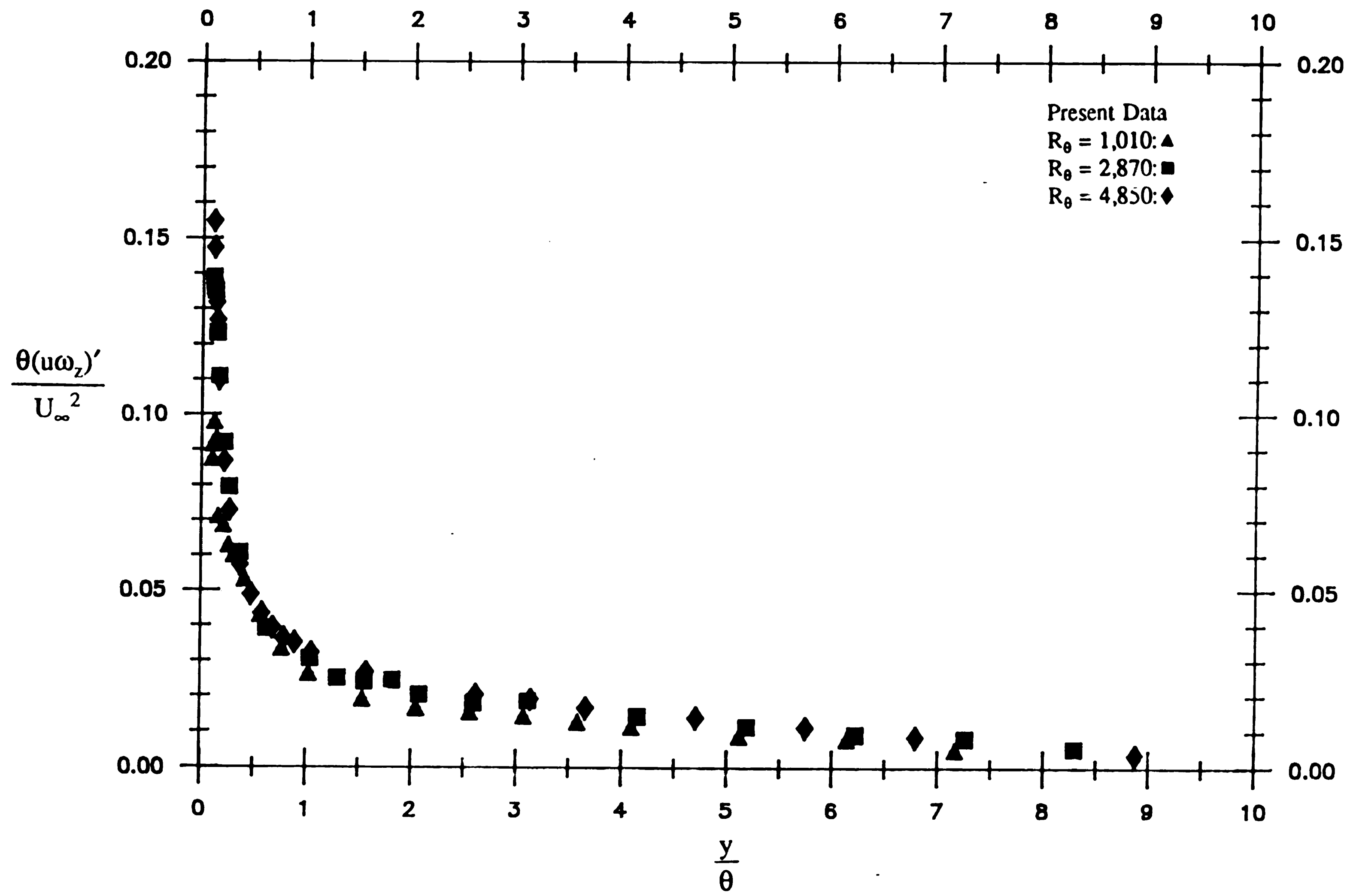

Figure A3.2.12 $(u\omega_z)'$ profiles normalized by θ and U_∞ and plotted versus y/θ.

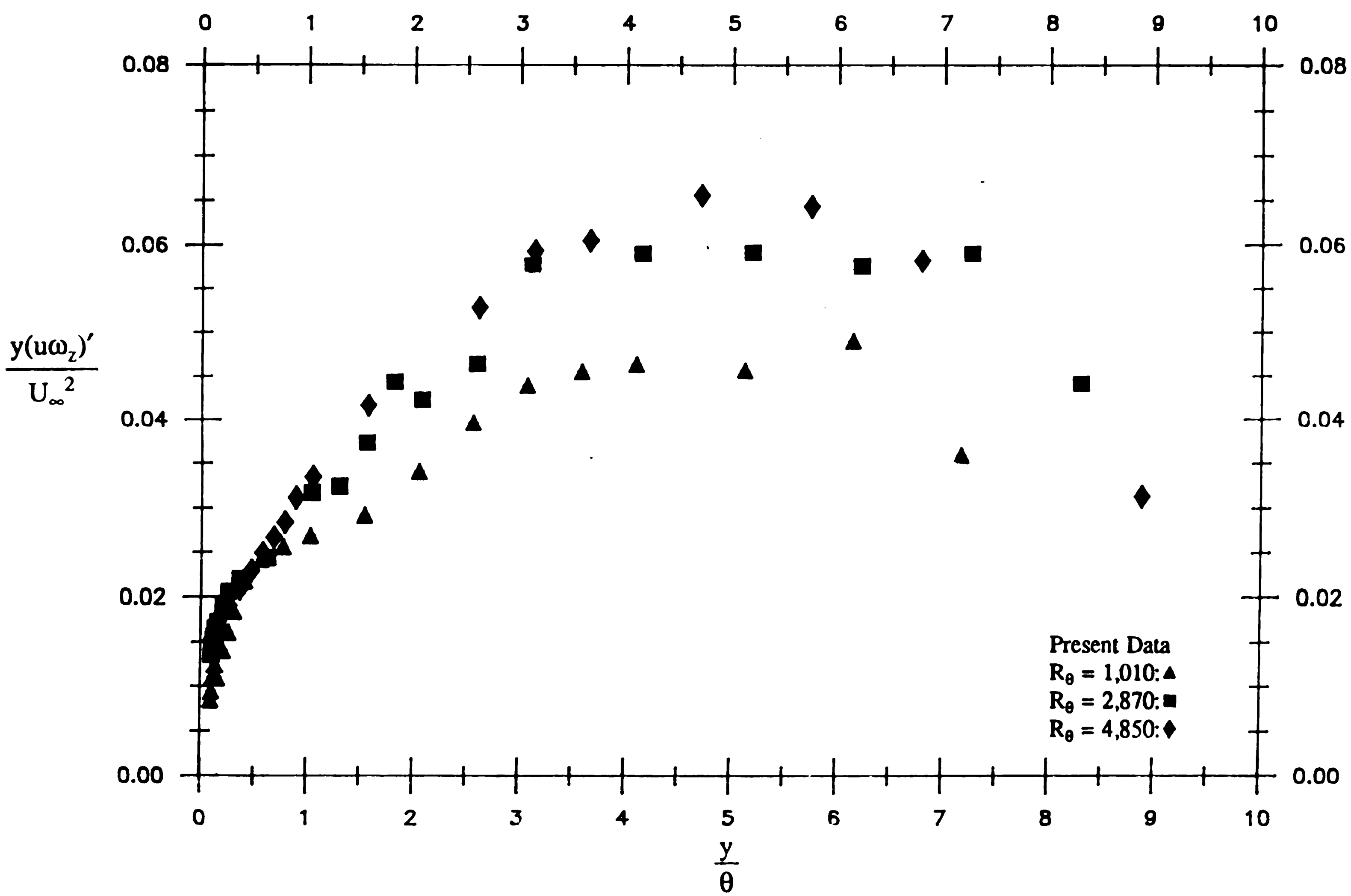

Figure A3.2.13 $(u\omega_z)'$ profiles normalized by the function y/U_∞^2 and plotted versus y/θ.

LIST OF REFERENCES

LIST OF REFERENCES

Alfredsson, P. H., Johansson, A. V., Haritonidis, J. H. and Eckelmann, H. 1988 Phys. Fluids 31, 1026.

Andreopoulos, J., Durst, F., Zaric', Z. and Jovanovic, J. 1984 Exp. in Fluids 2, 7.

Antonia, R. A., Browne, L. W. B. and Chambers, A. J. 1985 Phys. Fluids 28, 420.

Antonia, R. A. and Luxton, R. E. 1971 J. Fluid Mech. 48, 721.

Antonia, R. A., Rajagopalan, S., Subramanian, C. S. and Chambers, A. J. 1982a J. Fluid Mech. 121, 123.

Antonia, R. A., Satyaprakash, B. R. and Hussain, A. K. M. F. 1982b J. Fluid Mech. 119, 55.

Bakewell, H. P. and Lumley, J. L. 1967 Phys. Fluids 10, 1880.

Balint, J. L., Vukoslavcevic, P. and Wallace, J. M. 1987a In Advances in Turbulence, Proc. First European Turbulence Conference, Lyon, France (ed. G. Comte-Bellot and J. Mathieu) Springer-Verlag, Berlin, p. 456.

Balint, J. L., Vukoslavcevic, P. and Wallace, J. M. 1987b Bull. Am. Phys. Soc. 32, 2051.

Barenblatt, G. I. 1979 Similarity, Self-Similarity and Intermediate Asymptotics, Consultants Bureau, New York.

Barlow, R. S. and Johnston, J. P. 1985 Rep. MD-47, Dept. of Mech. Eng., Stanford University, Stanford, California.

Batchelor, 1967 An Introduction to Fluid Mechanics, Cambridge University Press.

Blackwelder, R. F. 1983 in Turbulent Shear Flows, Von Karman Institute for Fluid Dynamics Lecture Series 1983-03.

Blackwelder, R. F. and Eckelmann, H. 1979 J. Fluid Mech. 94, 577.

Blackwelder, R. F. and Haritonidis J. H. 1983 J. Fluid Mech. 132, 87.

Blackwelder, R. F. and Kovasznay, L. S. G. 1970 Rep. No. DA-31-124-ARO-D-313 The Johns Hopkins University Dept. of Mech., Baltimore, Maryland.

Bottcher, J. and Eckelmann, H. 1985 Exps. in Fluids 3, 87.

Bradshaw, P. 1967 J. Fluid Mech. 30, 241.

Bradshaw, P. 1971 An Introduction to Turbulence and its Measurement, Pergamon Press, Elmsford, New York, p. 123.

Brown, G. L. and Thomas, A. S. W. 1977 Phys. Fluids Suppl. 20, 243.

Browne, L. W. B., Antonia, R. A. and Rajagopalan, S. 1983 Phys. Fluids 26, 1222.

Browne, L. W. B., Antonia, R. A. and Shah, D. A. 1987 J. Fluid Mech. 179, 307.

Browne, L. W. B., Antonia, R. A. and Chua, L. P. 1989 Exps. in Fluids 7, 201.

Bull, M. K. and Thomas, A. S. W. 1983 J. Fluid Mech. 128, 283.

Burkhardt, W. M. 1982 M.S. thesis, Michigan State University, East Lansing, Michigan.

Bushnell, D. M. 1985 in Theoretical Approaches to Turbulence, (ed. D. L. Dwoyer, M. Y. Hussaini and R. G. Voigt) Springer-Verlag Applied Mathematical Sciences Series no. 58, Berlin, p. 1.

Champagne, F. H., Sleicher, C. A. and Wehrmann, O. H. 1967 J. Fluid Mech. 28, 153.

Chen, C. H. P. and Blackwelder R. F. 1978 J. Fluid Mech. 89, 1.

Chu, C. C. 1988 Ph.D. dissertation, Michigan State University East Lansing, Michigan.

Coles, D. E. 1956 J. Fluid Mech. 1, 191.

Coles, D. E. 1962 Report R-403-Pr, Rand Corporation.

Coles, D. E. 1968 in Proceedings of Computation of Turbulent Boundary Layers, AFOSR-IFP-Stanford Conference, (ed. Coles and Hirst), Stanford University, California.

Coles, D. E. 1987 in Perspectives in Turbulence Studies (ed. H. U. Meier and P. Bradshaw), Springer Verlag, Berlin, p. 93.

Comte-Bellot, G. 1963 Doctoral thesis, University of Grenoble, France.

Corino, E. R. and Brodkey, R. S. 1969 J. Fluid Mech. 37, 1.

Corrsin, S. and Kistler, A. L. 1954 NACA TN 3133.

deBray, B. G. 1967 Brit. Aero. Res. Council Rep. 29-271.

Eckelmann, H., Nychas, S. G., Brodkey, R. S. and Wallace, J. M. 1977 Phys. Fluids Suppl. 20, S225.

Emmerling, R. 1973 Max-Planck-Institut fur Stromungsforschung, Bericht 9/1973.

Falco, R. E. 1974 AIAA 74-99.

Falco, R. E. 1977 Phys. Fluids Suppl. 20, S124.

Falco, R. E. 1980 AIAA-80-1356.

Falco, R. E. 1982 in Structure of Turbulence in Heat and Mass Transfer, (ed. by Z. P. Zaric'), Hemisphere Publishing Corp., Washington, p. 43.

Falco, R. E. 1983 AIAA-83-0377.

Falco, R. E. 1987 in Communications to the Workshop on Turbulent Wall Layers (organized by R. L. Panton and D. G. Bogard), Fluid Dynamics Group of the Bureau of Engineering Research, University of Texas at Austin.

Foss, J. F., Klewicki, C. L. and Disimile, P. J. 1986a NASA CR 178098.

Foss, J. F., Ali, S. K. and Haw, R. C. 1986b in Advances in Turbulence, Proc. First European Turbulence Conference, Lyon, France (ed. G. Comte-Bellot and J. Mathieu) Springer-Verlag, Berlin, p. 446.

Foss, J. F. and Wallace, J. M. 1989 to appear in Frontiers in Experimental Fluid Mechanics (ed. by M. Gad-el-Hak in Lect. Notes in Engineering series), Springer-Verlag, New York.

Grass, A. J. 1971 J. Fluid Mech. 50, 223.

Guezennec, Y. G. 1985 Ph.D. dissertation, Illinois Institute of Technology, Chicago, Illinois.

Gupta, A. K. and Kaplan, R. E. 1972 Phys. Fluids 15, 981.

Head, M. R. and Bandyopadhyay P. 1981 J. Fluid Mech. 107, 297.

Hinze, J. O. 1975 Turbulence, McGraw-Hill Inc.

Hogenes, J. G. A. and Hanratty, T. J. 1982 J. Fluid Mech. 124, 363.

Huffman, G. D. and Bradshaw, P. 1972 J. Fluid Mech. 53, 45.

Hussain, A. K. M. F. 1986 J. Fluid Mech. 173, 303.

Johansson, A. V. and Alfredsson P. H. 1983 J. Fluid Mech. 137, 409.

Johnson, F. D. and Eckelmann, H. 1983 Phys. Fluids 26, 2408.

Jimenez, J., Moin, P., Moser, R. and Keefe, L. 1988 Phys. Fluids 31, 1311.

Kastrinakis, E. G. 1977 Max-Planck-Institut fur Stromungsforschung, Bericht 5/1977.

Kastrinakis, E. G. and Eckelmann, H. 1983 J. Fluid Mech. 137, 165.

Kim, H. T., Kline S. J. and Reynolds, W. C. 1971 J. Fluid Mech. 50, 133.

Kim, J., Moin, P. and Moser, R. 1987 J. Fluid Mech. 177, 133.

King, L. V. 1914 Phil. Trans. R. Soc. London A 214, 373.

Klebanoff, P. S. 1954 NACA TN 3178.

Klewicki, J. C. and Falco, R. E. 1986 Bull. Am. Phys. Soc. 31, 1685.

Klewicki, J. C. and Falco, R. E. 1987 Bull. Am. Phys. Soc. 32, 2061.

Kline, S. J. 1978 in Coherent Structure of Turbulent Boundary Layers, An AFOSR/Lehigh University Workshop, (ed. C. R. Smith and D. E. Abbott) Lehigh University, Bethlehem, Pennsylvania, p. 1.

Kline, S. J., Reynolds, W. C., Schraub, F. A. and Runstadler, P. W. 1967 J. Fluid Mech. 30, 741.

Kovasznay, L. S. G., Komoda, H. and Vasudeva, B. R. 1962 in Proc. Heat Transfer and Fluid Mech. Inst., Stanford Univ. Press, p. 1.

Kovasznay, L. S. G., Kibens, V. and Blackwelder, R. F. 1970 J. Fluid Mech. 41, 283.

Kovasznay, L. S. G. 1978 "Panel discussion on coherent structures" Second Shear Flows Conference, London, England.

Kreplin, H. P. and Eckelmann H. 1979 Phys. Fluids 22, 1233.

Lang, D. B. 1985 PhD dissertation, California Institute of Technology, Pasadena, California.

Laufer, J. 1950 NACA TN 2123.

Lee, M. K., Eckelman, L. D. and Hanratty, T. J. 1974 J. Fluid Mech. 66, 17.

Ligrani, P. M. and Bradshaw, P. 1987 Exps. in Fluids 5, 407.

Loerke, R. I. and Nagib, H. M. 1977 AGARD Report, R-598, AD-749-891.

Lovett, J. A. 1982 M.S. thesis, Michigan State University, East Lansing, Michigan.

Lu, L. J. and Smith C. R. 1988 Report FM-14, Dept. of Mech. Engr. and Mech., Lehigh Univerisity, Bethlehem, PA.

Lu, S. S. and Willmarth, W. W. 1973 J. Fluid Mech. 60, 481.

Luchik, T. S. and Tiederman, W. R. 1987 J. Fluid Mech. 174, 529.

Lueptow, R. M., Breuer, K. S. and Haritonidis, J. H. 1988 Exps. in Fluids 6, 115.

Magnus, G. 1853 Poggendorf's Annalen der Physik u. Chemie 88, 1.

Mestayer, P. 1982 J. Fluid Mech. 124, 475.

Mitchell, R. 1987 MSU-ENG-87-015-D-FSFL, Michigan State University Dept. of Mech. Eng., East Lansing, Michigan.

Murlis, J., Tsai, H. M. and Bradshaw, P. 1982 J. Fluid Mech. 122, 13.

Offen, G. R. and Kline, S. J. 1975 J. Fluid Mech. 70, 209.

Perry, A. E. and Abell, C. J. 1975 J. Fluid Mech. 67, 257.

Phillips, W. R. C. 1987 Phys. Fluids 30, 2354.

Praturi, A. K. and Brodkey, R. S. 1978 J. Fluid Mech. 89, 251.

Purtell, L. P., Klebanoff P. S. and Buckley F. T. 1981 Phys. Fluids 24, 802.

Rao, K. N., Narasimha, R. and Narayanan, M. A. B. 1971 J. Fluid Mech. 48, 339.

Rashidnia, N. 1985 PhD dissertation, Michigan State University, East Lansing, Michigan.

Roberts, J. B. 1973 Aeronaut. J. 77, 406.

Sabot, J. and Comte-Bellot, G. 1976 J. Fluid Mech. 74, 767.

Schewe, G. 1983 J. Fluid Mech. 134, 311.

Shah, D. A. and Antonia, R. A. 1988 submitted to Phys. Fluids.

Simpson, R. L. J. Fluid Mech. 42, 769.

Signor, D. B. 1982 M.S. thesis, Michigan State University, East Lansing, Michigan.

Smith, C. R. and Lu, L. J. 1988 in Proceedings of the Z. Zaric International Seminar on Wall Turbulence, (ed. S. J. Kline) Hemisphere Press, 1988 (in press).

Smith, C. R. and Metzler, S. P. 1983 J. Fluid Mech. 129, 27.

Spalart, P. 1988 J. Fluid Mech. 187, 61.

Spalding, D. B. 1961 Trans. of the A.S.M.E. 28E, 455.

Sreenivasan, K. R. 1989 to appear in Frontiers in Experimental Fluid Mechanics (ed. by M. Gad-el-Hak in Lect. Notes in Engineering series), Springer-Verlag, New York.

Subramanian, C. S., Kandola, B. S. and Bradshaw, P. 1985 IC Aero Rept. 85-01.

Tennekes, H. and Lumley, J. L. 1972 A First Course in Turbulence, M.I.T. Press.

Tennekes, H. and Wyngaard, J. C. 1972 J. Fluid Mech. 55, 93.

Townsend, A. A. 1956 The Structure of Turbulent Shear Flow, 1st ed., Cambridge University Press.

Townsend, A. A. 1961 J. Fluid Mech. 11, 97.

Townsend, A. A. 1976 The Structure of Turbulent Shear Flow, 2nd ed., Cambridge University Press.

Uberoi, M. S., and Kovasznay, L. S. G. 1953 Quart. Appl. Math. vol. X, no. 4, 375.

Ueda, H. and Hinze, J. O. 1975 J. Fluid Mech. 67, 125.

van Driest, E. R. 1956 J. Aeronaut Sci. 23, 1007.

Vukoslavcevic, P., and Wallace, J. M. 1981 Rev. Sci. Instrum. 52, 869.

Wallace, J. M., Brodkey, R. S. and Eckelmann, H. 1977 J. Fluid Mech. 83, 673.

Wallace, J. M. 1982 in Developments in Theoretical and Applied Mechanics vol. XI, 509.

Wallace, J. M. 1986 Exp. in Fluids 4, 61.

Wark C. E. 1988 Ph.D. dissertation, Illinois Institute of Technology, Chicago, Illinois.

Wei, T. 1987 Ph.D. dissertation, University of Michigan, Ann Arbor, Michigan.

White, B. R. 1981 Trans. of the A.S.M.E. 103, 624.

Willmarth, W. W. 1975 in Advances in Applied Mechanics, (ed. C. S. Yih), Academic Press, New York, p. 159.

Willmarth, W. W. and Bogar, T.J. 1977 Phys. Fluids Suppl. 20, S9.

Willmarth, W. W. and Sharma, L. K. 1984 J. Fluid Mech. 142, 121.

Willmarth, W. W. and Tu, B. J. 1967 Phys. Fluids Suppl. 10, S134.

Wyngaard, J. C. 1968 J. Phys. E. 1, 1105.

Wyngaard, J. C. 1969 J. Phys. E. 2, 983.